Developments for the laser spectroscopy of exotic nuclei with the S^3 Low Energy Branch and the FRIENDS^3 project

Wenling Dong

université PARIS-SACLAY

Developments for the laser spectroscopy of exotic nuclei with the S^3 Low Energy Branch and the FRIENDS^3 project

Développements pour la spectroscopie laser de noyaux exotiques avec la Branche de Basse Energie de S^3 et le projet FRIENDS^3

Thèse de doctorat de l'université Paris-Saclay

École doctorale n°576 : particules, hadrons, énergie et noyau : instrumentation, imagerie, cosmos et simulation (PHENIICS)
Spécialité de doctorat : Physique Nucléaire
Graduate School : Physique Référent : Faculté des sciences d'Orsay

Thèse préparée dans l'unité de recherche **IJCLab (Université Paris-Saclay, CNRS)**, sous la direction de **François LE BLANC**, directeur de recherche, et le co-encadrement de **Vladimir MANEA**, chargé de recherche

Thèse soutenue à Paris-Saclay, le 22 Novembre 2024, par

Wenling DONG

Composition du Jury

Membres du jury avec voix délibérative

Bertram BLANK Directeur de recherche, Université de Bordeaux, LP2I, Bordeaux	Président
Michael BLOCK Professeur, JGU Mainz, HIM/GSI, Allemagne	Rapporteur & Examinateur
Thomas Elias COCOLIOS Professeur, KU Leuven, Belgique	Rapporteur & Examinateur
Iolanda MATEA Maître de conférences, Université Paris-Saclay, IJCLab, Orsay	Examinatrice

THÈSE DE DOCTORAT

NNT : 2024UPASP149

université PARIS-SACLAY

ÉCOLE DOCTORALE
Particules, hadrons, énergie et noyau : instrumentation, imagerie, cosmos et simulation (PHENIICS)

Titre : Développements pour la spectroscopie laser de noyaux exotiques avec la Branche de Basse Energie de S^3 et le projet FRIENDS^3

Mots clés : spectroscopie laser, cellule gazeuse, déplacement isotopique, structure hyperfine, propriètes nucléaires, SPIRAL2

Résumé : Cette thèse présente une série de développements visant à réaliser la spectroscopie laser à ionisation résonante sur des isotopes à vie courte produits par le Spectromètre Super Séparateur (S^3) et stoppés dans la cellule à gaz de sa branche basse énergie (S^3-LEB). Cette recherche se concentre sur deux sujets.

Tout d'abord, des mesures de spectroscopie laser hors ligne ont été réalisées sur des isotopes stables d'erbium, l'élément de choix pour la mise en service en ligne de S^3-LEB. Ces mesures ont été réalisées en utilisant la configuration complète de S^3-LEB ainsi que la gamme de systèmes laser Ti:sa disponibles, représentant une validation des principes de fonctionnement de l'ensemble de l'appareillage. Pour identifier le schéma optimal pour les prochaines expériences en ligne, différentes transitions atomiques ont été étudiées par spectroscopie laser dans la cellule à gaz et dans le jet de gaz. Les déplacements isotopiques ont été déterminés pour les étapes d'excitation et d'ionisation. Les facteurs de champ F et de masse M des étapes d'excitation ont été extraits du déplacement isotopique à l'aide d'une analyse King-plot, et les incertitudes expérimentales associées aux deux facteurs ont été discutées. Des mesures de la puissance de saturation ont été effectuées et les coefficients d'élargissement et de décalage des raies dus à la pression ont été déterminés dans l'environnement de la cellule à gaz.

De plus, les coefficients hyperfins du premier état excité de la transition à 408,8 nm ont été extraits de la spectroscopie à jet gazeux à haute résolution avec une résolution spectrale d'environ 200 MHz. La transition à 408,8 nm de l'erbium est proposée comme une candidate appropriée pour les premières expériences sur S^3.

Deuxièmement, des simulations ont été réalisées afin de développer une future génération de cellule à gaz S^3-LEB optimisée pour l'étude des isotopes à courte durée de vie, ceux-ci présentant un temps d'extraction réduit et utilisant un mécanisme de neutralisation universel. Dans cette cellule à gaz, l'extraction rapide des ions est obtenue grâce à une combinaison du champ électrique et du flux gazeux. Des simulations ont été réalisées avec des logiciels de pointe afin de souligner l'aspect pluri-disciplinaire, notamment l'écoulement du gaz, le champ électrostatique, le transport des ions sous haute pression et la dynamique des électrons générés par l'ionisation des gaz. Sur la base de ces simulations, un prototype optimisé de cellule à gaz a été conçu en prenant en compte le temps d'extraction, l'efficacité, ainsi que le temps de neutralisation.

Title : Developments for the laser spectroscopy of exotic nuclei with the S^3 Low Energy Branch and the FRIENDS^3 project

Keywords : laser spectroscopy, gas stopping cell, isotope shift, hyperfine structure, nuclear properties, SPIRAL2

Abstract : This thesis presents a series of developments aimed to perform resonance-ionization laser spectroscopy on short-lived isotopes produced by the Super Separator Spectrometer (S^3) of SPIRAL2 at GANIL and stopped in the gas cell of its Low Energy Branch (S^3-LEB). This research focuses on two topics.

Firstly, off-line laser spectroscopy measurements were performed on stable isotopes of erbium, the element of choice for the on-line commissioning of S^3-LEB. These measurements were performed using the full S^3-LEB setup along with the range of available Ti:sa laser systems, representing a proof of principle of the entire apparatus. To identify the optimal scheme for the forthcoming on-line experiments, different atomic transitions were studied by laser spectroscopy in the gas cell and in the gas jet. Isotope shifts were determined for the excitation and ionization steps. Field and mass-shift factors for the excitation steps were extracted from the isotope-shift data using King-plot analysis, and the associated experimental uncertainties in the two factors were discussed. Saturation-power measurements were carried out and the pressure broadening and shift coefficients were determined in the gas-cell environment. Additionally, hyperfine coefficients for the first excited state of the 408.8 nm transition were extracted from the high-resolution gas-jet spectroscopy with a spectral resolution of around 200 MHz. The 408.8 nm transition of erbium is proposed as a suitable candidate for day-one experiments at S^3.

Secondly, simulations were performed to develop a future generation of the S^3-LEB gas cell optimized for the study of short-lived isotopes, featuring a reduced extraction time and using a universal neutralization mechanism. In this gas cell, fast ion extraction is achieved through a combination of electrical field and gas flow. Simulations were performed with state-of-the-art software for capturing the multiphysics aspect, including the gas flow, the electrostatic field, the ion transport in high pressure and the dynamics of electrons generated by the ionization of the gas. Based on these simulations, an optimized gas-cell prototype has been designed, taking into account the extraction time, the efficiency, as well as the time available for neutralization.

Acknowledgements

This thesis is a culmination of the contributions of many, and I deeply appreciate the support, encouragement and guidance I have received throughout this journey.

First and foremost, I wish to express my deepest gratitude to my supervisors, Dr. Vladimir Manea and Dr. François Leblanc. Thank you for your patience and for steering me through the challenges of this PhD. Vladimir, your unwavering guidance, insightful discussions, and constant encouragement have been invaluable throughout this journey. Your expertise and mentorship have shaped both my research and personal growth in ways that I will always cherish. My gratitude to you can only be expressed through words as a fraction of what I truly feel. François, your patience and support, especially in navigating the complexities of administrative matters, have been greatly helpful during my PhD. Thank you both for believing in me and for correcting and guiding me with your valuable feedback throughout this journey. I feel very fortunate to be Vladimir's first PhD student and François's last. I hope this journey has brought you both as much fulfillment as it has brought me.

I am also deeply grateful to the members of my jury for their time, thoughtful critiques, and valuable feedback, which provided critical insights and strengthened this research. My deepest thanks to Pr. Dr. Thomas Elias Cocolios (KU Leuven) as my rapporteur for your inspiring discussions, thorough review, and constructive suggestions. I extend my sincere gratitude to Pr. Dr. Michael Block (GSI), also as my rapporteur, for your detailed reports and insightful comments. I am equally grateful to Dr. Bertram Blank (LP2I) for your expertise as my examiner and for your thoughtful questions and meticulous corrections. My sincere thanks also to Dr. Iolanda Matea (IJCLab) for your detailed evaluation and valuable suggestions as my examiner. All your comments have greatly advanced this work and provided me with a broader perspective on my research.

I would also like to acknowledge the support of David Verney, Carole Gaulard, Fadi Ibrahim and Luc Perrot, as well as the doctoral school, for their invaluable assistance when I had to change my thesis topic. To my supervisors, Vladimir and François thank you for giving me the opportunity to contribute for my PhD projects and providing the resources and encouragement to build my work.

To my collaborators and colleagues in the FRIENDS^3 team, the S^3-LEB team and the

FIIRST group, your collective expertise and camaraderie have supported me throughout this journey. Special thanks to David Lunney, Enrique, Serge, Nathalie, Rafael, and Piet for their insightful suggestions during group meetings.

To my friends, Anahi, Anjali, Jekabs, Elodie, Sarina, Fedor, Alexandre and many others, thank you for making this journey memorable. The shared experiences at IJCLab, GANIL, and many conferences and workshops have been both intellectually stimulating and personally rewarding.

On a personal note, I am forever grateful to my family and friends for their unwavering support and belief in me. Your encouragement has been my constant source of strength and motivation.

Finally, I extend my sincere gratitude to IJCLab-CNRS for funding my thesis and to Université Paris-Saclay for providing academic affiliation and support, all of which made this work possible.

This journey has been both challenging and rewarding, and I deeply appreciate the contributions of everyone who has walked this path with me. Thank you.

Contents

List of Figures

List of Tables

Introduction

The study of atomic nuclei, composed of protons and neutrons, has been driven by the longstanding quest for scientific knowledge of the fundamental nature of matter. The field of nuclear physics traces back to Rutherford's discovery of the atomic nucleus in the early 20th century. Since then, understanding the structure and behavior of atomic nuclei has remained a central focus of scientific inquiry. Significant technological advancements have facilitated increasingly refined investigations into the behavior of individual nucleons and their collective dynamics within the nucleus, leading to significant progress in understanding nuclear structure and properties.

The properties of atomic nuclei evolve in a non-trivial way towards extreme proton-to-neutron ratios, particularly in heavy elements or towards the driplines. In heavy nuclei, the long-range Coulomb repulsion between protons becomes increasingly comparable to the short-range strong nuclear force, which poses challenges to nuclear stability. The evolution of the established shell closures and regions of deformation toward the driplines remains difficult to predict based on the properties of nuclei close to stability. The acquisition of new experimental data is therefore necessary to better constrain the trends of nuclear properties as functions of proton and neutron numbers and to rigorously test and refine nuclear models. The required radioactive and rare isotopes of interest for answering these questions are produced in trace amounts at Isotope Separator Online (ISOL) facilities or in-flight facilities through nuclear reactions such as fission, spallation, and fusion evaporation. These products are often very short-lived and accompanied by a substantial background of contaminant nuclei. Therefore, the development of highly selective, sensitive, efficient, and fast experimental techniques is essential. In this context, laser-based techniques, particularly step-wise resonant ionization spectroscopy (RIS), have become indispensable tools. RIS is a well-established technique that enables isomer-selective production of radioactive ions, allowing for the extraction of atomic properties such as energy levels, ionization potentials, isotope shifts, and hyperfine constants. From these atomic observables, nuclear properties such as spins, magnetic dipole and electric quadrupole moments, and differences in mean-square nuclear charge radii can be derived in a nuclear-model independent manner [YWWR23]. RIS takes advantage of the unique atomic level structure of different elements and exploits tunable lasers to implement a variety

of ionization schemes. This versatility makes it feasible to efficiently study by laser spectroscopy almost every element in the periodic table, which explains why the technique has recently become a key contributor to advancements in nuclear structure studies of rare and short-lived isotopes.

RIS techniques, including collinear resonance ionization, in-source hot cavity resonance ionization, and gas cell-based resonance ionization approaches, are widely implemented across facilities worldwide [CMP16]. All approaches face several challenges, related to the production rate, release time, chemical dependency and, with respect to laser spectroscopy, spectral resolution. Collinear RIS provides quasi-Doppler-free resolution but requires radioactive ion beam production rates of at least 20 p.p.s [dG$^+$17]. In-source hot cavity RIS offers high sensitivity down to 0.1 p.p.s. but its spectral resolution is limited to a few GHz due to the high temperatures (above 2000 K) of the ion source and is not applicable to refractory elements [F$^+$03]. Techniques to enhance spectral resolution as perpendicular illumination [H$^+$17a] typically come with a cost in efficiency.

The gas-cell-based RIS methods, specifically the in-gas-cell/jet laser ionization spectroscopy (IGLIS) techniques, have been significantly advanced at KU Leuven since the late 1980s [VD$^+$92, K$^+$01, KFH$^+$13, Zad18]. When coupled with an online isotope separator and performing the RIS measurements within the homogeneous, cold, and low-pressure gas jet, IGLIS enables highly sensitive measurements of radioactive isotopes at very low production rates (as low as 0.1 p.p.s), and at the same time provides high enough spectral resolution capable of resolving at least partially hyperfine structures. The in-gas-jet method is implemented at various radioactive ion beam (RIB) facilities, such as S^3-LEB at SPIRAL2 of GANIL (France) [A$^+$23], MARA-LEB at the University of Jyväskylä (Finland) [PMP$^+$16, Z$^+$23], RADRIS [L$^+$16, R$^+$23] and JETRIS [R$^+$20, L$^+$24b] setups at GSI (Germany), KISS [H$^+$17b] and PALIS [S$^+$13] setups at RIKEN RIBF (Japan). An overview of the heavy isotopes that can be studied using the in-gas-jet method [F$^+$17], based on experimental and estimated production cross sections and the projected performance of the technique, is shown in Section 2.1.1. The isotopes eligible for study must have half-lives longer than 100 ms, a threshold set by the gas cell extraction time, and must be produced at a minimal rate of 1 atom every 10 s, limited by the gas cell extraction and neutralization efficiency. In other words, the sensitivity of the IGLIS technique for studying rare and short-lived isotopes is inherently limited by the gas cell performance.

The SPIRAL2 facility of GANIL is designed to deliver heavy-ion beams with high intensities with its superconducting linac. The Super Separator Spectrometer (S^3), a high-resolution recoil separator, will use these high-intensity beams to produce neutron-deficient nuclei close to the proton dripline and superheavy nuclei via fusion–evaporation reactions. It is designed to separate the reaction products from the intense primary beams. The Low Energy Branch of S^3 (S^3-LEB), currently installed at

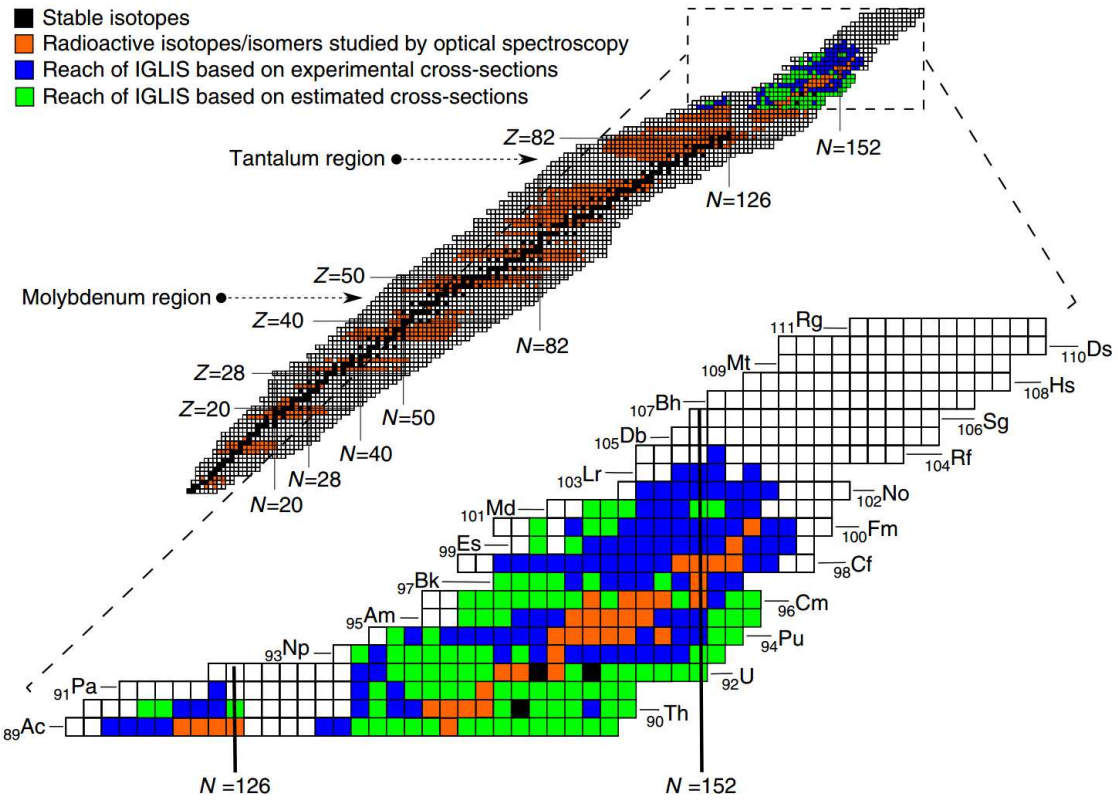

Fig. 1. Reach of IGLIS technique for the actinide region and beyond. The chart of nuclides illustrates the current status of isotopes investigated by optical spectroscopy. Black squares represent stable or very long-lived isotopes, while orange squares indicate the radioactive isotopes or isomers for which spectroscopic data has been published. The inset highlights the actinide and heavier mass region, blue (green) squares are isotopes that, based on experimental (calculated) cross-sections, can be produced in sufficient amounts (0.1 p.p.s. after gas cell extraction) to be studied using IGLIS. Figure taken from [F+17].

the focal plane of S^3, aims to study the ground state and isomeric states of the exotic nuclei with low production rates using the IGLIS technique.

The gas cell, a critical component of S^3-LEB, is filled with ultrapure argon buffer gas under constant flow and typically operated at pressures of 200–500 mbar. It is positioned on the S^3 beam axis at the interface between S^3 and S^3-LEB. Designed at KU Leuven [Mog13a, Mog13b, K+16], it has an extraction time of $\sim$ 600 ms for a 1 mm nozzle throat diameter. The S^3 products will be stopped and neutralized in the buffer gas cell, then extracted and studied by laser spectroscopy, mass spectrometry or decay spectroscopy. The integration of isomeric selectivity provided by the in-gas-jet RIS technique with mass selectivity of a high-resolution mass spectrometer, combined with high sensitivity and rapid detection capabilities, enables high-resolution investigation at S^3-LEB of radioactive isotopes with low production rates. A de-Laval nozzle with

a Mach number $M \sim 8$ [F+21] has been installed at the gas cell exit to create a homogeneous hypersonic [1] gas jet of low temperature and pressure. Probing the atoms with lasers in the jet will reduce the Doppler and pressure broadening by at least an order of magnitude compared to the gas cell while maintaining high efficiency.

The thesis is structured as follows. Chapter 1 presents the theoretical background essential for the laser spectroscopy research in this thesis, focusing on nuclear properties-related atomic observables from laser spectroscopy. Chapter 2 describes the IGLIS technique and the tunable Ti:sa lasers used in RIS measurements. Chapter 3 details the experimental setup S^3-LEB at SPIRAL2, focusing on its key components and the laser system.

Chapter 4 presents recent offline results of resonance ionization laser spectroscopy of stable erbium isotopes with S^3-LEB in both the gas cell and the supersonic gas jet. These measurements aim to identify optimal laser ionization schemes with high sensitivity to nuclear ground-state properties, which are critical for the forthcoming online experiments at S^3. Erbium was selected as the initial case for online commissioning due to its favorable laser ionization schemes with S^3-LEB laser system and good production rate at S^3.

Nuclear charge radii represent one of the key nuclear ground-state properties targeted in these studies. As shown in Fig. 2, the root mean square (RMS) nuclear charge radii [2] of erbium from the Fricke&Heilig evaluation [FH04], are plotted as a function of mass number A. In the upcoming commissioning experiment, ^{151,152}Er will be investigated and laser ionization schemes with high sensitivity to the nuclear ground-state properties such as changes in mean-square charge radius are needed to achieve accurate measurements.

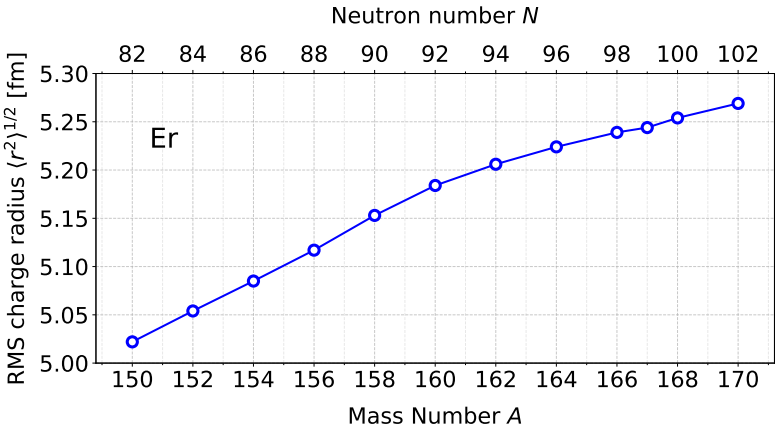

Fig. 2. RMS nuclear charge radii $\langle r^2 \rangle^{1/2}$ of erbium.

Three atomic transitions of Er I were selected from the literature and systematically

1. Although in [F+21] the gas jets with M > 5 have been named "hypersonic", throughout this work the name "supersonic" will be used and it is understood that it applies to any Mach number M > 1.

2. No error given due to the assumption SMS = 0, as stated in Eq. (1.15).

investigated, with first-step excitation at 393.7 nm, 400.8 nm and 408.8 nm in combination with second-step transitions to the same autoionizing state for subsequent ionization. We present for the 408.8 nm transition gas-jet laser spectroscopy measurements aimed at pinning down both its isotope shift and hyperfine structure. Field shift and mass shift factors for the three transitions measured in both the gas cell and the gas jet are systematically determined using King plots. A discussion is made on the precision of the resulting values and the underlying assumptions. Additionally, pressure broadening and shifts of the studied transitions are characterized through in-gas-cell laser spectroscopy.

Chapter 5 presents the development of a future version of the S^3-LEB gas cell aimed to extend the IGLIS technique to short-lived isotopes with half-lives on the order of 100 ms while maintaining high efficiency. The current S^3-LEB gas cell faces two main limitations: the extraction time on the order of a few hundred milliseconds leads to substantial losses for isotopes with half-lives under 100 ms, and the neutralization efficiency depends on the electrons created from the buffer gas by the incident beam during the stopping process, which can be a limiting factor for beams of low intensity. The chapter will present the steps taken to simulate and design a fast gas cell with extraction time around 100 ms and good extraction efficiency. Simulations are also presented for the creation and dynamics of electrons in the gas environment, a necessary step towards the design of a neutralization mechanism. The simulated phenomena include laminar gas flow, electrostatic field, plasma creation for neutralization, and species convection, migration and diffusion in the buffer gas or plasma environment.

Chapter 1

Nuclear properties from atomic spectroscopy

Nuclear ground-state properties, including nuclear spins, magnetic dipole and electric quadrupole moments, and mean-square charge radii, are fundamental for understanding the structure of nuclei across isotopic chains. These properties provide essential insights into nuclear forces, shell structure, and deformation, playing a critical role in nuclear physics research. Laser spectroscopy has proven to be a highly effective, model-independent method for probing nuclear ground-state properties by measuring the subtle effect of the nuclear moments and of the finite nuclear size on the energy levels of the atomic electrons. This section presents a detailed discussion of the atomic observables in laser spectroscopy that reflect the influence of these nuclear ground-state properties.

The structure of an atom is fundamentally determined by the interactions between the electrons and the nucleus, as well as between the electrons themselves. The quantum mechanical behavior of electrons in a hydrogen-like atom is initially described by the non-relativistic Schrödinger equation. In this framework, energy levels are quantized and inversely proportional to the square of the principal quantum number n and degenerate with respect to the orbital angular momentum quantum number l [Foo05]. Based on this simplified description, the incorporation of relativistic corrections describing the electron's motion, the interaction of the electron's spin with its orbital angular momentum, known as spin-orbit coupling and the Darwin term, leads to the phenomenon known as fine structure. The fine structure introduces small perturbations to the non-relativistic energy levels, with energy shifts typically on the order of a few meV for lighter atoms and extending up to tens of eV for heavier atoms.

As the atomic nucleus is not point-like but possesses spin, charge and current distribution, the interactions between the nucleus and the bound electrons lead to further shifts and splitting of the fine structure levels into the hyperfine levels. Hyperfine structure

manifests as isotope shifts and hyperfine splittings, which typically range from 10^{-3} to $1\,\mathrm{cm}^{-1}$, or 10^{-7} to $10^{-4}\,\mathrm{eV}$ [Dem14]. These interactions are driven by nuclear properties such as spin, magnetic and electric moments and charge radius. By probing the atomic energy levels using high-resolution laser spectroscopy techniques, these fundamental nuclear properties can be simultaneously accessed in a nuclear-model-independent way.

The interaction between an atomic nucleus and its surrounding electrons can be described by a Hamiltonian using an electromagnetic multipole expansion [Dra23]:

$$H_{\mathrm{eN}} = \sum_k \hat{T}_k(\mathrm{N}) \cdot \hat{T}_k(\mathrm{e}) \tag{1.1}$$

where $\hat{T}_k(\mathrm{N})$ and $\hat{T}_k(\mathrm{e})$ are spherical tensor operators of rank k acting on the nucleus and electrons, respectively. Only even values of k corresponding to the electric multipoles and odd values of k corresponding to the magnetic multipoles contribute to the series. The term k=0 electric monopole term corresponds to an exactly spherical nuclear charge distribution and results in a shift in the atomic energy levels. For most atoms, the k=1 magnetic dipole and k=2 electric quadrupole interactions dominate the hyperfine structure, as these represent the most significant deviations from sphericity in the nuclear charge or current distribution. Higher-order terms (k >2) describe progressively more complex nuclear interactions but with diminishing contributions on energy level shifts, being several orders of magnitude smaller than the k = 1, 2 terms. Higher-order terms are typically beyond the precision of current laser spectroscopy techniques for studies of radioactive isotopes, efforts are underway to develop higher-resolution laser spectroscopy methods and current observations have been limited to the k=3 interaction of a few stable isotopes [dGKK$^+$21, d$^+$22]. In most experimental studies at RIB facilities, the focus remains on the hyperfine interactions arising from the k = 1, 2 terms, with the multipole expansion after the electric quadrupole term typically truncated.

1.1 Hyperfine structure

The Hamiltonian of the hyperfine interaction can be expressed as the sum of contributions corresponding to the different nuclear moments:

$$H = H_{E0} + H_{M1} + H_{E2} + H_{M3} + \ldots, \tag{1.2}$$

where H_{E0} is the electric monopole interaction and corresponds to the field isotope shift, while H_{M1} and H_{E2} correspond to the magnetic dipole and electric quadrupole hyperfine splitting, respectively. $H_{M3}+\ldots$ represent higher-order terms such as magnetic octupole, electric hexadecapole, and so on. These terms describe more complex and increasingly weaker interactions as the order increases.

For an atomic level, the total angular momentum $\boldsymbol{F} = \boldsymbol{I} + \boldsymbol{J}$, arising from the coupling

of nuclear spin I and electronic angular momentum J, can take values ranging from $|I-J|$ to $|I+J|$ [Foo05]. The number of possible values is equal to $2I+1$ when $I \leq J$, and $2J+1$ when $J \leq I$. The hyperfine splitting means that atomic states with different total angular momentum will have different energy.

The hyperfine structure is thus observable for isotopes with non-zero nuclear spin ($I \neq 0$). The magnetic dipole splitting H_{M1} results from the interaction of the magnetic dipole moment $\boldsymbol{\mu}$ of the atomic nucleus with the magnetic field $\boldsymbol{B_e}$ generated by the motion of surrounding electrons at the nucleus position and can be written as [Dra23]:

$$H_{M1} = -\boldsymbol{\mu} \cdot \boldsymbol{B_e} = -\frac{\mu B_e(0)}{\hbar^2 IJ} \boldsymbol{I} \cdot \boldsymbol{J} \tag{1.3}$$

The change in energy of a hyperfine sublevel resulting from the magnetic dipole interaction is:

$$\Delta E_{M1} = \frac{1}{2} \frac{\mu B_e(0)}{IJ} \left[F(F+1) - I(I+1) - J(J+1)\right] = \frac{1}{2} AC, \tag{1.4}$$

with the so-called Casimir factor $C = F(F+1) - J(J+1) - I(I+1)$.

For atomic nuclei with spin $I > 1/2$, the electric quadrupole splitting H_{E2} results from the interaction of the nuclear spectroscopic quadrupole moment Q_s and the gradient of the electron field $V_{zz} = \left\langle \frac{\partial^2 V}{\partial z^2} \right\rangle$ at the location of the nucleus. This interaction leads to an additional energy shift of each hyperfine sublevel:

$$\Delta E_{E2} = eQ_s \left\langle \frac{\partial^2 V}{\partial z^2} \right\rangle_0 \frac{(3/4)C(C+1) - I(I+1)J(J+1)}{2I(2I-1)J(2J-1)}, \tag{1.5}$$

By keeping only the magnetic dipole term H_{M1} and the electric quadrupole term H_{E2} in the multipole expansion Eq. (1.2), the resulting approximation of the energy shift of each atomic hyperfine level with respect to the unperturbed fine structure is given by:

$$\Delta E_{\mathrm{HFS}} = \Delta E_{M1} + \Delta E_{E2} = A\frac{C}{2} + B\frac{(3/4)C(C+1) - I(I+1)J(J+1)}{2I(2I-1)J(2J-1)} \tag{1.6}$$

with the magnetic dipole constant A and the electric quadrupole constant B defined as:

$$A = \frac{\mu B_e(0)}{IJ}, \tag{1.7}$$

$$B = eQ_s \left\langle \frac{\partial^2 V}{\partial z^2} \right\rangle_0. \tag{1.8}$$

An example of hyperfine splitting is shown in Fig. 1.1.

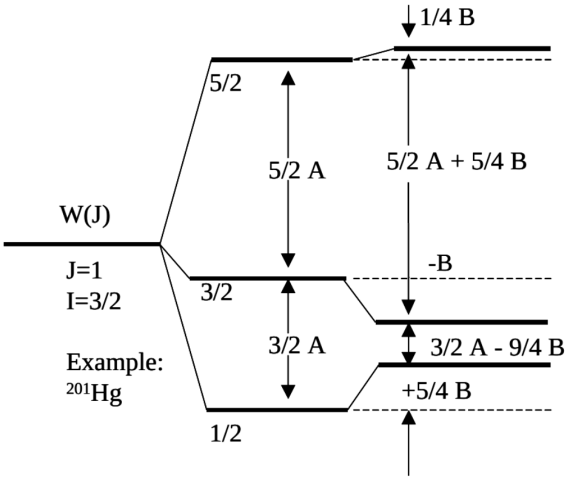

Fig. 1.1. The hyperfine structure of ^{201}Hg.

The magnetic moment of a nucleus arises from the magnetic field generated by the orbiting charged particles (protons) and intrinsic spin ($s = 1/2$) of its constituent nucleons. The electric quadrupole moment arises from the nucleus non-spherical charge distribution, reflecting deviations from spherical symmetry. These electromagnetic moments provide insight into the shape and deformation of the nucleus and serve as indicators of collective nuclear effects, such as rotational behavior. Precise measurement of the hyperfine splitting, ΔE_{HFS}, allows for the extraction of the magnetic and electric hyperfine structure constants, A and B. These parameters, along with accurate theoretical calculations of the magnetic field B_e and the electric field gradient V_{zz} at the nucleus [BanP01], enable the determination of the nuclear magnetic dipole μ and electric quadrupole moments Q_s.

Assuming an ideal point-like nucleus, the electromagnetic field B_e and V_{zz} are considered constant for all isotopes of a given element. Under this assumption, if the moments (μ' and Q'_s) of a reference isotope are known from other experiments such as nuclear magnetic resonance (NMR) and nuclear quadrupole resonance (NQR) spectroscopy, and there is in addition a determination of the HFS parameters A' and B' from laser spectroscopy of the reference isotope, the moments of interest can be extracted using the approximate relations [CMP16]:

$$\frac{A}{A'} \simeq \frac{\mu}{\mu'}\frac{I'}{I} \qquad \frac{B}{B'} \simeq \frac{Q_s}{Q'_s} \tag{1.9}$$

However, real nuclei deviate from the point-like approximation due to their finite size and the non-uniform distribution of charge and magnetism. Two primary effects introduce corrections to the magnetic dipole hyperfine structure constant A. The Breit-Rosenthal effect (BR) [RB32] arising from the finite spatial distribution of the nuclear charge, and the Bohr-Weisskopf effect (BW) [BW50] from the distribution of nuclear magnetism

within the nucleus. The A-coefficient is corrected by the addition of two factors:

$$A = A_{\text{point}}(1 + \epsilon_{\text{BW}})(1 + \epsilon_{\text{BR}}), \tag{1.10}$$

where A_{point} is the hyperfine A coefficient assuming a point-like nucleus. The ratio of the magnetic dipole hyperfine structure constants A and A' for two isotopes, taking into account the BR and BW corrections, can be written as:

$$\frac{A}{A'} = \frac{A_{\text{point}}(1 + \epsilon_{\text{BW}})(1 + \epsilon_{\text{BR}})}{A'_{\text{point}}(1 + \epsilon'_{\text{BW}})(1 + \epsilon'_{\text{BR}})} \approx \frac{\mu I'}{\mu' I}\left(1 + {}^{A}\Delta^{A'}\right). \tag{1.11}$$

Here the parameter ${}^{A}\Delta^{A'}$ is defined as the differential hyperfine anomaly between two isotopes. This anomaly can be accurately measured using high-precision experimental techniques, such as radio-frequency resonance spectroscopy, and can be found in reference [CMP16]. For most nuclei, particularly the light- and medium-mass ones, the hyperfine anomaly is typically negligible from systematic studies and treated as an error contribution. However, for heavier elements, this effect can become significant [YWWR23].

1.2 Isotope shift

The size and shape of atomic nuclei are important reference quantities for nuclear models. The nuclear mean square charge radius, denoted as $\langle r^2 \rangle$, represents the average squared distance of protons from the center of the nucleus. Laser spectroscopy techniques do not measure the $\langle r^2 \rangle$ directly but instead allow the extraction of the difference in $\langle r^2 \rangle$ between two isotopes A and A', denoted as $\delta\langle r^2 \rangle^{A,A'}$, from the measurement of isotope shifts.

The isotope shift in an atomic transition arises from variations in nuclear mass and charge distribution among isotopes, providing insights into nuclear structure and the spatial distribution of protons relative to changes in neutron number. The transition-dependent isotope shift denoted as $\delta\nu_i^{A'A} = \nu_i^{A'} - \nu_i^{A}$, represents the difference in frequency between an isotope with the mass number A' and a reference isotope with the mass number A for a specific atomic transition i. Two major effects contribute to the isotope shift:

$$\delta\nu_i^{A'A} = \delta\nu_{i,\,\text{MS}}^{A'A} + \delta\nu_{i,\,\text{FS}}^{A'A}. \tag{1.12}$$

where $\delta\nu_{i,\,\text{MS}}^{A'A}$ and $\delta\nu_{i,\,\text{FS}}^{A'A}$ are the mass shift and volume/field shift components, respectively.

The mass shift arises from changes in the nuclear mass between isotopes with different neutron numbers, which influences the reduced mass of the atomic system and thus leads to a shift in the fine structure energy levels. It can be decomposed into two

contributions: the normal mass shift (*NMS*), which is caused by the change in the reduced mass of electrons and nucleus, and the specific mass shift (*SMS*), which results from the influence on correlations in the motion of the electrons. Both *NMS* and *SMS* depend in the same way on the atomic masses A and A' :

$$\delta\nu_{i,\,\mathrm{MS}}^{A'A} = \delta\nu_{i,\,\mathrm{NMS}}^{A'A} + \delta\nu_{i,\,\mathrm{SMS}}^{A'A} = (M_{i,\mathrm{NMS}} + M_{i,\mathrm{SMS}})\frac{A'-A}{A'A} = M_i\frac{A'-A}{A'A}, \tag{1.13}$$

where M_i is the mass shift factor. $M_{i,\mathrm{NMS}}$, the normal mass shift factor for transition i, can be easily calculated with the transition frequency ν_i, electron mass m_e and proton mass m_p:

$$M_{i,\mathrm{NMS}} = \nu_i\frac{m_e}{m_p} = \frac{\nu_i}{1836.15}. \tag{1.14}$$

In recent years, considerable effort has been devoted to determining *SMS* contributions from atomic theory. However, the *SMS* strongly depends on the atomic transition, transitions involving the f and d open shells, where strong configuration mixing is expected, pose challenges for accurate atomic calculations. Nevertheless, for $ns^2 - nsnp$ transitions, estimates of *SMS* from *NMS* have been proven to be reasonable [ABP85].

$$\begin{aligned}\delta\nu_{i,\,\mathrm{SMS}}^{A'A} =& (0. \pm 0.5)\delta\nu_{i,\,\mathrm{NMS}}^{A'A} \\ & \text{for } ns^2 - nsnp \text{ transitions.}\end{aligned} \tag{1.15}$$

The field shift *FS* can be attributed to the change in the electrostatic potential felt by the electrons due to the change in the nuclear charge distribution:

$$\delta\nu_{i,FS}^{AA'} = F_i\lambda^{A,A'} \tag{1.16}$$

where F_i is the field shift factor depending on the change in electron density at the nucleus in the atomic transition i. $\lambda^{AA'}$ is the nuclear parameter, which can be expressed as a function of the change of even radial nuclear charge moments $\delta\langle r^{2n}\rangle^{AA'}$ [AHS87]:

$$\begin{aligned}\lambda^{AA'} &= \delta\langle r^2\rangle^{AA'} + \frac{C_2}{C_1}\delta\langle r^4\rangle^{AA'} + \frac{C_3}{C_1}\delta\langle r^6\rangle^{AA'} + ... \\ &\approx K(Z)\delta\langle r^2\rangle^{AA'}\end{aligned} \tag{1.17}$$

where $\delta\langle r^2\rangle^{AA'}$ is the changes in mean-square charge radius with the convention that $\delta\langle r^2\rangle^{AA'} = \langle r^2\rangle^{A} - \langle r^2\rangle^{A'}$, The expansion coefficients $C_2/C_1, C_3/C_1, ...$, describing the contribution from the higher order radial moments, can be theoretically calculated as detailed in [Sel69]. The atomic number Z-dependent correction factor $K(Z)$, accounting for higher radial moments, can be found in [TFR85]. For erbium ($Z = 68$), a value of $K = 0.95$ is obtained. In this work, the muonic X-ray data giving the parameters $\lambda^{A'A}$ of erbium isotope pairs 167-166, 168-166, 170-168 is available from [FH04].

In summary, the measured IS values for a specific transition i can be related to the change in nuclear mean-square charge radius $\delta\langle r^2\rangle^{A'A}$ between an isotope A' and the reference isotope A through two atomic factors F_i and M_i:

$$\begin{aligned}\delta\nu_i^{A'A} &= F_i \cdot \lambda^{A'A} + M_i \frac{A'-A}{A'A} \\ &\approx K(Z) \cdot F_i \cdot \delta\langle r^2\rangle^{A'A} + M_i \frac{A'-A}{A'A}\end{aligned} \tag{1.18}$$

1.3 Extracting nuclear observables from laser spectroscopy

1.3.1 Nuclear spin and moments

In laser spectroscopy experiments, the atomic hyperfine structure is probed by exciting atoms using laser photons. This process follows two fundamental conditions: the selection rule $\Delta F = 0, \pm 1$, with transitions between $F = 0 \rightarrow F = 0$ forbidden, and the photon energy $h\nu$ must match the energy difference between the upper hyperfine sublevel F_u and the lower sublevel F_l. The frequency of the laser photon, ν, for each allowed transition can be expressed as [CF10]:

$$h\nu = h\nu_0 + \Delta E_{\mathrm{HFS},F_u} - \Delta E_{\mathrm{HFS},F_l} = h\nu_0 + \alpha_\mathrm{u} A_\mathrm{u} + \beta_\mathrm{u} B_\mathrm{u} - \alpha_\mathrm{l} A_\mathrm{l} - \beta_\mathrm{l} B_\mathrm{l} \tag{1.19}$$

where ν_0 is the centroid frequency of the transition, and $\Delta E_{\mathrm{HFS},F_u}$ and $\Delta E_{\mathrm{HFS},F_l}$ represent the hyperfine energy shifts of the upper and lower levels, respectively, which are characterized by the corresponding magnetic dipole constants A_u, A_l and the electric quadrupole constants B_u, B_l. According to Eq. (1.6), α and β are coefficients that depend on the nuclear spin I and the total angular momenta J of the atomic states involved, which are given by:

$$\alpha = \frac{C}{2}, \quad \beta = \frac{(3/4)C(C+1) - I(I+1)J(J+1)}{2I(2I-1)J(2J-1)} \tag{1.20}$$

The hyperfine constants A_u, A_l, B_u, B_l, along with the centroid frequency ν_0, can be extracted from the hyperfine spectrum using a χ^2-minimization fitting method. The Python package SATLAS [GW+18] is commonly employed for this purpose. The magnetic and quadrupole moments of a given isotope can be determined using Eq. (1.9), from either the A_u and B_u of the upper state or A_l and B_l of the lower state, depending on their sensitivity to the moments.

For an atomic level with total angular momentum $\boldsymbol{F} = \boldsymbol{I} + \boldsymbol{J}$, in cases where $I \leq J$ the nuclear spin can be then assigned directly by counting the number of the observed

resonance peaks if they are all well resolved in the HFS spectrum. For isotopes where the nuclear spin is not directly observable, the ratio of the magnetic dipole hyperfine constants $A_\mathrm{u}/A_\mathrm{l}$ for the upper and lower atomic states is typically used for the spin assignment. As described by Eq. (1.9), this ratio remains constant across the isotopic chain if the hyperfine anomaly is negligible [CMP16]. The SATLAS fitting procedure requires a predefined nuclear spin I and is highly sensitive to the correct input, an incorrect assignment can lead to poor fitting results. In addition, only if the hyperfine spectrum is analyzed with the correct nuclear spin I, the correct ratio of the A-parameters can be extracted. These two approaches are thus often used for spin assignment [YWWR23].

Another method involves analyzing the relative intensities of the HFS resonance peaks, known as Racah intensity [MS69]. Theoretical calculations of these intensities can be performed using the formula:

$$I_{F_\mathrm{u}\to F_\mathrm{l}} \propto (2F_\mathrm{l}+1)(2F_\mathrm{u}+1)\begin{Bmatrix} J_\mathrm{u} & F_\mathrm{u} & I \\ F_\mathrm{l} & J_\mathrm{l} & 1 \end{Bmatrix}^2 \tag{1.21}$$

where F_u and F_l are the total angular momentum of the upper and lower hyperfine states of the allowed transition, the factor in brackets is a Wigner 6-j symbol that captures the coupling between these angular momenta. However, the experimentally observed relative intensities of the peaks are often affected by factors such as the power saturation and optical pumping effects, the effect of which is difficult to quantify in practical cases.

1.3.2 King plot for changes in mean-square charge radii

To extract the difference in the mean-square charge-radii $\delta\langle r^2\rangle^{AA'}$ from the experimentally measured isotope shift $\delta\nu^{A'A}$ using Eq. (1.18), knowledge of the atomic factors M_i and F_i is required. These factors can be determined using two main approaches: atomic calculations using theoretical models and calibration using a King plot analysis. For elements with few stable isotopes or when the charge radii of stable isotopes are unknown, theoretical calculations become the only feasible method. However, calculations can be particularly challenging for complex electronic configurations. The King-plot analysis calibrates the atomic factors of the transition probed by laser spectroscopy using either charge radii obtained from independent experimental techniques or reference transitions. For elements with a sufficient number of stable isotopes and well-documented charge radii data, such as erbium, which possesses five stable isotopes with known muonic data, the King plot method offers enhanced accuracy. This section will describe two types of King plot analyses used to refine the atomic factors.

The Type I King plot utilized in this study involves multiplying both sides of Eq. (1.18) by the inverse of the mass factor $A'A/(A'-A)$ and a modification factor $\mu_{\text{std}} = A'_{\text{std}} - A_{\text{std}}/(A'_{\text{std}}A_{\text{std}})$, where $A'_{\text{std}}A_{\text{std}}$ is an arbitrarily chosen standard isotope pair. This yields the modified *IS* of the transition of interest $\delta\nu^{A'A}_{i,\text{modif}}$ expressed as a function of the modified $\lambda^{A'A}$ data from the literature, as follows:

$$\frac{A'A}{A'-A} \cdot \mu_{\text{std}} \cdot \delta\nu_i^{A'A} = F_i \cdot \frac{A'A}{A'-A} \cdot \mu_{\text{std}} \cdot \lambda^{A'A} + \mu_{\text{std}} M_i \tag{1.22}$$

where $\delta\nu^{A'A}_{i,\text{modif}} = \frac{A'A}{A'-A} \cdot \mu_{\text{std}} \cdot \delta\nu_i^{A'A}$ is the modified *IS*, $\lambda^{A'A}_{\text{modif}} = \frac{A'A}{A'-A} \cdot \mu_{\text{std}} \cdot \lambda^{A'A}$ is the modified $\lambda^{A'A}$. The modification ensures that the plotted points lie on a straight line, resulting in the type I King plot with a slope of F_i and an intercept of $\mu_{\text{std}}M_i$.

However, given the limited number of stable isotopes for most elements, along with the restricted availability of muonic X-ray and electron scattering data for the stable isotopes, typically few data points are accessible when conducting this type of King plot. Consequently, significant uncertainties often accompany the extracted F_i and M_i values. One strategy to address this scarcity of data points is to theoretically compute the intercept $\mu_{\text{std}}M_i$, which equals to $\mu_{\text{std}}(M_{i,\text{NMS}} + M_{i,\text{SMS}})$, and incorporate it as an additional data point. As discussed previously, $M_{i,\text{NMS}}$ can be precisely estimated by $\nu_i/1836.15$. In contrast, $M_{i,\text{SMS}}$ is typically difficult to estimate with high precision due to its strong dependence on intricate electron-electron correlations and relativistic effects within the atomic structure. In the particular case of the $ns^2 - nsnp$ transitions, $\delta\nu_{i,\text{SMS}} = (0 \pm 0.5)\delta\nu_{i,\text{NMS}}$, thereby the intercept can be estimated as $\mu_{\text{std}}M_{i,\text{NMS}}$ with an uncertainty of $0.5\mu_{\text{std}}M_{i,\text{NMS}}$.

An alternative method to derive these factors involves employing type II King plot analysis with IS data from reference measurements using a reference transition [Kin13]:

$$\delta\nu_{\text{ref}}^{A'A} = F_{\text{ref}}\delta\langle r^2\rangle^{A'A} + M_{\text{ref}}\frac{A'-A}{A'A} \tag{1.23}$$

By eliminating the $\delta\langle r^2\rangle^{A'A}$ term between Eqs. 1.18 and 1.23, the following expression is obtained, establishing a relationship between the field- and mass-shift factors of the transitions i of interest and the reference transition:

$$\frac{A'A}{A-A'}\delta\nu_i^{A'A} = \frac{F_i}{F_{ref}} \cdot \frac{A'A}{A-A'}\delta\nu_{ref}^{A'A} + M_i - \frac{F_i}{F_{ref}}M_{ref} \tag{1.24}$$

where the modified IS of the transition of interest $\frac{A'A}{A-A'}\delta\nu_i^{A'A}$ is plotted against the modified IS of a reference transition $\frac{A'A}{A-A'}\delta\nu_{ref}^{A'A}$ from published literature. The type II King plot has a slope of $\frac{F_i}{F_{ref}}$ and an intercept of $M_i - \frac{F_i}{F_{ref}}M_{ref}$.

In this chapter, the theoretical background essential for the laser spectroscopy research

presented in this thesis has been discussed, with a focus on the nuclear properties-related atomic observables derived from laser spectroscopy and the methodologies used to interpret these observables. In the following Chapter 2, the in-gas laser ionization spectroscopy technique used in this thesis work and the principle of the tunable Ti:sa lasers used for RIS measurements will be explained in detail.

Chapter 2

Experimental techniques and laser physics

2.1 Laser spectroscopy in the gas environment

The HFS of atoms can typically be probed through either resonant laser excitation followed by laser-induced fluorescence (LIF) detection, or step-wise photoionization followed by ion or decay detection. The former technique is often used in collinear laser spectroscopy (CLS) where laser light is aligned collinearly with an accelerated ion beam, allowing for high-precision spectroscopy of exotic nuclei [CMP16, N$^+$17]. The large beam velocity reduces the relative velocity spread of the ions ($\Delta v/v$), thereby minimizing the Doppler broadening and achieving spectral linewidth down to a few tens of MHz. However, the sensitivity in CLS is limited by the LIF detection efficiency and background photon noise [BLR21].

The latter case, laser ionization spectroscopy, involves the sequential absorption of multiple photons to step-wise excite and finally ionize an atom. The HFS spectrum is then measured by detecting the ionized species or their decay products (e.g. α or β particles) as a function of the probing laser frequency. A crucial factor affecting the efficiency of this technique is the final ionization step, which can be realized through three different processes, as illustrated in Fig. 2.1. The first process is non-resonant ionization, where the valence electron residing in an excited state is promoted non-resonantly above the ionization potential by a strong laser field. Compared to the resonant excitation cross-section of $\sigma_{\text{res}} = \frac{\lambda^2}{2\pi} \approx 10^{-10}\,\text{cm}^2$, the cross-section of the non-resonant ionization is significantly lower with a value of $\sigma_{\text{cont}} \approx 10^{-17}\,\text{cm}^2$. Since the last step laser is not resonant with specific energy levels, this method is less selective and requires more energy, leading to potential background noise or unwanted ionization.

The second process involves auto-ionization, where the valence electron undergoes a further resonant excitation to an auto-ionizing state with a typical cross-section

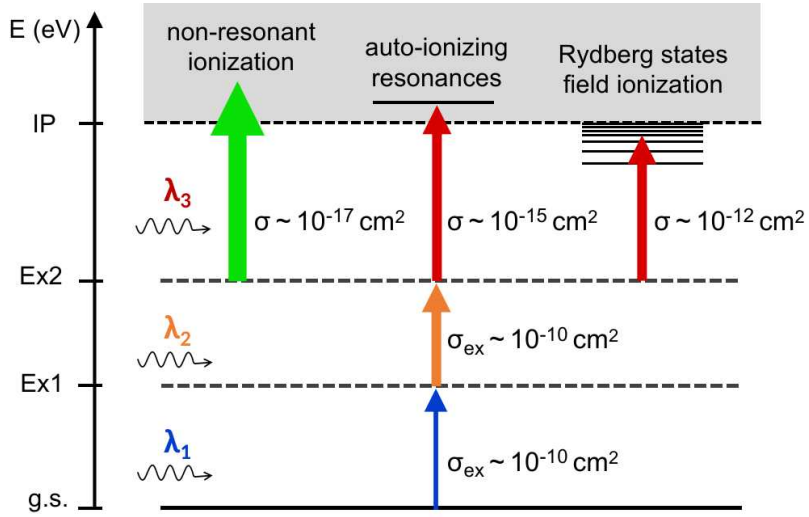

Fig. 2.1. Different step-wise ionization schemes with typical excitation and ionization cross sections. (Left) non-resonant ionization with high laser power after two steps of resonant excitation (λ_1 and λ_2). (Middle) ionization via auto-ionizing resonances. (Right) ionization through excitation to Rydberg states, with final ionization facilitated by collisions or field ionization.

of $\sigma_{\mathrm{AI}} \approx 10^{-15}\,\mathrm{cm}^2$. AI resonances are short-lived quasi-bound states above the IP involving more than one electron, which then rapidly decay due to electron-electron interactions, leaving behind an ion-electron pair.

The third process is the resonant ionization through the high-lying, weakly bound Rydberg states, which are situated very close to the ionization potential. In this process, the valence electron is resonantly excited to a Rydberg state with a cross-section of $\sigma_{\mathrm{Ry}} \approx 10^{-12}\,\mathrm{cm}^2$. Subsequent ionization occurs through the application of an external electric field or through collision due to the high sensitivity of the Rydberg states to external perturbations. For atoms with a single valence electron, such as hydrogen, Rydberg states are described using the Rydberg formula [Dem10]:

$$E_n = -R_y \frac{Z^2}{n^2} \tag{2.1}$$

where R_y is the Rydberg constant, Z is the atomic number of the nucleus, n is the principal quantum number. However, for atoms with more complex electronic configurations, such as transition metals or rare earth elements like erbium, the high-lying Rydberg states are not fully known due to the challenges of predicting and experimentally measuring them. Experimental factors such as the applied electric field, the temperature of the environment, and the collision rates can vary significantly between different experimental setups, which complicate the consistent measurement of these states.

The radioactive and rare isotopes of interest are produced in nuclear reactions in trace

amounts, alongside a substantial background of contaminant nuclei, the radioactive ion beam (RIB) production and detection techniques have to be selective, sensitive, efficient and fast. Step-wise resonant ionization takes advantage of the unique atomic level fingerprints and the high photon absorption cross-sections at resonances, making it highly effective for applications such as resonant ionization spectroscopy (RIS), isotope separation, and trace element detection. In this thesis work concerning erbium, auto-ionization resonances are known from previous work and utilized for in-gas RIS experiments. However, not all elements have known AI resonances and the theoretical understanding of these structures remains limited. Non-resonant ionization, being less selective, is generally used when resonant states cannot be identified or are not feasible. In the following sections, various RIS techniques currently utilized in nuclear physics will be introduced, with a particular focus on the method implemented at S^3-LEB.

2.1.1 Gas-cell resonance ionization spectroscopy

The RIS techniques broadly used in nuclear structure studies include collinear resonance ionization, in-source hot cavity resonance ionization, and gas cell-based resonance ionization approaches [CMP16]. Collinear resonance ionization spectroscopy (CRIS), where the high resolution in collinear geometry is combined with the high sensitivity of resonant ionization technique, was initially proposed at CERN-ISOLDE and demonstrated online by Schulz et al. [S^+91] in 1991. This technique provides quasi-Doppler-free resolution but requires radioactive ion beam production rates of at least 20 p.p.s due to the high speed of atoms affecting the effective overlap with the lasers [dG^+17]. In contrast, in-source laser resonance ionization spectroscopy in a hot cavity offers high sensitivity, down to 0.1 p.p.s. However, its spectral resolution is limited to a few GHz due to Doppler broadening caused by the high temperatures (above 2000 K) of the ion source [F^+03]. Additionally, this method is not applicable to refractory elements and currently does not extend to transuranium elements.

The gas-cell-based RIS methods, specifically the in-gas-cell/jet laser ionization and spectroscopy (IGLIS) techniques, have been significantly advanced at KU Leuven since the late 1980s [VD^+92, K^+01, KFH^+13, Zad18]. When coupled with an online isotope separator, IGLIS enables sensitive measurements of short-lived nuclear reaction products at very low production rates, reaching as low as 0.1 p.p.s after the extraction from the gas cell. By performing RIS within the homogeneous, cold, and low-pressure gas jet, Doppler broadening is predicted to be significantly reduced to $\sim$100 MHz under optimal gas jet conditions, with a Mach number of $M = 10$ [Zad18]. The in-gas-jet RIS thus provides a spectral resolution capable of resolving hyperfine structures in range of hundreds of MHz to several GHz. Additional advantages of this approach include the reduced experimental complexities related to beam alignment compared to collinear geometry and minimized non-isotopic contamination relative to high-temperature

in-source environments. The in-gas-jet method is implemented at various radioactive ion beam (RIB) facilities, such as S^3-LEB at SPIRAL2 of GANIL (France), MARA-LEB at University of Jyväskylä (Finland) [PMP$^+$16], RADRIS [R$^+$23] and JETRIS [L$^+$24b] setups at GSI (Germany), KISS [H$^+$17b] and PALIS [Z$^+$14] setups at RIKEN RIBF (Japan).

In the IGLIS approach implemented at S^3-LEB, nuclear-reaction products from the S^3 spectrometer of SPIRAL2 are thermalized, neutralized and transported within a high-pressure buffer gas cell towards the exit aperture. The neutralized atoms are then reionized using element-selective, step-wise resonant laser excitation, either inside the gas cell near the exit aperture or within the homogeneous, cold supersonic jet formed by a de Laval nozzle. The photoions are extracted from the jet area by a series of ion guides and delivered to a multi-reflection time-of-flight mass spectrometer (MR-TOF MS), where the ions can be separated by mass before counting. This procedure is illustrated in Fig. 2.2.

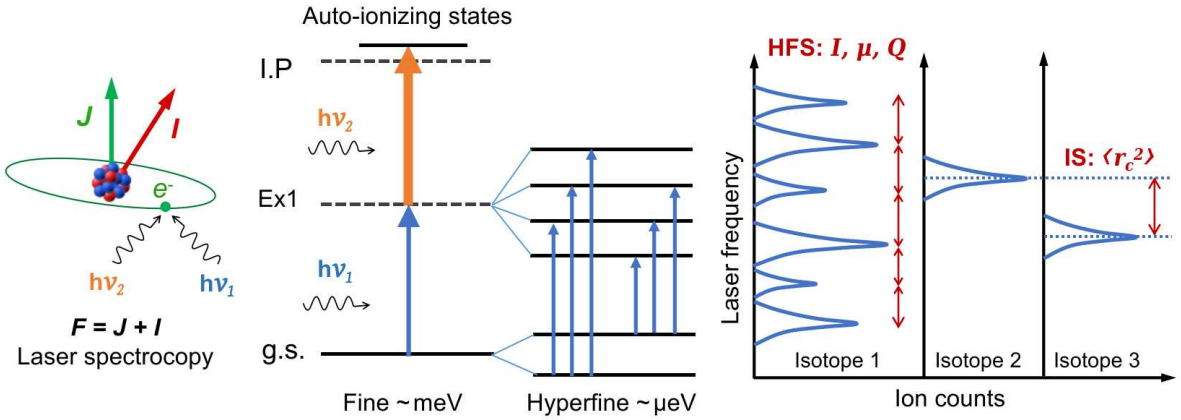

Fig. 2.2. Resonance ionization spectroscopy (RIS) to probe the fundamental nuclear properties.

The extraction efficiency, extraction time and neutralization efficiency of the ions are primarily determined by the gas cell design and the properties of the buffer gas. The extraction time however does not depend on the chemical properties of the atoms, which makes IGLIS particularly advantageous for studying refractory elements and short-lived isotopes, as long as the extraction time is within acceptable limits for the isotopes' half-life. The development of a gas cell for IGLIS measurements offering a faster extraction of the stopped nuclei is part of the objectives of this thesis and will be presented in Chapter 5.

Tunable pulsed Ti:sa lasers are widely utilized to optimize the ionization efficiency in RIS techniques due to their broad tunable bandwidth. The short pulse width produces high peak intensity to saturate the population of the excited states in atomic transition resonances, thereby facilitating efficient ionization. The high repetition rate increases

the ionization signal while managing the potential sample heating. Pulsed lasers of repetition rates ranging from 10 to 20 kHz and pulse widths on the order of tens of nanoseconds are commonly used for step-wise excitation and ionization. Further details on the principles of Ti:sa lasers can be found in Section 2.2.1.

The integration of isomeric selectivity provided by the in-gas-jet RIS technique with mass selectivity of the MR-TOF mass spectrometry, combined with the very sensitive ion detection, enables high-resolution investigation of isotopes with low production rates at S^3-LEB. The spectral resolution of this technique is dependent on the properties of the gas environment where the lasers interact with the atoms, therefore a comprehensive understanding of the gas jet formed by the de Laval nozzle is necessary to achieve optimal spectral resolution.

2.1.2 Supersonic gas jet

The gas stopping cell is typically filled with noble gas, such as argon and helium, to minimize unwanted chemistry with the stopped ions. For effectively stopping and neutralizing the reaction products, the argon is typically used at stagnation pressures of 100–500 mbar, which provides enhanced stopping power and a larger recombination coefficient. Helium, being lighter, is preferred when a faster release time is required, though it has a lower recombination cofficient. Additionally, the gas must be purified, with impurity concentrations in the ppb range, since impurities like water, oxygen, and nitrogen can interact with the atoms and create unwanted molecules, effectively reducing the rate of nuclei in atomic state [K+01].

As the gas flows out of the gas cell from high to low pressure through a small-diameter exit aperture, expansion of gas occurs. A de Laval nozzle is a convergent-divergent contoured nozzle, as shown in Fig. 2.3, widely used in various applications to achieve axisymmetric supersonic flow. The nozzle operates by converting the thermal energy of the gas into kinetic energy. As the subsonic flow ($M < 1$) enters the converging part of the nozzle, it is accelerated until it reaches the local speed of sound (Mach number $M = 1$) at the nozzle's throat. Beyond the throat, isentropic expansion occurs in the divergent part, resulting in a supersonic jet with $M > 1$. The behavior of the isentropic flow in convergent-divergent nozzles like the de Laval nozzle is explained by the area-velocity relation, derived from the conservation of mass, momentum, and energy in compressible flow [OC97]:

$$\frac{dA}{A} = \frac{du}{u}(M^2 - 1) \tag{2.2}$$

where dA is the change in cross-sectional area A of the nozzle and du the change in flow velocity u, M is the Mach number, which indicates the speed of the gas relative to the speed of sound at the local point.

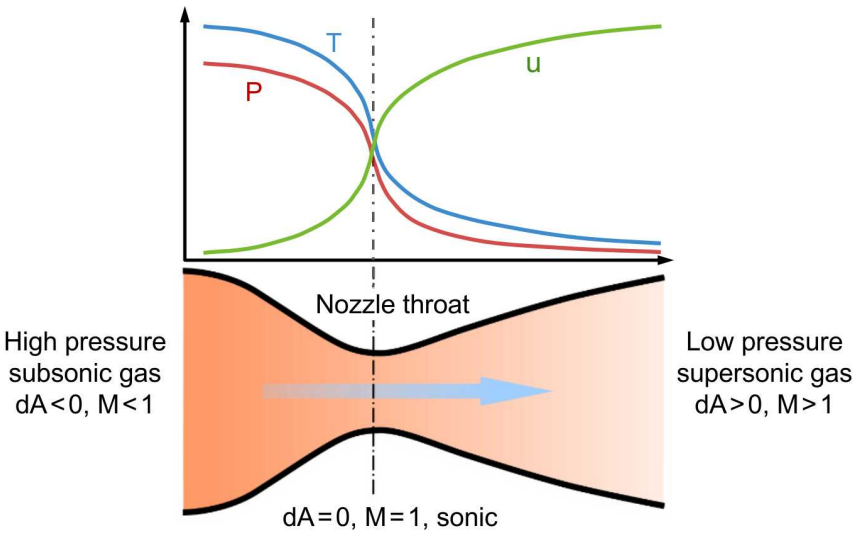

Fig. 2.3. Geometry of a convergent-divergent de Laval nozzle. Gas velocity increases while pressure and density decrease in the convergent section. At the throat, the flow reaches sonic (Mach 1). In the divergent section, the flow accelerates to supersonic speeds (Mach > 1) as pressure and density further decrease.

The gas cell has been designed to operate with an exit diameter $d^* = 1$ mm. The design of the nozzle has been optimized to ensure that the gas flow expands correctly and forms a uniform jet. The relationship between the cross-sectional area $A(x)$ at any point along the nozzle and the throat area A^* is derived by integrating the area-velocity relation Eq. (2.2) under isentropic flow conditions:

$$\frac{A(x)}{A^*} = \frac{1}{M}\left[\frac{2}{\gamma+1}\left(1+\frac{\gamma-1}{2}M^2\right)\right]^{\frac{\gamma+1}{2(\gamma-1)}} \tag{2.3}$$

where M is the Mach number at that point, $\gamma = C_p/C_v$ is the specific heat ratio, $\gamma = 5/3$ for monatomic gases. The nozzle exit diameter A_{exit} for argon gas and for a throat diameter $d^* = 1$ mm can be calculated for specific Mach numbers, $M_{\text{exit}} = 7$ and 10 results in $d_{\text{exit}} = 4.88$ mm and 8.14 mm, respectively. The carefully designed contour of the de Laval nozzle ensures that the streamlines are parallel and uniformly distributed when the gas exits the nozzle. The flow at the exit is characterized by the final Mach number of the jet (M), which is defined by the ratio of the jet velocity (u) to the local speed of sound (a), i.e., $M = u/a$. The speed of sound in an ideal gas is given by:

$$a = \sqrt{\frac{\gamma kT}{m}} \tag{2.4}$$

where k is the Boltzmann constant, T is the absolute temperature of the gas, m is the

gas molecular mass. The stream velocity at the exit of the nozzle can be derived from the conservation of mass and energy in the flow, and it is given by:

$$u = \sqrt{\frac{\gamma k T_0 M^2}{m(1 + [(\gamma - 1)/2]M^2)}} \tag{2.5}$$

where T_0 is the temperature of the gas in the gas cell, called stagnation temperature. For $T_0 = 300$ K, the stream velocity reaches 550 m/s in a jet of Mach number $M = 10$ [KFH$^+$13].

In isentropic supersonic flows, the thermodynamic properties temperature T, density ρ, and pressure P are related to their stagnation values T_0, ρ_0, and P_0 in the gas cell before expansion by:

$$\frac{T}{T_0} = \left[1 + \frac{\gamma - 1}{2} M^2\right]^{-1} \tag{2.6}$$

$$\frac{P}{P_0} = \left[1 + \frac{\gamma - 1}{2} M^2\right]^{\frac{-\gamma}{\gamma - 1}} \tag{2.7}$$

$$\frac{\rho}{\rho_0} = \left[1 + \frac{\gamma - 1}{2} M^2\right]^{\frac{-1}{\gamma - 1}} \tag{2.8}$$

In the supersonic gas jet, the temperature, pressure, and density decrease significantly with respect to the stagnation values and are smaller for larger values of the Mach number. For instance, as described by Eq. (2.6), the temperature of an isentropic jet decreases from $T = 100$ K for $M = 1$ to $T = 3$ K for $M = 10$ when $T_0 = 300$ K. As indicated by Eq. (2.7), a precise pressure ratio between the gas cell and the background pressure in the jet formation chamber, known as pressure matching, is essential. Incorrect pressure matching can lead to over-expansion or under-expansion of the jet. Over-expansion occurs when the background pressure is too low, causing excessive jet divergence and poor laser overlap, while under-expansion happens when the background pressure is too high, leading to insufficient jet expansion and reduced homogeneity. Both scenarios negatively impact the jet's performance and its interaction with the laser.

The low-atom density and low-temperature jet lead to a marked reduction in both collision- and Doppler broadening mechanisms compared to those in the gas cell, which is a critical aspect of the high-resolution IGLIS technique.

2.1.3 Spectral line broadening mechanisms

In laser spectroscopy, when probing atomic transitions between energy levels $|1\rangle$ and $|2\rangle$ in a two-level atomic system, the absorption or emission of photons with energy $E_{\text{photon}} = h\nu_0 = E_2 - E_1$ does not result in a strictly monochromatic spectral line. Instead, the spectral line manifests as a frequency distribution around the central frequency ν_0, which can be described by a line profile $P(\nu - \nu_0)$ with a full-width at half-maximum (FWHM) $\delta\nu$. Understanding these broadening mechanisms is critical for accurately extracting atomic observables from the spectra and enhancing the spectral resolution. The broadening mechanisms are categorized by their nature into Lorentzian and Gaussian contributions, as explained below.

Lorentzian linewidth

1. **Natural linewidth**.

   When probing atomic energy transitions in a non-degenerate two-level atomic system using a laser, interactions between atoms and photons result in three types of processes that involve changes in the populations of the ground state $|1\rangle$ and the excited state $|2\rangle$. These processes are governed by Einstein's coefficients and the spectral energy density $\rho(\nu)$ of the radiation field:

   Absorption Absorption occurs when an atom in the ground state absorbs a photon with an energy $h\nu_{21} = E_2 - E_1$ from the light field and transitions to the excited state. The rate of decrease in the number of atoms in the ground state N_1 is expressed as:

   $$\frac{dN_1}{dt} = -B_{12}N_1\rho(\nu), \tag{2.9}$$

   where B_{12} is the Einstein coefficient for absorption.

   Spontaneous emission In this process, an atom in the excited state spontaneously decays to the ground state, emitting a photon with energy $h\nu_{21} = E_2 - E_1$. The rate of decrease in the number of atoms in the excited state N_2 due to spontaneous emission is characterized by:

   $$\frac{dN_2}{dt} = -A_{21}N_2, \tag{2.10}$$

   where A_{21} is the Einstein coefficient for spontaneous emission.

   Stimulated emission This process occurs when an atom in the excited state is induced by an incident photon to decay to the ground state, emitting an additional photon with the same phase, frequency, and direction as the incident photon. The rate of stimulated emission, which leads to a decrease in the number

of atoms in the excited state, is given by:

$$\frac{dN_2}{dt} = -B_{21}N_2\rho(\nu), \tag{2.11}$$

where B_{21} is the Einstein coefficient for stimulated emission.

The natural broadening arises from the inherent uncertainty in the energy levels of atoms, as described by the Heisenberg uncertainty principle. The finite lifetime τ of an excited state leads to an uncertainty in state energy E by $\Delta E \simeq h/\tau$, which causes the corresponding emission or absorption line to exhibit a Lorentzian profile rather than a sharp delta function. The shorter the lifetime of the excited state, the broader the resulting spectral line. The natural linewidth Γ_{nat} for the transition can thus be defined as [Dem14]:

$$\Gamma_{\text{nat}} = \frac{A_{21}}{2\pi} = \frac{1}{2\pi\tau} \tag{2.12}$$

where A_{21} is the Einstein coefficient for spontaneous emission. The shorter the excited state's lifetime, the broader the natural linewidth. In RIS, natural broadening is usually small but can still affect high-resolution measurements.

2. **Power broadening**.

Power broadening occurs when the incident light intensity is sufficient to saturate the atomic transition. In a two-level atomic system with population densities N_1 and N_2, with weak incident light, most atoms remain in the ground state, and the absorption measured through the photoionized ion intensity detection in RIS experiments exhibits a linear dependence on the incident power. As the intensity of the incident radiation increases, the population in the absorbing level $|1\rangle$ will be depleted when the absorption rate becomes faster than the relaxation processes (spontaneous emission and stimulated emission) that can refill it. Therefore, the absorption decreases and the photoionized ion intensity deviates from linearity, reaching a constant value at saturation.

The population density difference between the two levels, $\Delta N = N_1 - N_2$, under optical pumping with rate P, can be expressed as [Dem14]:

$$\Delta N = \frac{\Delta N_0}{1 + 2P/(R_1 + R_2)} = \frac{\Delta N_0}{1 + S} \tag{2.13}$$

where $P = B_{12}\rho(\omega)$ is the probability of a transition $|1\rangle \rightarrow |2\rangle$ by absorption of photons with energy $\hbar\omega$. $\Delta N_0 = N_{10} - N_{20}$ is the population density difference at thermal equilibrium without an external radiation field ($P = 0$). R_1 and R_2 are the relaxation rates of levels $|1\rangle$ and $|2\rangle$, which represent the rates at which the populations of these energy levels return to their thermal

equilibrium values due to various physical processes. These processes typically include spontaneous emission, stimulated emission and absorption, as well as non-radiative mechanisms such as collision-induced transitions. The saturation parameter is defined as $S = P/\bar{R} = B_{12}\rho(\omega)/\bar{R}$, which represents the ratio of the pumping rate P to the average relaxation rate $\bar{R} = (R_1 + R_2)/2$. When the pump rate approaches infinity, $P \to \infty$, the population difference ΔN approaches zero, i.e., $N_1 = N_2$. In this state, no further changes in population occur, and additional excitation within the system is no longer possible.

The saturation parameter quantifies the extent of saturation of the absorption process by the incident light. For a homogeneous transition pumped by strong incident light with intensity $I(\omega)$, the pump rate $P = \sigma_{12}(\omega)I(\omega)/\hbar\omega$, where $\sigma_{12}(\omega)$ is the cross-section of the absorption transition at frequency ω. If the spontaneous emission of the upper level $|2\rangle$ is the only relaxation mechanism and the absorbing level $|1\rangle$ is the ground state, the saturation parameter $S(\omega)$ is directly proportional to the incident light intensity $I(\omega)$ and can be expressed as [Dem14]:

$$S(\omega) = \frac{2\sigma_{12}(\omega)I(\omega)}{h\omega A_{21}}. \tag{2.14}$$

The absorption coefficient $\alpha(\omega)$ [cm^{-1}] $= \sigma_{12}(\omega)\Delta N$ [Dem14] quantifies the attenuation of light intensity due to absorption processes. At saturation, it can be expressed as:

$$\alpha_s(\omega) = \frac{\alpha_0(\omega)}{1 + S(\omega)}, \tag{2.15}$$

where $\alpha_0(\omega)$ is the unsaturated absorption coefficient at frequency ω:

$$\alpha_0(\omega) = \alpha_0(\omega_0) \cdot \frac{(\gamma/2)^2}{(\omega - \omega_0)^2 + (\gamma/2)^2}. \tag{2.16}$$

Eq. (2.16) shows that the absorption coefficient $\alpha_s(\omega)$ has a Lorentzian line profile. The induced absorption probability of a monochromatic wave with frequency ω follows a Lorentzian line profile $B_{12}\rho(\omega) \cdot L(\omega - \omega_0)$. Eq. (2.15) shows that the saturation decreases the absorption coefficient $\alpha_s(\omega)$ by the factor $1 + S(\omega)$. At the resonance, this factor has its maximum value $1 + S(\omega_0)$, while it decreases for increasing $\omega - \omega_0$ to 1. The saturation is therefore strongest at the resonance ($\omega = \omega_0$) and approaches zero for $(\omega - \omega_0) \to \infty$. Therefore, the absorption coefficient $\alpha(\omega)$ is most significantly reduced at the line center compared to the wings of the line, and the line broadens at high power intensity. If the upper level $|2\rangle$ decay by spontaneous processes with a relaxation constant natural linewidth, its steady-state population probability ρ_{22} is a power-broadened Lorentzian

profile and can be derived using the Optical Bloch Equations [CCTG98]:

$$\rho_{22}(\omega) = \frac{1}{2}\frac{S(\omega)}{(\omega-\omega_0)^2/\gamma^2 + (1+S(\omega))} \tag{2.17}$$

The linewidth is increased by the factor $\sqrt{1+S_0}$ compared to the unsaturated natural linewidth γ and can be expressed as [Dem14]:

$$\gamma_s = \gamma\sqrt{1+S_0}\,, \quad S_0 = S(\omega_0) \tag{2.18}$$

Laser spectroscopy measurements should be performed at sufficiently low power to avoid power broadening. In this thesis work, power saturation tests were carried out for the transitions of interest before performing the RIS measurements. In these tests, the laser power was systematically varied, and the corresponding ion signal intensity was measured. The saturation parameter in Eq. (2.17) can be expressed as:

$$S(\omega) = \frac{I(\omega)}{I_s(\omega)} \tag{2.19}$$

where $I(\omega)$ is the intensity of the incident light, and $I_s(\omega)$ is defined as the saturation intensity, which depends on the properties of the atomic transition. By setting $I(\omega)$ below the saturation intensity determined from the saturation tests, $S(\omega) < 1$ is ensured in the subsequent RIS experiments. Further details are provided in Section 4.2.

3. **Pressure broadening**.

   Pressure broadening, also known as collisional broadening, arises from the interactions between the laser-probed atoms and the surrounding atoms or molecules in a gas mixture, which is the case in gas-cell RIS experiments. These collisions can be either elastic or inelastic, each contributing differently to the broadening of spectral lines. Elastic collisions alter the relative motion (velocity) of the particles, leading to perturbations in the emitted or absorbed radiation's phase. These perturbations depend on the interaction potential (the electronic configuration of both colliding partners A and B as well as the distance R between the centers of mass) and cause both broadening and small shifts in spectral lines.In a gas mixture, the mean value of R depends on the pressure and temperature of the gas.

   Inelastic collisions instead can lead to level depopulation, effectively reducing its lifetime (and thus inducing a broadening). The depopulation of the excited atoms in level E_i can be quantified by a collision-induced rate A_i^{coll}. The total depopulation rate A_i of the E_i level is then given by [Dem10]:

$$A_i = A_i^{\text{spont}} + A_i^{\text{coll}} \quad \text{with} \quad A_i^{\text{coll}} = N_B\sigma_i\bar{v} \tag{2.20}$$

Here, N_B is the number density of the collision partner B, σ_i is the collisional cross-section for the transition, and $\bar{v}$ is the mean relative velocity between the colliding particles, given by:

$$\bar{v} = \sqrt{\frac{8kT}{\pi\mu}}, \quad \mu = \frac{M_A M_B}{M_A + M_B} \tag{2.21}$$

where μ is the reduced mass of the colliding pair, k is the Boltzmann constant, T is the gas temperature. By the ideal gas law, the pressure of the collision partner B is $p_B = N_B kT$. Thus the total depopulation rate [1/s] can be expressed as [Dem10]:

$$A_i = \frac{1}{\tau_i^{\text{spont}}} + a p_B, \quad a = 2\sigma_i \sqrt{\frac{2}{\pi\mu kT}} \tag{2.22}$$

This additional pressure-dependent transition probability shortens the effective lifetime of the excited level and therefore results in a corresponding pressure-dependent linewidth [Dem14]:

$$\Gamma = \Gamma_{\text{nat}} + \Gamma_{\text{coll}} = \Gamma_{\text{nat}} + a p_B \tag{2.23}$$

Elastic collisions do not change the internal states of the colliding atoms but do change their velocities, which leads to a phase shift $\Delta\omega(R)$ in the emitted or absorbed electromagnetic waves associated with these particles. This phase shift, dependent on the interaction potential between particles, results in spectral line broadening and a shift of the line center. The combined effect of both elastic and inelastic collisions on the spectral line can be described by a Lorentzian profile [Dem14]:

$$I(\omega) = \frac{(I_0/2\pi)\Gamma}{(\omega - \omega_0 - \Delta\omega)^2 + (\Gamma/2)^2} \tag{2.24}$$

where $\Delta\omega = N_B \bar{v} \sigma_s$ is the line shift and $\Gamma = \Gamma_{\text{nat}} + N_B \bar{v} \sigma_b$ the linewidth. σ_s and σ_b are the cross-sections for the collision-induced shift and broadening. In laser spectroscopy performed in a buffer gas-filled cell at room temperature, the shift rate Γ_{sh} [MHz/mbar] and broadening rate Γ_{coll} [MHz/mbar] in a spectral profile can be expressed as linear functions of the buffer gas density ρ [KFH$^+$13]:

$$\begin{aligned} \Gamma_{\text{sh}} &= \gamma_{\text{sh}} \cdot \rho \\ \Gamma_{\text{coll}} &= \gamma_{\text{coll}} \cdot \rho \end{aligned} \tag{2.25}$$

The coefficients γ_{sh} and γ_{coll} characterize the rate of shift and broadening for specific atomic transitions and can be determined by analyzing the spectral lineshape at varying gas cell pressures. This analysis is further detailed in Section 4.4.2.

Gaussian linewidth

1. **Doppler broadening**. Doppler broadening in a gas arises due to the thermal motion of atoms, causing shifts in the observed frequency of light. In a gas at thermal equilibrium, atoms with velocity $v_i (i = x, y, z)$ exhibit random motion characterized by a Maxwell-Boltzmann velocity distribution. The one-dimensional velocity distribution of these atoms depending on their mass m and on the temperature of the gas T is given by [KFH+13]:

$$F(v_i) = \sqrt{\frac{m}{2\pi kT}} \exp\left(-\frac{mv_i^2}{2kT}\right) \tag{2.26}$$

where m is the particle mass, k is the Boltzmann constant, and T is the temperature.

When a laser beam interacts with these moving particles, the Doppler effect causes frequency shifts in the absorbed or emitted light. Specifically, particles moving toward the laser source experience a blue shift (increased frequency), while those moving away experience a red shift (decreased frequency). This velocity-dependent spread in the atomic transition frequency results in the broadening of spectral lines.

As the Maxwell-Boltzmann velocity distribution follows a Gaussian profile, and the Doppler frequency shift is directly proportional to velocity, the resulting spectral line intensity as a function of frequency also exhibits a Gaussian profile, mathematically expressed as:

$$G(\nu) = G_0 \exp\left[-\frac{c^2(\nu - \nu_0)^2}{\nu_0^2(2kT/m)}\right] \tag{2.27}$$

where $G(\nu)$ represents the intensity at frequency ν, G_0 is the peak intensity, ν_0 is the central frequency, c is the speed of light.

The FWHM of this Gaussian profile, known as the Doppler width $\Delta\nu_{\text{Dop}}$, is a measure of the broadening of the spectral line and is given by:

$$\Delta\nu_{\text{Dop}} = 2\sqrt{\ln 2}\frac{\nu_0}{c}\sqrt{\frac{2kT}{m}} \tag{2.28}$$

This equation can be simplified for practical use [Dem14]:

$$\Delta\nu_{\text{Dop}} = 7.16 \times 10^{-7}\nu_0\sqrt{T/A} \tag{2.29}$$

where ν_0 is the atomic transition frequency in cm^{-1}, T is the absolute temperature in K, and A is the atomic mass number.

According to Eq. (2.29), Eq. (2.3) and Eq. (2.6), Fig. 2.4 illustrates the contribution of Doppler broadening to the spectral line width for the first-step excitation at 408.8 nm in ^{170}Er and the diameter of the jet as a function of the Mach number.

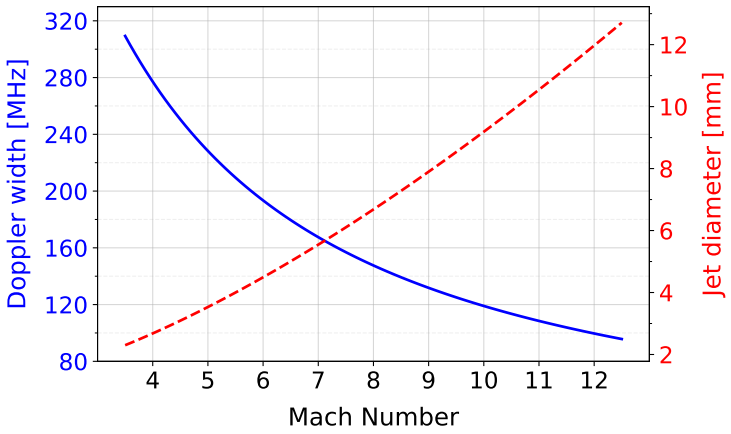

Fig. 2.4. Doppler broadening contribution to the spectral line width for the 408.8 nm transition in ^{170}Er (blue solid curve) and the supersonic jet diameter (red dashed line), produced by a de Laval nozzle with a 1 mm throat diameter, plotted as a function of the nozzle's Mach number.

2. **Fourier pulse linewidth**.

Pulsed lasers are used in RIS experiments by sending the pulsed pump laser through amplification cavities. When a Gaussian-shaped pump laser pulse is used, the envelope of the resulting spectral line profile is given by the Fourier transform of the temporal pulse profile, which also takes a Gaussian shape. For Gaussian functions, the product of the standard deviations in the time domain σ_t and its Fourier transform in the frequency domain σ_ν is constant:

$$\sigma_t \cdot \sigma_\nu = \frac{1}{2\pi} \tag{2.30}$$

The full width at half maximum (FWHM) of a Gaussian function is related to its standard deviation by $\mathrm{FWHM} = 2\sqrt{2\ln 2}\,\sigma$.

To estimate the spectral bandwidth of a pulse in the frequency domain, the relationship between the time duration Δt and bandwidth $\Delta\nu$ is utilized. Substituting the FWHM expressions for both domains into the time-frequency relation gives the time-bandwidth product:

$$\Delta t \cdot \Delta\nu = \mathrm{FWHM}_t \cdot \mathrm{FWHM}_\nu = (2\sqrt{2\ln 2}) \cdot (2\sqrt{2\ln 2}) \cdot \frac{1}{2\pi} \tag{2.31}$$

Simplifying, the FWHM of the spectral line $\Delta\nu_{\text{pulse}}$ [MHz] can be determined from the temporal width τ_{pulse} [ns] [KFH+13]:

$$\Delta\nu_{\text{pulse}} = 441/\tau_{\text{pulse}} \tag{2.32}$$

Laser pulses with durations of tens of nanoseconds are commonly used in resonance ionization spectroscopy (RIS) for step-wise excitation and ionization. These pulses have linewidths much smaller than other broadening mechanisms, such as Doppler or pressure broadening, making them suitable for high-resolution applications. The laser pulse of 50 ns length utilized in this thesis work gave a spectral bandwidth of 9 MHz.

The individual contributions to the total Lorentzian and Gaussian linewidths are computed as:

$$\Gamma = \sum \Gamma_i \tag{2.33}$$

where Γ_i represents the Lorentzian contributions from various Lorentzian-shape sources.

$$\Delta_G^2 = \sum \Delta_i^2 \tag{2.34}$$

where Δ_i denotes the Gaussian contribution from each Gaussian-shape broadening effect.

The observed spectral line shape can therefore be modeled as a convolution of a Lorentzian profile and a Gaussian profile including all the different broadening effects, known as a Voigt profile [OL77]:

$$\Delta_V = 0.5346\Gamma + \sqrt{0.2166\Gamma^2 + \Delta_G^2} \tag{2.35}$$

where Γ and Δ_G are the linewidths (FWHM) associated with the Lorentzian and Gaussian components, respectively.

2.2 Tunable solid-state lasers

Lasers represent a class of electromagnetic waves generated through the process of stimulated emission, characterized by high coherence, monochromaticity, and directionality. These properties are a direct consequence of the lasing process, wherein photons are emitted in phase with each other, at a single wavelength, and with minimal divergence. Tunable lasers, which can be adjusted to different wavelengths, have significantly advanced spectroscopic applications. Nonlinear optical processes, such as second and third harmonic generation, allow such lasers to provide a broad range of frequencies, facilitating the study of atomic and molecular transitions across a wide range of energies.

The RIS technique requires the use of multiple tunable lasers operating in the ultraviolet-visible range to target specific atomic transitions. Solid-state titanium:sapphire (Ti:sa) lasers, which exhibit a broad gain bandwidth centered around 800 nm, have been utilized in the off-line commissioning at S^3-LEB. This section describes the principles of the pulsed Ti:sa lasers, with a focus on the characteristics and behavior of the gain medium, the configuration of both linear and ring cavities, and the associated mechanisms for wavelength selection.

2.2.1 Laser principle

A laser resonator consists of three primary components: a gain medium where the light amplification occurs through the process of stimulated emission, a pump source that provides the necessary energy to maintain the population inversion ensuring that stimulated emission predominates over absorption and spontaneous emission, and a resonator composed of a minimum of two mirrors placed at opposite ends of the gain medium, which provides optical feedback ensuring only specific wavelengths that form standing waves within the cavity are amplified. One mirror is highly reflective (HR), while the other is partially reflective being an output coupler (OC), which allows a portion of the amplified light to exit the cavity as the laser output.

The resonator sustains laser oscillation only at frequencies where a round-trip phase shift $\Delta\phi$ is a multiple of 2π. For a Fabry–Perot resonator with two parallel mirrors separated by a distance d, the phase shift per round trip is $\Delta\phi = k2d$, where k is the wave vector given by [ST19]:

$$k = \frac{2\pi}{\lambda} = \frac{2\pi\nu}{c} \tag{2.36}$$

where $\lambda = \lambda_0/n$ and $c = c_0/n$ with λ_0/c_0 the wavelength/speed of light in vacuum and n the refractive index of the traversed medium, ν is the frequency of light. Substituting this into the phase shift equation $\Delta\phi = k2d = q2\pi$ $(q = 1, 2, ...)$, the condition for resonance is:

$$\nu_q = q\frac{c}{2d} \quad \text{or} \quad d = q\frac{\lambda}{2} \tag{2.37}$$

For lasing to start, the gain accumulated by light traveling through the cavity must compensate for all the losses within the resonator, including the absorption by the gain medium itself, scattering within the cavity, and transmission losses through the mirrors. The total losses in the cavity are quantified by a loss coefficient α, and the intensity of light after a round-trip through the cavity decreases by a factor of $e^{-\alpha}$. Round-trip losses originating from absorption and scattering are characterized by the attenuation coefficient α_s. The loss coefficient for the resonator mirrors with the reflectivity R_1 and R_2 is given by [ST19, Rot12]:

$$\alpha_m = \alpha_{m1} + \alpha_{m2} = \frac{1}{2d}\ln\frac{1}{R_1 R_2} \tag{2.38}$$

The loss per round trip is then $\alpha = \alpha_s + \alpha_m$. The photon lifetime is defined as:

$$\tau_p = \frac{1}{\alpha c} \tag{2.39}$$

where αc represents the loss of photons per second. The gain coefficient, which represents the amplification per unit length of the medium at a specific frequency ν, is defined as [ST19]:

$$\gamma_0(\nu) = N_0 \sigma(\nu) \tag{2.40}$$

where N_0 is the equilibrium population density difference between the excited and ground state, and $\sigma(\nu)$ is the frequency-dependent transition cross section:

$$\sigma(\nu) = \frac{\lambda^2}{8\pi\tau_{\text{sp}}} g(\nu) \tag{2.41}$$

where $\lambda = \lambda_0/n$ is the laser wavelength in the gain medium, $\tau_{\text{sp}} = 1/A_{21}$ is the effective spontaneous lifetime of the excited state, $g(\nu)$ is the transition line shape centered about the transition frequency $\nu_0 = (E_2 - E_1)/h$. Lasing is therefore most readily achieved at the frequency where the lineshape function is greatest $g(\nu_0)$.

The gain threshold condition for lasing can be then stated:

$$\gamma_0(\nu) > \alpha \tag{2.42}$$

From the above equations, the threshold population difference, N_t, can be derived as [ST19]:

$$N_t = \frac{\alpha}{\sigma(\nu)} = \frac{8\pi}{\lambda^2 c} \frac{\tau_{\text{sp}}}{\tau_p} \frac{1}{g(\nu)} \tag{2.43}$$

For simplified cases where the transition lineshape $g(\nu)$ is a Lorentzian function and the transition is limited by lifetime broadening, the expression for the threshold population difference further simplifies to:

$$N_t = \frac{2\pi\alpha}{\lambda^2} \tag{2.44}$$

To ensure that the electromagnetic waves within the cavity will be amplified over multiple round trips and that there is enough gain to compensate for losses, two lasing conditions must thus be satisfied:

$$\begin{aligned} &\text{Phase condition: } 2d = q\lambda, \quad (q = 1, 2, ...), \\ &\text{Gain condition: } N_0 > N_t. \end{aligned}$$

The resonator modes [Ren12] of a laser are classified into longitudinal modes and transverse modes, describing the standing wave patterns of light along and perpendicular

to the axis of the resonator respectively. The phase condition defines the longitudinal modes at eigenfrequencies [Ren12] of the resonator. In laser spectroscopy, the primary focus is on the longitudinal modes which determine the spectral properties and the wavelength of the laser light. The transverse modes [ST19], affecting the spatial distribution and beam profile, typically do not impact the spectral characteristics directly and are thus not addressed in this discussion.

2.2.2 Ti:sapphire

Solid-state lasers utilize metal ions embedded in optically transparent crystals as their gain medium. Titanium-doped sapphire (Ti^{3+}:Al_2O_3) lasing was first demonstrated [Mou82] and achieved in pulsed operation by Moulton et al. [Mou86] in the 1980s. Ti:sapphire is a four-level vibronic laser medium, which utilizes the vibronic energy levels [Ren12] arising from the interaction between electronic states and the host crystal lattice vibrations to achieve broad laser emission. The four-level laser system, which promotes effective population inversion, is illustrated in Fig. 2.5. In the Ti:sa laser medium, the active ions are the Ti^{3+} ions with an electron configuration of [Ar]$3d^1$, doped into a sapphire host by substituting the Al^{3+} ions at the lattice sites. Each Ti^{3+} ion is surrounded by an octahedral coordination of oxygen ions (O^{2-}), forming the crystal field which splits the $3d$ electronic state of Ti^{3+} into a three-fold degenerate ground state $^2T_2$ and a two-fold degenerated excited state ^2E. Phonon coupling leads to vibronic levels on top of the electronic states. The four-level structure of the Ti:sapphire system is shown on the right of Fig. 2.5.

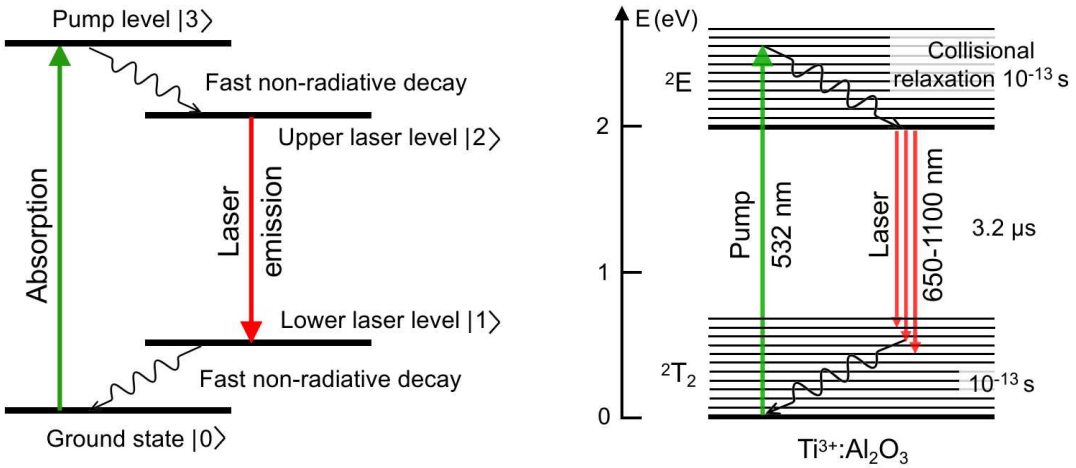

Fig. 2.5. Four-level description of the titanium-sapphire laser. Left: a typical four-level laser scheme. Right: pump absorption and laser emission transitions involving the phonon-coupled states of the $3d$ electron of Ti^{3+}.

Ti^{3+} ions in the sapphire host can be excited from the ground state $|0\rangle$ to a higher energy vibronic level $|3\rangle$ of the ^2E state using a pump light source. In this work

the frequency-doubled Nd:YAG pump laser at 532 nm is utilized. Fast non-radiative relaxation results in the electrons quickly reaching the lower energy vibronic states $|2\rangle$ within the ^2E electronic band with a typical relaxation time on the order of 10^{-13} s. The excess energy is dissipated into the vibrational modes (phonons) of the sapphire lattice without emitting a photon. Laser radiation is generated by stimulated emission from the upper laser level $|2\rangle$ to the lower laser level $|1\rangle$, a vibronic level within the $^2T_2$ electronic band above the ground state. The spontaneous emission having a significantly longer lifetime of around 3.2 μs compared to the collisional relaxation, facilitates effective population inversion. After stimulated emission, electrons in the lower band rapidly decay to the ground state $|0\rangle$ via non-radiative relaxation, preparing them for the next pump cycle.

Due to the strong electron-vibration coupling, the electronic transitions of $3d$ electrons involving numerous electron-phonon coupled states within the broad electronic ^2E and $^2T_2$ bands give rise to a broad absorption bandwidth in the blue-green region centered around 490 nm and the wide emission range from 650 nm to 1100 nm centered around 800 nm, as illustrated in Fig. 2.6. This broad spectral bandwidth enables tunability by selectively amplifying specific wavelengths, depending on the cavity mode. Further details about wavelength selection can be found in Section 2.2.4.

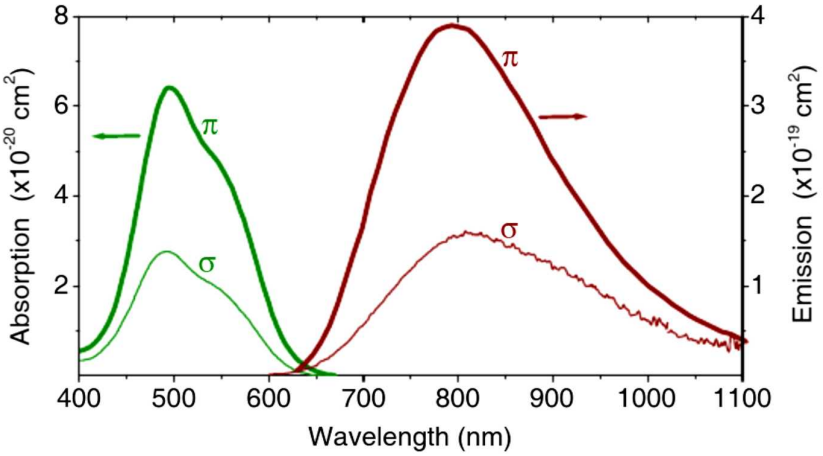

Fig. 2.6. Absorption (green) and emission (red) cross sections of Ti:sapphire at room temperature. Note the fivefold vertical scale difference between absorption and emission. The terms π and σ refer to different polarization components: π-polarized light oscillates parallel, while σ-polarized light oscillates perpendicular to the plane of incidence. π-polarized light interacts more strongly with the crystal due to its alignment with the crystal structure, leading to enhanced absorption and emission cross sections. Figure taken from [Sor04].

2.2.3 Resonator configurations

The configuration of the optical cavity significantly influences the laser's operational characteristics and performance. Laser resonators can have either a standing wave (linear) or a traveling wave (ring) configuration, depending on the feedback mechanisms used [Rot12].

Standing wave (linear) cavity

A standing wave cavity, also known as a linear resonator, consists of two parallel mirrors facing each other that reflect light back and forth along a single axis, effectively forming a Fabry Perot cavity. In this configuration, light oscillates back and forth along the resonator axis between the two mirrors, creating a standing wave pattern characterized by nodes and antinodes due to the constructive and destructive interference of counter-propagating waves. Only frequencies that are constructively superimposed will be amplified and sustained in the cavity, forming the longitudinal resonator modes. The mode structure is defined by the resonance condition $2d = q\lambda$, where d is the cavity length, q is an integer, and λ is the laser wavelength. The frequency difference between adjacent longitudinal modes, also known as the free spectral range (FSR), can be deduced from Eq. (2.37):

$$\Delta\nu_{\mathrm{FSR}} = \nu_q - \nu_{q-1} = \frac{c}{2d} \tag{2.45}$$

where c is the speed of light in vacuum. For lasing to occur, the gain profile $G(\nu)$ must overlap with the resonator modes. Fig. 2.7 illustrates the distribution of these resonator modes within the gain profile of the active medium for a simple two-mirror resonator cavity with active medium length L and resonator length d. The overlap between the gain profile and the mode frequencies determines which modes can be excited and contribute to laser output. The resonator modes define the frequency structure of the laser, while the gain profile restricts the number of modes that can oscillate.

The spectral width $\delta\nu$ of each of the resonator modes is determined by the FSR and finesse $\mathcal{F}$ of the resonator:

$$\delta\nu = \frac{\Delta\nu_{\mathrm{FSR}}}{\mathcal{F}} \tag{2.46}$$

The finesse is a measure of the sharpness of the resonator modes and depends on the reflectivity of the resonator mirrors, R_1 and R_2, which is expressed as [Ren12]:

$$\mathcal{F} = \frac{\pi\sqrt{|r_1 r_2|}}{1 - |r_1 r_2|} \tag{2.47}$$

where $r_i = \sqrt{R_i}$ are the amplitude reflectances of the cavity mirrors. Higher reflectivity mirrors lead to higher finesse, which implies that the resonator can more precisely select

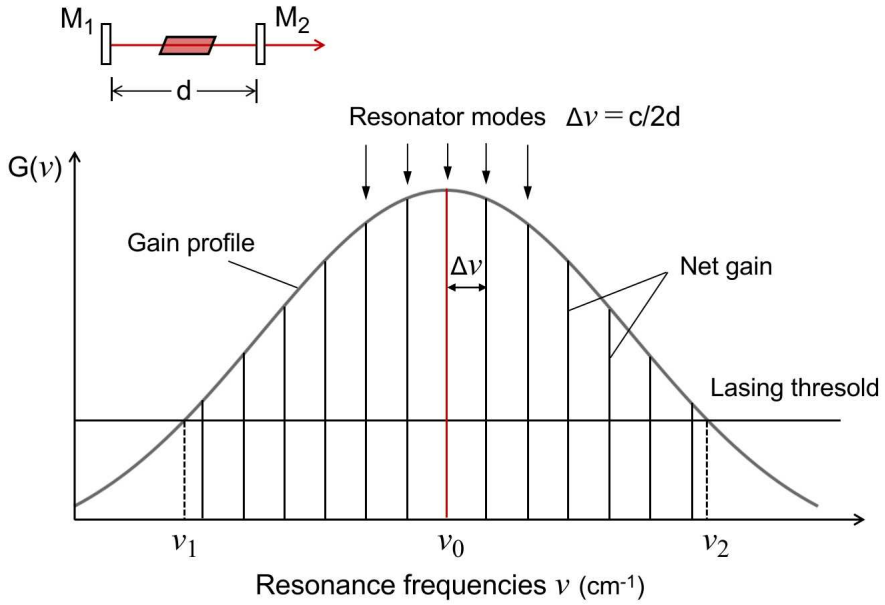

Fig. 2.7. Net gain $G(\nu)$ for resonator modes within the gain profile of the active medium in a Fabry-Perot resonator. The gain profile, peaked around a central frequency ν_0, represents the amplification provided by the laser medium across different frequencies. Vertical black lines, spaced by the Free Spectral Range ($\delta\nu = c/2d$), indicate the resonance frequencies of the longitudinal resonator modes that satisfy the threshold condition and fall within the gain bandwidth, where sufficient gain is available to support oscillation and contribute to the laser output.

specific wavelengths of light through better mode discrimination. To achieve high finesse, cavity mirrors are often coated for high reflectivity for a specified wavelength range, thereby increasing the transmission efficiency at those wavelengths. The transmittance function $\mathcal{T}(\nu)$ of a Fabry-Perot resonator is given by [Ren12]:

$$\mathcal{T}(\nu) = \frac{\mathcal{T}_{\max}}{1 + (2\mathcal{F}/\pi)^2 \sin^2[\pi\nu/\Delta\nu_{\mathrm{FSR}}]} \tag{2.48}$$

where $\mathcal{T}_{\max}$ is the maximum transmittance.

Linear cavities typically support multiple longitudinal modes lasing simultaneously, which can lead to mode competition and less stable output if not properly managed. Precise control of these modes and thus frequency selection is enabled by the insertion of additional intracavity optical elements such as a birefringent filter and etalon, described in Section 2.2.4. The laser cavities are typically designed in geometries such that higher transverse modes are already suppressed and single transverse mode (TEM_{00} mode) operation is favored.

The standing wave pattern in the gain medium causes spatial hole burning [Dem14], where the uneven spatial intensity distribution leads to non-uniform gain saturation

due to the stationary nodes and antinodes. This effect can cause multimode operation of the laser and broaden the output linewidths $\delta\nu$ to the order of a few GHz. While such broadening is a limitation for high-resolution laser spectroscopy, it is advantageous for applications such as in-source beam production in hot cavities and in gas cells. The broadened linewidth of the probing light effectively covers the full Doppler- and pressure-broadened absorption profiles of the isotope ensemble of a few GHz, thereby enhancing the efficiency of pure ion beam production.

Traveling wave (ring) cavity

A traveling wave cavity, often implemented as a ring resonator, consists of a set of mirrors arranged such that light circulates unidirectionally around a closed loop. Optical isolators [ST19] are commonly used in laser systems to protect against back reflections. The ring resonator also supports modes where the round-trip phase shift is a multiple of 2π, the resonator modes are therefore determined by $L = q\lambda$, where L is the total length of the ring. The FSR for a ring resonator is given by:

$$\Delta\nu_{\mathrm{FSR}} = \frac{c}{L} \tag{2.49}$$

The unidirectional propagation in a ring cavity prevents the formation of standing wave patterns within the gain medium, thereby avoiding the spatial hole burning effects. The resulting uniform gain medium saturation and reduced mode competition, make ring resonators suitable for single-mode operation and applications requiring stable, narrow linewidths.

Another significant difference between ring cavities and linear cavities is their wavelength selection mechanisms. Linear cavities typically rely on passive wavelength-selective elements such as etalons and birefringent filters, which can add complexity and potential optical losses to the system. In contrast, ring cavities primarily use active wavelength selection mechanisms, providing greater flexibility and minimizing the need for passive optical components without interfering with the active locking mechanism. Passive elements can still be incorporated into ring cavities when necessary. For example, they can be used to shift the laser operation towards the edges of the broad Ti:sa emission spectrum.

For high-resolution laser spectroscopy, excitation lasers require a narrow linewidth on the order of MHz to resolve hyperfine structures. Conversely, the ionization laser should have a linewidth equal to or greater than the atomic transition resonance width at the autoionizing state to effectively cover the resonance profile and maximize ionization efficiency.

In this thesis work, two broadband cavities with the Z-type linear configuration and a narrowband cavity with the bow-tie ring configuration were used. The geometries of

these simple linear and ring Ti:sa laser configurations, differing in their optical layouts and component arrangements, are illustrated in Fig. 2.8.

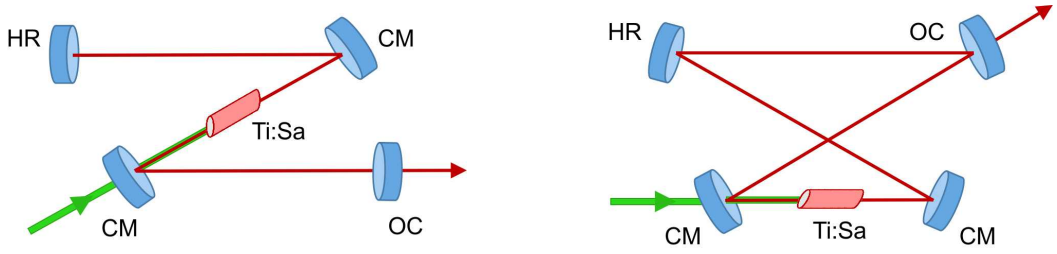

Fig. 2.8. Illustration of Ti:sa laser configurations: (Left) Z-type linear configuration, and (Right) bow-tie ring configuration. Labels: CM - curved mirror, HR - high reflecting mirror, OC - output coupler.

2.2.4 Wavelength selection

In standing wave Ti:sa lasers, the broad gain profile of the active medium allows multiple longitudinal modes of the laser cavity to be amplified and participate in the laser oscillation. The wavelength selection is achieved by introducing losses for the unwanted frequencies through intracavity passive wavelength-selective elements such as a birefringent filter and etalon(s). Furthermore, the cavity mirrors with specific coatings can be used to select from the full gain profile a $\sim$ 100 nm range wavelength.

The bow-tie ring cavity utilizes an active wavelength selection mechanism through the use of an external continuous-wave laser acting as a seeding source. This process, known as injection locking, requires active frequency stabilization, ensuring precise wavelength control and stabilized single-mode operation. Further details about the injection-locking technique are provided in Section 3.2.1.

Birefringent filter

A tunable birefringent filter is an optical filter frequently used within laser resonators to narrow output bandwidth, utilizing the birefringence property inherent in optically anisotropic materials like quartz or calcite. A birefringent plate is typically cut from a birefringent crystal so that its optical axis (OA) lies in the plane of the plate. These filters are typically composed of either a single birefringent plate or multiple plates with different thicknesses stacked together with air as the medium between them. Typically oriented at Brewster's angle, the filter minimizes the reflection losses for p-polarized beams but causes high losses for the s-polarized light at the surfaces. When a p-polarized light passes through the birefringent plate, it splits into two orthogonal polarized beams: an ordinary (o) wave along the OA, which propagates with the wave number $k_o = n_o k$

and the phase velocity $v_o = c/n_o$, and an extraordinary (e) wave perpendicular to the OA, which experiences a refractive index that varies with the direction of propagation, with $k_e = n_e k$ and $v_e = c/n_e$. The difference in propagation speeds causes a relative delay between the two polarized components with a phase shift $\Delta\phi$ of [Dem14]:

$$\Delta\phi = k(n_e - n_o)L = \frac{2\pi(n_e - n_o)L}{\lambda}, \tag{2.50}$$

where $\Delta n = n_e - n_o$ is the difference in refractive indices, λ is the wavelength of the light, L is the optical path length within the birefringent material. The wavelength-dependent transmission $T(\lambda)$ through a single birefringent plate is determined by the interference pattern and is given by [Dem14]:

$$T(\lambda) = T_0 \cos^2\left(\frac{\pi\Delta nL}{\lambda}\right), \tag{2.51}$$

where T_0 is the maximum transmission. When the phase shift $\Delta\phi$ is such that $\cos^2\left(\frac{\pi\Delta nL}{\lambda}\right)$ is close to 1, the transmission is at a maximum $T(\lambda) = T_0$. For wavelengths not aligned with the transmission peaks, the phase shift causes the light to become s-polarized and effectively filtered out due to high reflection losses. For specific wavelengths in the transmission peak, the birefringent filter transmits light that maintains p-polarization, which is the polarization that the cavity is designed to support.

The transmission through N plates in parallel orientation is given by [KS92]:

$$T(\lambda) = \frac{\sin^2\left(\frac{2^N\pi\Delta nl}{\lambda}\right)}{2^{2N}\sin^2\left(\frac{\pi\Delta nl}{\lambda}\right)} \tag{2.52}$$

where l is the thickness of the thinnest plate. The phase shift is cumulative for each additional plate in the stack. The spectral width $\delta\nu$ of the transmission peaks, or the filter's resolution, depends on the thickness D of the thickest birefringent plates and the total number of plates N:

$$\delta\nu = \frac{c}{2^{N-1}}\Delta nD \tag{2.53}$$

The free spectral range $\Delta\nu_{\mathrm{FSR}}$ is given by the thinnest plate

$$\Delta\nu_{\mathrm{FSR}} = \frac{c}{\Delta nl} \tag{2.54}$$

The wavelength is tuned by rotating the birefringent filter around an axis perpendicular to the plate surface, which alters the refractive index difference Δn by changing the angle between the crystal's optical axis and the propagation direction of the laser beam, thereby shifting the transmission to a different wavelength.

The use of multiple plates of varying thicknesses enables the filter to achieve both a narrow transmission bandwidth and a large FSR, thereby providing precise wavelength selection combined with a broad wavelength range over which this precision can be applied.

Thin and thick etalon

Finer wavelength selection is performed by the use of an etalon, a passive Fabry–Perot resonator that acts as an optical filter. The etalon consists of two parallel reflective surfaces separated by a medium with a refractive index n and a thickness d. It operates based on the constructive and destructive interference of beams arising from the multiple reflections and transmissions between the two surfaces. When the light of frequency ν enters an etalon at an incidence angle θ relative to the surface normal, the frequency-dependent transmission mathematically expressed as [ST19]:

$$\mathcal{T}(\nu) = \frac{\mathcal{T}_{\max}}{1 + (2\mathcal{F}/\pi)^2 \sin^2[\pi\nu/\Delta\nu_{\mathrm{FSR}} \cos\theta]} \tag{2.55}$$

where $\mathcal{F}$ is the finesse of the etalon, given for equal surface reflectivities $R_1 = R_2 = R$ as [Dem10]:

$$\mathcal{F} = \frac{\pi\sqrt{R}}{1 - R} \tag{2.56}$$

$\Delta\nu_{\mathrm{FSR}}$ is spacing between the highest transmission peaks, which is obtained for the wavelengths that match the integer multiple of optical path length nd within the etalon [Dem10]:

$$\Delta\nu_{\mathrm{FSR}} = \frac{c}{2nd} \tag{2.57}$$

The spectral resolution of the etalon is then given by $\delta\nu = \Delta\nu_{\mathrm{FSR}}/\mathcal{F}$.

Etalons are typically made from materials with high refractive indices to enhance their wavelength-selective capabilities. Common materials include YAG (Yttrium Aluminum Garnet) and other crystals or glasses with well-defined optical properties. Reflective coatings are applied to the etalon surfaces for specific reflectivity R, which varies the finesse and free spectral range (FSR) of the etalon. Thick etalons with high reflectivity are ideal for narrow linewidths selection, while thin etalons with moderate reflectivity are better suited for selecting broader bandwidths. For a typically thin $d = 0.3$ mm glass substrate ($n \approx 1.5$) etalon, with a broad-band reflective coating of R = 40% on both sides, $\Delta\nu_{\mathrm{FSR}} \approx 330$ GHz, and $\delta\nu \approx 100$ GHz. While for a thick $d = 6$ mm YAG ($n \approx 1.8$) etalon, with R = 80% reflective coating on both sides, $\Delta\nu_{\mathrm{FSR}} \approx 14$ GHz and $\delta\nu \approx 1$ GHz.

This thesis work with S^3-LEB utilized two broadband Z-type cavities, a single-etalon Ti:sa cavity incorporating a BRF and a thin etalon, and a dual-etalon Ti:sa cavity with

improved resolution including a BRF along with both thin and thick etalons. Using two etalons aims to achieve an extended free spectral range (FSR) and to minimize mode hopping issues associated with single thick etalons. Detailed descriptions are provided in Section 3.2. The standing wave configurations with broadband resolution in the order of GHz do not allow a single-mode operation. A schematic overview of the transmission profiles of different wavelength-selective elements and the transmitted resonator modes is presented in Fig. 2.9. The total bandwidth of the laser emission depends on the width of the overall gain profile of the selected longitudinal modes.

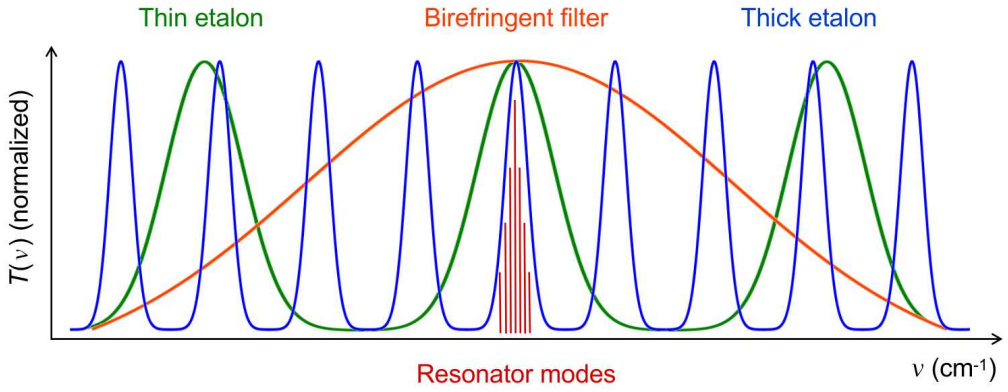

Fig. 2.9. Comparison of the spectral linewidth of transmission peaks for various passive wavelength-selective elements in a Ti:sa resonator. The dense red lines represent the selected longitudinal modes resulting in the spectral profile.

2.2.5 Nonlinear optical frequency conversion

In RIS experiments, most atomic transitions lie in the UV or visible range and cannot be directly probed by the fundamental Ti:sa laser. To expand the accessible wavelength range, nonlinear frequency conversion techniques are used to mix laser beams of different frequencies in nonlinear media to generate coherent output at sum and difference frequencies. These techniques include second-harmonic generation (SHG), sum-frequency generation (SFG), and difference-frequency generation (DFG), which produce new wavelengths through nonlinear optical processes.

In a vacuum, electromagnetic waves do not normally interact with each other due to the linear nature of Maxwell's equations in free space, except for certain extreme conditions such as those approaching the Schwinger limit [Rot12]. However, this is far beyond the typical conditions in atomic spectroscopy experiments. In contrast, within nonlinear crystals such as beta barium borate (BBO), lithium niobate (LBO), and potassium dihydrogen phosphate (KDP), electromagnetic waves can interact with each other given sufficiently high laser intensities. This is due to the material's nonlinear optical properties, where the polarization is no longer proportional to the applied electric field strength at high laser intensities. Instead, the nonlinear polarization P (the dipole

moment per unit volume) includes higher-order terms:

$$\mathbf{P} = \epsilon_0 \left(\chi^{(1)}\mathbf{E} + \chi^{(2)}\mathbf{E}^2 + \chi^{(3)}\mathbf{E}^3 + \ldots \right) = \epsilon_0 \chi^{(1)}\mathbf{E} + \mathbf{P}_{\mathrm{NL}} \tag{2.58}$$

where ϵ_0 is the permittivity of free space, $\chi^{(1)}$ is the linear susceptibility, $\chi^{(2)}$, $\chi^{(3)}$, etc., are the nonlinear susceptibilities, which describe the material's response to higher powers of the electric field. $\chi^{(i)}\mathbf{E}^i$ is the i-th order nonlinear polarization. $\mathbf{P}_{\mathrm{NL}}$ describes the nonlinear contributions to the polarization.

For two electric fields, $\mathbf{E_1}$ and $\mathbf{E_2}$, with frequencies ω_1 and ω_2, the second-order nonlinear polarization generates several electromagnetic waves with frequency mixing. These include second harmonic generation (SHG) at frequencies $2\omega_1$ and $2\omega_2$, sum-frequency generation (SFG) at the frequency $\omega_1 + \omega_2$, difference-frequency mixing (DFG) at the frequency $\omega_2 - \omega_1$, and optical rectification (OR) at zero frequency arising from terms $\omega_2 - \omega_2 = \omega_1 - \omega_1 = 0$. Further details can be found in [Dem10, Dem14].

For frequency doubling of single fundamental input light with electric field $E(\omega) = E_0 \cos(\omega t - kz)$ with wave vector $k = n\omega/c$, the nonlinear polarization causes the generation of a secondary wave in the crystal with amplitude $E(2\omega)$, frequency 2ω and wave vector $k(2\omega)$. For efficient SHG, the second harmonic wave $E(2\omega)$ must constructively interfere with itself as it builds up within the crystal. This requires the fundamental wave and the second harmonic wave to maintain a constant phase relationship known as phase matching. Mathematically, this condition is expressed as [Dem14]:

$$\Delta\phi = \Delta k L = [2k(\omega) - k(2\omega)]L = 0 \quad \Rightarrow \quad k(2\omega) = 2k(\omega) \tag{2.59}$$

Here, $\Delta\phi$ is the phase difference between the waves, and L is the optical length in the nonlinear medium. With $c/n = \omega/k$ the condition becomes $n(\omega) = n(2\omega)$. This condition can be fulfilled in negative uniaxial birefringent crystals, where light propagates in two orthogonal polarization eigenmodes, the ordinary wave with refractive index n_o and the extraordinary wave with refractive index n_e ('negative' means $n_e < n_o$). The ordinary wave has its **E** field vector always perpendicular to the optical axis of the crystal. Its propagation direction **k** is independent of light polarization **P**. The extraordinary wave is polarized in a plane defined by the optical axis and the incident beam. While the ordinary index n_o does not depend on the propagation direction of the wave, the extraordinary index n_e depends on the relative orientations of both **E** and **k**. To achieve phase matching, the crystal is often oriented at a specific angle (phase-matching angles θ_{pm}) with respect to the incident light beam to optimize SHG:

$$n_e(2\omega, \theta_{\mathrm{pm}}) = n_o(\omega) \tag{2.60}$$

Phase matching inside the negative uniaxial birefringent BBO crystal is used for the laser system at S^3-LEB. Further details about positive uniaxial birefringent material,

phase matching by temperature adjustment of the crystal or quasi-phase-matched crystals can be found in [Dem14].

The intensity of the second harmonic (SH) wave is given by [Dem14]:

$$I(2\omega, L) = I^2(\omega)\frac{2\omega^2|\chi^{(2)}_{\text{eff}}|^2L^2}{n^3c^3\epsilon_0} \cdot \frac{\sin^2(\Delta kL)}{(\Delta kL)^2} \tag{2.61}$$

The SHG intensity, I_{SHG}, is proportional to the square of the intensity of the fundamental wave, I^2_{fund}. This intensity relationship affects the spatial beam width. Due to the nonlinear processes, the spectral linewidth of the SHG beam, $\Delta\nu_{\text{SHG}}$, increases by a factor of $\sqrt{2}$ with respect to the fundamental beam linewidth, $\Delta\nu_{\text{fund}}$:

$$\Delta\nu_{\text{SHG}} = \sqrt{2}\,\Delta\nu_{\text{fund}} \tag{2.62}$$

SHG can be performed inside or outside the laser resonators. In the Ti:sa laser system used for this thesis work, the intracavity BBO crystal was used in the broadband Z-type cavities for efficient frequency doubling. While an external frequency doubling unit was employed for the injection-locked single-mode cavity to enhance stability by reducing sensitivity to temperature fluctuations and alignment issues. Descriptions of the laser system are provided in Section 3.2.

In addition to the theoretical foundation established in Chapter 1, this chapter has discussed the IGLIS technique and the tunable Ti:sa lasers used for the measurements presented in this thesis. The next Chapter 3 will provide a detailed description of the S^3-LEB setup at SPIRAL2, focusing on its key components and the laser system for implementing the IGLIS technique.

Chapter 3

The S^3-Low Energy Branch

The Low Energy Branch of the Super Separator Spectrometer (S^3) within the framework of the SPIRAL2 facility of GANIL [Gal10], is designed for high-resolution laser spectroscopy and nuclear structure studies of rare isotopes. SPIRAL2 represents a next-generation nuclear-research facility, aiming to deliver intense secondary radioactive ion beams following reactions with primary beams accelerated by its superconducting linear accelerator (SC-LINAC). The schematic layout of the SPIRAL2 facility is shown in Fig. 3.1. The LINAC is capable of delivering high-intensity deuterons and stable heavy-ion beams, ranging from helium to uranium [G$^+$06, T$^+$12a]. The beam energies for heavy ions will be up to 14.5 MeV/u with intensities reaching 10^{14} ions per second, which are cutting-edge intensities compared to existing facilities.

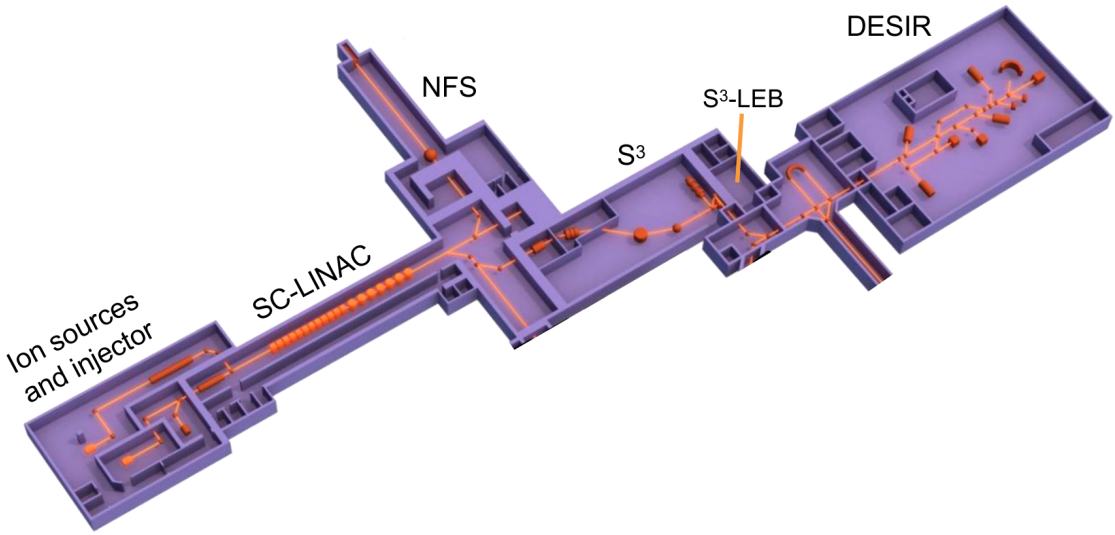

Fig. 3.1. Schematic of the GANIL SPIRAL2 facility.

These high-intensity beams are intended for two experimental areas: the Super Separator Spectrometer (S3) [D$^+$15, DNSc20], which is designed to synthesize rare isotopes, and

Neutrons For Science (NFS), which is built to produce a high-intensity neutron beam from deuterons [L$^+$17].

S^3 has been designed with the aim to produce rare isotopes by fusion-evaporation reactions, such as neutron-deficient nuclei close to the proton dripline and superheavy nuclei. Both physics cases require effective discrimination of the rare reaction products from predominant background events. As a high-resolution recoil separator, S^3 facilitates this discrimination by two stages of separation [D$^+$15], as shown in Fig. 3.2. After the primary beam impinges on the target, the nuclear reaction products pass through the first separation stage, known as the momentum achromat, where the unreacted primary beam particles are rejected due to their different momentum as compared to the desired reaction products. Following the momentum separation, the remaining reaction products enter the mass-to-charge (m/q) spectrometer (MS), which provides additional mass selectivity for precise separation of the reaction products.

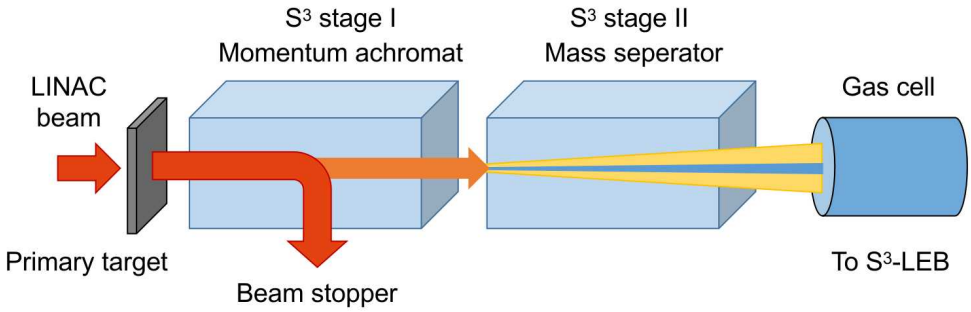

Fig. 3.2. Schematic representation of the S^3 design.

The design of S^3 is characterized by its versatility, allowing for the implementation of various optical modes tailored to specific experimental requirements and detection systems. Established optical modes, including high-resolution mode, high-transmission mode, converging mode, and high-beam rejection mode, have been developed to address anticipated experimental conditions. S^3 also maintains the flexibility to incorporate future specialized modes in response to emerging experimental needs [D$^+$15]. Among these, the converging mode is specifically optimized to maximize the transmission of the nuclei of interest through the S^3-LEB gas cell entrance window. Simulations for the S^3 converging mode have been leading to predictions about the beam properties at the focal plane. These results have been used in the gas cell design simulations presented in this thesis, enabling the evaluation of its performance under on-line conditions at SPIRAL2. Further details can be found in Chapter 5.

3.1 The S^3-LEB setup

The S^3 Low Energy Branch (S^3-LEB), currently installed at the focal plane of S^3, aims to study the ground state and isomeric states of the fusion-evaporation products using the in-gas laser ionization and spectroscopy (IGLIS) technique, mass spectroscopy or decay spectroscopy. The layout of the S^3-LEB setup during its off-line commissioning at Laboratoire de Physique Corpusculaire (LPC), Caen is shown schematically in Fig. 3.3.

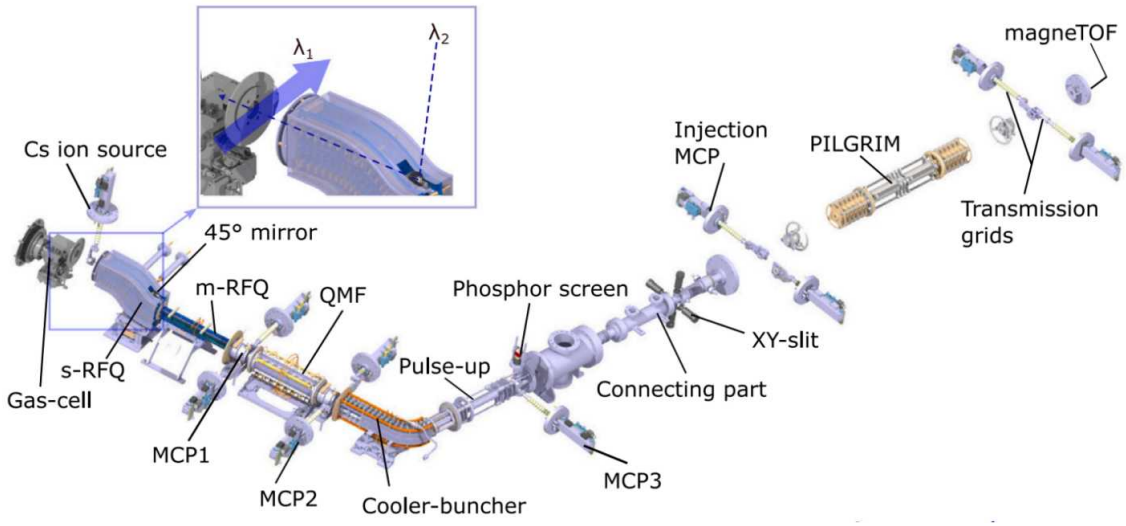

Fig. 3.3. Layout of the S^3-LEB setup. Figure taken from [A$^+$23].

In on-line conditions at SPIRAL2, the S^3 products will enter the gas cell through a micrometer-thick titanium or Mylar window. To efficiently stop and neutralize the radioactive ions, the cell will be filled with ultrapure argon and operate at stagnation pressure in range of 200–500 mbar. The window is designed to separate the high-pressure environment within the gas cell from the vacuum region of S^3. During off-line commissioning, the gas cell was operated under the same conditions as those expected during on-line use, but with the entrance window replaced by a blind flange. Stable isotopes of erbium were deposited in solution on two tantalum filaments, which were subsequently dried and installed in the gas cell. Neutral atoms were then evaporated into the gas environment through resistive heating of one of the filaments.

A de-Laval nozzle [F$^+$21] featuring a Mach number $M \sim 8$, achieved through precisely optimized geometry and high-precision manufacturing, was installed at the gas cell exit to produce a homogeneous, collimated supersonic gas jet characterized by low temperature and pressure. The neutralized atoms under investigation were extracted out of the gas cell via the gas flow through the nozzle. In the context of IGLIS studies, two-step resonance laser ionization takes place at the intersection of the first and second-step laser beams within the gas cell near the exit or in the supersonic jet.

The excitation step is oriented transversely with respect to the axis of the neutralized atom beam, while the ionization step is directed longitudinally. In the supersonic jet configuration, the transverse laser beam can be expanded through optical lenses to ensure complete temporal overlap between the pulsed lasers and the atoms in the high-velocity flow, and thus ensure a high ionization efficiency. For an argon jet at a velocity of $v = 550$ m/s and a laser repetition rate of 10 kHz, an optimal beam width of 55 mm is established [KFH$^+$13]. In the offline measurements conducted in this work, the first step laser beam is not expanded, as sufficient counts for the measurements were ensured through filament evaporation and high resolution was desired first and foremost.

The laser-produced ions are then confined and transported through a sequence of radio-frequency quadrupole (RFQs) ion guides. Along the RFQ path, micro-channel plates (MCPs) are positioned at different stages to detect and monitor the ion counts. The ions are subsequently directed to a multi-reflection time-of-flight mass spectrometer (MR-TOF-MS), which separates the ions based on their mass-to-charge ratio and allows for precise mass measurements for resonance ionization spectroscopy. A deflector [Aja23] can also bend the ions to future experimental setups such as the decay station called Spectroscopy Electron Alpha in Silicon bOx couNter, (SEASON) [Van20], or the Decay, Excitation and Storage of Radioactive Ions facility (DESIR) [Bla10].

The S^3-LEB setup integrates the isomeric selectivity and high sensitivity provided by the in-gas-jet RIS technique with the mass selectivity of the MR-TOF mass spectrometry and rapid detection capabilities. A more comprehensive description of the S^3-LEB setup, including the first offline commissioning results, can be found in [R$^+$22, Aja23]. The subsequent sections focus on the principle of the S^3-LEB gas cell, the ion behaviors in the gas environment, and the limitations of the current gas cell design.

3.1.1 S^3-LEB gas cell, RFQ ion guides and mass spectrometer

Gas cell

The gas cell represents an essential component of the S^3-LEB installation, being the interface between the high-energy S^3 beam line and the low-energy ion-transport system [D$^+$16]. The fusion-evaporation recoils from S^3 enter the gas cell through a thin window that separates the high-pressure argon-filled volume from the spectrometer vacuum and loses energy by collisions with the buffer gas. A section through the 3D model of the current version of the S^3-LEB gas cell [K$^+$16, Zad18] and the de Laval nozzle [M$^+$13, F$^+$21] designed at KU Leuven are shown in Fig. 3.4.

Since S^3 will be operated in converging mode for maximum transmission efficiency, the gas cell entrance is designed with a 50 mm diameter to allow the entire beam to pass

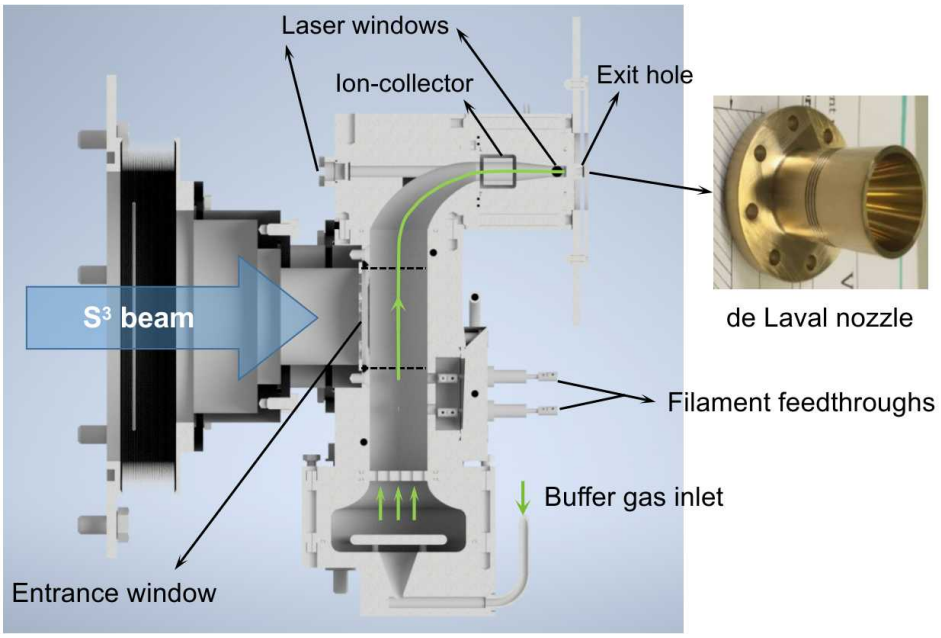

Fig. 3.4. Section through the 3D model of the S^3-LEB gas cell.

through, and the cell volume was adapted to the projected stopping volume of the S^3 beam in converging mode. The internal cross-section of the gas cell has a 30 mm depth and a 70 mm width. This gas cell is designed with a 90° bend, separating the S^3 axes (the stopping region) from the laser-ionization region. This separation facilitates easier laser coupling and enhances laser ionization efficiency by preventing photoionized ions from being re-neutralized in the plasma created by the S^3 beam.

Two filaments can be installed in the gas cell via the filament feedthroughs, and can be resistively heated to evaporate ions in the stopping volume during the offline tests. Prior to the exit of the gas cell, two ion-collector electrodes are installed to remove non-neutralized ions, thereby eliminating background noise during the RIS measurements. The gas cell has three laser windows, two just before the exit, facing each other, to allow the laser beam to enter in a transverse geometry, and one is opposite to the exit hole to facilitate the alignment of the anti-collinear laser beam. At the exit of the gas cell, a de Laval nozzle is installed for the in-gas-jet RIS measurements.

RFQs

The ion extraction system at S^3-LEB consists of a series of radio frequency quadrupoles (RFQs) designed to transport, filter and cool ions through differential pressure stages. The layout of the full S^3-LEB ion guide can be seen in Fig. 3.3. After ionization in the gas cell, ions are extracted through an S-shaped RFQ (S-RFQ), which is hosted in the same gas cell chamber and operates at a pressure ($\sim 10^{-2}$–10^{-1} mbar) matched to the gas jet. The S-RFQ serves to decouple the laser and ion beam axes, while a linear DC

gradient, combined with RF voltage, drives the ions through the system.

Following the S-RFQ, ions pass through a mini-RFQ (m-RFQ) that transitions them from the relatively high-pressure gas cell chamber to a high-vacuum environment. The m-RFQ chamber is independently pumped to maintain a low pressure of 10^{-4}–10^{-3} mbar. It enhances differential pumping, moving ions efficiently to the next stage.

A quadrupole mass filter (QMF) is then used to pre-select ions based on their mass-to-charge ratio (M/q). The QMF can operate in filtering mode with a resolving power of $m/\Delta m \approx 100$ or high-transmission mode without mass selection.

After the QMF, the ions are transported to an RFQ cooler-buncher, where they are cooled in helium gas ($\sim 10^{-2}$ mbar) at a flow rate of 90–120 mL/min [A$^+$23]. The ions are accumulated and trapped in an electric potential well, cooled via collisions with helium atoms, and extracted in bunches at a typical repetition rate of 20 Hz by switching voltages on the final electrodes for further injection into the PILGRIM MR-TOF-MS.

PILGRIM

The PILGRIM system at S^3-LEB is a multi-reflection time-of-flight mass spectrometer (MR-TOF-MS) designed for precise mass measurement and isobar separation [C$^+$16]. After ions are cooled and bunched in the RFQ cooler-buncher, they are re-accelerated to $\sim$ 3 - 3.5 keV using a pulse-up (PU) drift tube. PILGRIM is housed in a vacuum chamber pumped with turbomolecular pumps to achieve the high vacuum conditions necessary for optimal operation in the range of 10^{-9} - 10^{-8} mbar. This ultra-high vacuum ensures minimal interaction between the ions and residual gas molecules, critical for achieving high mass-resolving power.

As shown in Fig. 3.5, the PILGRIM MR-TOF-MS is a linear ion trap consisting of electrostatic mirrors that sandwich a field-free drift tube. Ions are injected as bunches into the trap and travel back and forth between the mirrors, achieving a long flight path to enhance mass separation. The setup compensates for the ion energy spread using controlled mirror potentials, which focus the time of flight (ToF) by forcing faster ions to travel a longer distance. This process ensures that the PILGRIM MR-TOF-MS can achieve a high mass-resolving power of approximately $R = m/(\Delta m) = t/2\Delta t \approx 10^5$. This high-resolution mass spectrometry enables precise identification of rare isotopes and isobaric species.

The MR-TOF-MS traps ions using the ”in-trap lift” method, where ions are injected with higher kinetic energy than the mirror potentials. Upon entry, the drift tube potential is pulsed down to trap the ions, and for ejection, the potential is pulsed back up, allowing the ions to overcome the potential barrier of the exit mirror. This method requires switching a single potential, ensuring larger voltage stability than if the mirror

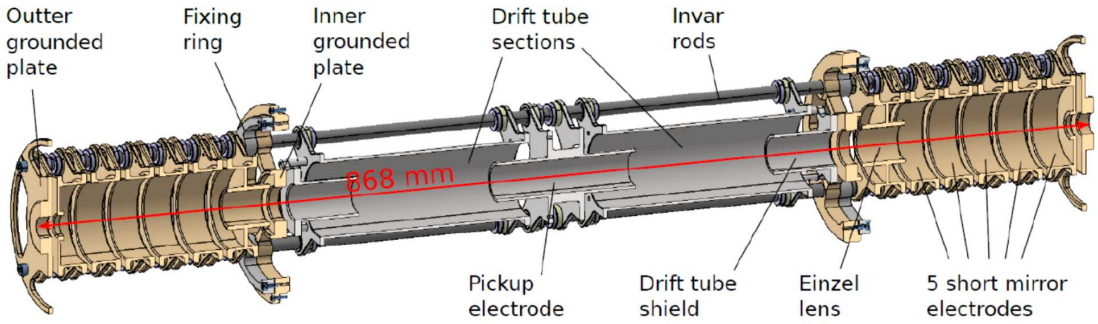

Fig. 3.5. Layout of the PILGRIM multi-reflection time of flight mass spectrometer for S^3-LEB [Cha16].

voltages were switched, improving operational stability.

The transmission efficiency from the gas cell exit to the end of PILGRIM has been optimized to exceed 80%, as shown in [Aja23].

3.1.2 Ion behavior in the gas cell and gas jet

In Resonance Ionization Spectroscopy (RIS) experiments, the behavior of ions within the gas cell and gas jet plays a critical role in determining the overall efficiency and resolution of the technique. The ion behavior in both environments is shaped by gas dynamics, pressure conditions, ion-neutral interactions, and the laser ionization process.

When ions enter the gas cell, they undergo rapid energy loss through collisions with the buffer gas atoms, effectively stopping within the gas cell. After stopping, ions are neutralized primarily through three-body but also dissociative recombination during extraction. The former process involves an ion capturing an electron followed by stabilization through collision with a buffer-gas atom, resulting in the formation of a neutral atom. The efficiency of this neutralization depends on factors such as gas pressure, temperature, and the density of free electrons ejected from the argon atoms due to collisions with the energetic S^3 beam. Once neutralized, the atoms experience thermal motion and drift within the gas cell, driven by the laminar flow of the buffer gas to the exit hole.

Neutral atoms that exit the gas cell through a de Laval nozzle undergo supersonic expansion and form a gas jet with a velocity v $\approx$ 550 m/s. During expansion, the thermal energy of the gas within the cell is converted into the kinetic energy of the jet. This expansion leads to substantial cooling of the gas and a significant reduction in both gas pressure and density. As a result, a marked decrease in the collision and Doppler broadening is achieved compared to those occurring in the gas cell.

The optimized de Laval nozzle is designed to generate a long, homogeneous supersonic

jet over 200 mm [F$^+$17], which ensures full coverage of the several tens of millimeters distance between the radiofrequency ion guide and the nozzle exit. According to the relationships given by Eq. (2.6), Eq. (2.7) and Eq. (2.8), the temperature, the relative density, and the relative pressure of the jet are functions of the Mach number. For a stagnation temperature $T_0 = 300$ K, along with stagnation pressure P_0 and stagnation density ρ_0, the behavior of these parameters in the jet can be calculated. Fig. 3.6 shows the rapid drop of the temperature, the relative density, and the relative pressure in the supersonic argon jet with increasing Mach number.

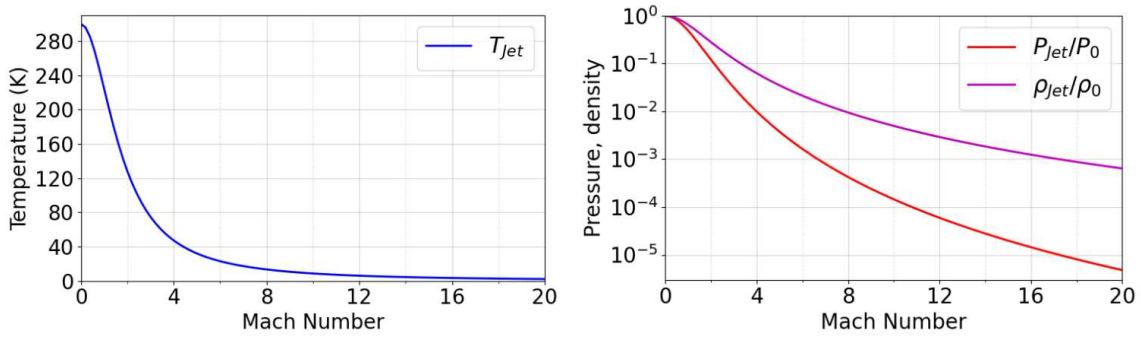

Fig. 3.6. Temperature, pressure and density reduction in the supersonic jet for a monoatomic gas ($\gamma = 5/3$) with the stagnation temperature $T_0 = 300$ K in the gas cell. Left: temperature in the jet as a function of the Mach number. Right: pressure and density reduction in the supersonic jet relative to those in the gas cell as a function of the Mach number.

The Mach number of the gas jet, determined by the nozzle geometry and gas flow rate, plays a critical role in achieving optimal collimation and cooling. In this thesis work, a nozzle with Mach number ~ 8 was utilized. As indicated by Eq. (2.29), the contribution of Doppler broadening is reduced by a factor of $\sqrt{T_0/T_{\text{jet}}}$ in the jet compared to that in the gas cell. According to Eq. (2.25), the collisional broadening contribution is diminished by ρ_0/ρ_{jet}. For a Mach number $M = 8$, the atomic beam attains a temperature of $T_{\text{jet}} = 13$ K and a density of $\rho = 0.0095\rho_0$.

The Mach number of the nozzle is limited to around 8 due to practical constraints, including viscous effects that thicken boundary layers, limitations in vacuum pumping capacity for achieving lower pressures, and nucleation onset at low stagnation temperatures, which locally increases the gas temperature and reduces the Mach number [F$^+$21]. These factors collectively make it challenging to achieve uniform and stable flow at higher Mach numbers.

The calculated various components contributing to the spectral linewidth of the 408.8 nm transition in erbium are presented in Fig. 3.7. The top panel illustrates the linewidth components for the in-gas-cell spectroscopy at different buffer gas pressures, whereas

the bottom panel presents the contributions for the supersonic gas jet with a Mach number $M = 8$. The natural linewidth of the transition is also displayed in both panels for comparative analysis.

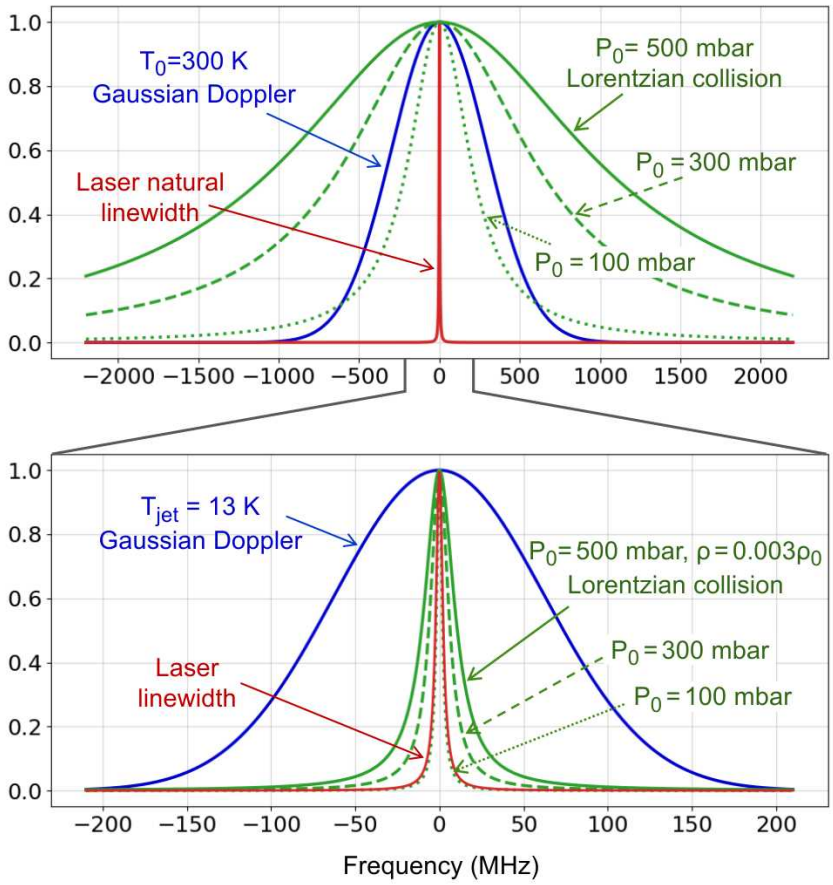

Fig. 3.7. Comparison of the Gaussian Doppler broadening, Lorentzian collision broadening, and laser natural linewidth contributions to the shape of the 408.8 nm spectral line. (top) in the gas cell $P_0 = 500$, 300 or 100 mbar, $T_0 = 300$ K, (bottom) in the supersonic gas jet of Mach number $M = 8$, $T_{\text{jet}} = 13$ K, and $\rho = 0.0095\rho_0$. The collision broadening coefficient takes the value for the 408.8 nm transition of 4.5 MHz/mbar (see Section 4.4.2).

The notable reduction in Doppler and collisional broadening in the supersonic jet significantly enhances spectral resolution in laser spectroscopy, which is essential for resolving hyperfine structures. However, the ionization process in the jet must be optimized to account for the fast atom velocity in the interaction region. In online studies with radioactive nuclei produced with low production rates, to achieve complete temporal overlap between the pulsed laser radiation and the atoms in the continuous high-velocity flow, and thus ensure a high ionization efficiency, the transverse laser beam must be expanded to at least 55 mm for an argon jet as calculated before. In addition, sufficient laser intensity should be maintained to saturate the ionization transitions.

An increase in the jet velocity would necessitate either the utilization of a laser with a higher repetition rate ($f > 10$ kHz) or the formation of a longer laser sheet ($l > 55$ mm) to maintain the high efficiency of the method.

Dedicated spectra of a specific transition acquired in the gas cell and the gas jet allows the investigation of the contributions of the different broadening mechanisms to the line shape. Specifically, the in-gas-cell measurements acquired varying the operational pressure facilitate the characterization of the collisional broadening and frequency shift due to atom–atom interactions in the high-pressure gas-cell environment. This part of work is detailed in Section 4.4.2.

3.1.3 Limitations of the current gas cell

In the current version of the S^3-LEB gas cell, ions are guided from the stopping region to the exit only by a laminar argon gas flow. During the extraction process, ions are neutralized through three-body recombination with argon atoms and free electrons ejected from the argon atoms due to collisions with the energetic S^3 beam. The extraction efficiency is enhanced by the high operational pressure (generally 300 - 500 mbar), which reduces diffusion losses and increases stopping power. Nevertheless, a minimal stopping volume is necessary to accommodate the large S^3 beam, which leads to an extraction time of about 600 ms for a 1 mm nozzle throat diameter, and roughly half that time for a 1.5 mm diameter throat [Mog13a, Mog13b, K$^+$16]. Further reduction of the extraction time can be achieved by increasing the throat diameter, but the neutralization efficiency decreases with a shorter extraction time, and the maximum achievable Mach number of the gas jet will be constrained by the pumping capacity of the S^3-LEB vacuum system. Achieving a high Mach number, ideally approaching $M = 10$, is crucial for optimal spectral resolution to resolve the complicated hyperfine structures in IGLIS measurements [Zad18]. In addition, a larger throat diameter also requires a larger laser beam size, which reduces the laser power density in the jet and can affect the efficiency of saturating the atomic transitions.

The limited extraction time leads to a significant challenge for the study of short-lived S^3 products with half-lives in the 100 ms range. As illustrated in Fig. 3.8, the isotopes from the S^3 yield database which can be produced based on calculations (open squares) include nuclei of particular interest near the proton dripline, especially in the heavy region towards the $N = Z = 82$ shell closures. A significant number of these isotopes, marked by red dots, exhibit half-lives below 250 ms. The properties of these nuclei are indicative for the understanding of nuclear structure and for testing and improving nuclear models. To facilitate their investigation using laser spectroscopy, a gas cell with an extraction time below 100 ms is essential.

Achieving both rapid extraction and efficient neutralization of ions remains a critical challenge for the optimization of gas-cell-based RIS experiments in radioactive-ion-beam

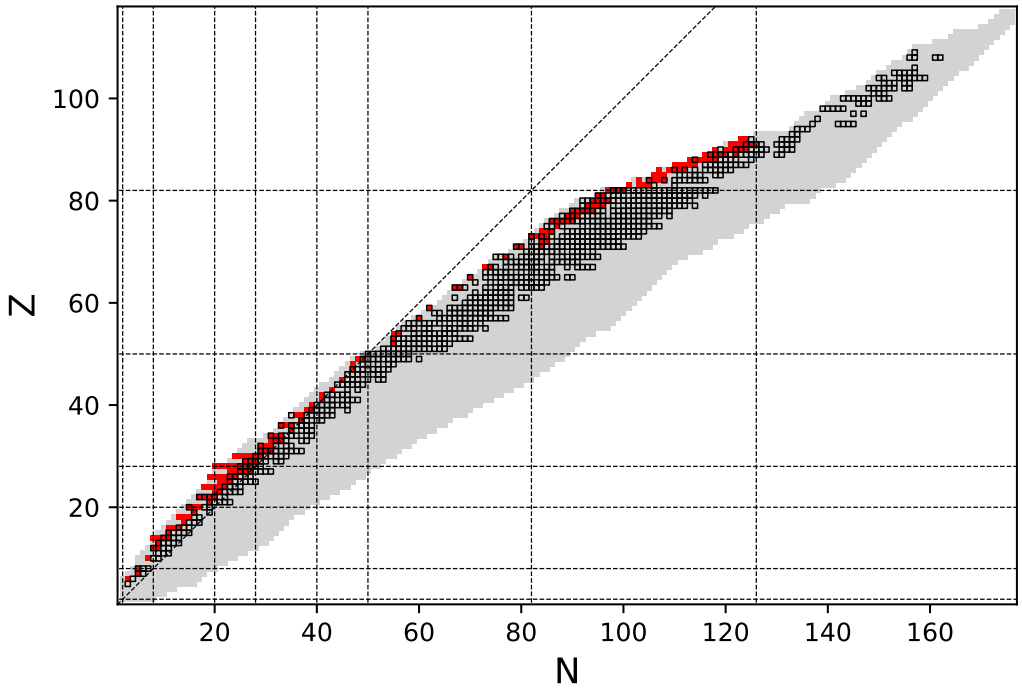

Fig. 3.8. Isotopes from the S^3 yield database. Empty squares: S^3 products, red squares: isotopes with half-lives $T_{1/2} < 250$ ms.

facilities. Gas cells aiming for fast extraction achieve ion extraction times as short as 10 - 20 ms by utilizing electric fields, such as the SHIPTRAP helium-filled gas cell [D$^+$14]. For gas cells aimed at efficient neutralization, such as the argon-filled S^3-LEB gas cell, if an electric field is applied in the stopping region to accelerate ion extraction, the current neutralization mechanism, which relies on free electrons ejected from the gas, becomes ineffective as these electrons are rapidly swept away by the applied field. The RADRIS and JetRIS gas cells at GSI utilize a filament collector followed by re-evaporation for neutralization [R$^+$20, L$^+$24b]. While this neutralization method can function in the electric-field-assisted gas cell, its efficiency is highly element-dependent because some elements with high melting temperatures require longer re-evaporation times. A more efficient and versatile neutralization technique needs to be developed to work with fast extraction. Chapter 5 outlines the design and optimization of a fast gas cell that aims to achieve both fast extraction and efficient neutralization, as explored in this thesis.

3.2 The laser system of S^3-LEB

For the step-wise resonance ionization spectroscopy (RIS) measurements, the Ti:sapphire laser system at S^3-LEB consists of three main components: a high-power frequency doubled 532 nm Nd:YAG laser for pumping, multiple tunable Ti:sa lasers integrating nonlinear frequency conversion techniques, and computer control system for regulating the spatial, spectral and temporal properties of the laser beams.

All essential components, including the primary optical elements responsible for beam transport, overlap, and focusing, as well as a wavemeter for real-time wavelength measurement, are compactly arranged on a laser table. The following sections will provide a detailed description of the Ti:sa laser system and the nonlinear optical frequency conversion techniques.

3.2.1 Ti:sa laser system

Solid-state titanium:sapphire (Ti:sa) lasers pumped by a frequency-doubled Nd:YAG of 100 – 200 ns pulse length and 10 kHz maximum repetition rate [F$^+$12] are utilized at S^3-LEB. As explained in Section 2.2.1, standing wave lasers, with their simpler design, are suitable for high-power applications where multimode operation is acceptable. In contrast, traveling wave lasers are preferable for precision applications requiring narrow linewidths and stable single-mode operation due to their inherent suppression of spatial hole burning and reduced mode competition. In the in-gas-cell and in-gas-jet measurements in this thesis work, three types of Ti:sa cavities available at S^3-LEB were utilized: the mid-resolution (1.5 - 2 GHz) dual-etalon cavity and high-resolution ($\sim$ 35 MHz) injection-locked single-mode cavity for the excitation step, and the high-power broadband ($\sim$ 5 GHz) single-etalon cavity for the ionization step.

Broad band (BB)Ti:sapphire lasers

The broadband (BB) Ti:sapphire laser system uses a 20 mm Ti:sapphire crystal in a Z-shaped resonator, pumped by a 532 nm pulsed laser with 10 kHz repetition rate and 10 - 20 W power. The output pulse width is 35 - 50 ns, with up to 3 W average power at 12 W pump power. Wavelength tuning is achieved using coating mirror sets for a specific wavelength range alongside frequency-selective elements like birefringent filters (BRF) and etalons. The working principle of these elements has been presented in Section 2.2.4.

In a single-etalon cavity, the integration of a thin solid etalon alongside the birefringent filter enables tuning capabilities with a FWHM linewidth of approximately 5 GHz. The etalon is motorized and allows for continuous remote tuning by adjusting its angle relative to the incident light. The single-etalon cavity (see left panel of Fig. 3.9) has

been utilized as the ionization step laser for all the RIS measurements in this work.

The dual-etalon Ti:sapphire laser system (see right panel of Fig. 3.9) enhances wavelength selection by incorporating both a thin etalon (0.3 mm) and a thick etalon (6 mm), effectively reducing the number of laser modes that can exist within the cavity. This configuration results in a significantly narrower linewidth of approximately 1–2 GHz. In this setup, both etalons are motorized, allowing for precise tuning. During operation, the thick etalon's angle is adjusted to scan for the desired wavelength. Simultaneously, the thin etalon's angle is fine-tuned to remain centered on its transmission peak, ensuring optimal performance and preventing mode hopping during the scanning process.

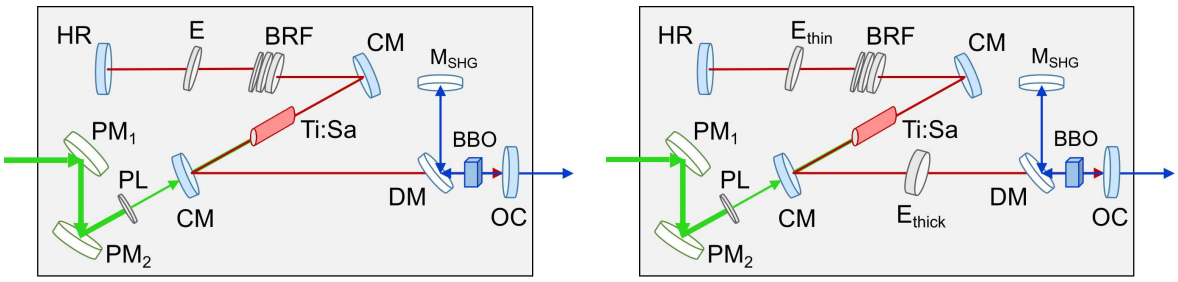

Fig. 3.9. The single-etalon Ti:sa cavity (left) and the dual-etalon Ti:sa cavity (right). Labels: PM - pump mirror, PL: pump lens, CM - curved mirror, OC - output coupler, E - etalon, BRF - birefringent filter, BBO - beta barium borate crystal, DM - dichroic mirror, M_{SHG} - SHG reflecting mirror.

Second harmonic generation (SHG) is achieved using the intracavity BBO crystals within the broadband Z-type laser cavities to enable efficient frequency doubling. To further enhance the conversion efficiency by utilizing the SHG light emitted in the backward direction, an additional dichroic mirror (DM) and a high reflectivity mirror (M_{SHG}) in the blue wavelength range are incorporated into the resonator.

Injection-locked single-mode Ti:sapphire laser

For high-resolution laser spectroscopy requiring several MHz resolution, single-mode operation of the cavity is necessary. This can be achieved by ring-resonator configurations used with the active wavelength-selective mode-locking technique.

The injection-locked laser system utilizes a master-slave feedback loop, where the ring cavity clones the highly stable and narrow-linewidth continuous wave (CW) seed laser. The seed laser can be an external cavity diode laser (ECDL), single-mode CW Ti:sapphire laser or dye laser, which provides a stable single-mode output at the desired wavelength. The seed laser is injected into a folded bow-tie Ti:sa cavity for pulsed amplification while retaining the narrow linewidth and stability. In this thesis work,

the seed light is generated by ECDL laser diodes/gain chips with maximum output powers between 50 and 200 mW. With the ECDL system, one is constrained by the narrow diode emission range of 10-50 nm and necessary retuning after approximately one nm wavelength change for stable SM operation.

Fig. 3.10 presents the layout of the injection-locked laser cavity and the ECDL seed laser. The $\lambda/2$ (half-wave) plate between the seed and slave lasers in the injection-locking system adjusts the polarization of the seed laser to match the slave laser's polarization. This maximizes injection efficiency and ensures stable frequency locking. A lens telescope system is employed to match the seed laser's beam size to the fundamental TEM_{00} mode of the cavity, maximizing injection efficiency. The cavity is pumped by the same high-power, pulsed Nd:YAG laser as the Z-type cavities, which drives the amplification of the seed laser's output. The amplifier bow-tie cavity allows multiple round trips and the multifold amplification of the low-power seed input while preserving its frequency characteristics.

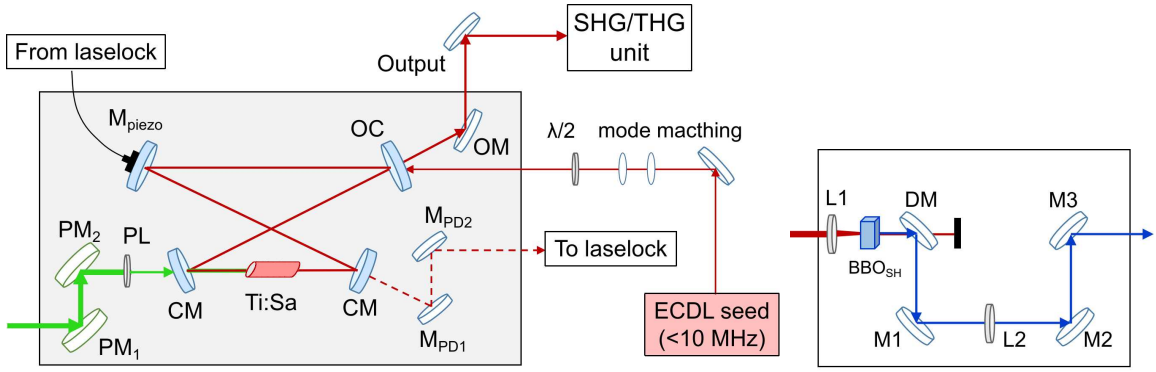

Fig. 3.10. Left: bow-tie Ti:sa amplifier cavity and ECDL seed laser layout. Labels: PL - pump laser convex lens, $PM_{1,2}$- pump laser mirrors, M_{piezo} - Piezo mirror, CM - curved mirrors, OC - output coupler mirror, OM - output mirror, $M_{PD1,2}$ - photo-diode mirrors. Right: the external frequency doubling SHG unit. Labels: DM - dichroic mirror, M - reflecting mirror, L - lens, BBO_{SH} - doubling crystal.

To ensure continuous resonance between the seed laser and the amplifier cavity, active stabilization of the cavity length is performed using a piezo-actuated mirror. The piezo element is connected to a proportional-integral-derivative (PID) feedback control system, which dynamically adjusts the cavity length to $n\lambda_{seed}$ to maintain resonance with the seed laser, where n is an integer. This stabilization compensates for both internal and external perturbations, ensuring that the cavity remains locked to the seed laser's wavelength.

For the injection-locked system using a grating-based ECDL as the seed laser, wavelength regulation during the RIS measurements is performed by regulating the seed laser wavelength. This is accomplished through a proportional control system, which adjusts

the voltage applied to the piezo actuator that controls the seed laser's grating, ensuring accurate wavelength tuning and stability.

An external frequency doubling unit was used for the injection-locked single-mode cavity, as shown in the right panel of Fig. 3.10. The external SHG unit enhances stability by reducing sensitivity to temperature fluctuations and alignment issues, which is essential for maintaining the narrow linewidth of the output laser. This external configuration also avoids the complexities and variabilities associated with intracavity elements. To achieve a high power density of the SH beam, it is typically necessary to focus the fundamental beam onto the BBO crystal using a lens.

Fig. 3.11 shows the layout of the Ti:sa laser system at S^3-LEB utilized in this offline commissioning work. One can refer to [Aja23] for a comprehensive description of the full laser system that will be deployed at S^3-LEB for future online experiments.

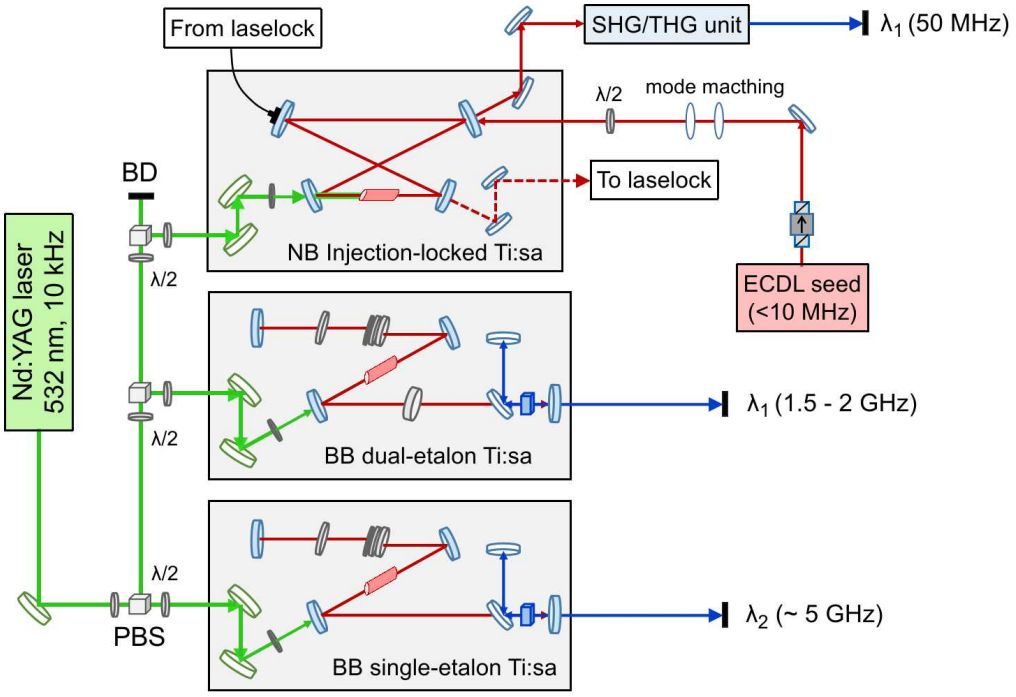

Fig. 3.11. Ti:sa laser systems for the offline commissioning at LPC. Labels: PBS - polarizing beam splitter cube, $\lambda/2$ - half wave plate, BD - beam dump.

With the S^3-LEB setup, a series of RIS measurements on stable erbium isotopes with different transitions were conducted in both the gas cell and the gas jet as part of this thesis work. Chapter 4 will present the analysis results of these measurements, focusing on the determination of isotope shift factors and hyperfine structure (HFS) coefficients, as well as the characterization of pressure broadening and shift of the studied transitions. The primary objective is to identify a highly sensitive laser ionization scheme in preparation for the forthcoming online studies of erbium at S^3.

Chapter 4

RIS experiment of stable Er

Studies of the resonant ionization spectroscopy of stable Er are essential in the preparation for the first online experiment of S^3. To investigate the exotic radioactive Er isotopes in the scope of the first physics cases, a laser ionization scheme that demonstrates both high efficiency and sensitivity to the nuclear observables, i.e. the magnetic dipole moment, electric quadrupole moment and changes in mean square charge radius, needs to be developed.

Erbium has six stable isotopes with natural abundance being 33.5% for ^{166}Er, 27.0% for ^{168}Er, 22.9% for ^{167}Er, 14.9% for ^{170}Er, 1.61% for ^{164}Er, and 0.14% for ^{162}Er [Tab]. ^{167}Er is the only stable odd-A isotope with non-zero nuclear spin ($I = 7/2$), showing a hyperfine structure. For this PhD work, the measurements were performed with the high-abundance stable isotopes, namely ^{164,166,167,168,170}Er, by evaporation from a resistively heated tantalum filament installed in the stopping volume of the gas cell. The isotopes were evaporated into ultrapure argon buffer gas under constant flow. The stagnation pressure P_0 inside the gas cell was kept at 100 mbar for all isotope shift and hyperfine-structure measurements. During the measurements aimed at characterizing pressure broadening and shift in the gas cell, the operating pressure was varied from 100 to 300 mbar.

In this chapter, section 4.1 discusses considerations for selecting excitation schemes and introduces the chosen candidate schemes for the in-gas-cell and in-gas-jet measurements. Section 4.3 describes the analysis methods to investigate the isotope shifts and hyperfine structure from the measured spectra and the estimations of statistical and systematic uncertainties of the relevant observables. Section 4.4 presents the results of the isotope shift measurements and discusses their connections to atomic factors. Section 4.5 presents the extraction of hyperfine constants.

4.1 Ionization schemes chosen for RIS on Er I

Our criteria for choosing excitation schemes for the in-gas-cell RIS measurements are:

- Preference for two-step excitation schemes, where the transition wavelengths for both steps can be conveniently generated using frequency-doubled Titanium:sapphire cavities pumped by 532 nm pump lasers.
- Large Einstein coefficients of the first excited states, facilitating efficient ionization.
- Schemes exhibiting significant isotope shifts $\delta\nu_i^{166,170}$, as determined from previous measurements, are of particular interest. Further measurements are warranted to verify whether the predominant component of the shift is attributed to the field shift, which indicates the sensitivity to changes in the mean-squared charge radius.

Transitions exhibiting large isotope shifts are promising candidates for laser-spectroscopy studies in the supersonic jet. Two additional factors were considered when choosing the case for high-resolution in-gas-jet RIS measurements:

- Unknown hyperfine parameters for the excited state. Notably, of the three selected schemes, the 400.8 nm scheme has already been thoroughly studied with high-resolution spectroscopy.
- The first-step wavelength is easily accessible via the frequency-doubled, injection-locked Ti:sapphire laser, seeded by the available external-cavity diode laser (ECDL) centered at 840 nm. Achieving a wavelength smaller than 405 nm with the available ECDL has proven challenging.

Given these considerations, three laser ionization schemes [1] of stable Er isotopes were chosen to be investigated in this work, as illustrated in Fig. 4.1. The Erbium isotopes underwent first-step resonant excitations from the [Xe]$4f^{12}6s^2(^3H_6)$, $J = 6$ ground state to three first excited states(FES):

- the [Xe]$4f^{11}(^4F)5d6s^2$, $J = 6$ state at 25392.779 cm^{-1} with the 393.7014 nm line.
- the [Xe]$4f^{12}(^3H)6s6p$, $J = 7$ state at 24943.272 cm^{-1} with the 400.7965 nm line.
- the [Xe]$4f^{11}(^4I)5d6s^2$, $J = 6$ state at 24457.139 cm^{-1} with the 408.7632 nm line.

and then ionized via the same autoionizing state at 49293.6 cm^{-1} above the ionization potential (IP), by a second-step laser tuned to 402.9 nm, 410.9 nm and 418.6 nm respectively. This autoionizing state (AI) was selected based on prior research [Stu20] to ensure optimal ion production efficiency. In addition, the previously studied scheme where the Er atoms were promoted from the ground state to FES $4f^{12}(^3H)6s6p$, $J = 5$ by 415.1 nm laser light and then ionized via the same AI state by a laser tuned to 396.7 nm is shown in Fig. 4.1 by dashed arrows. This scheme has been studied both in the atomic beam unit (ABU) measurements [R$^+$22] and in the supersonic gas jet at S^3-LEB

1. All wavelengths in this work are systematically referred to air wavelengths.

[A+23].

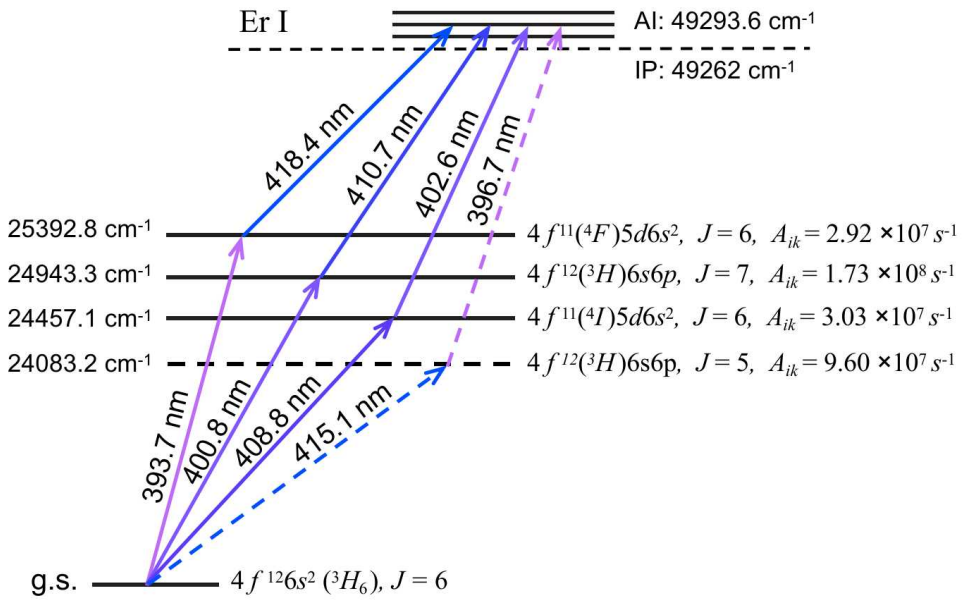

Fig. 4.1. Ionization schemes for Er I that have been investigated at S^3-LEB so far. The solid arrows indicate the transitions studied in this work and the dashed ones show the previously studied case. The energies of the excited states are given in cm^{-1}. The electron configuration is shown on the right-hand side. Information is taken from [KYRN23]. Notice that the splittings of the excited and AI states are not to scale and the wavelengths for the excitation and ionization steps are given in vacuum.

In this work, the three FES transitions 393.7 nm, 400.8 nm and 408.8 nm have been investigated in the gas cell. A frequency-doubled, dual-etalon Ti:sapphire laser cavity, with an average fundamental linewidth of 1.8 GHz FWHM, was utilized for the first excitation step for the in-gas-cell ionization. For the second ionization step, a frequency-doubled, single-etalon Ti:sapphire laser with an average fundamental linewidth $\leq$ 5 GHz FWHM was employed. Consequently, systematic studies of the isotope shifts for these three schemes were carried out in the gas cell with GHz resolution.

Of the three candidates, the 408.8 nm scheme was chosen for the in-gas-jet hyperfine structure studies, mainly due to its largest isotope shift $\delta\nu_{408.8}^{166,170}$ [AD15], unknown hyperfine splitting parameters for the FES and the feasibility of obtaining the required wavelength with the available single-mode Ti:sa laser system. The injection-locked Ti:sapphire laser, seeded by an external-cavity diode laser, was frequency-doubled and applied to the first excitation step for the in-gas-jet measurements, featuring an average fundamental linewidth of approximately 35 MHz. The frequency-doubled, single-etalon Ti:sapphire laser used in the gas-cell configuration was employed for the ionization step. Consequently, within the gas-jet measurements, in addition to facilitating high-resolution studies of hyperfine structure, isotope shifts for the 408.8 nm scheme were investigated

with significantly enhanced resolution in the tens of MHz range. These outcomes are further discussed and compared with the gas-cell measurements with GHz resolution in Section 4.4.

4.2 Optimization of the experimental conditions

A wealth of information can be extracted and analyzed from the spectra obtained from the RIS measurements performed in the gas environment. By scanning the laser wavelength of the first excitation step with sufficient resolution, while the second step laser is kept fixed, some of the key pieces of information were extracted from the scanning spectra:

- Line positions: the centroids of ^{164,166,167,168,170}Er were extracted from the RIS using the 393.7 nm, 400.8 nm, and 408.8 nm schemes in the gas cell, as well as with the 408.8 nm scheme in the gas jet.
- Isotope shifts: differences in spectral line positions between different isotopes are sensitive to changes in the mean-squared charge radius.
- Hyperfine structure: the hyperfine splitting observed with the odd isotope ^{167}Er in the RIS measurements conducted in the supersonic jet using the high-resolution single-mode injection-locked laser cavity. The HFS spectra of ^{167}Er can provide information on the hyperfine coupling constants of the excited state of Er, which can later be used to extract nuclear electromagnetic moments of radioactive Er isotopes.
- Doppler shift or linewidth which can be used to determine the gas-jet velocity and temperature and, consequently, its Mach number.
- Pressure broadening and shifts: the broadening and displacement of spectral lines can be observed as gas pressures increase during the in-gas-cell RIS measurements. From the systematic observation of their pressure dependence, the collisional coefficients of the transition can be determined (see Eq. (2.25)).
- Power saturation effects: at lower laser intensities, the signal intensity exhibits a linear dependence on the intensity of the laser radiation. However, with increasing laser power, a departure from linearity occurs, leading to a nonlinear response between the signal intensity and the laser radiation intensity, as detailed in Section 2.1.3. A comprehensive understanding and characterization of the power saturation behavior is important for optimizing experimental conditions in RIS experiments. The optimal laser intensity needs to be determined so that measurements are carried out at sufficient signal intensities and to minimize power saturation effects. Additionally, comparisons of the power saturation effects with different excitation schemes under identical measurement conditions, as well as for the same scheme in different gas environments, namely gas cell and gas jet, provide additional insights into how the gas environment influences the

saturation mechanism, such as the interplay between laser power and linewidth, collisional quenching of excited states and Doppler broadening. The analysis method to probe these features is presented in Section 4.3.

To ensure accurate and reliable results for the in-gas RIS measurements, it is necessary to implement optimal experimental conditions and employ appropriate analysis techniques. This entails attention to various experimental parameters, including laser intensity, beam alignment, pulse duration, and timing synchronization. Moreover, precise regulation of the gas pressure, temperature, and purity is crucial to minimize background interference and enhance the signal-to-noise ratio, as detailed in Section 2.1.2. Additionally, robust and appropriate data analysis methodologies, such as spectral fitting algorithms, statistical and systematic error analysis, should be employed to extract meaningful information from the obtained spectra. This aspect will be discussed in the subsequent content of this section.

Throughout the experiment, in all investigated RIS schemes, the first-step laser was oriented transversely, while the second-step laser was directed anti-collinearly to the atomic beam without expansion, as shown in Fig. 4.2. The first-step laser was directed

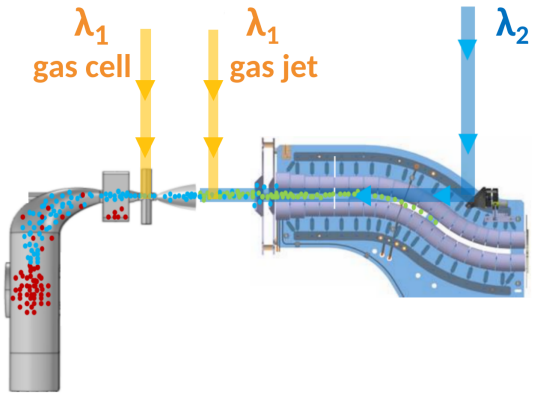

Fig. 4.2. The in-gas-cell and in-gas-jet laser alignments. The first step laser λ_1, represented by yellow lines and arrows, is oriented transversely into the gas cell near the nozzle for the gas-cell measurements and the supersonic jet for the gas-jet measurements. The second step laser λ_2, in blue, is always directed anti-collinearly. Notably, the first step laser beam spots are not expanded in the gas jet.

into the gas cell through a window positioned before the nozzle for in-gas-cell ionization or into the gas jet between the nozzle and the RFQ for in-gas-jet ionization, with precise adjustments facilitated by a mirror moved on a motorized stage. Spatial and temporal overlaps were optimized at the outset of the measurements to ensure that the two steps of laser beams interact effectively with the atomic ensemble. To perform the measurements, the frequency of the excitation step lasers was scanned with sufficient resolution, while the ionization step lasers remained fixed, and the ion counts after PILGRIM were recorded using a Time to Digital Converter (TDC) developed by KU

Leuven.

PILIGRIM was operated at two revolutions to improve the resolution of the time-of-flight (TOF) spectra. An illustrative TOF spectrum obtained with PILIGRIM for the 408.8 nm scheme in gas cell configuration is depicted in Fig. 4.3, where the blue line represents ion counts of Er isotopes versus their time of flight from the buncher (in bunching configuration) to the end of PILGRIM. The ^{170}Er peak was fitted using a Gaussian profile, indicated by the red solid curve. The resolving power obtained is R = TOF/(2 × FWHM) ≈ 330, with mean $\mathrm{TOF}_{^{170}Er}$ ≈ 150 μs for two revolutions and $\mathrm{FWHM}_{^{170}Er}$ = 224 (3) ns, which was sufficient to completely separate the different isotopes. The TOF difference between two successive masses is ∼ 450 ns for mass difference $\delta m = 1$ and ∼ 900 ns for $\delta m = 2$.

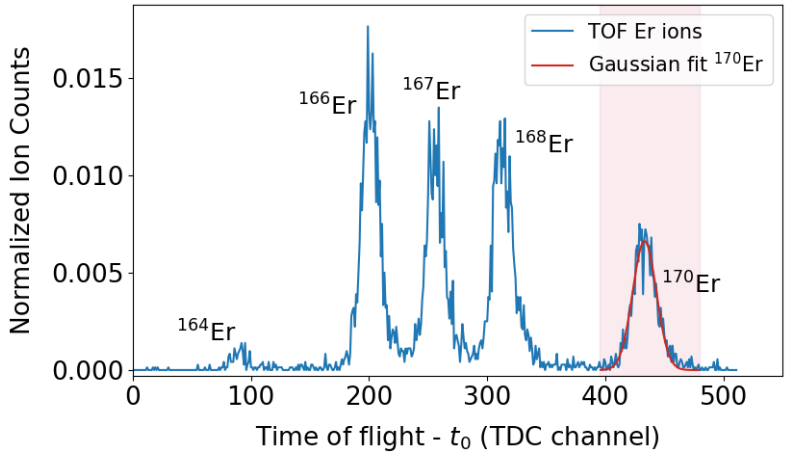

Fig. 4.3. Example time-of-flight spectrum of laser-produced Er ions in a two-revolution mode of the PILGRIM.

It is important for high-resolution RIS measurements to have the laser output power below saturation power to minimize power-broadening effects. Therefore following the laser alignment and PILGRIM tuning, saturation curve tests were performed for the 400.8 nm and 408.8 nm schemes in the gas cell and the gas jet. During these tests, laser power P was adjusted by rotating a continuously variable reflective filter wheel inserted into the wave path, while the ion count rate I of ^{166}Er was simultaneously monitored. Rotating the wheel allows for precise adjustment of the laser power of the beam transmitted to the ion source between a hundred mW (full power output from the cavity) to almost 0 mW, which is at the measurable limit of the power meter. This allowed the identification of the linear regime below the saturation power P_0.

The investigation commenced with the 400.8 nm scheme due to its well-established isotope shift and hyperfine structure parameters in existing literature [F$^+$13]. RIS measurements employed a dual-etalon Ti:sa cavity for the first step laser, and a single-etalon cavity for the second step. In an effort to examine and optimize the

multimode structure of the dual-etalon Ti:sa cavity, the 400.8 nm scheme and the characteristics of the laser system were initially investigated in the gas jet configuration, where pressure broadening effects are minimal.

However, due to the minimal Doppler broadening in the low-temperature supersonic jet, with linewidths of approximately 200 MHz, which are narrower than the 1.8 GHz natural linewidth of the double-frequency dual-etalon Ti:sa cavity laser, the multimode structure was observable in the spectrum. The left panel of Fig. 4.4 represents an example scan performed in the gas jet, the right panel depicts measurements for the same RIS scheme with the same laser system and laser powers but performed in the gas cell for comparison. The FWHM of the resonance peaks in the gas cell measurements at 100 mbar is approximately 4.8 GHz, nearly twice that observed in the gas jet scans, which is approximately 2.6 GHz. Therefore, the pressure broadening effect helps to smooth out the multimode structure, resulting in more easily fittable RIS spectra, therefore subsequent IS measurements utilizing the dual-etalon Ti:sa cavity for the excitation-step scanning were conducted in the gas cell. It is also noteworthy that the available Fabry-Pérot interferometer (FPI) used to optimize the multimode structure has a free spectral range of 1 GHz, narrower than the laser linewidth FWHM of around 1.8 GHz, which limited tuning possibilities.

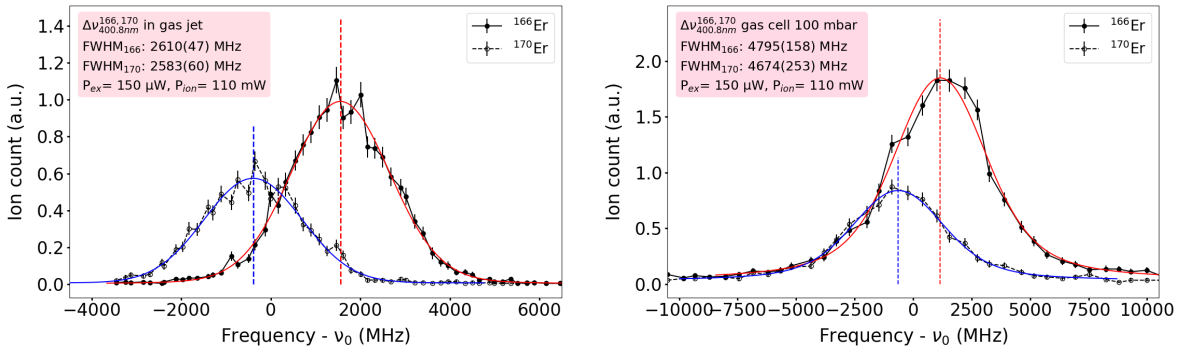

Fig. 4.4. Isotope shift measurements of ^{166}Er and ^{170}Er isotopes for the 400.8 nm scheme with dual-etalon BRF Ti:sa cavity used for the first step scanning in the gas jet (left) and gas cell at 100 mbar (right). The reference frequency is $\nu_0 = 747780$ GHz for both measurements. Fits using Voigt functions for the resonance peaks ^{166}Er and ^{170}Er are represented by red/blue curves. Experimental gas environments, FWHMs of ^{166}Er and ^{170}Er, and excitation and ionization step powers are presented in the text box.

As discussed in Chapter 2, when a two-level system with levels $|1\rangle$ (lower) and $|2\rangle$ (upper) is exposed to a radiation field $E = E_0 \cos \omega t$, and the upper level $|2\rangle$ can decay by spontaneous processes with the spontaneous decay rate γ, the steady-state population ρ_{22} of the excited state $|2\rangle$ can be derived using the Optical Bloch Equations [CCTG98] (OBE), see Eq. (2.17). On resonance, $\omega = \omega_0$ and Eq. (2.17) becomes:

$$\rho_{22} = \frac{1}{2} \cdot \frac{S_0}{S_0 + 1} \tag{4.1}$$

where $S_0 = P/P_0$ is the resonant saturation parameter with P_0 being the saturation power.

Saturation curve tests were conducted in both gas cell and gas jet for the 400.8 nm scheme prior to the RIS measurements, by assessing the count rate on the resonance of the highest statistics peak ^{166}Er while adjusting the intensity of one laser step and keeping the intensity of the other constant. Fig. 4.5 illustrates the saturation curves for both steps measured in the two configurations. Blue points represent the count rates recorded on the TDC at varying laser powers while red curves represent the saturation curves obtained through least-squares fitting. The laser frequencies were set in resonance with ^{166}Er. The data set has been fitted using the following equation:

$$I(P) = A \cdot \frac{\frac{P}{P0}}{\frac{P}{P0} + 1} + B \cdot P + C \tag{4.2}$$

where:

- $I(P)$ represents the ion signal intensity at laser power P.
- the term $A \cdot \frac{P/P0}{P/P0+1}$ is obtained according to Eq. (4.1).
- the additional linear term $B \cdot P$ takes into account two-step ionization involving two photons of the same wavelength (either two excitation step lasers or two ionization step lasers, whichever is power scanned).
- C is an offset describing the background signal, which may arise from sources such as dark current on the MCP or surface ions. If background correction is applied to the data, this term can be set to 0.
- P_0 is the saturation power, indicating the end of the linear regime in the saturation curve.

For all the saturation power plots given below, the power values are measured on the optical table (not in the cell/jet). There are some beam transport losses up to the atom-laser interaction region. The first excitation steps are always easily saturated at low-intensity levels, while the second step, which is the AI transition, is typically far from saturation even at high intensities. Therefore, the saturation curve tests for the second steps are often performed within the linear regime, thus the saturation curve can be described using Eq. (4.2) with $A = 0$ (P_0 tends to infinity rather).

The fitting results for P_0[400.8 nm] and the parameters A, B and C are listed in Table 4.1. It can be observed that the saturation power P_0 for the first step in the gas jet is twice that observed in the gas cell. The underlying reasons for this difference are as follows:

- Different gas velocities in the gas cell and supersonic jet lead to each atom

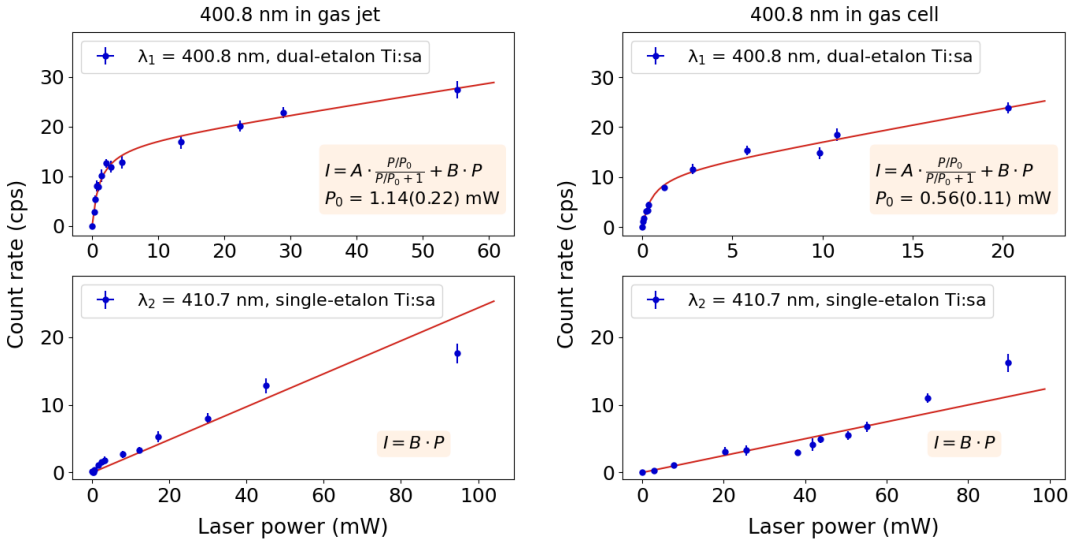

Fig. 4.5. Saturation curves for the first and second laser steps for the 400.8 nm scheme measured in the gas jet (left) and gas cell (right). Left: in the gas jet, the first step laser reaches saturation at $P_{0,\,\mathrm{jet}}[400.8\ \mathrm{nm}]$=1.14(0.22) mW. The second step was fitted using only the linear term in Eq. (4.2), as indicated by the textbox on the bottom panel. Right: in the gas cell, the first step laser saturated at $P_{0,\,\mathrm{cell}}[400.8\ \mathrm{nm}]$=0.56(0.11) mW and the second step is still far from saturation.

interacting with a different number of laser pulses on average. For both cases, the ionization area has a length L approximately equal to the non-expanded diameter of the transverse first-step laser $D_{\lambda_1} \approx 4$ mm generated by the Dual-etalon Ti:sa cavity for the 400.8 nm transition. The time of flight of an atom through the ionization area is approximately $T = L/v$, where v is the velocity of the atoms which is equivalent to the gas velocity. In the gas cell, $v_{\mathrm{cell}} \approx 10$ m/s near the exit, whereas in the supersonic jet, $v_{\mathrm{jet}} \approx 550$ m/s [K^+16]. Both lasers were operated at the same repetition rate of $\nu = 10$ kHz, the pulse period is $\tau = 1/\nu$. Therefore each atom experiences the number of pulses given by $n = T/\tau = L/(v\tau)$ $(n \geq 1)$. The atoms in the jet receive no more than a single laser pulse, while those in the gas cell are exposed to approximately $n_{\mathrm{cell}} \approx 4$ pulses per atom.

- More power is required in the gas cell to counteract quenching effects, namely the de-excitation of the FES resulting from collisions with argon atoms. Achieving temporal overlap between the two laser steps is crucial in the gas cell to compete with quenching, whereas such temporal alignment is unnecessary in the gas jet configuration.

Considering the quenching compensation factor, a larger saturation power is expected for the in-gas-cell configuration. However, the difference in the gas velocity plays a more significant role. The combined influence of these two effects ultimately results in the observed different saturation power values.

Additionally, we notice the possible presence of an auto-ionizing state excited by a second photon of 400.8 nm, as indicated by the observation of a strong background during the saturation curve test for the second-step laser with the first step at full power. The Er isotopes can be fully ionized by the 400.8 nm first-step laser, which was confirmed by checking the count rate with the second-step laser blocked. Consequently, saturation power measurements for the second step must be conducted with the first step set at a minimal power level. This background also disfavors the use of the 400.8 nm scheme for laser ionization spectroscopy.

In the same way, preceding the RIS measurements with the 408.8 nm scheme, saturation curves were measured in both the gas cell and gas jet configurations. These saturation curves are presented together in Fig. 4.6 for comparison. The fitting results for P_0[408.8 nm], A, B and C for all the measured steps are listed in Table 4.1. As for the 400.8 nm scheme, in the gas cell, the first-step laser was generated by the dual-etalon Ti:sa cavity, while in the gas jet, the injection-locked Ti:sa cavity was used. In both configurations, the second-step lasers for ionization were provided by the single etalon BRF Ti:sa cavity. In the gas cell, the second-step laser was far from saturation. Considering the gas jet, the saturation test for the second step laser could not be concluded due to unexpected instabilities of the pump laser.

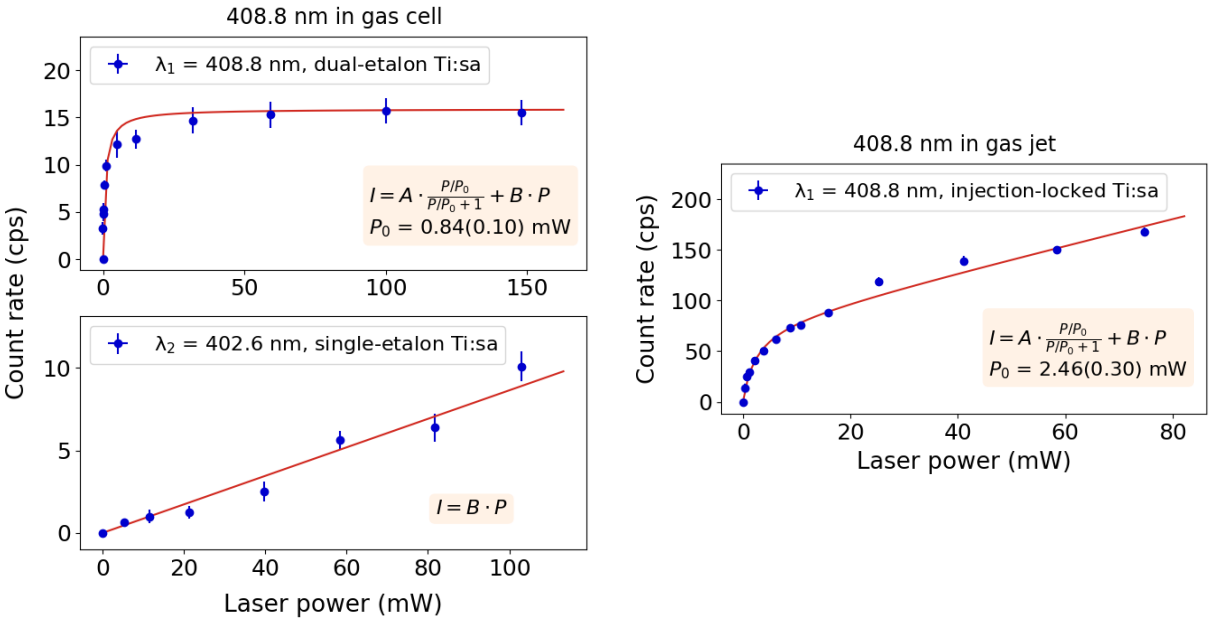

Fig. 4.6. Saturation curves for the first and second laser steps for the 408.8 nm scheme. Blue points represent the count rates while the red curves represent the least square fits for the saturation curves.

The fitting results revealed that the saturation power P_0[408.8 nm] for the first step in the gas jet is 2.46(0.30) mW, which is three times larger than in the gas cell, 0.84(0.10) mW. This can also be explained by the following factors:

- Different gas velocities, as explained before.
- More power is required in the gas cell to counteract quenching effects.
- Laser linewidth for the in-gas-jet RIS measurements is several orders of magnitude narrower compared to in-gas-cell measurements. The frequency-doubled NB Ti:sa system exhibits linewidth of $\Delta f \sim 50$ MHz, while the frequency-doubled dual-etalon Ti:sa cavity has $\Delta f \sim 2.5$ GHz.

The quenching compensation results in an increase of the saturation power $P_{0,\,\mathrm{cell}}$, while the significantly narrower laser linewidth in the gas jet configuration leads to a reduction in the saturation power $P_{0,\,\mathrm{jet}}$ for the same transition. However, the difference in gas velocity plays a more significant role, resulting in an ultimate higher saturation power for the gas jet configuration. Nevertheless, this increase is not as substantial as would be anticipated based solely on the velocity ratio.

Table 4.1 – Saturation power $P_0[\lambda_1]$ of first excitation steps of the 400.8 nm and 408.8 nm RIS scheme, obtained from the saturation curve tests conducted in the gas cell and the gas jet. The uncertainties are given in parentheses, which are only the estimates from the fitting procedure.

	400.8 nm				408.8 nm			
	P_0 (mW)	A	B	C	P_0 (mW)	A	B	C
Gas cell	0.56(0.11)	11.11(1.11)	0.64(0.09)	-	0.84(0.10)	15.90(0.91)	-	-
Gas jet	1.14(0.22)	16.61(1.42)	0.21(0.04)	-	2.46(0.30)	78.88(4.04)	1.30(0.07)	-

'-' means the values were fixed to zero during the fit.

The saturation power of the 400.8 nm transition exhibits a smaller value compared to the 408.8 nm for both gas-cell and gas-jet measurements. This difference arises from the intrinsic properties of the transitions. As indicated by Eq. (2.14), the saturation power is expressed as:

$$I_{\mathrm{sat}} = \frac{\hbar\omega A_{21}}{2\sigma}, \tag{4.3}$$

which depends on the angular frequency of the transition ω, the Einstein coefficient for spontaneous emission A_{21}, and the absorption cross-section of the transition σ, which is directly related to the dipole moment and oscillator strength [Dem14].

The reduced laser saturation power in gas-cell measurements compared to gas-jet conditions arises primarily due to differences in the gas environment. The effects of pressure and temperature, which contribute to line broadening through Doppler and pressure broadening mechanisms, alter the absorption cross-section, thereby impacting the efficiency and intensity of saturation for each transition.

Another notable observation is the distinct trends in the first-step laser saturation curves

for laser powers exceeding P_0 in the gas-cell and gas-jet configurations. Specifically, while the saturation curve obtained in the gas cell configuration exhibits a flat profile after reaching the saturation power, a moderate increase in ion count rate is observed with the increase of laser power beyond the saturation point in the gas jet configuration. This distinction can be attributed to the substantially narrower laser linewidth in the gas-jet measurements. Fig. 4.7 shows a comparison of the linewidths of ^{166}Er from two representative scans conducted utilizing the 408.8 nm excitation scheme, one performed in the gas cell at 100 mbar and one in the supersonic jet. The component analysis and value estimation of the spectral linewidth is presented in Section 4.3.

In the in-gas-jet scan, $\delta_{\text{doppler}} \approx 150$ MHz, whereas in the in-gas-cell scan, $\delta_{\text{doppler+collision}} \approx 2$ GHz. The Doppler broadening in the jet is almost five times larger than the narrowband laser linewidth, while in the gas cell the total broadening is comparable to the linewidth of the dual-etalon laser. As the laser power increases, the ratio of $\delta_{\text{laser+power}}$ to δ_{doppler} increases in the gas-jet case, facilitating the resonance with a larger number of atoms from the Doppler distribution. Consequently, the saturation curve beyond P_0 exhibits a progressive increase rather than remaining flat. This phenomenon is absent in the gas-cell case using the broadband laser, where the laser linewidth covers the broadened distribution even at low power.

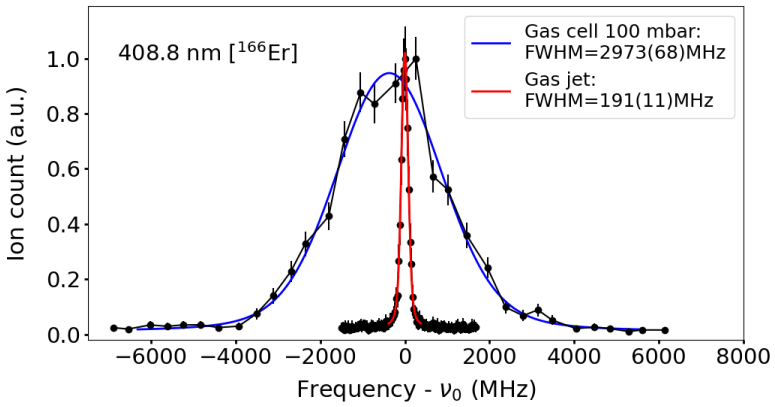

Fig. 4.7. Comparison of the linewidths of the highest statistics peak ^{166}Er from the scans performed in gas cell with the dual-etalon Ti:sa laser and supersonic jet with the injection-locked Ti:sa laser. The gas jet data exhibits a resolution of about 200 MHz, while the gas cell data obtained at 100 mbar shows a total linewidth of about 3 GHz.

From the saturation curves shown in Figs. 4.5 and 4.6, it is apparent that the excitation step saturates with laser powers ranging from several hundred μW to several mW. However, saturation of the second step transition is not reached in any of the conducted tests. This outcome is expected due to orders of magnitude higher cross-sections σ associated with excitation transitions compared to the ionization step. Consequently, in all RIS measurements with the three selected schemes, the power of the first-step

laser was attenuated to approximately 100 μW, reaching the sensitivity limit of the available powermeter, while full-power laser beams were utilized for the second step. No additional saturation power test was conducted for the 393.7 nm scheme because its Einstein coefficient is similar to the 408.8 nm transition, suggesting comparable saturation power.

4.3 Analysis methods and uncertainties

In this work, scans for all selected schemes were conducted on the FES transition in the gas cell for systematical isotope shift analysis. Additionally, scans were performed in the supersonic jet with the 408.8 nm scheme for the hyperfine structure investigation. Prior to RIS measurements for each scheme investigated in a different gas environment, manual wavelength scans of both laser steps were conducted to define the scan range and identify the resonances of both transitions.

Using the TDC, data from all measurement devices was combined in a time-synchronized manner. The optical spectra of each isotope were derived by plotting the acquired data against the excitation laser frequency within their defined TOF gates. As illustrated in Fig. 4.8, while the specified gates for peaks ^{164}Er($\sim$ 60 TDC channels) and ^{170}Er($\sim$ 80 TDC channels) encompassed the entirety of their respective signals, the TOF peaks for ^{166,167,168}Er which were not fully separated required narrower TOF gate selection($\sim$ 50 TDC channels for ^{166,168}Er and $\sim$ 30 TDC channels for ^{167}Er) to avoid potential mass contamination while keeping sufficient statistics. Subsequent sections will delve into the analysis and uncertainty estimation of these gated spectra for individual isotopes.

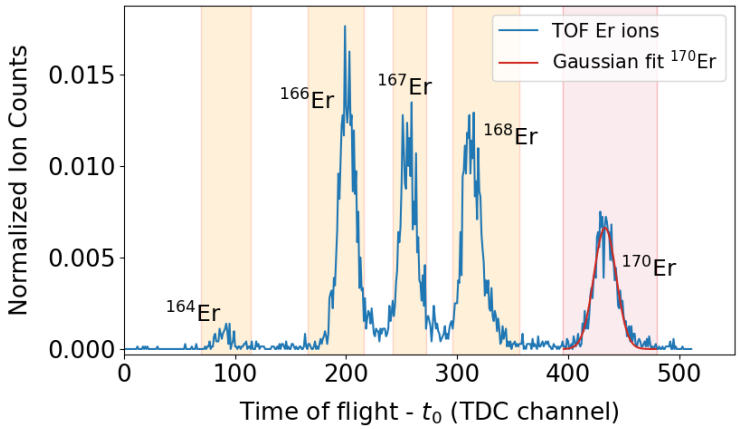

Fig. 4.8. An illustrative TOF spectrum with gates marked for each isotope. One TDC channel has a width of 8 ns.

4.3.1 Data fitting method

The RIS spectra were fitted with a Voigt profile, using the chi-square fit method in the Statistical analysis toolbox for laser spectroscopy (SATLAS) python package [GW+18]. The FWHM of the Voigt profile, which is a convolution of Gaussian and Lorentzian functions, is given by Eq. (2.35). The Gaussian linewidth arises from a convolution of three factors as discussed in Section 2.1.3 and Section 2.2.5:

$$\Delta_G = \sqrt{\Delta\nu^2_{\text{Doppler}} + \Delta\nu^2_{\text{pulse}} + \Delta\nu^2_{\text{SHG}}} \tag{4.4}$$

where $\Delta\nu_{\text{Doppler}}$ is the Doppler broadening linewidth, $\Delta\nu_{\text{pulse}}$ is the Fourier pulse linewidth, and $\Delta\nu_{\text{SHG}}$ is the Frequency doubling linewidth. The Lorentzian linewidth is also composed of three terms:

$$\Gamma = \Gamma_{\text{nat}} + \Gamma_{\text{power}} + \Gamma_{\text{coll}} \tag{4.5}$$

where Γ_{nat} is the natural linewidth of the atomic transition arising from the excited state's finite lifetime, Γ_{coll} is the collisional broadening FWHM induced by the collisions between the Er atoms with the buffer gas, and Γ_{power} denotes the laser power broadening. The influence of the latter two components can be minimized, even eliminated, through optimized experimental conditions. For instance, conducting measurements in a low-pressure supersonic gas jet and employing minimal laser power below the saturation threshold.

The {408.8|402.6} scheme

From the first-step transition spectra of even-even isotopes obtained in-gas-cell and in-gas-jet, the parameters can be extracted utilizing the chi-square fit model *HFSModel* in the SATLAS package. By fixing the hyperfine parameters of the ground state (g.s.) and first excited state (FES) as well as the nuclear spin to zero, the model facilitates the extraction of the peak centroids, width, peak heights and a constant background. The evaluation of fit quality and estimation of parameter value certainty were conducted through the calculation of the reduced chi-square (χ^2/n_{Dof}). For each even-even resonance peak, fitting was conducted within a specified range centered on the peak centroid, spanning ± 2 times the FWHM (± $2\Delta_V$). To apply these constraints to the measured data, for each scan, the FWHM values were initially extracted from a preliminary χ^2 fit covering the entire scanning range. Subsequently, a second fit was performed with the ± $2\Delta_V$ range. This approach ensures coverage of the peak profile while minimizing the influence of the background.

The hyperfine parameters can only be approached with the high-resolution in-gas-jet first-step scan of the ^{167}Er isotope. The fit function *HFSModel* provided by SATLAS

was employed again for the HFS analysis, but with nuclear spin $I = 7/2$ and fixed hyperfine A and B values for the Er I ground state from the literature. The fitting range of ^{167}Er was not constrained but spanned the whole scanning range.

The χ^2 fit of a single scan of the 408.8 nm first-step transition performed in the gas cell and the gas jet respectively are represented together in Fig. 4.9 for comparison. The five

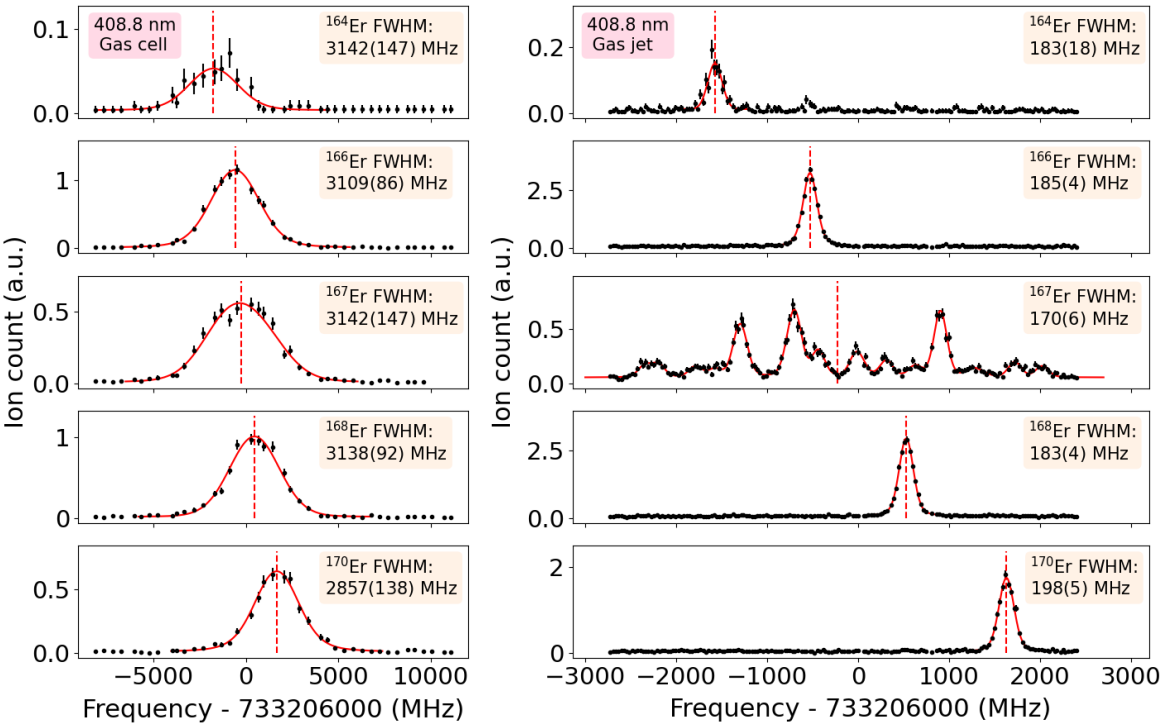

Fig. 4.9. Comparison of the 408.8 nm spectrum from an illustrative single scan performed in the gas cell (left) and gas jet (right). The five panels in both cases present successively the ToF gated spectrum for ^{164,166,167,168,170}Er with corresponding centroids indicated by the red dashed lines. The red solid curve represents the χ^2 fit for the measured data. The in-gas-cell measurement was performed with the power of the first and second steps $P[\lambda_1 = 408.8\text{ nm}] = 500\ \mu$W and $P[\lambda_2 = 402.6\text{ nm}] = 120$ mW, while the in-gas-jet measurement was performed with $P[408.8\text{ nm}] = 530\ \mu$W and $P[402.6\text{ nm}] = 140$ mW. The in-gas-cell spectrum has ≈ 3 GHz FWHM, while the in-gas-jet spectrum has ≈ 200 MHz FWHM. The hyperfine structure of ^{167}Er can only be resolved in the high-resolution in-gas-jet spectrum.

panels on both the left and right represent the ToF gated spectrum for ^{164,166,167,168,170}Er, arranged from top to bottom. The FWHM extracted from the fit for each isotope are presented on the upper right of each corresponding panel. For ^{167}Er, the in-gas-cell spectrum displays a broad single peak, indicating insufficient resolution in resolving individual hyperfine components. In contrast, the high-resolution in-gas-jet spectrum

exhibits distinct splitting of the hyperfine structure. Therefore the HFS analysis is feasible and the hyperfine A and B values of the first excited state of the 408.8 nm scheme can be extracted.

For the 402.6 nm ionization-step transition from the first excited state (FES) to the autoionizing (AI) state, the total electronic angular momentum J and hyperfine parameters A and B of the AI state are unknown. This lack of information makes it impossible to constrain the SATLAS fit for the odd-mass isotope ^{167}Er. Therefore, only the even-even isotopes were fitted using the SATLAS package within a $\pm 2\Delta_V$ range. An example of the second-step spectrum with fitting is presented in Fig. 4.10. The isotope shifts for this 402.6 nm transition were also extracted, and the results are shown in Table 4.3. The larger uncertainties of the IS compared to the first-step transitions are attributed to the limited number of scan files and broad linewidths of the spectrum. The FWHM is approximately 13 GHz due to the wide natural linewidth of the single-etalon Ti:sa laser.

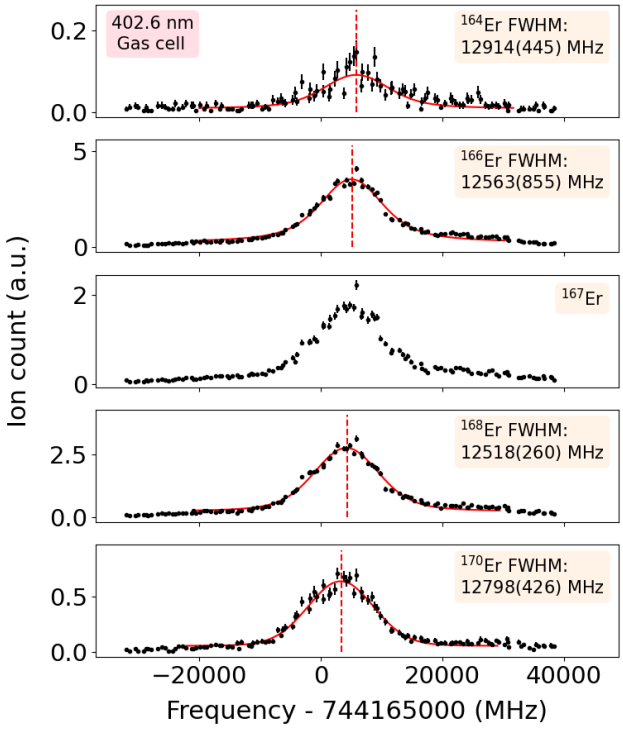

Fig. 4.10. An illustrative in-gas-cell spectrum of the second-step of the {408.8|402.6} scheme. The measurement was performed with the first step utilizing the dual-etalon Ti:sa cavity at a laser power of P[408.8 nm] = 400 μW. The second step employed the single-etalon Ti:sa cavity with P[402.6 nm] = 140 mW.

In the in-gas-cell spectrum, fitting and extracting the resonance for ^{164}Er and ^{167}Er posed challenges due to low statistics and unresolved lineshape, respectively. To address this, reducing the number of degrees of freedom of the fitting parameters became necessary. There are several choices made during the analysis:

- In SATLAS, the χ^2 fitting yields separate values for the FWHM of the Gaussian (Δ_G) and Lorentzian (Δ_L) components, along with the combined total FWHM (Δ_V). For the high-statistics, even-even isotopes ^{166,168,170}Er the two widths were left as free parameters. For ^{164}Er and ^{167}Er, the FWHM of the Gaussian and Lorenztian components were fixed to values estimated from the weighted average of the values of high-statistics peaks ^{166,168,170}Er within the same scan. Values deemed outliers, such as excessively large or small fitting results, were excluded from the estimation process. This approach ensures more reliable estimates of the linewidth components for the problematic peaks.
- In analyzing the gas-cell ^{167}Er spectrum, the hyperfine A and B values for the g.s. and FES are fixed during the fitting process. For the 400.8 nm and 393.7 nm schemes, the values are sourced [F$^+$13, JNKM09]. For the 408.8 nm, the parameters for the g.s. are obtained from literature, while those for the FES are derived from the in-gas-jet measurements conducted in this study.

To check the reliability of the analysis, comparisons were made whenever possible between the obtained first-step experimental gas-cell, gas-jet results and literature values, as compiled in Table 4.2. The second-step IS results from this work are presented in Table 4.3.

The {400.8|410.7} scheme

For the {400.8|410.7} scheme, both steps were scanned in the gas cell and the gas jet. Illustrative spectra for the first- and second-step transitions are presented in Fig. 4.11 and Fig. 4.12, respectively. All the measurements were performed with the first laser step provided by the dual-etalon Ti:sa cavity and the second laser step provided by the single-etalon Ti:sa cavity.

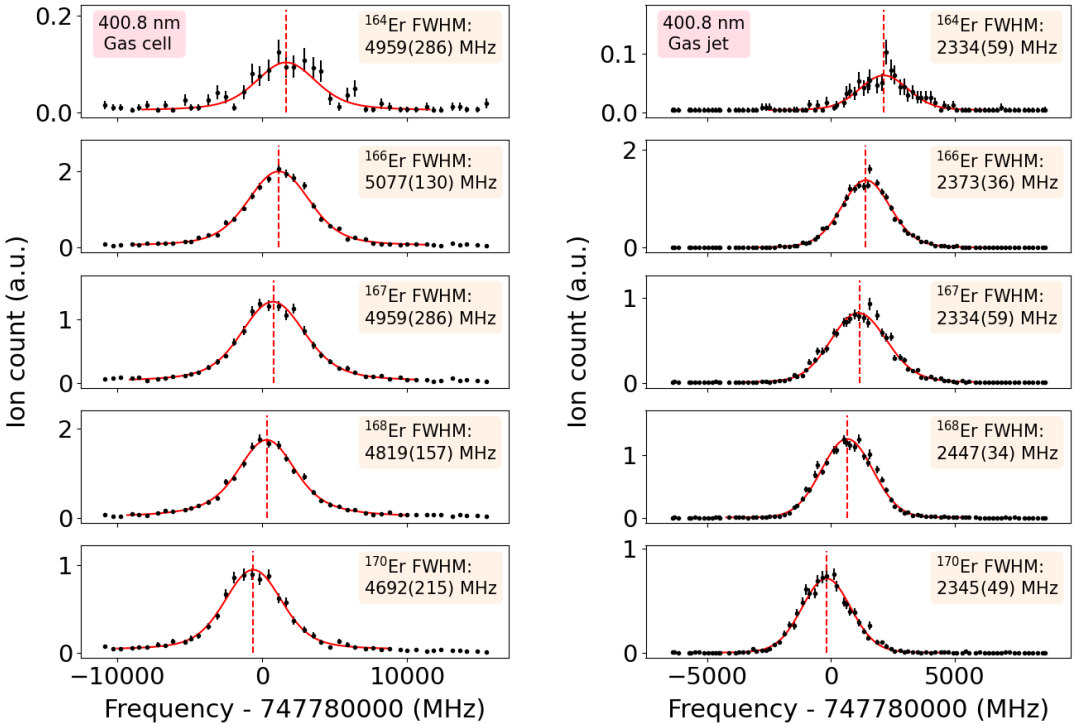

Fig. 4.11. Comparison of the 400.8 nm spectrum from an illustrative single scan performed in the gas cell at 100 mbar (left) and gas jet (right). Both the in-gas-cell and in-gas-jet measurements were performed with the power of the first and second steps $P[400.8\text{ nm}] = 550\ \mu\text{W}$ and $P[410.7\text{ nm}] = 110$ mW.

As shown in the first step spectra in Fig. 4.11, the in-gas-cell spectrum has ~ 5 GHz FWHM due to the pressure broadening and multimode nature of the dual-etalon Ti:sa laser, while the in-gas-jet spectrum has ~ 2.3 GHz FWHM. In both cases, the hyperfine structure of ^{167}Er cannot be resolved.

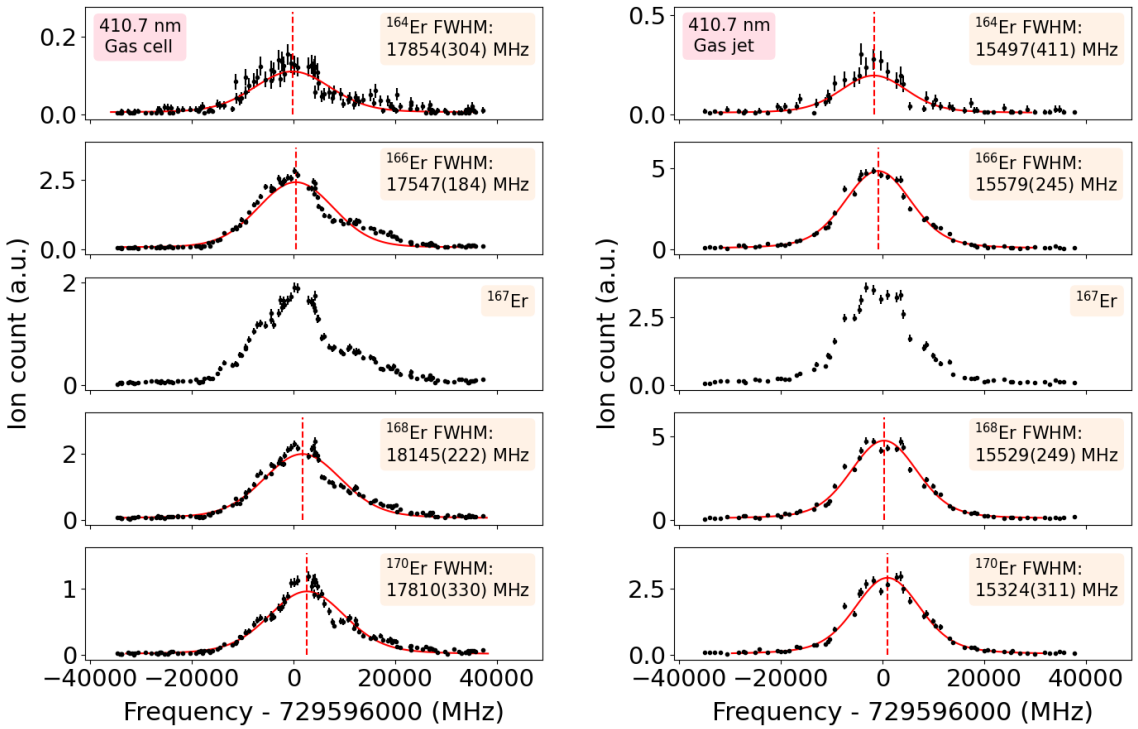

Fig. 4.12. The 410.7 nm spectrum from illustrative scans performed in the gas cell at 100 mbar (left) and gas jet (right). The in-gas-cell measurement was performed with the power of the first and second steps $P[400.8\text{ nm}] = 500\ \mu\text{W}$ and $P[410.7\text{ nm}] = 30$ mW. The in-gas-jet measurements were performed with $P[400.8\text{ nm}] = 95$ mW and $P[410.7\text{ nm}] = 110$ mW.

The second-step in-gas-cell spectrum shows $\sim$ 18 GHz FWHM due to the pressure broadening, more than 7 GHz frequency-doubled linewidth of the single-etalon Ti:sa laser and the natural width of the AI state, which is expected to be much larger than the one of the FES. The in-gas-jet spectrum has $\sim$ 15.5 GHz FWHM. The ^{167}Er spectrum cannot be analyzed due to the unknown spin and hyperfine parameters of the AI state.

The {393.7|418.4} scheme

Both steps of the {393.7|418.4} scheme were scanned in the gas cell. Illustrative spectra for the first- and second-step transitions are presented in Fig. 4.13. All the measurements were performed with the first laser step provided by the dual-etalon Ti:sa cavity and the second laser step provided by the single-etalon Ti:sa cavity.

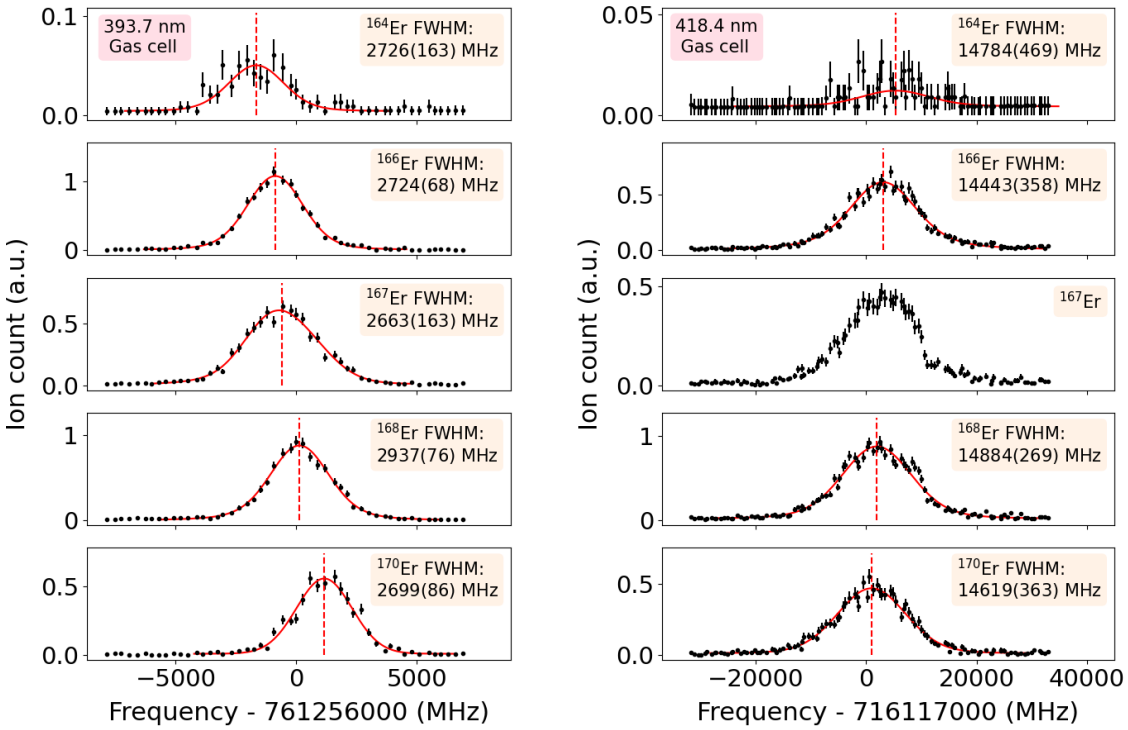

Fig. 4.13. Illustrative spectra of the first(left) and second(right) step transitions of the {393.7|418.4} scheme performed in the gas cell. Both the first and second step measurements were performed with the power of the first and second steps P[393.7 nm] = 500 μW and P[418.4 nm] = 145 mW.

The first-step in-gas-cell spectrum exhibits a FWHM of $\sim$ 3 GHz, while the second-step in-gas-cell spectrum has a FWHM of $\sim$ 15 GHz.

4.3.2 Uncertainty estimation

For every individual scan i, the fit parameter values and uncertainty intervals (labeled by index i_k) are obtained for each isotope or pair of isotopes (labeled by index k). To combine these estimates from multiple measurements, the weighted average $\bar{\theta}_k$ of the parameter θ_k, with an estimated uncertainty σ_k were extracted using the following formulae:

$$\bar{\theta}_k = \frac{1}{\sum_{i=1}^{n} 1/\sigma_{i_k}^2} \sum_{i=1}^{n} \frac{\theta_{i_k}}{\sigma_{i_k}^2} \tag{4.6}$$

$$\sigma_k^2 = \frac{1}{\sum_{i=1}^{n} 1/\sigma_{i_k}^2} \tag{4.7}$$

In the case that reduced (chi-square per degree of freedom) $\chi^2 > 1.5$, σ_k^2 is scaled with the reduced chi-square:

$$\sigma_k^2 = \frac{1}{\sum_{i=1}^{n} 1/\sigma_{i_k}^2} \cdot \frac{\chi^2}{n-1} \ , \quad \chi^2 = \sum_{i=1}^{n} \frac{(\bar{\theta}_k - \theta_{i_k})^2}{\sigma_{i_k}^2} \tag{4.8}$$

To propagate the errors in mathematical operations, the basic error propagation formula based on the first order of the Taylor expansion of a function with respect to each variable that has uncertainty was utilized. For any differentiable function of n variables denoted as $f(x_1, ..., x_n)$, the variance of f, represented as σ_f^2, can be approximated using partial derivatives:

$$\sigma_f^2 \approx \sum_{i=1}^{n} \Big(\frac{\partial f}{\partial x_i} \sigma_{x_i} \Big)^2 + 2 \sum_{i=1}^{n} \sum_{j=i+1}^{n} \rho_{x_i x_j} \Big(\frac{\partial f}{\partial x_i} \sigma_{x_i} \Big) \Big(\frac{\partial f}{\partial x_j} \sigma_{x_j} \Big) \tag{4.9}$$

where σ_{x_i} represents the standard deviation of x_i, $\sigma_{x_i x_j} = \rho_{x_i x_j} \sigma_{x_i} \sigma_{x_j}$ is the covariance between x_i and x_j. Square terms inherently yield positive values, as they involve the multiplication of a quantity by itself. In contrast, cross terms may be negative, as they involve the multiplication of two distinct quantities that could have opposite signs. In the case that the variables x_i are uncorrelated, the cross terms cancel out and σ_f^2 simplifies further to:

$$\sigma_f^2 \approx \sum_{i=1}^{n} \Big(\frac{\partial f}{\partial x_i} \sigma_{x_i} \Big)^2 \tag{4.10}$$

A case of great interest is related to the King plot analysis, the field coefficient F and mass coefficient M of one selected excitation scheme can be determined from the isotope shifts of the stable Er isotopes in this study. For future online experiments using the same ionization scheme, the changes in mean-square charge radius of the radioactive isotope under investigation, $\delta\langle r^2 \rangle^{A,A'}$, can be expressed as a function of the measured

isotope shift (IS), field shift factor (F), and mass shift factor (M), mathematically written as $\delta\langle r^2\rangle^{A,A'}=f(IS,F,M)$. The total uncertainty, $\sigma^2_{\delta\langle r^2\rangle}$, can be approximated through error propagation principles as:

$$\sigma^2_{\delta\langle r^2\rangle} \approx \left(\frac{\partial f}{\partial IS}\right)^2\sigma^2_{IS} + \left(\frac{\partial f}{\partial F}\right)^2\sigma^2_{F} + \left(\frac{\partial f}{\partial M}\right)^2\sigma^2_{M} + 2\frac{\partial f}{\partial F}\frac{\partial f}{\partial M}\sigma_{FM} \tag{4.11}$$

4.4 Isotope shift extraction

The isotope shift $\delta\nu_i^{A',A} = \nu_i^{A'} - \nu_i^{A}$, between two isotopes with mass number A' and A for an transition i, can be observed in the wavelength scanning spectrum, as depicted in Fig. 4.9. In this work, the isotope shifts for each scan for all three investigated schemes were extracted with ^{170}Er as the reference isotope. A positive isotope shift $\delta\nu_i^{A',170} = \nu_i^{A'} - \nu_i^{170}$ indicates that the peak of the isotope with $m = A'$ is shifted to higher frequencies than the reference. The final isotope shifts are calculated as the weighted average $\Delta\nu_{\mathrm{WA}}^{A',170}$ of multiple scans using Eq. (4.6). Associated uncertainties $\sigma(\Delta\nu_{\mathrm{WA}}^{A',170})$ encompass both statistical and systematic uncertainties. The statistical component arises from the uncertainty of each individual scan, computed using either Eq. (4.7) or Eq. (4.13) in cases where $\chi^2 > 1.5$. The systematic uncertainty is taken as 6 MHz [V$^+$20], attributed to the wavemeter readout precision. Other potential sources of systematic error, such as temperature fluctuations and laser frequency instabilities, which could introduce measurement inconsistencies, were not accounted for in this work, as their contribution was considered negligible relative to the resolution and accuracy of the measurements.

The extracted isotope shifts for all scans performed in the gas cell for the 400.8 nm, 408.8 nm, and 393.7 nm schemes are presented from left to right in Fig. 4.14. The blue points are the isotope shifts $\delta\nu^{A',170}$ extracted from single scans. The weighted averages $\Delta\nu_{\mathrm{WA}}^{A',170}$ of multiple scans conducted with each scheme are indicated by the red lines in each panel, with the associated statistical and systematic uncertainties indicated as underlying yellow square bars.

All the presented in-gas-cell measurements were performed at 100 mbar stagnation pressure. The excitation step lasers were provided by the dual-etalon Ti:sa cavity, with minimal powers maintained to ensure negligible power broadening: P[400.8 nm] = 550 μW, P[408.8 nm] = 500 μW, and P[393.7 nm] = 500 μW. The ionization step lasers, provided by the single-etalon cavity, were operated at full power ($\approx$ 120 mW) to achieve a sufficient ionization rate. A systematic comparison of the isotope shifts of the three transitions is feasible. Notably, the absolute larger isotope shifts of the 408.8 nm and 393.7 nm transitions suggest possible large field shifts which indicate enhanced sensitivity to nuclear properties. The common larger uncertainties $\sigma(\Delta\nu_{\mathrm{WA}}^{164,170})$ are due to the low statistics of the ^{164}Er resonances.

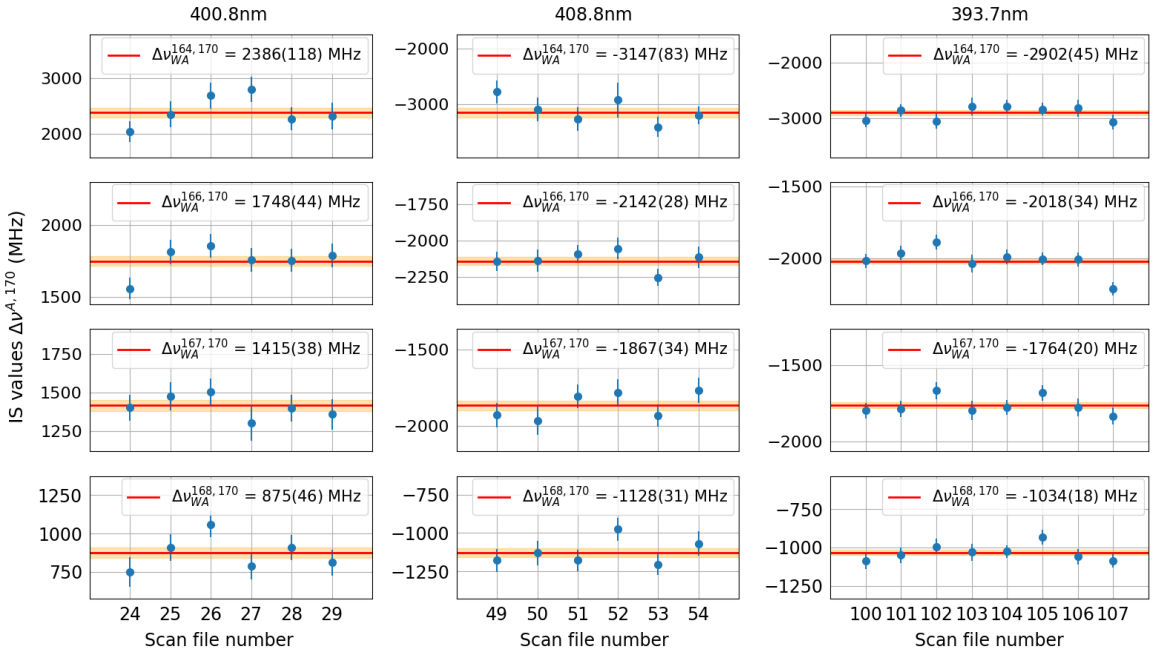

Fig. 4.14. Scatter plots of the extracted isotope shifts from scans of the excitation step laser performed with the 400.8 nm (left), 408.8 nm (middle) and 393.7 nm (right) scheme in the gas cell. The four panels in each scheme case present successively the IS for ^{164,166,167,168}Er with respect to ^{170}Er. The legends represent the extracted $\Delta\nu_{\mathrm{WA}}^{A',170}$ values and the uncertainties $\sigma(\Delta\nu_{\mathrm{WA}}^{164,170})$ in parenthesis on each panel.

The extracted isotope shifts for all scans performed in the gas jet for 408.8 nm and 400.8 nm transitions are presented in Fig. 4.15. All the 408.8 nm in-gas-jet measurements were performed with the injection-locked single-mode Ti:sa cavity, with laser power P[408.8 nm] = 530 - 630 μW for negligible power broadening. However, the 400.8 nm scans were performed on discontinuous days. The dual-etalon Ti:sa cavity was used for the first step with laser power varied between 550 μW to 4 mW.

Owing to the high resolution achieved in the in-gas-jet 408.8 nm RIS measurements with the injection-locked SM Ti:sa laser, the results exhibit significantly reduced uncertainties compared to the gas-cell measurements. However, for the 400.8 nm in-gas-jet measurements, the inconsistent laser powers and the multi-mode nature of the double-etalon laser for individual scans induce count rate fluctuations, leading to large fluctuations in the determined isotope shifts.

The weighted averaged IS values with their corresponding uncertainties for the first step transitions of the three investigated schemes obtained in this work are presented in Table 4.2. For the measurements carried out with the 408.8 nm transition, the in-gas-cell and in-gas-jet results exhibit good agreement. In the case of the 400.8 nm transition, the results obtained from the in-gas-jet measurements agree within one standard deviation

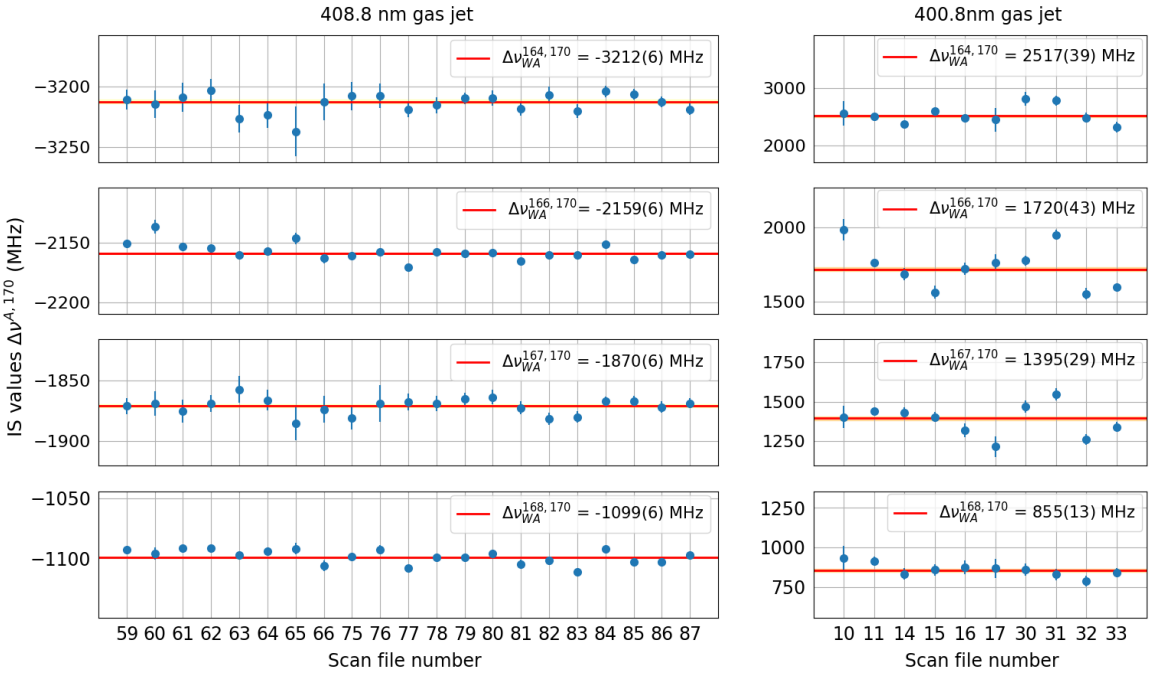

Fig. 4.15. Scatter plots of the extracted isotope shifts $\Delta\nu^{A',170}$ from multiple scans of the excitation step laser performed in the supersonic jet. Left: the 408.8 nm scheme measurements with the first-step laser provided by the injection-locked single-mode Ti:sa cavity. Right: the 400.8 nm scheme measurements with the first-step laser provided by the dual-etalon Ti:sa cavity.

(σ) with the literature values. However, discrepancies observed in the in-gas-cell data compared to literature values, particularly $\Delta\nu_{400.8}^{164,170}$, have been attributed to the power broadening effect exacerbated by the previously described multimode nature of the dual-etalon Ti:sa cavity. The highly efficient 400.8 nm transition led to power broadening even at power levels considered "safe", also taking into account that the used power meter exhibited a negative offset, which led to an underestimation of the real laser power.

Results from this work for the 393.7 nm transition consistently exhibit about 100 - 200 MHz larger absolute values compared to those reported in the literature [JNKM09]. However, the value of $\Delta\nu_{393.7}^{166,170}$ from this work is in good agreement with the literature [AD15]. One should notice that for the analysis of the ^{167}Er spectrum of the 393.7 nm transition, as presented in Fig. 4.14, hyperfine parameters A_u and B_u were not constrained to literature values reported in [JNKM09], as attempts to fit the data with the published values led to unstable fit results. This contrasts with the gas-cell measurements using the 400.8 nm and 408.8 nm schemes, where such constraints with the literature values ([F$^+$13] for 400.8 nm scheme) or gas-jet values (A_u and B_u extracted from the gas-jet measurements of the 408.8 nm scheme) were successful.

Further validation is warranted for the 393.7 nm transition. One should note that the simultaneous laser spectroscopy of all isotopes in our measurements cancels out any offset or drift in the wavemeter readout when isotope shifts are determined.

The extracted weighted average IS values with their corresponding uncertainties for the second step transitions of the three investigated schemes obtained in this work are listed in Table 4.3.

Table 4.2 – Extracted weighted average IS values $\Delta\nu_{\mathrm{WA}}^{A',170}$ of stable $^{164-168}$Er isotopes with respect to ^{170}Er for the first step transitions of the three investigated schemes, compared where possible to the literature. The $\sigma(\Delta\nu_{\mathrm{WA}}^{A',170})$ indicated in parenthesis represents the combined statistical and systematic uncertainties.

A'	Isotope shifts (MHz) $\Delta\nu_{\mathrm{WA}}^{A',170}$						
	408.8 nm		400.8 nm			393.7 nm	
	gas cell	gas jet[1]	gas cell	gas jet[2]	[F$^+$13]	gas cell	[JNKM09]
164	-3147(83)	-3212(6)	2386(118)	2517(39)	2530(22)	-2902(45)	-2681.8(21)
166	-2142(28)	-2159(6)	1748(44)	1720(43)	1681(14)	-2018(34)[3]	-1804(16)
167	-1867(34)	-1870(6)	1415(38)	1395(29)	1384(15)	-1764(20)	
168	-1128(31)	-1099(6)	875(46)	855(13)	841(20)	-1034(18)	-918.4(12)

[1] In-gas-jet measurements with the injection-locked single-mode Ti:sa cavity for the excitation step.

[2] In-gas-jet measurements with the dual-etalon Ti:sa cavity for the excitation step.

[3] In [AD15] this IS value is reported as -67.6(3.0) $\times$ 10^{-3} cm^{-1}, equivalent to -2027(90) MHz.

Table 4.3 – Extracted weighted average IS values $\Delta\nu_{\mathrm{WA}}^{A',170}$ of stable ^{164,166,168}Er isotopes with respect to ^{170}Er for the second step transitions of the three investigated schemes. The large uncertainties in parenthesis are due to the limited data set (one or two scans per transition) and possible systematic errors due to the multimode structure.

A'	Isotope shifts (MHz) $\Delta\nu_{\mathrm{WA}}^{A',170}$			
	402.6 nm	410.7 nm		418.4 nm
	gas cell	gas cell	gas jet	gas cell
164	2562(277)	-2790(396)	-2714(312)	2420(883)
166	1776(162)	-2171(323)	-1962(170)	2060(121)
168	915(163)	-874(295)	-780(170)	917(121)

4.4.1 Determination of field shift coefficients

In this work, all the King plots were made with the IS between adjacent isotopes, referred to as the ladder type ($\Delta\nu_{\mathrm{WA}}^{164,166}$, $\Delta\nu_{\mathrm{WA}}^{166,167}$, etc.). Despite the IS listed in Table 4.2 being computed between ^{164,166,167,168}Er versus the reference ^{170}Er, the ladder type IS were utilized to ensure the largest range coverage in the King plot diagrams.

In principle, all modified reference data and modified IS data pairs should fall on a straight line. To account for the uncertainties in both the x-axis and y-axis data points, the linear Orthogonal Distance Regression (ODR) method was used for the King plot fitting. The Python *Scipy* package provides the *scipy.odr* function [BR90] for the implementation. As shown in Fig. 4.16, unlike Ordinary Least Squares (OLS) regression, which treats the data with independent variables as error-free and measures errors vertically with respect to the fitted line (gray lines), ODR involves minimizing the orthogonal distance of the points with respect to the fitted line. This allows for taking into account errors in measurements for both independent and dependent variables along the x and y-axis, as shown by the red dashed lines in the figure.

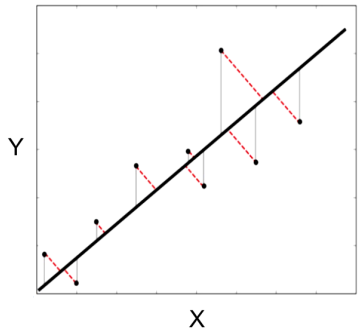

Fig. 4.16. Schmatic illustration of the difference between ODR and OLS fitting. ODR involves finding a line that minimizes the sum of the orthogonal distance (red dashed lines) of the points, while OLS looks for a line that minimizes the sum of the vertical distance (grey lines) of the points.

The field- and mass-shift coefficients F and M, along with their associated σ_F and σ_M were derived from the slope and intercept of both types of King plots using the *scipy.odr* function. Summaries of type I and type II King plot results obtained with the three schemes under investigation in different gas environments are provided in Table 4.4 and Table 4.5, respectively. Special consideration was given to the correlation between the parameters F and M when determining their associated uncertainties. Each ODR fit $y = ax + b$ generates a covariance matrix Σ for the fitting parameters a and b, represented as:

$$\Sigma = \begin{bmatrix} \sigma_a^2 & \sigma_{ab} \\ \sigma_{ba} & \sigma_b^2 \end{bmatrix}$$

the diagonal elements σ_a^2 and σ_b^2 represent the variances of the intercept and slope

parameters, and the off-diagonal elements $\sigma_{ab} = \sigma_{ba}$ represent the covariances between the parameters.

For a type I King plot with $a = F_i$ and $b = \mu_{\text{std}} M_i$,

$$\sigma_{F_i} = \sigma_a \ , \quad \sigma_{M_i} = \sigma_b / \mu_{\text{std}} \ , \quad \sigma_{F_i M_i} = \sigma_{ab} / \mu_{\text{std}} \tag{4.12}$$

While for a type II King plot with $a = \frac{F_i}{F_{ref}}$ and $b = M_i - a \cdot M_{ref}$,

$$\sigma_{F_i} = F_i \sqrt{(\frac{\sigma_a}{a})^2 + (\frac{\sigma_{F_{\text{ref}}}}{F_{\text{ref}}})^2} \ , \quad \sigma_{M_i} = \sqrt{\sigma_b^2 + \sigma_a^2 \cdot M_{\text{ref}}^2 + \sigma_{M_{\text{ref}}}^2 \cdot a^2 + 2\sigma_{ab} \cdot M_{\text{ref}}} \tag{4.13}$$

No uncertainties were provided for M_{583} in the literature [FH04]. Therefore, in this work, the uncertainties σ_{M_i} extracted from the type II King plot represent only the lower limits.

The King plots will be described herein according to the RIS scheme classification. For all the type I King plot analyses in this work, the standard isotope pair 168-170 has been used for the factor μ_{std}. The field- and mass-shift factors for the three investigated FES transitions with different datasets extracted from the type I and type II King plots are presented in Table 4.4 and Table 4.5, respectively. Reduced χ^2 values for each fit, as well as the variances and covariances of the slopes and intercepts for each analysis, are presented in both tables. These values are essential for computing the uncertainties of the two factors and facilitating future studies on radioactive Er isotopes, as illustrated by Eq. (4.11).

The 400.8 nm transition

The King plots of the 400.8 nm scheme data obtained in the gas cell are presented in Fig. 4.17. The left panel illustrates the type I King plot, showing the modified ladder type IS of the 400.8 nm transition plotted versus the muonic X-ray $\lambda^{A',A}$ data from [FH04]. The right panel displays the type II King plot, presenting the modified IS of the 400.8 nm transition plotted against the modified IS of the 582.7 nm transition from [FH04]. In both panels, the blue points represent the modified IS data points of the ladder-type isotope pairs, while the orange lines depict the linear ODR fits.

The obtained field- and mass-shift coefficients F and M, along with their associated uncertainties σ_F and σ_M, are provided in the text boxes in each panel. Additionally, the reduced χ^2 of the fit for each dataset has been presented in the legend, providing an indication of the goodness of the fit. A noticeable deviation of the IS data point from the linear trend, evident in the type II King plot, suggests that the gas-cell measurements of the 400.8 nm scheme suffered from the multi-mode nature of the dual-etalon Ti:sa laser. The power broadening effect during the gas-cell measurements amplified the side

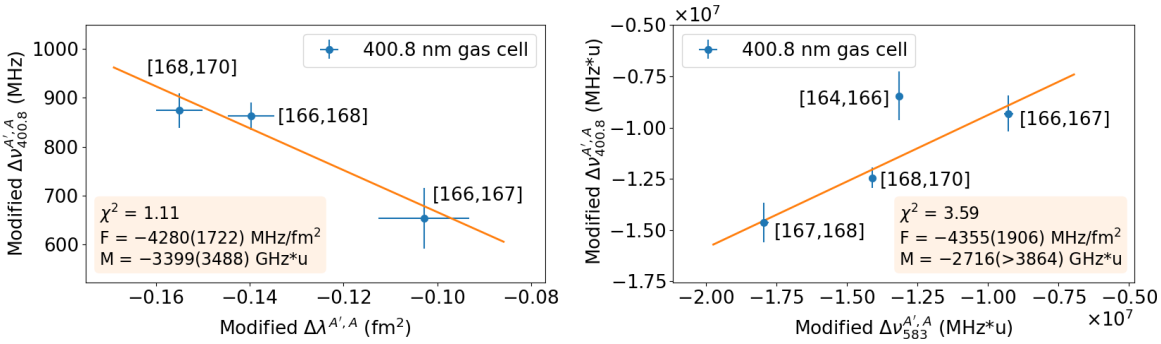

Fig. 4.17. Left: Type I King plot of the modified $\Delta\nu^{A',A}_{400.8}$ plotted against the muonic X-ray $\Delta\lambda^{A',A}$. Right: Type II King plot of the modified $\Delta\nu^{A',A}_{400.8}$ plotted against the modified $\Delta\nu^{A',A}_{582.7}$.

modes, leading to systematic resonance fluctuations, which was more pronounced for the low statistics ^{164}Er resonance.

Two types of King plots of the 400.8 nm FES transition data measured in the gas jet with the dual-etalon Ti:sa laser from this work and the literature data [F$^+$13] are presented in Fig. 4.18. The legends on each panel indicate the analyzed datasets. The left two panels depict the type I King plots for the two sets of data, while the right two panels present the type II King plots.

As introduced previously, for this 400.8 nm $6s^2 - 6s6p$ transition, the intercept of the type I King plot can be theoretically estimated as the modified normal mass shift factor $\mu_{\text{std}}M_{i,\text{NMS}}$, with the modified specific mass shift factor $\mu_{\text{std}}M_{i,\text{SMS}} = (0\pm0.5)\mu_{\text{std}}M_{i,\text{NMS}}$ as the associated uncertainty. The type I King plots with the intercept estimated from *MS* are shown in Fig. 4.19.

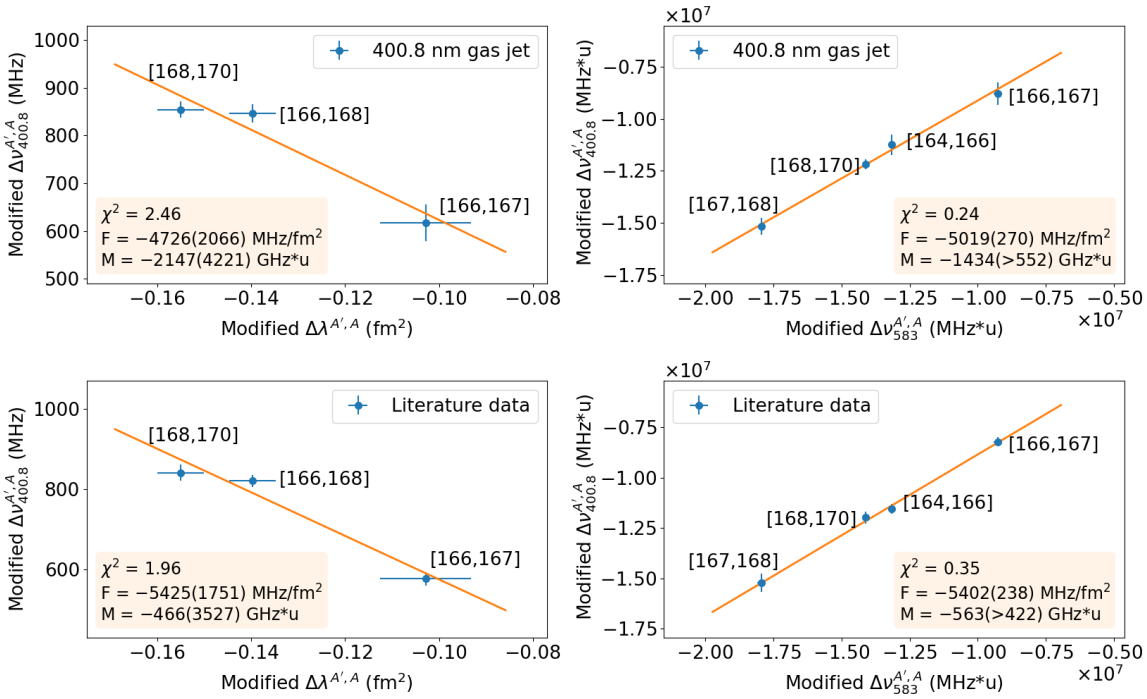

Fig. 4.18. King plots of the 400.8 nm FES transition data measured in the gas jet from this work and the literature data[F+13]. Left: Type I King plot of the modified $\Delta\nu_{400.8}^{A',A}$ plotted against the muonic X-ray $\Delta\lambda^{A',A}$ for the gas-jet data from this work(top) and the literature data(bottom). Right: Type II King plot of the modified $\Delta\nu_{400.8}^{A',A}$ plotted against the modified $\Delta\nu_{582.7}^{A',A}$ for the two datasets.

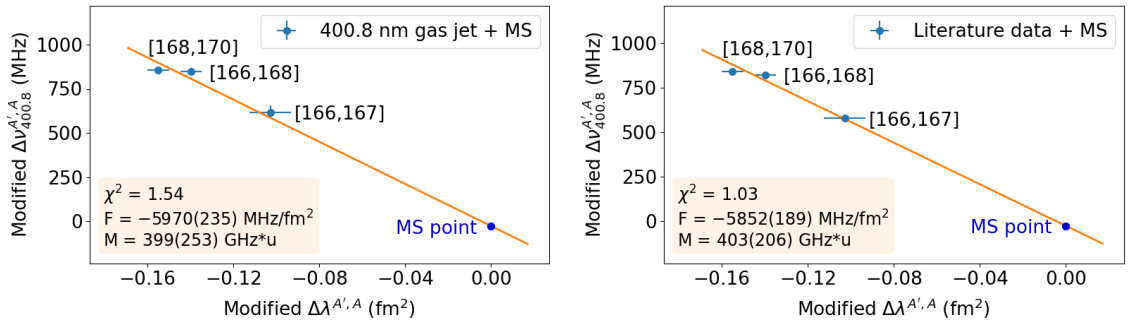

Fig. 4.19. Type I King plots of the modified IS of the 400.8 nm transition plotted against the muonic X-ray $\lambda^{A',170}$ data from [FH04] with the intercept estimated as $NMS(\pm 0.5NMS)$. Left: King plot performed with the 400.8 nm gas-jet RIS data. Right: King plot performed with the 400.8 nm literature data [OM87].

The 415.1 nm transition

It is noteworthy that the 415.1 nm FES transition which was studied by previous work [R+22, A+23] is also a $6s^2 - 6s6p$ transition. To verify if the estimation of *SMS* is valid for this transition, type I King plot analyses with or without the intercept estimated have been performed with the data from the published work [A+23]. This 415.1 nm data was measured as the first commissioning case at S^3-LEB with the same laser system. The results of the two King plot analyses are presented in Fig. 4.20 for comparison. The intercept was estimated as $\mu_{\mathrm{std}} M_{i,\mathrm{NMS}} (\pm 0.5 \mu_{\mathrm{std}} M_{i,\mathrm{NMS}})$ with *NMS* calculated by Eq. (1.14) with ν_0= 721 995 054 MHz, referenced from [KYRN23].

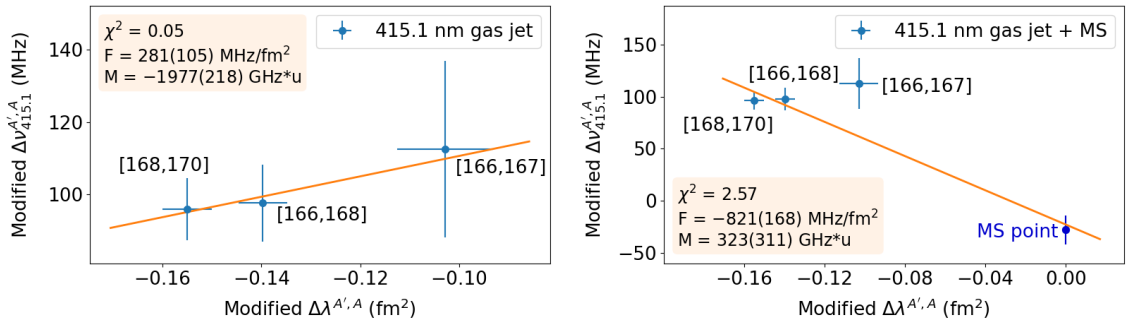

Fig. 4.20. Type I King plots of the modified IS of the 415.1 nm transition plotted against the muonic X-ray $\lambda^{A',A}$ data from [FH04]. Left: King plot performed with the 415.1 nm IS data from [A+23]. Right: King plot performed with the same IS data with the intercept estimated as $NMS(\pm 0.5 NMS)$.

The inconsistent results from the two King plot analyses invalidate the $SMS = (0. \pm 0.5) NMS$ estimation for this transition. Therefore this estimation is not generally valid for all the $ns^2 - nsnp$ transitions. The possible reasons for this discrepancy could be:

- The influence of the atomic spin on the *SMS*. The 400.8 nm and 582.7 nm transitions involve a change from $J = 6$ to $J = 7$ from the ground state to the FES, while $J = 6$ to $J = 5$ for the 415.1 nm transition.
- The electron configuration change for a specific atomic transition, as presented on the NIST database, reflects only the main configuration change, which represents a portion of the overall wavefunction of the atomic transition. The complete wavefunction may be more complex, involving contributions from additional configurations. Consequently, the 415.1 nm and 400.8 nm FES transitions, which both involve main transitions from $4f^{12}6s^2(^3H_6)$ to $4f^{12}(^3H)6s6p$, may not be fully described by this representation alone.

The 408.8 nm transition

Two types of King plots of the 408.8 nm FES transition data obtained in the gas cell and the gas jet are presented in Fig. 4.21. The gas-cell data were acquired using the dual-etalon Ti:sa laser, while the gas-jet data were obtained with the injection-locked Ti:sa laser.

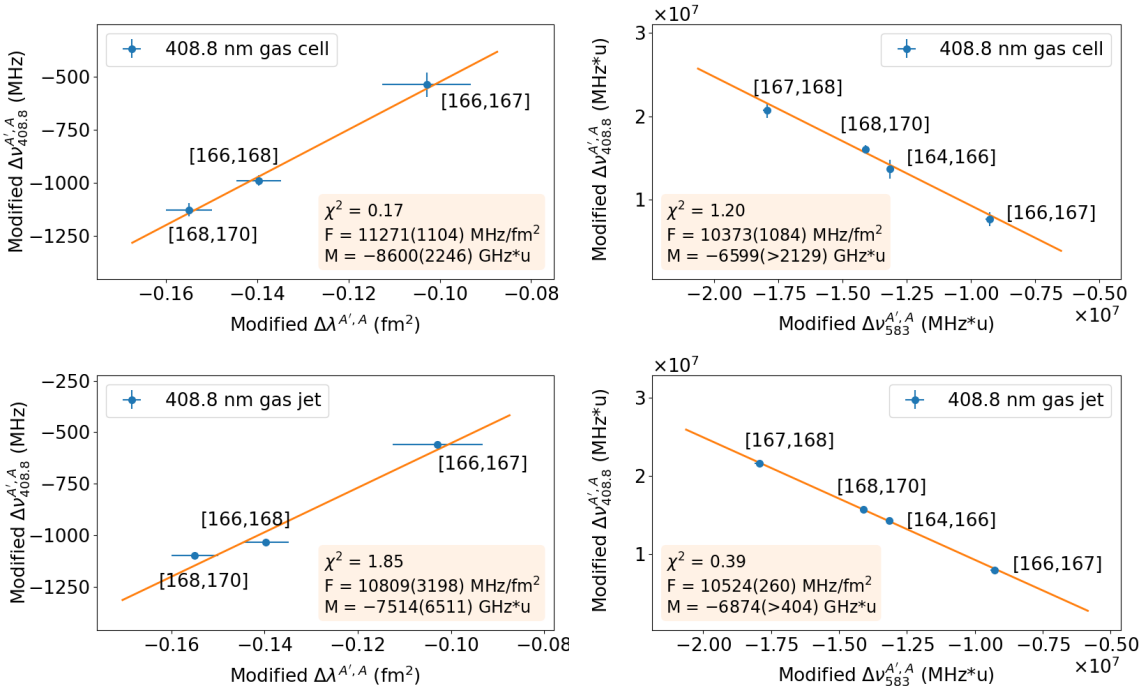

Fig. 4.21. King plots of the 408.8 nm FES transition data measured in the gas cell and the gas jet. Left: Type I King plot of the modified $\Delta\nu_{408.8}^{A',A}$ plotted against the modified muonic X-ray $\Delta\lambda^{A',A}$ for the gas-cell data(top) and the gas-jet data(bottom). Right: Type II King plot of the modified $\Delta\nu_{408.8}^{A',A}$ plotted against the modified $\Delta\nu_{582.7}^{A',A}$ for the gas-cell and gas-jet datasets.

The 393.7 nm transition

Two types of King plots of the 393.7 nm FES transition data obtained in the gas cell using the dual-etalon Ti:sa laser for the first-step laser are presented in Fig. 4.22.

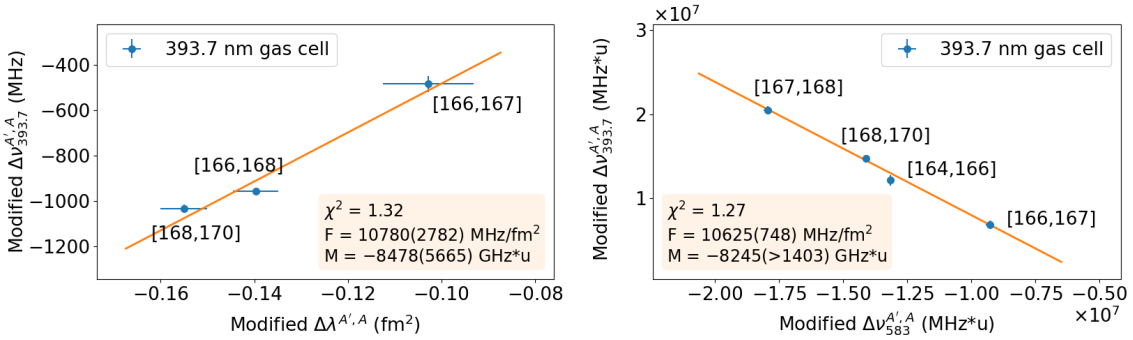

Fig. 4.22. King plots of the 393.7 nm FES transition data measured in the gas cell. Left: Type I King plot of the modified $\Delta\nu^{A',A}_{393.7}$ versus modified muonic X-ray $\Delta\lambda^{A',A}$. Right: Type II King plot of the modified $\Delta\nu^{A',A}_{393.7}$ plotted against the modified $\Delta\nu^{A',A}_{582.7}$.

In conclusion, for the 400.8 nm transition, the gas-jet data from this work and the literature data were analyzed using three methods: type I King plot, type I King plot with mass shift estimation, and type II King plot. However, for the 408.8 nm and 393.7 nm transitions, where the theoretical estimation of *SMS* is not available, experimental data were analyzed only with the type I King plot and type II King plot methods. The comparison of results in the two tables leads to the following conclusions:

- For the 400.8 nm transition, the extracted $F_{400.8}$ and $M_{400.8}$ factors from the type I King plot analyses agree with the other two methods within a 1 σ uncertainty interval, although the results from the type I King plot inherently exhibit an order of magnitude larger uncertainties due to the limited number of data points available. The consistent results between this work and the literature provide confidence in the dual-etalon Ti:sa system performance in the supersonic jet. However, results from the type I King plot with mass shift estimation by $\delta\nu_{i,\mathrm{SMS}} = (0 \pm 0.5)\delta\nu_{i,\mathrm{NMS}}$ and type II King plot which relies on the same assumption, but for the 583 nm transition, are in agreement within 2σ uncertainty interval. Therefore, the consistency of the assumption on the *SMS* for the $ns^2 - nsnp$ transition has been empirically validated.
- For the 408.8 nm transition, a comparison between resonance ionization spectroscopy in the gas cell and in the supersonic gas jet in terms of extracted field and mass shift factors has been conducted. The results obtained from both gas-cell and gas-jet data in this study are in agreement within a 1 σ uncertainty interval with both types of King plot analyses. However, the broader resonance linewidths observed in gas-cell spectroscopy impacted the accuracy of the measured resonance frequencies. As a result, larger uncertainties were observed

for the modified $\Delta\nu_{408.8}^{A',A}$ values derived from the gas-cell data, as indicated by the vertical error bars in Fig. 4.21.

- For the 393.7 nm transition, the results of the gas-cell data analyzed by type I and type II King plots are also in good agreement.
- After systematically studying the four RIS schemes (400.8 nm, 408.8 nm, 393.7 nm, and 415.1 nm [R^+22, A^+23]), the 408.8 nm and 393.7 nm FES transitions, characterized by large F_i values, demonstrate high sensitivity to the isotopic variation of the mean-square nuclear charge radius $\delta\langle r^2\rangle^{A',A}$. Consequently, these two RIS schemes are considered potential candidates for online RIS experiments on radioactive erbium isotopes with the S^3 spectrometer.

Table 4.4 provides an overview of the extracted field F_i and mass M_i coefficients, along with the associated uncertainties, derived from the Type I King plots analysis for the 400.8 nm, 408.8 nm and 393.7 nm FES transitions.Table 4.5 presents the results of these three transitions obtained from the Type II King plots analysis.

Table 4.4 – Extracted field and mass coefficients and the associated uncertainties, reduced χ^2 of the linear fit, variances and covariances for F_i and M_i from Type I King plots analysis for the 400.8 nm, 408.8 nm and 393.7 nm FES transitions.

Dataset	F (GHz/fm^2)	M (GHz·u)	χ^2	σ_F (GHz/fm^2)	σ_M (GHz·u)	σ_{FM} (GHz^2·u/fm^2)
400.8 nm						
Gas jet	-4.73(2.07)	-2147(4221)	2.46	1.32	2689	-3521
Gas jet + MS	-5.97(0.24)	399(253)	1.54	0.19	203	-20
[F^+13]	-5.43(1.75)	-466(3527)	1.96	1.25	2522	-3134
[F^+13] + MS	-5.85(0.19)	403(206)	1.03	0.19	203	-20
408.8 nm						
Gas cell	11.27(1.10)	-8600(2246)	0.17	2.65	5394	-14211
Gas jet	10.81(3.20)	-7514(6511)	1.85	2.35	4786	-11188
393.7 nm						
Gas cell	10.78(2.78)	-8478(5665)	1.32	2.42	4932	-11877

* The uncertainties of F and M in the parenthesis were obtained as $\sigma_F\sqrt{\chi^2}$ and $\sigma_M\sqrt{\chi^2}$, respectively.

Table 4.5 – Extracted field and mass coefficients and the associated uncertainties, reduced χ^2 of the linear fit, variances and covariances for the slope and intercept of the fit from Type II King plots analysis for the 400.8 nm, 408.8 nm and 393.7 nm FES transitions.

Dataset	F^1 (GHz/fm^2)	$M^{1,2}$ (GHz·u)	χ^2	σ_a	σ_b (GHz·u)	σ_{ab} (GHz·u)
			400.8 nm			
Gas jet	-5.02(0.27)	-1434(>552)	0.24	7.95×10^{-2}	1141.77	89.53
[F$^+$13]	-5.40(0.24)	-568(>422)	0.35	5.66×10^{-2}	732.00	40.54
			408.8 nm			
Gas cell	10.37(1.08)	-6599(>2129)	1.20	1.49×10^{-1}	2080.7	304.85
Gas jet	10.52(0.42)	-6874(>404)	0.39	4.78×10^{-2}	662.21	31.39
			393.7 nm			
Gas cell	10.63(0.67)	-8245(>1403)	1.27	9.07×10^{-2}	1272.6	113.76

[1] The uncertainties of F and M were obtained through error propagation with σ_a, σ_b and σ_{ab}.
[2] The uncertainties of M represent the lower limits due to the unknown $\sigma_{M_{583}}$

4.4.2 Study of the collisional shift and broadening of spectral lines

For precise laser-spectroscopic studies, the centroid and width of the measured resonant spectral line should be as close as possible to the natural laser line. However, as discussed in Section 4.3.1, the experimental width is a convolution of many effects adding to the intrinsic laser linewidth. The total linewidth includes three Gaussian shape components: the Doppler broadening linewidth $\Delta\nu_{\text{Doppler}}$, the Fourier pulse linewidth $\Delta\nu_{\text{pulse}}$ and the frequency doubling linewidth $\Delta\nu_{\text{SHG}}$, as well as three Lorentzian distribution components: the natural linewidth Γ_{nat} of the excited state, the collision broadening linewidth Γ_{coll} and the power broadening linewidth Γ_{power}. All the Gaussian components can be calculated easily using Eq. (2.29), 2.32 and 2.62, and the Lorentzian component Γ_{nat} can be deduced as $A_{21}/2\pi$. While power broadening can be eliminated during the experiment by reducing the laser power below the saturation power, characterization of the pressure broadening, which cannot be expressed by an analytical formula, is of particular interest.

Non-resonant collisions of the atoms of interest with the buffer gas atoms cause broadening as well as shifts of the spectral lines. These effects were previously studied with stable Erbium isotopes using the 415.1 nm FES transition as part of the first commissioning experiments at S^3-LEB [A$^+$23]. To systematically investigate whether the collisional shift and broadening are transition-dependent for a certain element,

further characterization was performed in the gas cell with the same laser system for the 400.8 nm and 408.8 nm transitions in this work.

For each transition, 10 gas-cell scans were performed at pressures ranging from 100 mbar to 300 mbar with a step of 50 mbar, with 2 scans for each pressure. The dual-etalon Ti:sa cavity was used for the first-step laser with hundreds of μW to minimize the power broadening and the second step at full power. By setting the appropriate TOF gate for different isotopes, the collisional shift and broadening effects were investigated for three isotopes (^{166,168,170}Er) which exhibited high statistics and allowed for the extraction of FWHM and centroid.

The 408.8 nm transition

For the 408.8 nm transition, the resonance shifts of each isotope were extracted with respect to the resonances obtained from the gas-jet data in this work, with ν_0^{166} = 733205483.6(0.5) MHz, ν_0^{168} = 733206542.1(0.6) MHz and ν_0^{170} = 733207643.1(0.7) MHz (the uncertainties are statistical). A comparison of the gas-cell spectroscopy for different gas pressures and the gas-jet spectroscopy of the highest statistics ^{166}Er is presented in Fig. 4.23. The first-step laser power for the gas-cell spectroscopy was maintained at 600 μW, with a determined saturation power of $P_{0,\mathrm{cell}}$[408.8 nm] = 0.84(10) mW, while for gas-jet spectroscopy, it was set to 500 μW, with a saturation power of $P_{0,\mathrm{jet}}$[408.8 nm] = 2.46(30) mW. The gas-jet data exhibits a resolution of about 200 MHz, while the gas-cell data obtained at 100 mbar shows a total linewidth of about 3.0 GHz, increasing to 3.3 GHz at 200 mbar and 3.8 GHz at 300 mbar. A slight redshift of the resonance with increasing pressure can also be observed.

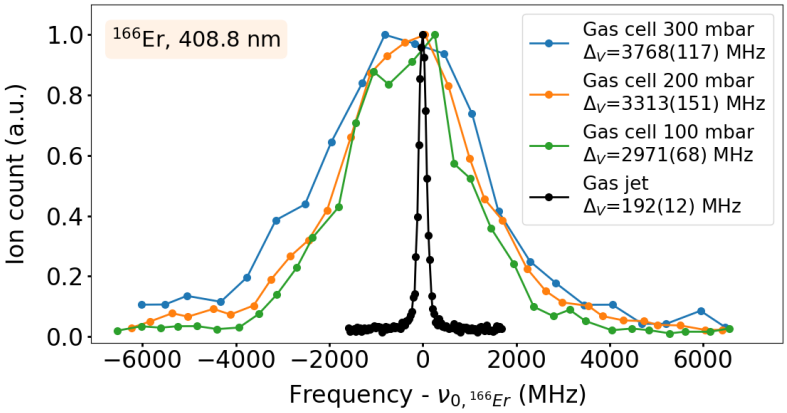

Fig. 4.23. Comparison of the linewidths of the highest statistic peak ^{166}Er from the scans performed in the gas cell at different pressures and in the supersonic jet for the 408.8 nm FES transition relative to ν_0 = 733 205 483.6 MHz, which is the resonance of ^{166}Er derived from the gas-jet data.

Fig. 4.24 shows the extracted collisional broadening FWHM (left) and centroid shift (right) values for the 408.8 nm FES transition as a function of pressure. The results for isotopes ^{166,168,170}Er are lined up from top to bottom panels. Linear fits in red lines are applied to extract the pressure broadening Γ_{coll} and shift Γ_{sh} coefficients from the slope of the data distributions. The final results are derived as the weighted average for the three isotopes. For the 408.8 nm FES transition Γ_{coll} =4.53(0.66) MHz/mbar, Γ_{sh} = -0.13(0.29) MHz/mbar.

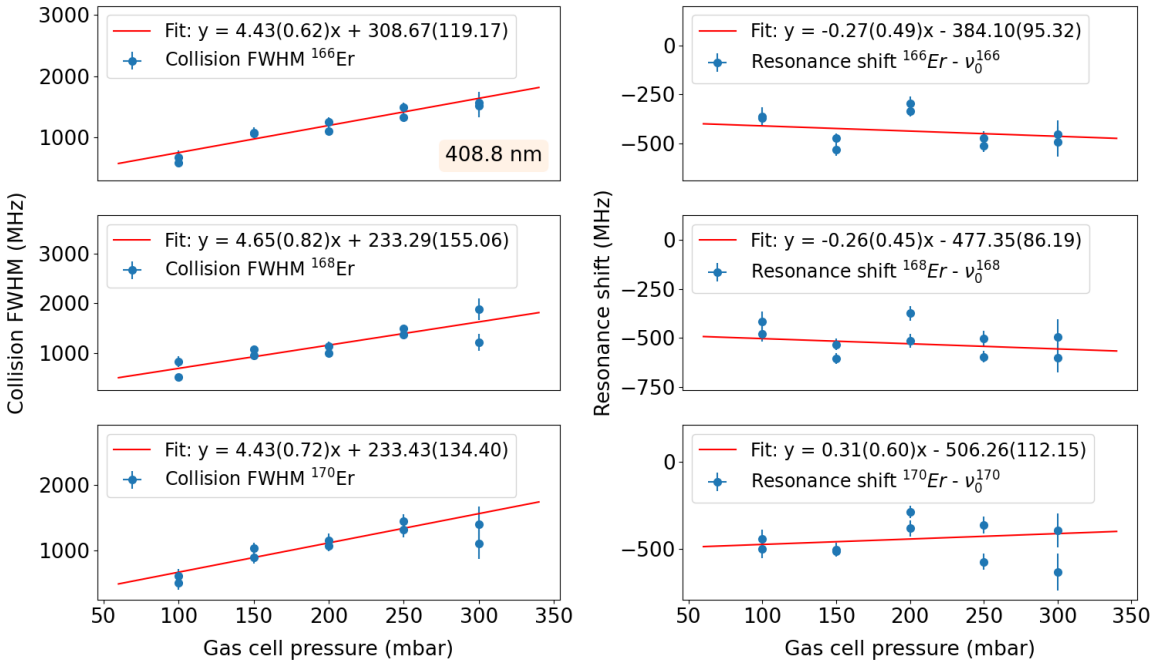

Fig. 4.24. Collisional broadening FWHM and centroid shift were determined for all spectra of 408.8 nm FES transition as a function of pressure for isotopes ^{166,168,170}Er, as lined up from top to bottom panels. Linear fits are applied to the spectra to extract the pressure broadening and pressure shift coefficients.

The 400.8 nm transition

For the 400.8 nm transition, the resonance shifts of each isotope were extracted with respect to the resonance ν_0 = 747 780 482 MHz from the literature. A comparison of gas-cell spectroscopy for different gas pressures of ^{166}Er is presented in Fig. 4.25. The first-step laser power was maintained at 800 μW, while the second-step laser was set at full power 108 mW. However, the excessively large total linewidth of about 6 GHz at 100 mbar indicated the presence of additional broadening during the measurements, which is attributed to power broadening. This is understood because the saturation power for this transition was determined to be $P_{0,\text{cell}}[400.8\text{ nm}] = 0.56(0.11)$ mW. Consequently,

in the left panel of Fig. 4.26, intercepts around 3.5 GHz are observed for the fits of all three isotopes, representing the power broadening FWHM.

The pressure broadening Γ_{coll} and shift Γ_{sh} coefficients have been extracted for ^{166,168,170}Er for the 400.8 nm transition, as presented in Fig. 4.26. The weighted averages of the results of the three isotopes are Γ_{coll} =19.32(1.00) MHz/mbar, Γ_{sh} = -1.95(0.32) MHz/mbar.

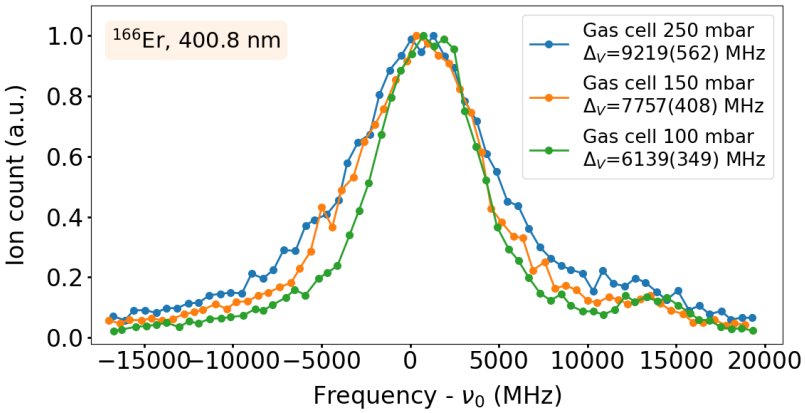

Fig. 4.25. Comparison of the linewidths of ^{166}Er from the scans performed in the gas cell at different pressures for the 400.8 nm FES transition relative to ν_0 = 747 780 482 MHz.

Table 4.6 presents the extracted pressure broadening and shift coefficients for the 408.8 nm and 400.8 nm transitions obtained in this study, in comparison with previously published values for the 415.1 nm transition. These results demonstrate that pressure broadening and shift effects are transition-dependent, indicating the need for systematic studies across different transitions for erbium to fully characterize these effects. Further in-gas-cell measurements can be performed with the injection-locked Ti:sa laser to explore additional transitions and refine the understanding of the pressure broadening and shift effects. Among the three transitions in Table 4.6, the 408.8 nm transition shows reduced sensitivity to high pressure, making it particularly advantageous for in-gas-cell spectroscopy applications.

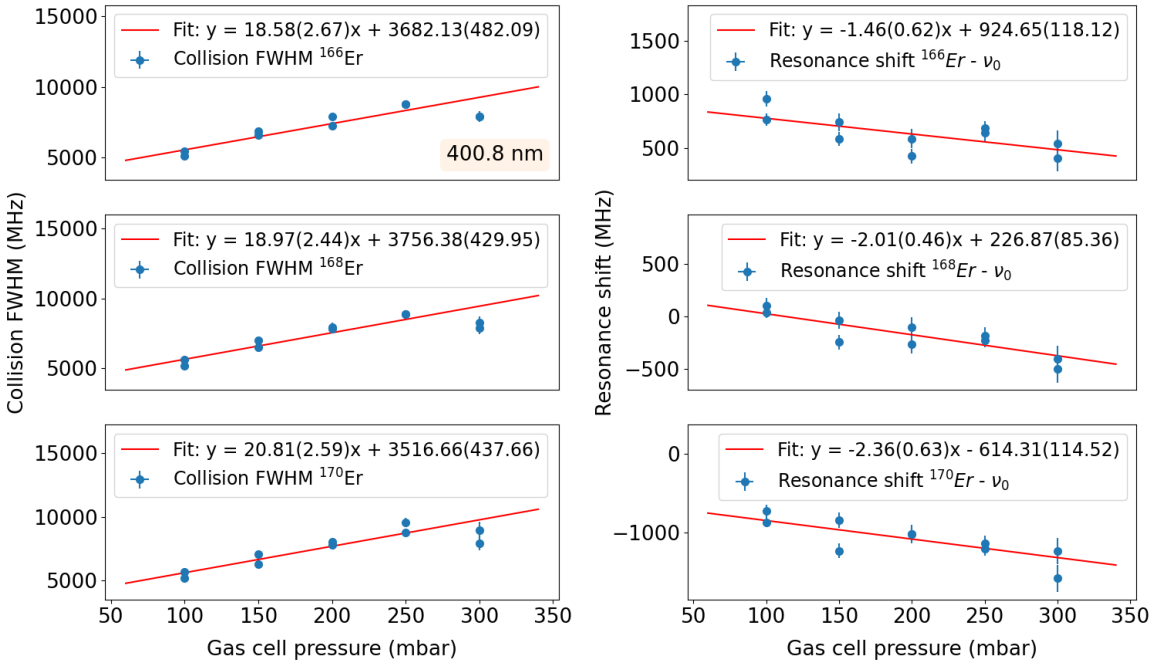

Fig. 4.26. Collision FWHM and centroid shift were determined for the spectra as a function of pressure. A linear fit is applied to the data to extract the pressure broadening and pressure shift coefficients discussed in the text.

Table 4.6 – Collisional broadening and shift coefficients of the 408.8 nm and 400.8 nm transitions investigated in the gas cell in this thesis work, compared with the coefficients for the 415.1 nm transition reported in [A$^+$23].

Atomic states	Excitation step (nm)	Broadening coef. Γ_{br} (MHz/mbar)	Shift coef. Γ_{sh} (MHz/mbar)
$4f^{11}(^4I)5d6s^2, J = 6$	408.8	4.53(0.66)	-0.13(0.29)
$4f^{12}(^3H)6s6p, J = 7$	400.8	19.32(1.00)	-1.95(0.32)
$4f^{12}(^3H)6s6p, J = 5$	415.1 [A$^+$23]	11(1)	-4(1)

4.5 Hyperfine structure analysis

The hyperfine structure details have to be resolved by a high-resolution probing technique. It was not possible to deduce HFS from the gas-cell measurements due to the spectral linewidth being in the few GHz range. The in-gas jet spectroscopy technique with the injection-locked Ti:sa laser employment was thus used with its $\approx$ 200 MHz linewidth, leading to a partial resolving of the complicated HFS.

In this section, an experimental investigation of the hyperfine structure of the odd-even erbium isotope ^{167}Er is presented. In particular, we obtain the magnetic dipole constant, A, and the electric quadrupole constant, B, for the electronically excited state $4f^{11}(^4I)5d6s^2$, $J = 6$ of ^{167}Er.

4.5.1 Hyperfine coefficients

As indicated in the TOF spectrum of stable erbium (see Fig. 4.3), the only odd-even erbium isotope ^{167}Er is surrounded by neighboring ^{166,168}Er peaks. To obtain the ^{167}Er HFS spectrum without potential contamination, the TOF gate was constrained carefully avoiding the overlapping tails.

To extract the hyperfine coefficients, the SATLAS fit function *HFSModel* was again used. Similar to the chi-square fit of the even-even isotopes, if the calculated reduced $\chi^2 \geq 1.5$, the extracted variable uncertainties are multiplied by the square root of the reduced χ^2, otherwise the original error estimate σ is used.

An important boolean optional parameter, 'use_racah', in the function significantly influences the fitting quality. When set to True, the relative peak intensities are fixed to the Racah intensities. Conversely, if set to False, the initial intensities are equal, allowing the peak intensities to vary during fitting. To assess the influence of the Racah parameter, a comparative analysis of the HFS results with and without Racah intensities was conducted, as shown in Fig. 4.27. The top panel presents the ^{167}Er HFS fit without using the Racah coefficients, while the bottom panel shows the fit with them. Both cases yielded fit results within a 2 combined sigma uncertainty interval. However, the fitting without Racah intensities achieved a significantly better fit.

Fig. 4.28 presents the extracted HFS coefficients A and B of the FES of the 408.8 nm transition of ^{167}Er deduced from the gas jet measurements. The blue dots with error bars represent the results from individual scans and the red lines indicate the weighted averages of the A and B coefficients.

Table 4.7 shows the hyperfine A and B constants of the odd isotope ^{167}Er determined for the FES of the 408.8 nm transition in this work, compared with published results for the FES of the 415.1 nm transition [SAW85] and the ground state [CGP83].

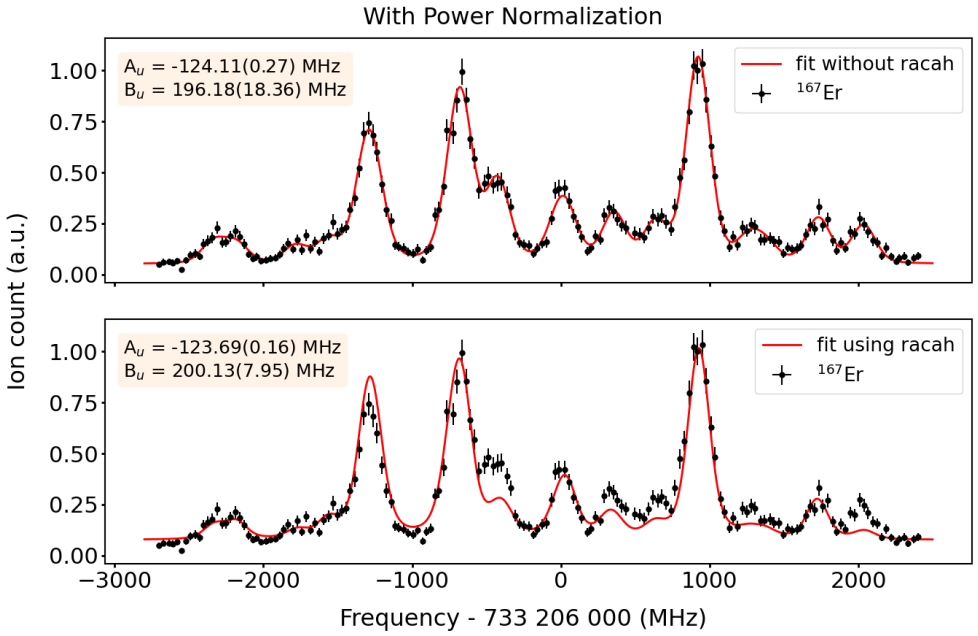

Fig. 4.27. Measured in-gas-jet spectrum (black dots) of the hyperfine splitting in the 408.8 nm $4f^{12}6s^2(^3H_6)$, $J = 6 \rightarrow 4f^{11}(^4I)5d6s^2$, $J = 6$ transition, shown as the ion-counts versus the frequency with respect to the value of the center of gravity. The red curve shows the χ^2-minimized fit of the HFS Voigt profile to the scan data. Top: fit with 'use_racah = False'. Bottom: fit with 'use_racah = True'.

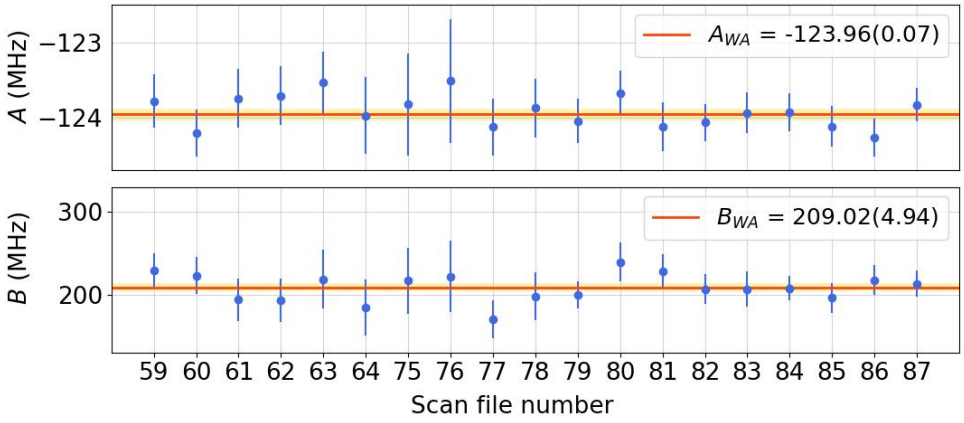

Fig. 4.28. Scatter plots of the extracted ^{167}Er HFS coefficients A and B from scans performed with the 408.8 nm transition in the gas jet. Measurements were carried out at excitation and ionization steps of 500 μW and 140 mW.

In conclusion, the 408.8 nm FES transition exhibits large isotope shifts, providing high sensitivity to variations in the nuclear charge radius. However, its HFS constants are smaller compared to those of the 415.1 nm transition, making it less optimal for detailed investigations of nuclear electromagnetic moments. For such studies in online

Table 4.7 – Extracted ^{167}Er HFS coefficients for the 408.8 nm RIS scheme. The σ indicated in parenthesis represents the combined statistical and systematic uncertainties.

Atomic states	Excitation step (nm)	A (MHz)	B (MHz)
$4f^{11}(^4I)5d6s^2, J = 6$	408.8	-123.96(6.0)	209.02(7.8)
$4f^{12}(^3H)6s6p, J = 5$	415.1 [SAW85]	-146.6(3)	-1874(16)
g.s.	- [CGP83]	-120.487(1)	-4552.984(10)

experiments, alternative transitions with larger hyperfine constants A and/or B should be considered to enhance sensitivity for determining the magnetic dipole moment μ and/or the spectroscopic quadrupole moment Q_s.

The 393.7 nm FES transition is also a promising candidate for future high-resolution resonance ionization spectroscopy (RIS) measurements at S^3-LEB to determine its hyperfine constants, given its comparable field shift factor (F) to the 408.8 nm transition. However, successful implementation would require generating seed light for the single-mode Ti:sa laser system. This was not achieved in the present work due to the limited emission range of the available diode seed laser.

The efficiency, sensitivity, and applicability of the IGLIS technique at S^3-LEB, particularly for short-lived isotopes, are intrinsically tied to the performance of the S^3-LEB gas cell. In this chapter, the in-gas-cell and in-gas-jet RIS measurements conducted on stable erbium isotopes were not constrained by the extraction time of the gas cell. However, in online experiments involving radioactive isotopes, the gas cell extraction time becomes a critical parameter that directly influences the feasibility and scope of the IGLIS method. As detailed in Chapter 5, ongoing developments are focused on the design and implementation of a future version of the S^3-LEB gas cell, with the objective of extending the applicability of the laser ionization spectroscopy at S^3-LEB to isotopes with half-lives on the order of 100 ms, while maintaining high extraction efficiency.

Chapter 5

Simulation and experimental studies in the FRIENDS^3 project

The present chapter concerns a key deliverable of the FRIENDS^3 ANR project, namely the design of a new gas cell for S^3-LEB and the study of electron production for ion neutralization in the gas phase. The chapter is organized into three main sections that detail the comprehensive efforts undertaken during this stage. The first section outlines the motivation and objectives of the project. The second section offers an overview of the phenomena that need to be accounted for in gas-cell simulations, along with a discussion of the various approaches available for modeling them. The third section presents simulation results obtained using these approaches, including benchmarks and preliminary optimization studies.

5.1 Motivation and objectives of the project

As discussed in Section 3.1.3, the current S^3-LEB gas cell shown in Fig. 3.4 has an extraction time of approximately 600 ms for a 1 mm exit hole diameter, and roughly half that value for a 1.5 mm diameter exit [Mog13a, Mog13b, K$^+$16]. Furthermore, its neutralization mechanism relies on electron-ion recombination within the plasma created by the S^3 ion beam, a process inherently dependent on the beam intensity. These limitations underscore the need for a faster and universally neutralization-capable gas cell, which is the primary motivation of the FRIENDS^3 project.

The initial approach is to design a gas cell with a DC field region for fast ion extraction and a no-field region for neutralization before the exit. In this configuration, DC electric fields enhance ion extraction from the stopping region, where the gas flow is nearly stagnant, while neutralization is achieved through an artificially generated electron cloud within the no-field region, before the gas flow accelerates to sonic velocity.

The work of the FRIENDS^3 project is dedicated to two main objectives: simulation

design and experimental tests. The simulation aspect focuses on modeling the gas-cell phenomena relevant to the project objectives in a geometry compatible with the additional constraints imposed by the S^3-LEB setup, such as the S^3 interface, spatial layout, and pumping capacity. The simulated geometry would eventually translate into a gas-cell prototype which will be built and tested off-line. This prototype will later be converted into a design which can be implemented at S^3-LEB. This two-stage approach ensures that in the initial development phase some of the S^3-LEB constraints can be relaxed for a gain in simplicity and cost, while focusing on the more fundamental aspects of the studied performances. It also means that the first simulations can use a simplified geometry.

The simulation work package has several stages, with experimental work conducted simultaneously. The simulation design has been refined based on actual experimental conditions. The initial stage of the simulation work package involved a preliminary study of the software tools (including programs, physics interfaces, modules, and approaches) necessary for modeling gas-cell phenomena. This stage also included validating the chosen simplified geometry, using these tools, in terms of key quality factors such as gas cell extraction efficiency, extraction time, and the time available for the neutralization process. As the preliminary design neared completion, the construction of the test bench for neutralization mechanism tests began. To facilitate the practical implementation of the simulated geometry, the second stage simulation is dedicated to adjusting the geometry of the prototype considering the cost of parts. The adjustments involved, for instance, reducing the number of electrodes, utilizing industrial standard-dimension components, and temporarily removing the convergent section near the exit.

5.2 Phenomena involved in gas-cell simulations

To accurately model the processes of stopping, extraction, and neutralization of radioactive ion species within a gas cell, it is necessary to address the following key phenomena:

1. Gas flow dynamics: the gas enters the cell through an inlet window and evacuates through the exit hole, creating stagnation pressure, temperature, and velocity fields in the gas cell. The simulation focuses on the gas-cell volume, the supersonic jet formed after the exit (nozzle throat) is not taken into consideration.
2. Electromagnetic field: the distribution of electric fields within the gas cell, which are generated by specified voltage distributions on the electrodes, needs to be characterized.
3. Ions motion: before being neutralized, the ions move under the combined influences of gas flow and electromagnetic fields.
4. Free-electron generation in the buffer gas: a free-electron cloud for ion

neutralization is created as an artificially generated plasma via discharge or irradiation by an external beta source. Complex plasma-chemical reactions between the buffer gas, ions and the resulting secondary electron density in equilibrium need to be studied.

5. Ion-plasma interactions: as ions traverse the generated plasma, a variety of reactions occur between the ions of interest and plasma species, among which the recombination with free electrons leads to the neutralization of the ions.

The subsequent sections will detail the methodologies used to simulate these phenomena.

5.2.1 Simulation of the gas flow

The gas flow in the cell can be simulated using the COMSOL [COM] Laminar Flow Interface, which can solve the equations for compressible laminar flow in a low Mach number ($M < 0.3$). The Navier-Stokes equations are used and adapted to account for compressibility effects while assuming that the Mach number is sufficiently small such that the flow remains close to incompressible. In this regime, the equations account for density variations due to pressure and temperature changes but the velocity field is still primarily governed by the incompressible approximation. The governing continuity and momentum equations for such a flow are expressed as:

$$\nabla \cdot (\rho \mathbf{u}) = 0 \tag{5.1}$$

$$\rho(\mathbf{u} \cdot \nabla)\mathbf{u} = \nabla \cdot [-p\mathbf{I} + \mathbf{K}] + \mathbf{F} \tag{5.2}$$

where ρ is the gas density, $\mathbf{u}$ is the gas velocity, p is the pressure, $\mathbf{I}$ is the identity matrix, $\mathbf{F}$ is the volume force vector, which in our case is zero. The term $\mathbf{K}$ represents the viscous stress tensor, which is expressed as:

$$\mathbf{K} = \mu \left(\nabla \mathbf{u} + (\nabla \mathbf{u})^T \right) - \frac{2}{3}\mu(\nabla \cdot \mathbf{u})\mathbf{I}, \tag{5.3}$$

where μ is the dynamic viscosity of the gas. This equation reflects how the internal friction (due to viscosity) affects the fluid flow, the term $\mu \left(\nabla \mathbf{u} + (\nabla \mathbf{u})^T \right)$ represents the shear stress component, which accounts for the internal friction between adjacent layers of fluid moving at different velocities. The term $-\frac{2}{3}\mu(\nabla \cdot \mathbf{u})\mathbf{I}$ represents the volumetric stress component arising from fluid compressibility.

Eq. (5.1) reflects that mass is conserved despite changes in density and Eq. (5.2) represents the balance of forces. These equations can be solved by also taking into account the boundary conditions and the gas properties. In the present simulations, the effect of turbulence from the gas injection is not taken into account. The window of the gas cell is used as the inlet for gas injection. The inlet condition is given by a specific mass-flow value derived from the desired stagnation pressure. The outlet

can be defined as a constant pressure boundary ($p = 0$), but close to the outlet the gas velocities rapidly approach the speed of sound, thereby breaking the condition of $M < 0.3$. The solution is to end the simulation volume before the outlet, at an axial coordinate where the $M < 0.3$ condition is always satisfied. The outlet would thus be slightly before the actual position of the nozzle throat.

The outlet boundary condition can be established based on the conservation of mass, which means the mass flow rate $\dot{m}$ through a tube remains constant and is given by:

$$\dot{m} = \rho v A, \tag{5.4}$$

where ρ is the density, v is the flow velocity, and A is the flow area. For an ideal compressible gas, the mass flow rate can be calculated as [L$^+$24a]:

$$\dot{m} = \sqrt{\frac{\gamma}{(R/M_{\mathbf{gas}})T}} M \left(1 + \frac{\gamma - 1}{2} M^2\right)^{\frac{1+\gamma}{2(1-\gamma)}} p_0 A, \tag{5.5}$$

where γ is the isoentropic expansion coefficient, which for argon and helium is 5/3, R is the universal gas constant and is equal to 8.314 J·mol^{-1}·K^{-1}, $M_{\mathbf{gas}}$ is the molar mass of the gas, T is the gas absolute temperature, p_0 is the stagnation pressure, and M is the Mach number. At the nozzle throat, M =1 and the flow is choked. With the nozzle throat diameter d, the mass flow rate of the choked flow $\dot{m}_{\text{choked}}$ is given by:

$$\dot{m}_{\text{choked}} = \sqrt{\frac{\gamma}{(R/M_{\mathbf{gas}})T}} \left(\frac{2}{\gamma + 1}\right)^{\frac{1+\gamma}{2(\gamma-1)}} p_0 \frac{\pi}{4} d^2, \tag{5.6}$$

From the conservation of mass, the mass flow rate $\dot{m}$ through the new outlet should be equal to $\dot{m}_{\text{choked}}$. Therefore, the volume flow rate Q_V through the new outlet can be determined via:

$$Q_V = \dot{m}/\rho_0 = \dot{m}_{\text{choked}}/\rho_0 \tag{5.7}$$

where ρ_0 is the stagnation gas density in the gas cell and can be estimated using the ideal gas law:

$$\rho_0 = \frac{M_{\text{gas}} p_0}{RT}, \tag{5.8}$$

Substituting Eq. (5.6) and Eq. (5.8) into Eq. (5.7) gives:

$$Q_V = \sqrt{\frac{\gamma RT}{M_{\text{gas}}}} \left(\frac{2}{\gamma + 1}\right)^{\frac{\gamma+1}{2(\gamma-1)}} \frac{\pi}{4} d^2, \tag{5.9}$$

A quick formula derived from Eq. (5.9) for computing the volume flow rate through the

outlet of the simulation volume is:

$$Q_V[\mathrm{L/s}] = 0.052(d[\mathrm{mm}])^2\sqrt{\frac{T}{A_{\mathrm{gas}}}}, \tag{5.10}$$

where A_{gas} is the atomic mass of the gas. Also from the conservation of mass across the gas cell, the inlet mass flow rate Q_{in} [kg/s] should be equal to the outlet mass flow rate:

$$Q_{\mathrm{in}} = \rho_0 \cdot Q_V = \frac{p_0 M_{\mathrm{gas}}}{RT} \cdot Q_V, \tag{5.11}$$

The operational temperature T of the gas cell is an input parameter of the simulation which is fixed to the room temperature 293.15 K. For a specified nozzle throat diameter d and a constant temperature T, various targeted stagnation pressures within the gas cell can be obtained by modifying the inlet mass flow rate.

The temperature parameter T does not enter the Navier-Stokes equations, its role is limited to defining the values of the material properties. Coupling the Navier-Stokes problem with a heat-transfer problem is however possible, which allows the inclusion of the temperature values from a dedicated simulation. The effect of temperature gradients is however a higher-order refinement of the simulations of the gas cell performance, therefore simply giving the temperature as a constant input parameter is sufficient for this work.

The simulation results can be re-injected as input parameters to other COMSOL simulations, or they can be saved to a file and used with other simulation programs, such as SIMION [Dah00] with the Statistical Diffusion Simulation model [AD05], which requires the gas velocities, pressures and temperatures to be given as input arrays. The conversion of data from COMSOL to SIMION can be facilitated using a program, as detailed in Section 5.3.3.

5.2.2 Electric and magnetic fields

Computing the shape and strength of the electromagnetic fields requires solving Maxwell's equations [Fai14] using certain boundary conditions given by the gas-cell and electrode geometry together with the applied voltages and currents. Both COMSOL and SIMION have the capability to solve these equations for given configurations of electrodes and coils. In the absence of magnetic fields in our case, Poisson's equation, as a simplified form of Maxwell's equations for static DC fields, is solved:

$$\nabla \cdot (\varepsilon_0 \varepsilon_r \mathbf{E}) = \rho_c \tag{5.12a}$$

$$\mathbf{E} = -\nabla V \tag{5.12b}$$

where $\mathbf{E}$ is the electrical field strength, V is the electrical scalar potential, ρ_c is the charge density and $\varepsilon_{0,r}$ are the vacuum and relative electrical permittivity of the medium. Substituting Eq. (5.12b) in Eq. (5.12a) gives Poisson's equation:

$$\nabla^2 V = \frac{\rho_c}{\varepsilon_0 \varepsilon_r} \tag{5.13}$$

If no charges are present, Eq. (5.13) becomes Laplace's equation:

$$\nabla^2 V = 0 \tag{5.14}$$

The fact that each software can perform its own calculations means that no data exporting will be necessary.

5.2.3 Plasma creation for neutralization

Plasma is a special phase of ionized gas that generally consists of free electrons, positively charged ions, and neutral particles (atoms, molecules, radicals). The abundance of free electrons in the plasma makes it a suitable electron source for ion neutralization in our gas cell. For our purpose, plasma can be created through two primary methods: decay source irradiation and electrical discharge. In our work, we have studied the use of a beta source because it can be procured in sealed form for large activities and versions (like ^{90}Sr) exist without gamma emission, which makes it safer to operate.

Beta source irradiation allows control of the ionization by directing high-energy beta particles to argon gas within the neutralization tube. By positioning the beta source with adequate source activity near the tube entrance, plasma is created as sufficient quantities of free electrons and ions are produced through the ionization of gas atoms. The degree of ionization and the characteristics of the resulting plasma depend on the energy and intensity of the beta particles and the pressure of the argon gas. These processes need to be investigated through both simulations and experimental tests to optimize the plasma generation for enhanced neutralization efficiency.

A number of models have been developed in recent years to describe and simulate plasma, ranging from detailed particle-based kinetic models [BL18, TMST07], which provide a detailed description of particle distributions and collisions, to more simplified fluid models [Bra65, Che12] that offer a macroscopic, averaged perspective of the collective plasma behavior. Instead of solving the high-dimensional, nonlinear Boltzmann equation, the fluid models rely on a set of continuum equations, including continuity, momentum and energy conservation equations. These equations describe the collective behavior of the plasma by averaging over the microscopic details and focusing on bulk properties such as density, velocity, and temperature, thereby providing computational efficiency and capturing essential plasma dynamics. The choice of the model depends on the

specific properties of the plasma and the phenomena being studied.

In our study, the discharge generated in argon gas through continuous beta source irradiation is characterized as a weakly ionized, non-thermal, low-temperature plasma within the gas flow. As the high-energy beta particles travel through the gas, they lose energy primarily through ionization and excitation of the argon atoms. These processes result in the generation of secondary electrons and metastable atoms which can further ionize other atoms. The betas continuously transfer energy to the gas to sustain the plasma. To develop a high-density electron source through gas discharge, our study focuses on the collective properties of plasma within a multiphysics framework, specifically equilibrium electron density and electron energy, which significantly influence the ion neutralization rate. To achieve this, the COMSOL Plasma Module [COM], which implements fluid models using continuum-based finite element methods to simulate plasma in the multiphysics environment including gas flow and electrical fields, has been chosen for our plasma simulation.

In the COMSOL Plasma interface, distinct fluid equations are used to simulate electrons and heavy species due to the substantial differences in their physical properties, behavior, and interactions within the plasma. In the weakly-ionized, low-temperature plasma, the concentration of ions and electronically excited species is much lower than that of the ground state atoms and they can be considered diluted. The free electrons typically have a much higher temperature up to several eV, compared to the heavy species (ions and neutrals), which remain near ambient temperature [Che12, Bal88]. Given this dilute and 'cold' nature of the heavy species, the plasma can be effectively modeled without explicitly solving energy equations for these species. As a result, a comprehensive model self-consistently solves the continuity, momentum and energy conservation equations along with the Poisson's equation for the rapid dynamics, energy distribution and interactions of the free electrons. For heavy species, a simpler fluid model that neglects the ion energy and focuses on mass transport and chemical reactions provides a sufficiently accurate and effective representation.

In the drift-diffusion model used in COMSOL for plasma simulations, the continuity equations governing the electron number density n_e are:

$$\frac{\partial n_e}{\partial t} + \nabla \cdot \mathbf{\Gamma}_e = R_e - (\mathbf{u} \cdot \nabla) n_e \tag{5.15}$$

where R_e is the source coefficient that quantifies either a growth or decay of electron density, summing over the contributions of all electron-involved reactions. $\mathbf{u}$ is the fluid velocity vector computed from a Laminar Flow Interface and used as input for the Plasma Interface. $\mathbf{\Gamma}_e$ is the electron flux vector, which is derived from the momentum conservation and expressed as:

$$\mathbf{\Gamma}_e = -n_e \mu_e \mathbf{E} - D_e \nabla n_e \tag{5.16}$$

where μ_e and D_e are the electron mobility and diffusion coefficients. $\mathbf{E}$ is the electric field calculated by Poisson's equation Eq. (5.12), where the charge density ρ_c is given by $e(n_i - n_e)$:

$$\nabla \cdot (\varepsilon_0 \varepsilon_r \mathbf{E}) = e(n_i - n_e) \tag{5.17}$$

with e being the elementary charge, n_i the ion number density.

The first term on the left-hand side of Eq. (5.15) describes the time evolution of electron density, the second term is the divergence of the electron flux which accounts for the drift (migration) of electrons due to the electric field and the diffusion due to concentration gradients. On the right-hand side, the electron production rate R_e allows the inclusion of the effect of reactions yielding or consuming electrons such as ionization and excitation, and the convection term arises from the gas flow affecting local electron densities. The local energy approximation is used and simplifies the modeling by using the local mean electron energy to parameterize transport and source coefficients. The equations governing the electron energy density n_ε are:

$$\frac{\partial n_\varepsilon}{\partial t} + \nabla \cdot \mathbf{\Gamma}_\varepsilon + \mathbf{\Gamma}_\varepsilon \cdot \mathbf{E} = S_{en} - (\mathbf{u} \cdot \nabla) n_\varepsilon \tag{5.18}$$

$$\mathbf{\Gamma}_\varepsilon = \frac{5}{3}(-n_\varepsilon \mu_e \mathbf{E} - D_e \nabla n_\varepsilon) \tag{5.19}$$

where $\mathbf{\Gamma}_\varepsilon$ is the electron energy flux vector, S_{en} is the energy loss/gain due to inelastic collisions. The mean electron energy $\bar{\varepsilon}$ in electronvolts, is computed through the expression:

$$\bar{\varepsilon} = \frac{n_\varepsilon}{n_e} \tag{5.20}$$

The mixture-averaged diffusion model in COMSOL Plasma Module provides an effective description of the heavy species transport in the multicomponent plasma. For heavy species i, the continuity equation is expressed in terms of mass fraction w_i, which helps to avoid dealing with very large or very small numbers that can occur when working with number densities, particularly in systems characterized by a wide concentration range, such as those involving dilute species. The governing equation is:

$$\rho \frac{\partial w_i}{\partial t} + \rho(\mathbf{u} \cdot \nabla) w_i = \nabla \cdot \mathbf{j}_i + R_i \tag{5.21}$$

where ρ denotes the density of the mixture, R_i is the net production or consumption rate of the species i due to chemical reactions or other processes. $\mathbf{j}_i$ is the diffusive flux vector of species i, which is defined as:

$$\mathbf{j}_i = \rho w_i \mathbf{V}_i \tag{5.22}$$

where $\mathbf{V}_i$ is the multicomponent diffusion velocity for species i, the definition of which

depends on the chosen diffusion model. If the mixture averaged model is chosen, $\mathbf{V}_i$ is given by:

$$\mathbf{V}_i = D_i^m \frac{\nabla w_i}{w_i} + D_i^m \frac{\nabla M_n}{M_n} - z_i \mu_i \mathbf{E} \tag{5.23}$$

where D_i^m is the mixture averaged diffusion coefficient for species i, M_n is the mean molar mass of the mixture, z_i is the charge number, μ_i^m is the mixture averaged mobility, $\mathbf{E}$ is the electric field vector. Equations 5.21, 5.22 and 5.23 provide a comprehensive description of the heavy species transport in the plasma, including contributions from convection with gas flow, diffusion due to concentration gradients and molar mass gradients, and migration in electric field. Thermal diffusion is neglected here, given the low temperature of the heavy species in our case. By putting $R_i = 0$ in Eq. (5.21) for a specific species i, one obtains an equation that can describe the transport of an initial ion cloud in the gas under the action of the gas flow and electrical fields, which allows for the extraction of the residence time of the species in the tube.

The behavior of particles at boundaries such as wall or outlet must be accurately simulated to get meaningful results. In the other words, equations solved for the transport for each species need to be supplemented by appropriate boundary conditions. For the grounded wall, the boundary condition is:

$$V = 0 \tag{5.24}$$

The normal component of the electron flux at the boundary is given by:

$$\mathbf{n} \cdot \mathbf{\Gamma}_e = \frac{1 - r_e}{1 + r_e} \left(\frac{1}{2} v_{e,th} n_e + n_e (\mu_e \cdot \mathbf{E}) \cdot \mathbf{n} \right) - \sum \gamma_j (\mathbf{\Gamma}_j \cdot \mathbf{n}) \tag{5.25}$$

where $\mathbf{\Gamma_e}$ is given in Eq. (5.16). r_e is the reflection coefficient (typically 0), $v_{e,th}$ is the thermal velocity, γ_j is the secondary electron emission coefficient which defines the average number of electrons emitted per ion impact, $\mathbf{\Gamma_j}$ is the ion flux of the jth positive ion species at the wall. Correspondingly, the normal component of the electron energy flux at the boundary is:

$$\mathbf{n} \cdot \mathbf{\Gamma}_\varepsilon = \frac{1 - r_e}{1 + r_e} \frac{5}{3} \left(\frac{1}{2} v_{e,th} n_\varepsilon + n_\varepsilon (\mu_e \cdot \mathbf{E}) \cdot \mathbf{n} \right) - \sum \gamma_j \bar{\varepsilon_j} (\mathbf{\Gamma}_j \cdot \mathbf{n}) \tag{5.26}$$

No secondary emission was taken into account in my simulations so the last terms in Eq. (5.25) and Eq. (5.26) are 0. Ions are assumed to stick to the metallic wall upon contact. The sticking boundary condition can be mathematically expressed as:

$$\mathbf{\Gamma}_i \cdot \mathbf{n} = 0 \tag{5.27}$$

5.2.4 Ion motion in the gas environment

The ions traversing the gas cell are subject to two key processes:

1. Extraction in the cage and funnel regions: Ions are extracted by the DC electric field within the buffer gas environment with stagnation pressure varying between 100 and 500 mbar.
2. Neutralization in a no-field tube: The ions that survive the extraction process enter a neutralization tube, where they are transported through the plasma present within. Interaction with free electrons facilitates recombination processes, leading to the neutralization of the ions as they move through the tube.

Accordingly, our simulation of the ion motion is divided into two distinct stages:

1. The initial stage focuses on simulating ion extraction without accounting for the neutralization process. The primary objective here is to optimize ion extraction performance and ensure sufficient residence time of the ions in the neutralization tube.
2. After achieving optimized geometry, the second stage involves the ion motion in the plasma created in the tube. This stage aims to investigate the ion transport and interactions in the gas, enabling a detailed study of the neutralization process.

In the following, we will discuss the two-stage studies conducted to gain a comprehensive understanding of ion behavior in response to the two distinct gas environments: neutral gas and plasma.

5.2.4.1 Ion flying in the DC field in the presence of gas

In the DC field region, ions evolve under the combined action of the acceleration by the electrical field and of collisions with the background buffer gas. While explicitly modeling the ion-neutral collisions alongside the electrical forces can capture all relevant dynamics, this approach is only practical within a primary vacuum regime, typically at pressures below or around 1 mbar. However, at the 100 - 500 mbar pressure of interest in this study, the computational time required to explicitly model the collisions becomes prohibitive.

Collisions between ions and the buffer gas give rise to two primary phenomena that significantly affect the ions trajectories and behavior. The first one is the drag force, which is a continuum effect emerging from the relative motion between the ion and the gas atoms. The second one is the diffusion phenomenon which causes ions to spread out along the concentration gradient. In the presence of an electric field, diffusion adds a random component to the ion's trajectory, causing deviations from the deterministic path resulting from the electric and drag force.

In fluid mechanics, the drag force can be described using models like Stokes' Law for spherical particles in a viscous fluid. For ions in buffer gas, the drag force can be expressed as:

$$\mathbf{F}_{\text{drag}} = -m\delta(\mathbf{v} - \mathbf{u}) \tag{5.28}$$

where m is the mass of the ion, δ is the damping(or drag) coefficient. $\mathbf{v}$ is the ion velocity, $\mathbf{u}$ is the gas flow velocity. In a stationary gas environment, $\mathbf{u}$ is zero, simplifying the drag force to $\mathbf{F}_{\text{vis}} = -m\delta\mathbf{v}$. In the presence of an electric field, the drag force on an individual ion balances the electric force $\mathbf{F}_{\text{e}} = q\mathbf{E}$, where q is the charge of the ion and $\mathbf{E}$ is the electric field. The equilibrium (or drift) velocity of an ion is determined by the condition:

$$\mathbf{F}_{\text{e}} + \mathbf{F}_{\text{vis}} = 0 \tag{5.29}$$

Solving for the drift velocity $\mathbf{v}_{\text{drift}}$:

$$\mathbf{v}_{\text{drift}} = \frac{q}{m\delta}\mathbf{E} = K\mathbf{E}, \tag{5.30}$$

where K is by definition the ion mobility, often expressed as:

$$K = K_0 \frac{T/T_N}{P/P_N}, \tag{5.31}$$

with K_0 the so-called reduced mobility [MM73], which is constant for an ion species and buffer gas type at low kinetic energies. T and P are the absolute gas temperature and pressure, while $T_N = 273.15$ K and $P_N = 1$ atm denote the standard conditions.

To compute ion trajectories in the gas cell, a standard approach is to neglect for simplicity the ion-ion interaction and solve the equation of motion for each ion, accounting for all forces acting upon it. To have a statistical analysis of ion behavior, aiding in the evaluation of the gas cell's transport efficiency and extraction times, a sufficient quantity of ions must be flown in the simulation.

COMSOL and SIMION are both equipped to model electrical forces, which is an inherent feature of both programs. Moreover, they can both incorporate drag force as a user-defined force. Consistent modeling of these deterministic forces is therefore possible across both platforms. At the first stage of geometry and voltage setting optimization in COMSOL, to expedite the numerous modifications, the diffusion effect is not considered. The COMSOL simulation of the deterministic ion trajectories involves a stationary study for the electric fields and gas flow using the Electrostatics Interface and the Laminar Flow Interface (see Section 5.3.2). A following time-dependent study for ion tracing is performed using the Charged Particle Tracing interface (see Section 5.3.3), with the results from the stationary calculation serving as input parameters, such as the electric field for determining the electric force and the pressure, temperature, and gas-velocity fields for calculating the ion mobility and the drag force. The optimized geometry,

voltage settings, and gas-velocity fields from COMSOL are transferred to SIMION for deterministic ion trajectories simulation (refer to Section 5.3.3), the agreement between SIMION and COMSOL validates the simulation methodology.

For the diffusion effect, the Charged Particle Tracing Interface in COMSOL only favors the simulation of individual collisions, which is computationally prohibitive in the pressure range of interest. The Statistical Diffusion Simulation (SDS) model [AD05] in SIMION offers a more efficient approach by treating diffusion as a statistical process, where the diffusion is interpreted as a random walk of ions deviating from deterministic trajectories. It is observed that after a sufficiently high number of collisions with the buffer gas atoms, the average displacement λ_N of an ion from its starting position, is proportional to the square root of the number of collisions N:

$$\lambda_N \propto \sqrt{N} \tag{5.32}$$

This relationship holds even when the ion mass differs significantly from the buffer gas atoms. In the pressure regime of interest, the collision rate is sufficiently large so that the condition of a large number of collisions is satisfied for one integration step.

The implementation of the SDS model relies on precomputed statistical distributions of scattering radii derived from extensive Monte Carlo simulations. These simulations cover a broad range of mass ratios between ions and buffer gas molecules, providing comprehensive distributions of unit-normalized scattering radii R_{N_0} after numerous ($N_0 = 10^5$) collisions. For each integration step, the SDS model uses these data to linearly interpolate the scattering radius for the specific ion-gas mass ratio. The expected number of collisions N_1 for each step is determined by considering the integration step duration, local pressure, and gas temperature. The physical scattering radius λ_{N_1} for N_1 collisions is:

$$\lambda_{N_1} = R_{N_0} \cdot \sqrt{\frac{N_1}{N_0}} \cdot \lambda_0(P, T) \tag{5.33}$$

where R_{N_0} is the unit-normalized scattering radius after 100,000 collisions, $\lambda_0(P, T)$ is the mean free path of the ion at the given pressure and temperature conditions. The unit-normalized scattering radius is converted to a radius in units of length by multiplying it with the mean free path of the ion. For each integration step, after computing the trajectory using the deterministic forces, the SDS model induces a jump of the ion in a random direction by the scattering radius determined for the given step as described above.

5.2.4.2 Ion transport and neutralization in plasma

After being extracted by the DC electric field in the cage and funnel region in the gas cell, the surviving ions enter the plasma created in the no-field neutralization tube, where they can potentially recombine with the free electrons. The efficiency of the

neutralization process is contingent upon the residence time of the ions in the tube and the plasma properties, particularly the distributions of equilibrium electron number density and energy density. In the simulation to evaluate the neutralization performance of the created plasma, a group of $^{133}Cs^{+}$ ions with a Gaussian profile, characterized by specified radius and depth dispersion, is released near the entrance of the tube. The transport of $^{133}Cs^{+}$ ions in plasma can be effectively simulated by equations 5.21, 5.22, 5.23 and 5.27. By recording the time-dependent concentration of the ions and Cs atoms created from recombination reaction, the neutralization efficiency can be characterized.

In an argon gas discharge, the neutralization of atomic ions involves multiple channels, the specific prominence of which depends on plasma properties such as pressure, temperature, and the number density and the energy density of free electrons. The primary mechanisms involved in the neutralization of an atomic ion X^{+} are as follows [Fri08]:

1. Radiative recombination: this non-resonant, one step recombination process occurs when a free electron is captured by a positive ion, emitting excess energy in the form of a photon:
$$X^{+} + e^{-} \rightarrow X + h\nu \tag{5.34}$$

2. Three-body recombination: in this mechanism, a positive ion recombines with a free electron with the aid of a third body, usually a neutral gas atom B, which carries away the excess energy. The third body stabilizes the recombined system through collision:
$$X^{+} + e^{-} + B \rightarrow X + B \tag{5.35}$$

3. Dissociative recombination: in this process, a free electron with kinetic energy is attracted to a weakly bounded molecular ion, typically a positive diatomic ion, such as XB^{+}, due to electrostatic forces, where X^{+} can be an ion of interest or a buffer gas ion [F^{+}04], and B is a buffer gas atom. The electron capture results in the formation of a highly excited intermediate Complex. The energy gained from the recombination of an electron with a molecular ion is typically greater than the bond dissociation energy of a molecule. As a result, the $(XB)^{*}$ complex rapidly dissociates into neutral fragments, which may also be in excited states:
$$e + XB^{+} \rightarrow (XB)^{*} \rightarrow X + B \tag{5.36}$$

The radiative recombination is favored in low-density environments due to fewer collisions between particles. In contrast, three-body recombination is predominant in high-density plasmas where frequent collisions between particles facilitate the process. Dissociative recombination is the fastest electron neutralization mechanism in gases with the presence of molecular ions [Fri08]. All these mechanisms play a role when the ions pass through the neutralization tube and will be modeled by COMSOL Plasma Module. Further

details are provided in Section 5.3.5.

5.3 Prototype simulations

5.3.1 General considerations

The simulations of the FRIENDS^3 gas-cell prototype are constrained by a variety of factors: project objectives, the capacity of the S^3-LEB vacuum chamber holding the gas cell, the accuracy and ease of the simulation software in modeling physical phenomena, and the practical feasibility of laboratory implementation. In addition, at the current stage, the prototype design is constrained by the necessity for simplicity, even at the expense of some extraction efficiency. For instance, the current prototype utilizes a pure DC guiding field despite its efficiency limitations compared to RF fields. The potential for enhancing efficiency through the inclusion of RF fields will be evaluated in subsequent stages of the project. For the same reason, all studies so far have been conducted in 2D models assuming cylindrical symmetry, which significantly reduces the computational time required for a 3D model.

There are several optimization goals for the performance of the gas cell:

1. Short extraction time: to extend the laser spectroscopy study to short-lived S^3 products, the particle extraction time from the entry to the exit of the gas cell should be targeted to approximately 100 ms, or preferably less.
2. Maximized extraction efficiency: the extraction efficiency of the particles of interest should be optimized to the highest possible level, ensuring that extraction losses are less than decay losses during the extraction time.
3. Free electron generation for neutralization: A robust mechanism should be developed to generate a stable electron cloud of sufficient equilibrium density in the gas flow before the ions exit. The risk of electrons leaving the neutralization zone rapidly due to the electric field should be avoided.
4. Adequate neutralization time: the neutralization process is estimated to take at least a few tens of milliseconds. Adequate residence time for the ions in the electron cloud should be ensured before extraction.

All these goals need to be comprehensively considered and balanced when they cannot be satisfied simultaneously, such as between achieving short ion extraction time and ensuring adequate neutralization time.

The total length of the gas cell is constrained by the available space in the S^3-LEB vacuum chamber, taking into account that the S-RFQ would most likely be redesigned. Furthermore, the S^3 beam enters the gas cell through a dedicated inlet window with a diameter of 74 mm, adapted to the S^3 beam size in convergent mode. Ideally, we would maintain the window holder design and by this also maintain a broad acceptance.

The standard diameter of the gas cell exit hole is 1 mm and can be increased up to a maximum of 2 mm, the latter being the limit from the available pumping capacity.

The typical S^3 beam in convergent mode has a radius of about 20 - 30 mm and the longitudinal straggling in the argon gas spreads the stopped ions longitudinally over 10 mm. In the present simulations, the initial particle release distribution in the stopping volume takes into account the realistic beam shape and depth. For the existing argon-filled gas cell, the ion distribution within the stopping volume has been calculated for several S^3 beams with different entrance window thicknesses and operating pressures ranging from 100 to 500 mbar. Based on these beam dimension characterization calculations, our simulations assume that ions are released in a 3D Gaussian distribution, with depth dispersion of $\sigma_z = 5$ mm and radius dispersion of $\sigma_r = 10$ mm.

COMSOL is chosen for the first stage of geometry design and performance optimization, taking into account the simplicity of modifying the geometry and the accuracy of the multiphysics simulation based on finite element analysis (FEA) [Zim06]. In general terms, the prototype has been designed to have two functional sections:

1. An electric field applied region for the fast extraction. DC field is created in this region through sets of voltage-decreasing electrodes. By optimizing the voltage setting, the ion extraction time can be minimized and the ions can also be focused and deflected to avoid losses on the cell walls and electrodes. See details in Section 5.3.2.

2. A long, no-field region following the electric field region and preceding the exit for efficient neutralization of ions. In this region, ion transport is slowed down and governed exclusively by gas flow. Additional high-density electron generation will be incorporated in this volume for effective neutralization. The length of this region should be optimized considering both the extraction time and the residence time of ions within this volume.

The prototype geometry and operating parameters (i.e. pressure, voltage configuration) are optimized in COMSOL without considering diffusion effects, since it is not possible to simulate collisions at high pressure on an individual basis during the optimization process. The diffusion is then re-coupled via SIMION with the design and gas flow from COMSOL as input parameters.

For the experimental validation of the simulation results, the construction of test setups has been ongoing simultaneously with the simulation work. Considering manufacturing challenges and the cost of parts, the optimal design of the prototype has to be fine-tuned. Two practical versions will be presented in Section 5.3.4.

5.3.2 Geometry design and optimization, stationary multiphysics simulation

The initial geometry of the gas cell prototype was constructed with COMSOL using a 2D axisymmetric model for efficient optimization. The design features a cylindrical prototype with total length and radius constrained by the capacity of the S^3-LEB vacuum chamber holding the gas cell, as depicted in the left panel of Fig. 5.1. The region where the electric field is applied includes two sets of electrodes [Wad13]: the cage, which comprises five identical cylindrical electrodes, and the funnel, which consists of five electrodes with progressively decreasing diameters. The exit of the funnel is connected to a long cylindrical tube where no electric field is present, tapering gradually towards its end to facilitate a seamless connection with the de Laval nozzle.

All the simulation work is performed with $^{133}Cs^+$ due to its well-known reduced ion mobility, $k_0(^{133}Cs^+) = 2.1$ cm^{2}V^{-1}s^{-1} [AD05], and its planned use for the subsequent experimental verifications. The argon gas is added as a user-defined material in COMSOL by specifying two material properties: dynamic viscosity $\mu = 2.26 \times 10^{-5}$ Pa·s [HH11], and pressure-dependent density $\rho(p) = 1.664$ kg/m$^3 \cdot p/(1$ atm). It should be noted that the simulations for optimization are conducted in fine meshing [COM] for high optimization efficiency without seriously sacrificing the accuracy of the physics interpretation. In the ultimate stage of the simulation work, the mesh size is adjusted to extremely fine for more accurate results.

To comprehensively simulate the behavior of ions within the electric field and their interactions with the argon gas flow, three physics interfaces in COMSOL were utilized. The simulation is structured into two studies:

1. Stationary study: this study involves the calculation of gas flow and electric field using two interfaces:
   - Laminar Flow interface models the gas flow assuming pure argon gas in a laminar flow regime. Given the Mach number limit (M < 0.3) imposed by this interface, the simulation domain covers the entire subsonic gas volume, except the region 2 mm before the nozzle throat where the gas velocity approaches sonic levels.
   - Electrostatics interface simulates the static electric field generated by applied voltages on electrodes.
2. Time-dependent study: building on the gas flow and electric field distribution from the stationary study, this study utilizes the Charged Particle Tracing interface to simulate the time-dependent trajectories of ions under the electric force and the drag force exerted by the argon gas flow. Rather than explicitly modeling the drag force for individual collisions, a Stokes-type viscous damping force was defined as an effective drag force, as stated in section Section 5.2.4.

The diffusion effect is not considered in COMSOL.

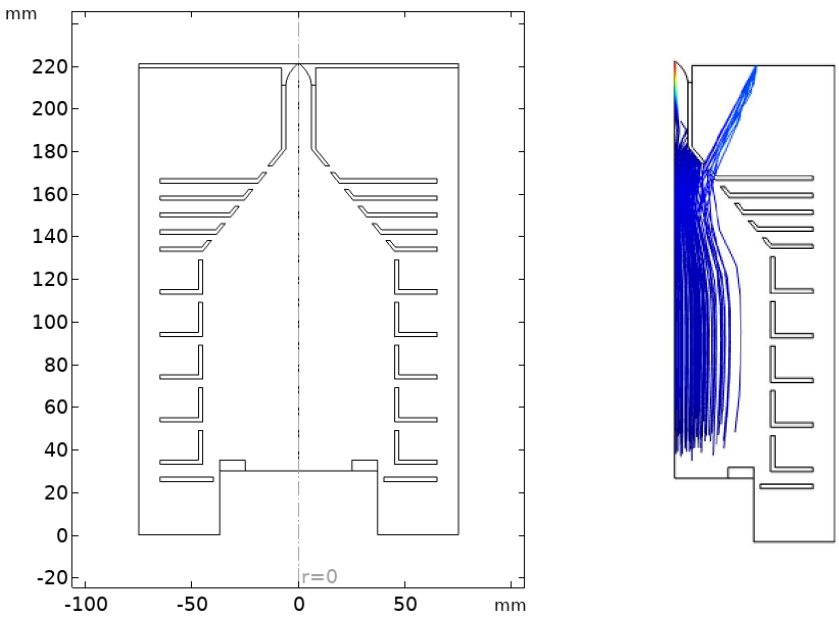

Fig. 5.1. Left: the 2D schematic diagram of the initial cylindrical prototype geometry, illustrating the key components: the cage, the funnel and the neutralization tube before the exit, and their respective placements. Right: the simulated ion extraction performance of this initial geometry with a preliminary voltage setting.

The right panel of Fig. 5.1 illustrates the trajectories of 1000 $^{133}Cs^{+}$ released in the stopping volume of the initial geometry with a preliminary voltage setting on the cage and funnel. The depiction shows only half of the geometry due to cylindrical symmetry. The simulation indicates that less than 10% of the released ions reached the exit, with an average extraction time of 200 ms. The ion trajectories reveal significant losses primarily due to the distribution divergence at the stopping region, leakage between electrodes, and collisions with the wall at the entrance of the neutralization tube. In light of these issues, extensive modifications and optimizations were made to the prototype's dimensions and construction to improve ion extraction efficiency and reduce extraction time. The key optimizations, following the order from the inlet (window) to the outlet (the nozzle throat) of the prototype, are listed below:

- The diameter of the prototype was decreased and voltages applied to the window/window ring and the cage electrodes were optimized to orient the electric field isopotential line in the stopping volume region towards the axis of the cell. The final optimized field is illustrated in Fig. 5.6. This configuration converges the released ions in the stopping volume via electric forces directed towards the axis of the cylindrical prototype, significantly reducing ion loss due to collisions with the electrodes and the narrow tube, thereby improving extraction efficiency.

- The number of funnel electrodes was increased and the distance between the funnel electrodes was decreased to prevent ions from escaping between the electrode gaps, ensuring more efficient guidance of ions towards the exit.
- The voltage step between the funnel electrodes was increased to create a stronger electric field, thereby accelerating the extraction process. The optimized voltages on the electrodes were first estimated using a point field assumption, as illustrated in Fig. 5.2. This method involves calculating the voltages that should be applied to each funnel electrode, based on the known voltage on the last cage electrode and the approximate distance of the funnel electrodes to the center of the point field at the entrance of the neutralization tube. Fine-tuning of these values was then performed to achieve optimal performance, ensuring the electric field effectively guides and focuses the ions to enter the neutralization tube.

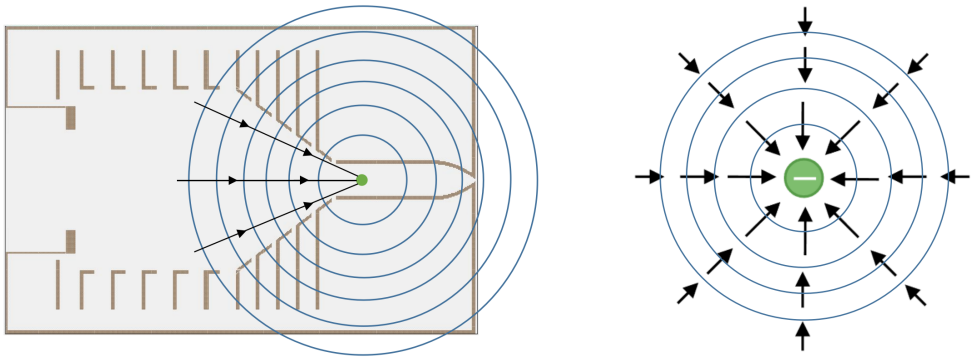

Fig. 5.2. The point field method for optimizing the voltages on the last cage electrode and the funnel electrodes.

- The neutralization tube was segmented at its entrance to avoid a sudden disappearance of the electric field, which could cause ions to be attracted to the tube wall. By gradually reducing the voltage on the segmented rings to 0 V along the tube wall, the significant loss of ions due to attraction on the tube entrance is mitigated.
- In the first phase of optimization using COMSOL, the length of the neutralization tube was increased, and the radius was optimized to achieve an average ion residence time in the tube, denoted as T_N (ms) in this chapter, of approximately 50 ms. This was done while ensuring the total length of the prototype remains within the spatial constraints of the S^3-LEB gas cell chamber. Further refinement needs to consider the diffusion effects using SIMION, as diffusion losses primarily occur in the neutralization tube. Consequently, the final optimized dimensions of the tube were determined by achieving a balance between extraction efficiency, the total extraction time and the time available for neutralization (T_N).

It is important to note that focusing ions within the stopping volume prior to their movement toward the exit can significantly enhance the extraction efficiency. However,

this process can be time-consuming, particularly for ions positioned at the edges of the distribution, which may take tens of milliseconds to migrate toward the center before extraction.

Additionally, while the long neutralization tube is beneficial for efficient neutralization, it increases the ion residence time in the cell. The optimization of the dimensions and configurations made a compromise between the different tendencies. The optimized design is represented in both 3D and 2D schematics in Fig. 5.3.

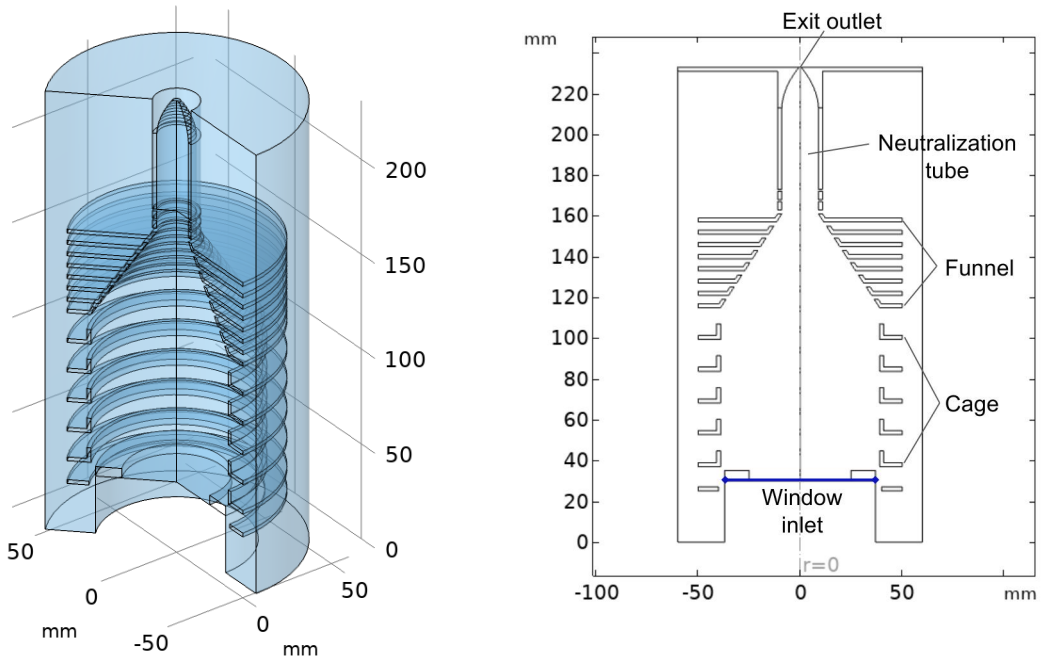

Fig. 5.3. Optimized geometry of the prototype: 3D model (left) and 2D schematic (right).

To simulate the properties of the gas flow in the optimized geometry through the Laminar Flow interface, an inlet and outlet of the simulation volume need to be defined. In the simulation work reported in this thesis, the argon gas is set to enter the gas cell homogeneously through the 74 mm diameter inlet window and exit through the 1 mm hole. The simulation inlet is shown on the right of Fig. 5.3 as a blue line. In the real gas cell, a lateral gas inlet would be used, but the cylindrical symmetry cannot represent such an inlet. Nevertheless, for the scope of the simulation (and not considering turbulence), using the window as the inlet is sufficient because it provides an accurate representation of the gas flow close to the neutralization tube, where the gas flow starts to influence the ion motion. As stated in Section 5.2.1, the pressure of the gas cell can be regulated by varying the inlet mass flow rate Q_{in} (kg/s). The performance of the designed gas cell has been simulated for 50 - 500 mbar pressure

in steps of 50 mbar. A pressure of 100 mbar is expected to provide a good working condition for the gas cell featuring a 1 mm diameter of the nozzle throat, balancing fast extraction and sufficient efficiency. For gas flow simulation at different stagnation pressures, the input parameter Q_{in} was calculated by Eq. (5.11). The simulated gas velocity distribution at 100 mbar is shown on the left of Fig. 5.4, with the window as the inlet and the 1 mm hole as the outlet.

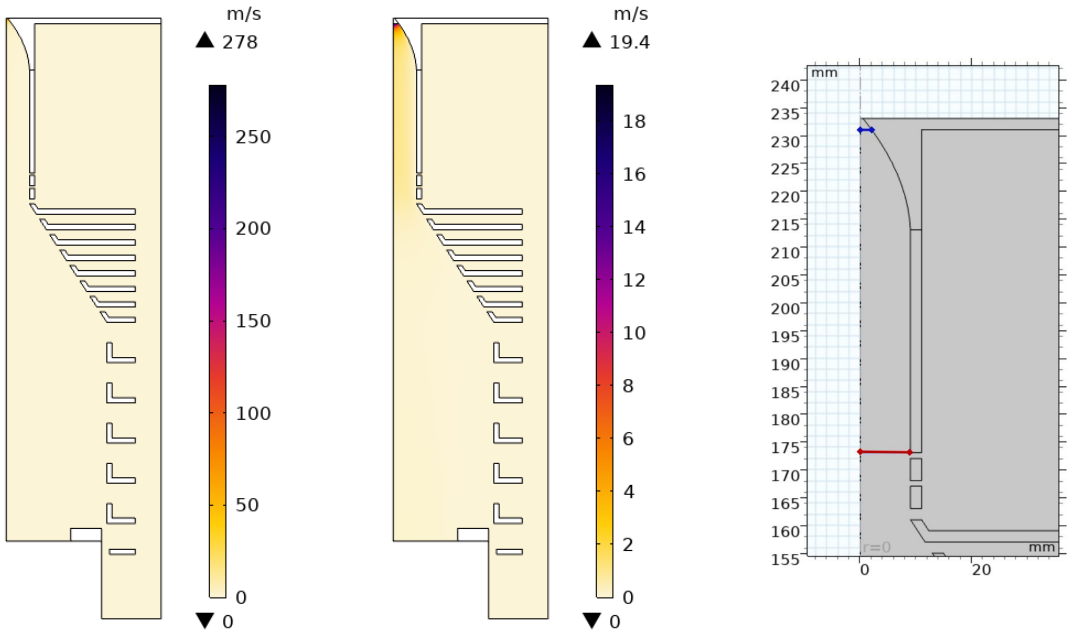

Fig. 5.4. Gas velocity distribution resulting from the Laminar Flow study with the real and virtual outlets chosen for the simulation volume. Left: using the 1 mm real exit. Middle: using a virtual outlet 2 mm before the real exit as the simulation outlet. The maximum and minimum values of the presented gas velocities are indicated at the top and bottom of the legend. Right: Geometry detail shows the new outlet 2 mm below the exit hole, indicated by the blue line. Cylindrical symmetries apply.

One notices in Fig. 5.4 that the resulting velocity near the exit hole is almost 300 m/s, which exceeds the Mach number limit ($M < 0.3$) of the Laminar Flow interface. To address the problem, a new outlet 2 mm before the real exit, is chosen to restrict the simulation volume, as shown on the right of Fig. 5.4 by the blue line. The volume flow rate through the new outlet calculated by Eq. (5.10) is used as the outlet boundary condition. The stagnation gas density and pressure within the redefined simulation volume, calculated using the Laminar Flow interface for a target pressure of 100 mbar, are presented in Fig. 5.5.

The optimization of the electric field with the electrostatic interface is also essential for optimizing the gas cell's performance. A stronger electric field in the prototype facilitates faster ion extraction. However, it is crucial to constrain the voltage difference between electrodes to prevent high-voltage breakdown [Fai14], which occurs in regions

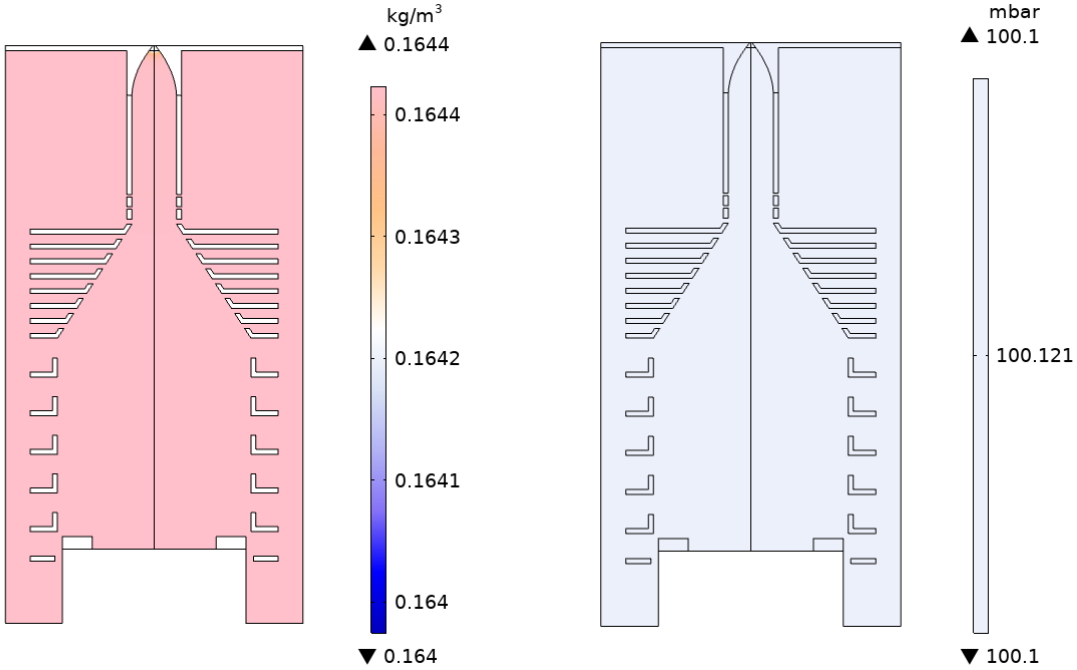

Fig. 5.5. Stagnation gas density (left) and pressure (right) within the redefined simulation volume, calculated using the Laminar Flow interface for a target pressure of 100 mbar.

of excessively high electric field strength due to the avalanche process. The breakdown voltage of a gas between two electrodes depends on the electron mean free path, the distance between the electrodes, and the dimensions of the electrodes. Specifically, for two flat electrodes in argon, the Paschen curve provides the breakdown voltage as a function of the product of gas pressure and the distance between the electrodes [T$^+$12b].

In our design, the voltage between electrodes has been limited to 80 V to maintain safe operational limits and prevent breakdown. Initially, a low-voltage version with a maximum electrode voltage of approximately 260 V was developed, as depicted on the left in Fig. 5.6. This diagram shows the electrodes with individually applied voltages and presents the resulting electric field described by potential contours as colored curves. In a subsequent design phase, a high-voltage version with a maximum electrode voltage of 386 V was proposed, as shown on the right of Fig. 5.6. As illustrated by the potential contours, in both configurations, the electric field has been aligned with the desired ion trajectory, ensuring minimum ion losses. The optimized low- and high-voltage settings for the electrodes are detailed in Table 5.1.

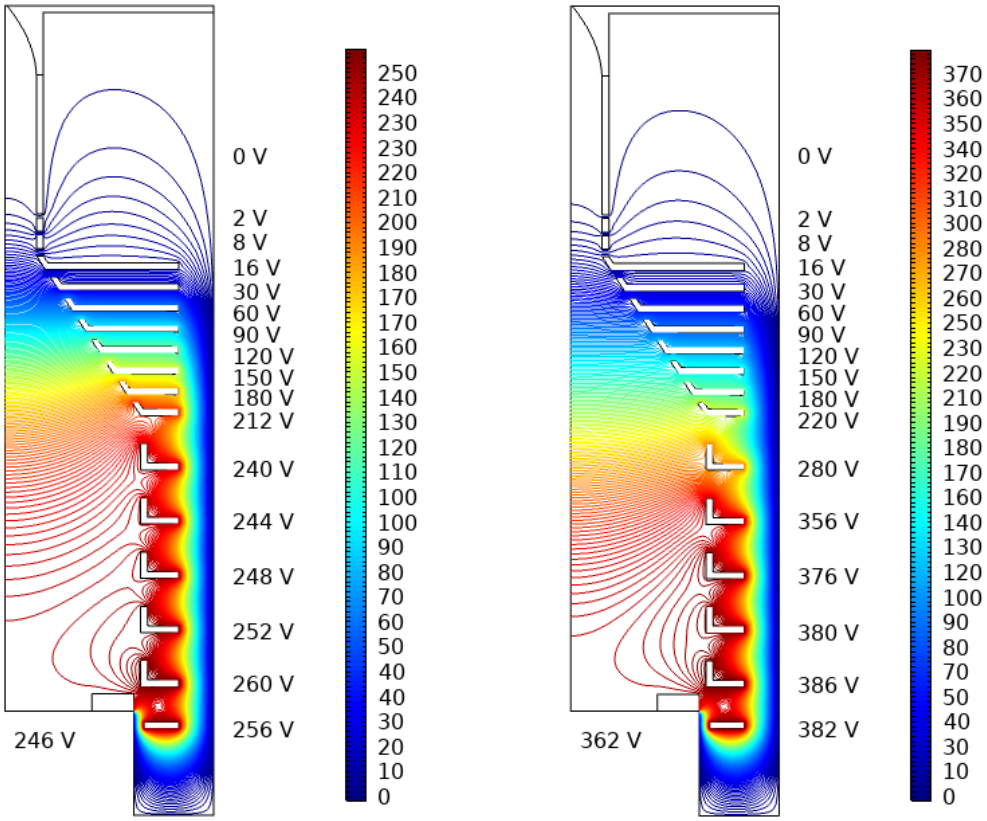

Fig. 5.6. Optimized low (left) and high (right) voltage settings for the gas cell, showing the electric field as potential contours. The low-voltage configuration has a maximum electrode voltage of approximately 260 V, while the high-voltage configuration reaches up to 386 V.

Table 5.1 – Optimized voltage settings for the low/high-voltage version.

No.	Component	DC voltage (V)		No.	Component	DC voltage (V)	
		LV	HV			LV	HV
1	Window/ring	246	362	10	Funnel 3	150	150
2	Cage disk	256	382	11	Funnel 4	120	120
3	Cage 1	260	386	12	Funnel 5	90	90
4	Cage 2	252	380	13	Funnel 6	60	60
5	Cage 3	248	376	14	Funnel 7	30	30
6	Cage 4	244	356	15	Funnel 8	16	16
7	Cage 5	240	280	16	Tube segment 1	8	8
8	Funnel 1	212	220	17	Tube segment 2	2	2
9	Funnel 2	180	180	18	Tube segment 3	0	0

5.3.3 Simulation of the ion motion

The Charged Particle Tracing physics interface in COMSOL was employed to simulate the time-dependent motion of ions within the gas cell. The secondary time-dependent study utilized the gas properties and electric field distribution obtained from the preceding stationary study as input parameters. Ions were tracked taking into account the drag force and the electric force acting on them during their flight. In this study, the $^{133}Cs^{+}$ ions, assumed to be thermal and without initial velocity, were introduced in the expected stopping volume within the prototype. These ions were distributed according to a Gaussian profile, characterized by a 10 mm radius dispersion and a 5 mm depth dispersion, to replicate a typical S^3 beam.

To determine the ion extraction efficiency and extraction time, two `Particle Counters` from the COMSOL Particle Tracing Module were used. By selecting domain or boundary elements as counters, the number of particles arriving at the selected locations as well as their arrival times are recorded. The positions of the counters in this study are indicated by the red and blue lines in the right panel of Fig. 5.7. One counter is placed

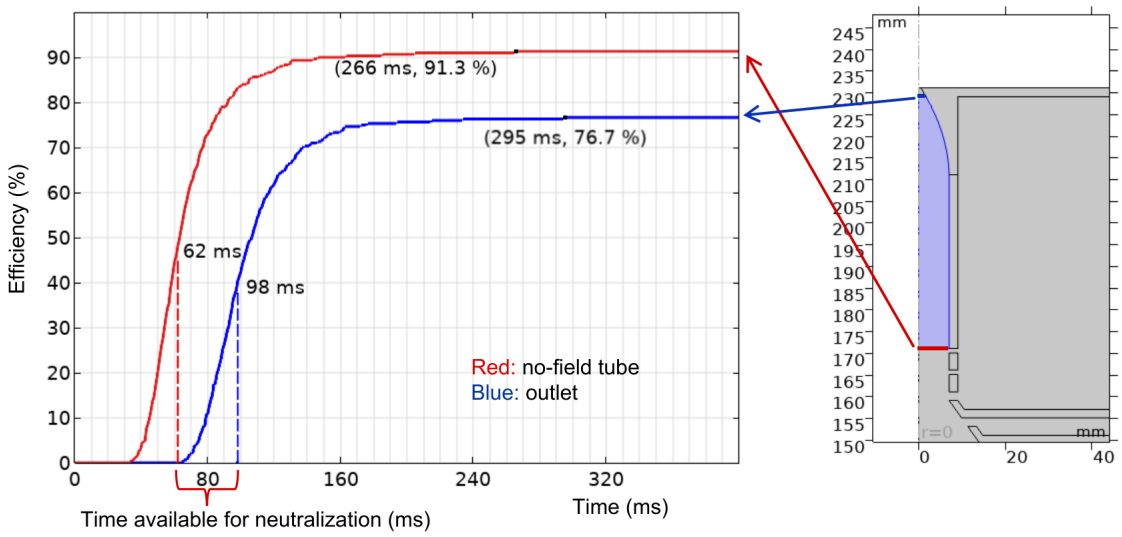

Fig. 5.7. COMSOL simulation to quantify the extraction performance of the optimal design. The plot shows the fraction of ions arriving at defined particle counters as a function of elapsed time from their release for the low-voltage settings at 100 mbar pressure. The maximum value of the curves shows the transmission efficiency and the dashed lines at the half maximum indicate the median arrival times of the particles crossing the two counters. The red curve shows that 91% of the particles arrive at the no-field tube region in 266 ms with a median arrival time of 62 ms, and the blue curve presents that 77% of the particles are extracted from the gas cell in 295 ms with a median time of 98 ms. The ions' average residence time in the neutralization tube is around 36 ms.

at the entrance of the neutralization tube to record particles entering the no-field region, while the other is positioned at the virtual outlet to record particles exiting through the outlet.

The left panel of Fig. 5.7 displays the number of particles arriving at the tube entrance and the virtual outlet over time, represented by red and blue curves, respectively. These simulations were performed for the optimized low-voltage design at 100 mbar. The maximum values of the two curves indicate the efficiencies in the sense of the gas cell performance. The residence time of the ions in the neutralization tube (volume between the two particle counters) represents the time available for neutralization (T_N), which can be determined by the difference between the median times of flight (ToF) of the particles through the two counters.

The efficiency values presented in COMSOL simulations are not yet fully representative of the actual performance of the prototype due to the absence of diffusion effects. The diffusion effect will be statistically simulated using the SDS module in SIMION [MD11]. The geometry constructed in COMSOL was mathematically implemented in SIMION via a GEM file with a resolution of 0.1 mm/grid unit. The SDS module requires an array of gas velocities as input, which was provided based on the COMSOL stationary study using the finest meshing possible.

Since COMSOL employs irregular mesh elements (triangular or quadrilateral for 2D geometries), whereas SIMION uses uniform square (2D) grids, a Python script utilizing the "griddata" class from the "scipy.interpolate" module was employed to linearly interpolate to equidistant grid values from the mesh-based values generated in COMSOL. The gas velocity field converted using Python to a 0.1 mm grid compatible to SIIMON is depicted in Fig. 5.8. The same voltage settings were used in SIMION as in COMSOL, with the electrostatic fields computed and stored in potential arrays.

The $^{133}Cs^+$ ions were released with the same initial Gaussian profile as in COMSOL. In addition to the mobility of $^{133}Cs^+$, which serves as an input parameter for the SDS model, the radii of the $^{133}Cs^+$ ion and of the argon atom are also required. These radii are necessary to estimate the collision cross section and the corresponding collision frequency. For Ar, a recent value from the literature was used, $r_{Ar} = 0.17$ nm [KGBT22]. For $^{133}Cs^+$, the radius was automatically calculated by the SDS module based on the user-provided mobility.

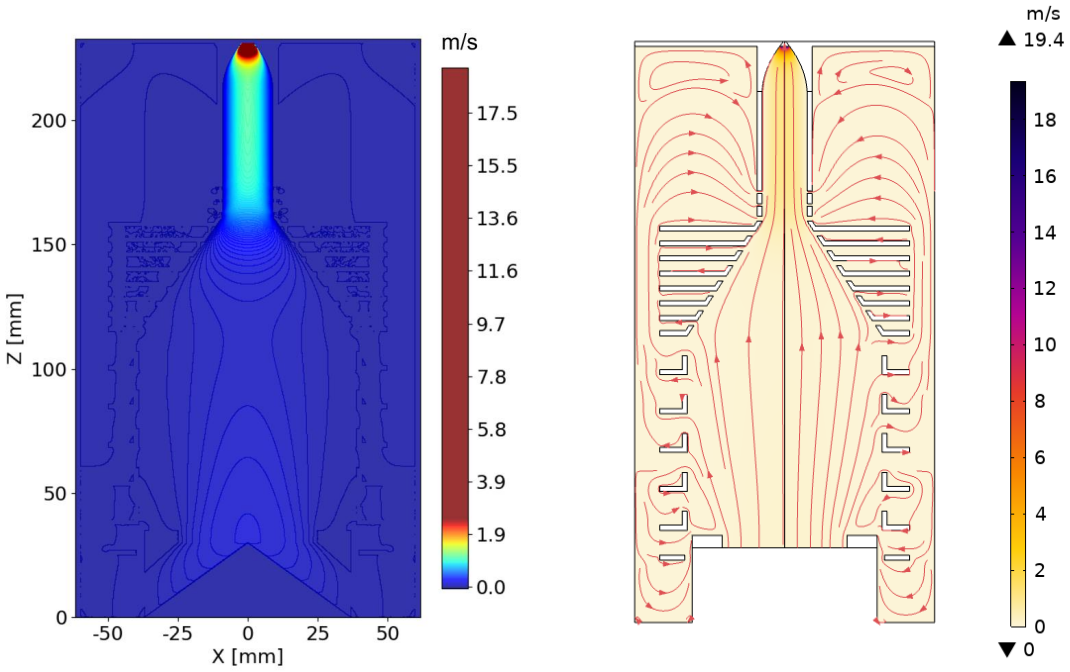

Fig. 5.8. Left: Gas velocity field with a 0.1 mm grid resolution converted using Python from the COMSOL mesh-based gas flow calculations to a SIMION-compatible array. Right: the corresponding COMSOL result.

Figure 5.9 presents the ion trajectories simulated with the high-voltage version prototype at 100 mbar using both COMSOL and SIMION. The left panel displays 200 $^{133}Cs^{+}$ trajectories, 300 ms after their release, which are calculated by COMSOL in the absence of diffusion effects. The red dots indicate ion collisions with the wall, demonstrating that the primary losses occur due to ion attraction at the window and at the entrance of the tube. The right panel represents 1000 $^{133}Cs^{+}$ trajectories calculated by SIMION, with and without the inclusion of diffusion effects. The incorporation of diffusion introduces a stochastic component to the trajectories, resulting in an increased ion beam cross-section and consequently increasing ion losses within the narrow neutralization tube.

The performance of the designed low-voltage settings was simulated by both COMSOL and SIMION at different pressures from 50 mbar to 500 mbar, by steps of 50 mbar. Fig. 5.10 represents the simulated extraction efficiency and average extraction time at different stagnation pressures. Several observations can be made from the plots:

- In the absence of diffusion, the extraction time is largely influenced by the drag force experienced by the ions, which is affected by the gas pressure. According to Eq. (5.30) and Eq. (5.33), ion mobility, and thus ion drift velocity, are inversely proportional to the pressure. Therefore, higher pressure results in a longer time for the ions to pass through the cage area and be extracted.
- Higher pressure leads to a stronger drag force at the entrance of the no-field

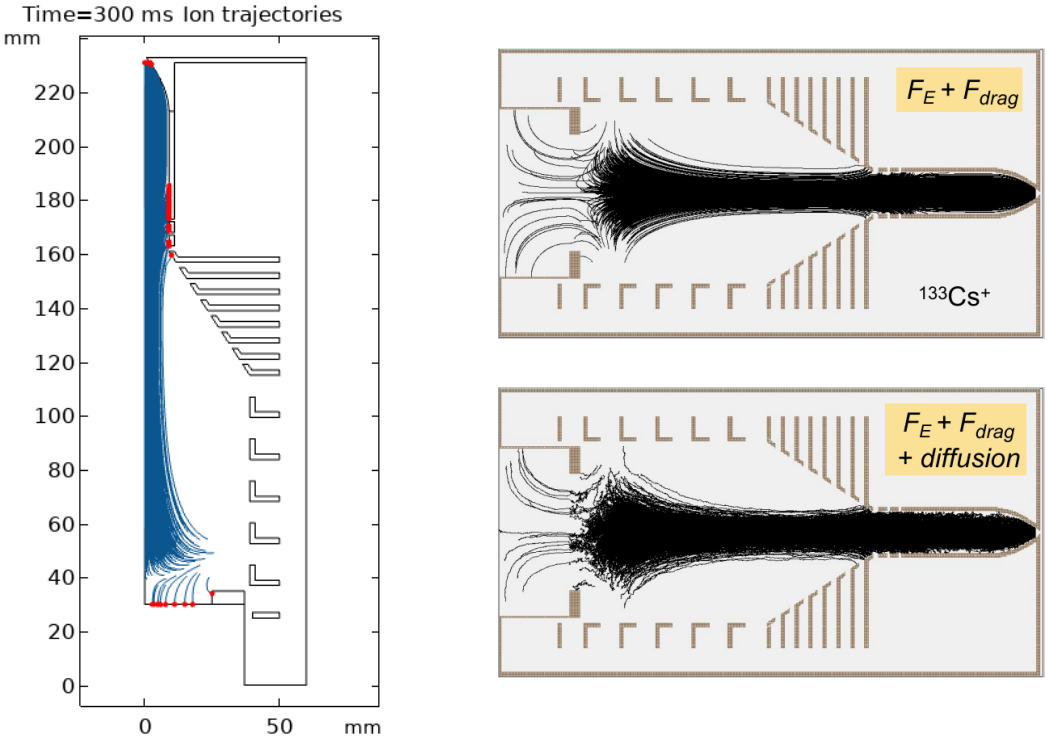

Fig. 5.9. $^{133}Cs^+$ ion trajectories simulated with the high-voltage settings at 100 mbar. Left: COMSOL simulation without diffusion. Right: SIMION simulations without (top) and with (bottom) diffusion effects.

area, where both residual electric fields and gas convection affect ion movement. In this region, ions experience substantial losses due to electrical forces guiding them towards the tube wall. A stronger drag force provides greater resistance to these electrical forces, resulting in fewer ion losses at the tube entrance. Similarly, higher pressure enhances the drag force against ion movement towards the window, further reducing ion losses through this channel.

- While diffusion affects efficiency, it does not significantly alter the total residence time of ions within the cell. The extraction times derived from both COMSOL and SIMION simulations, with or without diffusion effects, are remarkably consistent. In addition, the extraction efficiencies calculated by COMSOL and SIMION without considering diffusion, indicated by the blue and yellow curves on the top plot, were quite comparable. These consistencies validate the integrated simulation methodology, which combines the strengths of COMSOL for rapid geometry adjustments and gas flow calculations with SIMION for diffusion modeling during particle tracing.

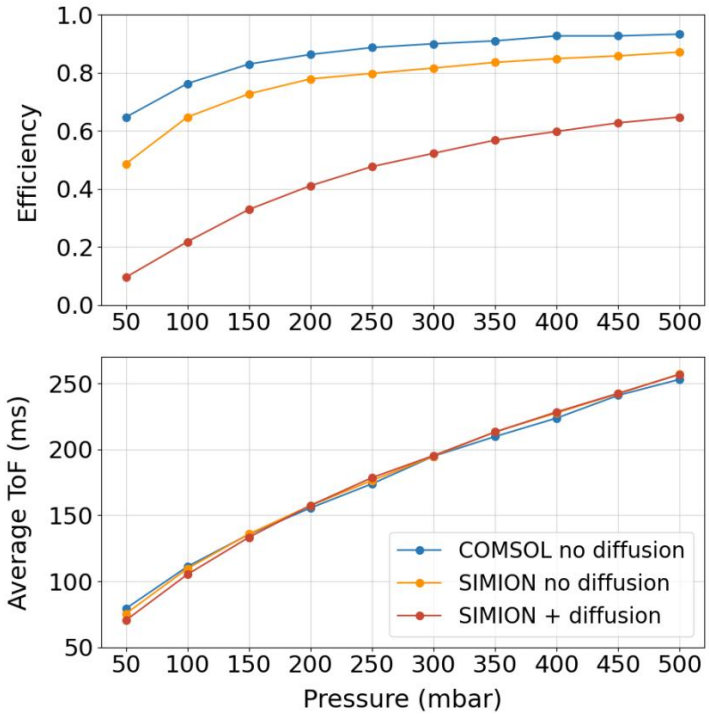

Fig. 5.10. Simulated extraction efficiency (top) and average extraction time (bottom) for the low-voltage settings as functions of pressure obtained from COMSOL without diffusion effects in blue curves and SIMION with/without diffusion effects in red/orange curves.

The performance of the designed prototype, with both low- and high-voltage configurations, was systematically evaluated using SIMION across a pressure range from 50 mbar to 500 mbar by steps of 50 mbar. Fig. 5.11 represents the comparative analysis between the two configurations in terms of extraction efficiency (top panel), average time of flight (middle panel), and average time available for neutralization (bottom panel). The solid curves represent the results at the simulation outlet while the dashed curves show the results at the tube entrance. The red curves represent the high-voltage prototype, while the blue curves correspond to the low-voltage configuration. The following conclusions can be drawn from the simulations:

1. The enhanced electric field in the high-voltage prototype enables a more rapid extraction, approximately 50 ms faster, but with a sacrifice in extraction efficiency by roughly 5%. This trade-off becomes more significant at higher pressures.
2. The residence time of the ions in the neutralization tube, which is considered as the time available for neutralization (T_N), is nearly equivalent for both the high- and low-voltage prototypes. This observation is consistent with the fact that the ion extraction in the tube only relies on the gas flow, where the gas velocities are a function of stagnation pressures but independent of the electric field strength.

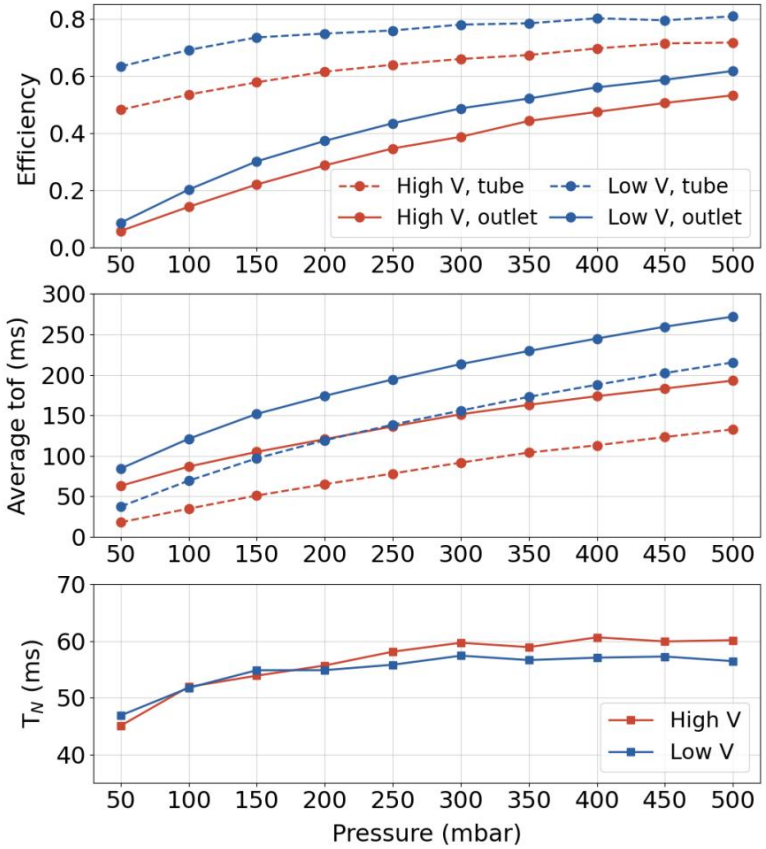

Fig. 5.11. Simulated SIMION results for the performance of the designed gas cell as a function of pressure. (Top) Extraction efficiency. (Middle) Extraction time. (Bottom) Residence time of the ions in the no-field tube, which is the difference between the continuous and dashed lines for each set of voltages shown in the middle panel. The preliminary design guarantees more than 50 ms for neutralization under all simulated pressures $\geq$ 100 mbar.

3. At 100 mbar, around 14% of the particles reach the outlet with an average ToF for 87 ms of the high-voltage settings, with an ions' average residence time in the neutralization tube of 52 ms. This indicates satisfactory performance in accordance with the predefined objectives, whereas at 200 mbar, the extraction efficiency can be doubled with an extraction time of around 120 ms. Table 5.2 lists the results at the possible working pressures.

Table 5.2 – Performance of the low/high-voltage prototypes at expected working pressures.

Pressure (mbar)	Prototype	Efficiency	Average ToF (ms)	T_N (ms)
100	HV	14 %	87	52
	LV	20 %	121	52
150	HV	22 %	105	54
	LV	30 %	152	55
200	HV	29 %	121	56
	LV	37 %	174	55

The diameter of the nozzle throat is another sensitive parameter that can highly influence the performance of the prototype. Fig. 5.12 illustrates the comparison between 1 mm and 0.8 mm throat diameter for the high-voltage prototype.

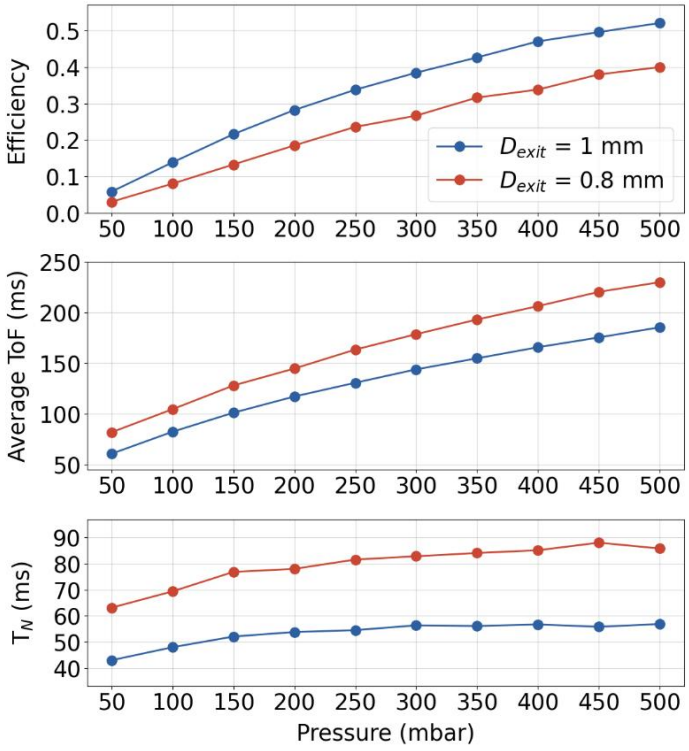

Fig. 5.12. SIMION simulation of the performance obtained with the high-voltage settings versus pressure for different exit hole diameters.

It can be concluded that a smaller throat diameter leads to less efficiency and longer extraction time at the same pressures, however, relatively more time available for neutralization can be achieved. To ensure sufficient residence time of ions in the neutralization tube during the development of a feasible neutralization technique, a

smaller exit hole size was employed in the preliminary experimental tests.

The beams of radioactive ions, discussed in the context of the designed gas cell, are typically fusion evaporation residues. The stopping position of the ions, i.e. the particle release position in the current simulations, depends on their incident energies and mass, the window thickness and the pressure of the gas cell. Therefore the performance of the designed prototypes may also vary from case to case due to the variation of the stopping position. In all the previous simulations, the initial distribution of the ions was taken with a size comparable to a typical S^3 beam in convergent mode and to be centered at coordinate $z = 50$ mm. It would be interesting however to also study how the extraction efficiency and time depend on the exact particle stopping position. In this case, instead of a wide ion distribution corresponding to the full S^3 beam, a much narrower ion distribution was released from different starting positions at 100 mbar for the optimized low-voltage settings. In each run, 10^4 $^{133}Cs^+$ ions at rest were released from a 3D Gaussian distribution with $\sigma_z = 1$ mm and $\sigma_r = 2$ mm centered at different (z, r) coordinates, the efficiency and extraction time were thus determined. The resulting contour maps are shown in Fig. 5.13, from which the optimal stopping volume for high efficiency and fast extraction can be estimated. For ions stopped at coordinate $z = 43$ - 50 mm, the electric field exhibits the most pronounced convergence effect on the ions. Ions situated deeper and closer to the axis experience more rapid extraction.

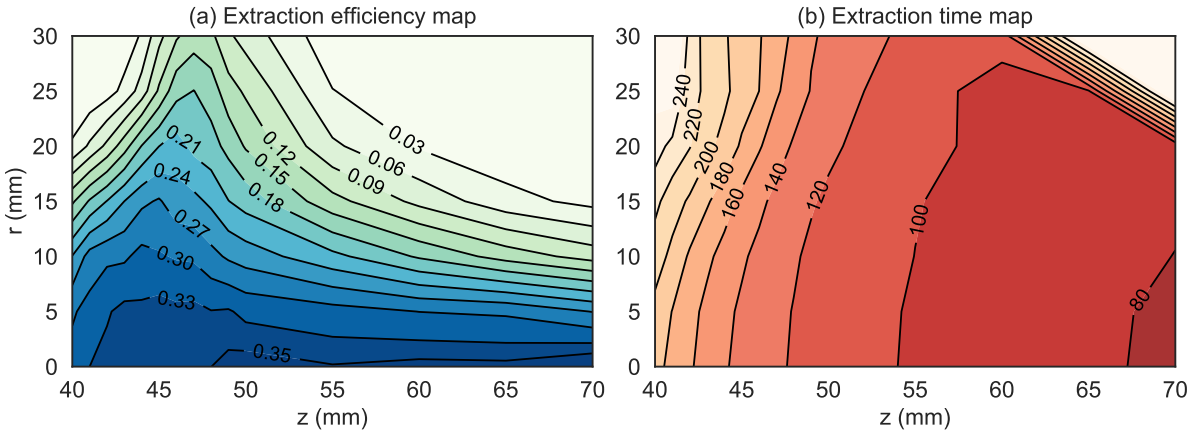

Fig. 5.13. SIMION simulation of the extraction efficiency and time as a function of the position in the gas cell at which the ions are stopped. The results are presented as a contour map.

5.3.4 Practical versions of the prototype

The practical realization required modifications to the initial simulated design due to mechanical constraints, such as the cost and complexity of manufacturing and the need for adequate electrode mounting and spacing. The first version, shown in Fig. 5.14 on the right, has some differences from the idealized design on the left. The inner diameter of the cage electrodes was increased to prevent the stopped S^3 beam or the created plasma from approaching the electrodes. Furthermore, the number of funnel electrodes was decreased, and the segmented tube entrance was removed to simplify assembly and reduce manufacturing costs for electrodes of specific dimensions. The chamber size was increased to ensure appropriate distances between the electrodes and the ground, as well as the space for the supporting structures and cabling.

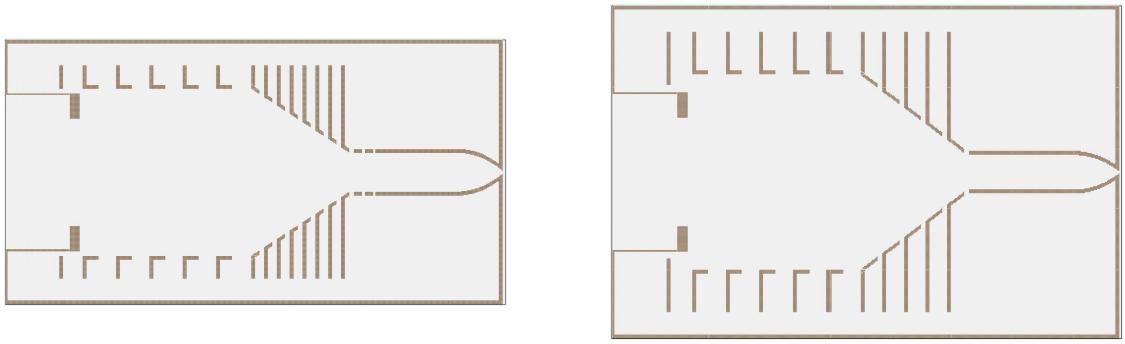

Fig. 5.14. Geometry comparison between the initially simulated version of the prototype (left) and the first practical realization (right), shown to scale.

New simulations were performed to quantify the impact of the applied changes. The newly optimized voltage settings and corresponding DC electric field of the practical design, represented as potential contours calculated by COMSOL, are shown on the left of Fig. 5.15. As before, the typical S^3 beam size is a Gaussian profile with a depth dispersion $\sigma_z = 5$ mm and a radius dispersion $\sigma_r = 10$ mm. However, in our experimental tests, $^{133}Cs^+$ ions are produced by evaporation from a heated tantalum filament installed in the gas cell. Laser ionization will be used for non-surface ionized species such as erbium (Er) following their evaporation from the filament. The ion beam size can be simulated according to the dimension of the filament, as a Gaussian profile with $\sigma_z = 3$ mm and $\sigma_r = 2.5$ mm. The right panel of Fig. 5.15 displays the trajectories of 10^4 Cs^+ ions in the modified prototype at 100 and 200 mbar, comparing the typical S^3 beam size with the beam size used in the off-line tests.

The performance of this first-version prototype has been evaluated using SIMION simulations at expected operational pressures of 100 mbar, 150 mbar and 200 mbar, considering the two different beam sizes. The extraction efficiency, the average ToF of the surviving ions, and the average time available for neutralization T_N are detailed in Table 5.3. A comparison of these results with those shown in Table 5.2 indicates that

this first practical prototype achieves performance comparable to that of the low-voltage initial design. Although the practical cell exhibits slightly higher extraction efficiency and maintains a similar time available for neutralization, it requires a longer extraction time.

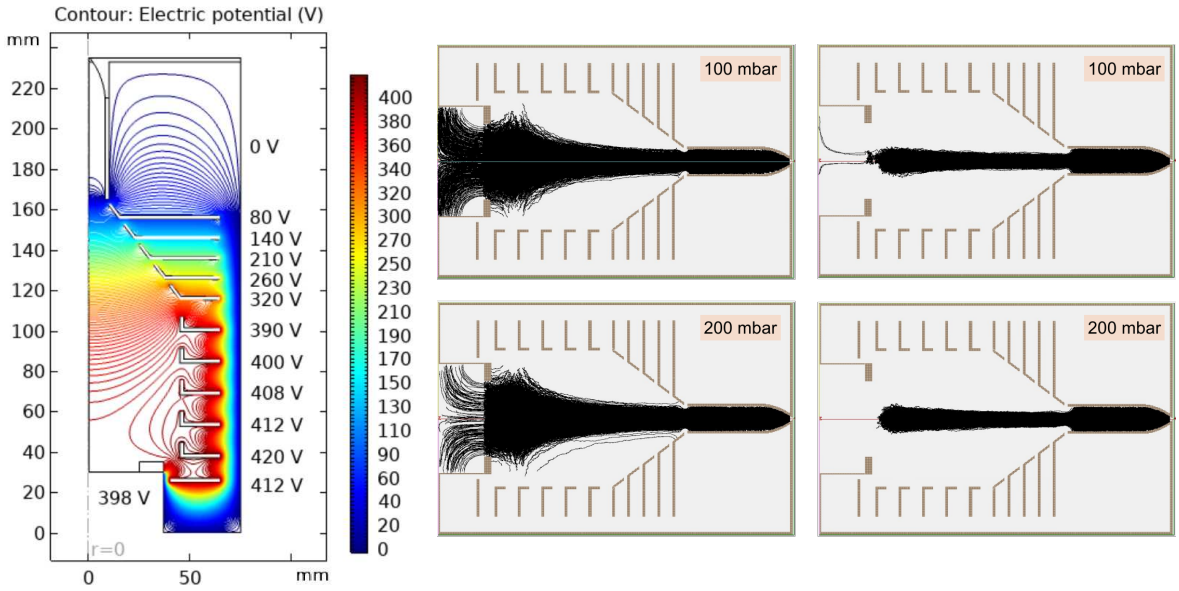

Fig. 5.15. Left: optimized voltage settings for the first practical prototype, showing the electric field as potential contours simulated by COMSOL. Right: SIMION simulation of the ion trajectories in this prototype at 100 and 200 mbar with beam sizes corresponding to S^3 in converging mode ($\sigma_z = 5$ mm, $\sigma_r = 10$ mm, center) and evaporation from a filament ($\sigma_z = 3$ mm, $\sigma_r = 2.5$ mm, center).

Table 5.3 – Performance of the first practical prototype presented in Fig. 5.15 at expected working pressures with beam sizes corresponding to S^3 in converging mode ($\sigma_z = 5$ mm, $\sigma_r = 10$ mm) and evaporation from a filament ($\sigma_z = 3$ mm, $\sigma_r = 2.5$ mm).

Beam size		100 mbar	150 mbar	200 mbar
$\sigma_z = 5$ mm $\sigma_r = 10$ mm	Efficiency (%)	15	24	32
	Ave. tof (ms)	98	124	140
	T_N (ms)	53	58	58
$\sigma_z = 3$ mm $\sigma_r = 2.5$ mm	Efficiency (%)	26	41	53
	Ave. tof (ms)	87	105	121
	T_N (ms)	48	50	50

In order to couple the gas cell to the test bench, an adapter flange was designed and built, which modified both the length and the contour of the neutralization tube during the offline tests. The gas-cell version with the adapter flange is depicted in Fig. 5.16. It is therefore necessary to characterize the diffusion losses due to the different dimensions

of the tube. The voltage setting has been optimized for the test bench ion beam, which is evaporated from the heated filament. The left panel represents the electric field calculated by COMSOL and the right panel shows the trajectories of 10^4 $^{133}Cs^+$ ions created with the filament-evaporated beam size at 100 mbar and 200 mbar. The performance of this prototype has been evaluated using SIMION, as listed in Table 5.4.

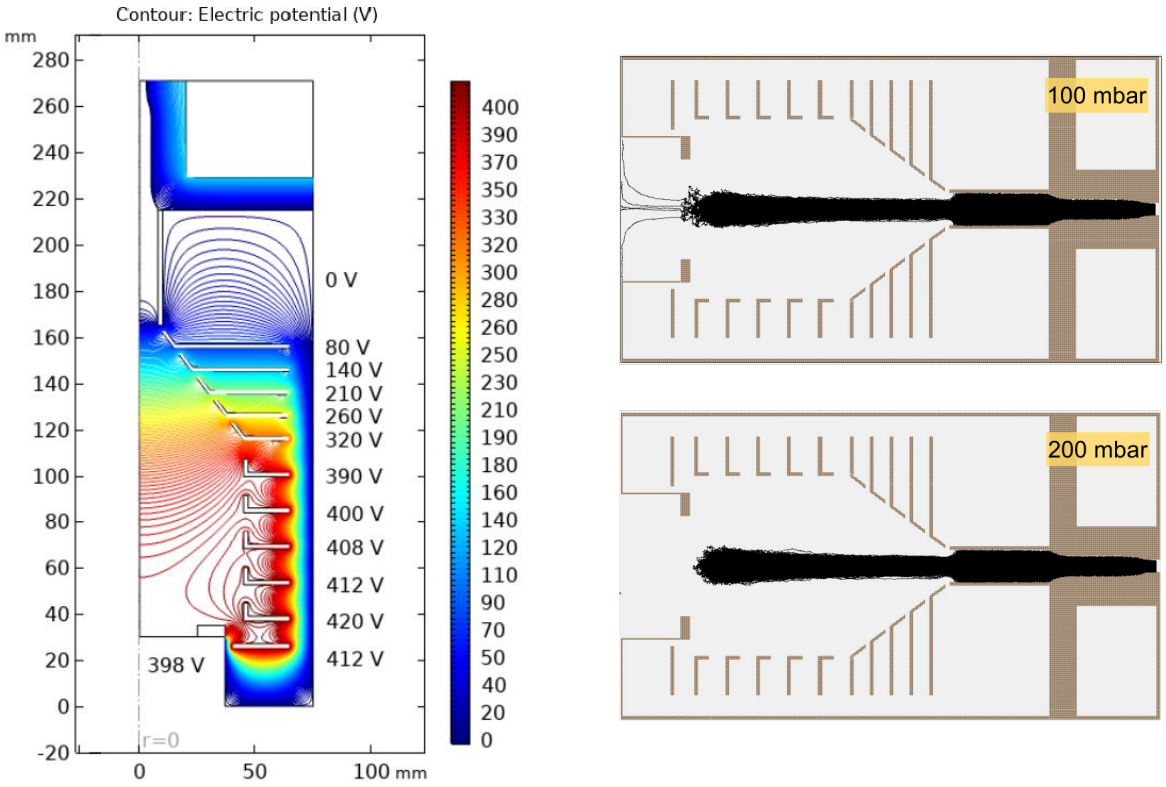

Fig. 5.16. Left: optimized voltage settings for the practical prototype adapted to the test bench, showing the electric field as potential contours simulated by COMSOL. Right: SIMION simulation of the ion trajectories in this prototype at 100 and 200 mbar with beam sizes corresponding to evaporation from a filament ($\sigma_z = 3$ mm, $\sigma_r = 2.5$ mm, center).

Table 5.4 – Performance of the first practical prototype at expected working pressures when using an adapter flange to the test bench with a beam size corresponding to evaporation from a filament.

Beam size		100 mbar	150 mbar	200 mbar
$\sigma_z = 3$ mm $\sigma_r = 2.5$ mm	Efficiency (%)	17.3	30.7	43.1
	Ave. tof (ms)	97.3	115.3	130.6
	T_N (ms)	62.5	63.9	64.1

In the versions of the prototype simulated so far, the cage diameter was only slightly larger than the S^3 beam cross-section in convergent mode. To prevent the stopped S^3 beam or the created plasma from approaching the cage and funnel electrodes, a final revision of the practical prototype was undertaken. The diameters of the cell chamber and the electrodes were increased to enlarge the stopping volume. This final version is depicted in Fig. 5.17.

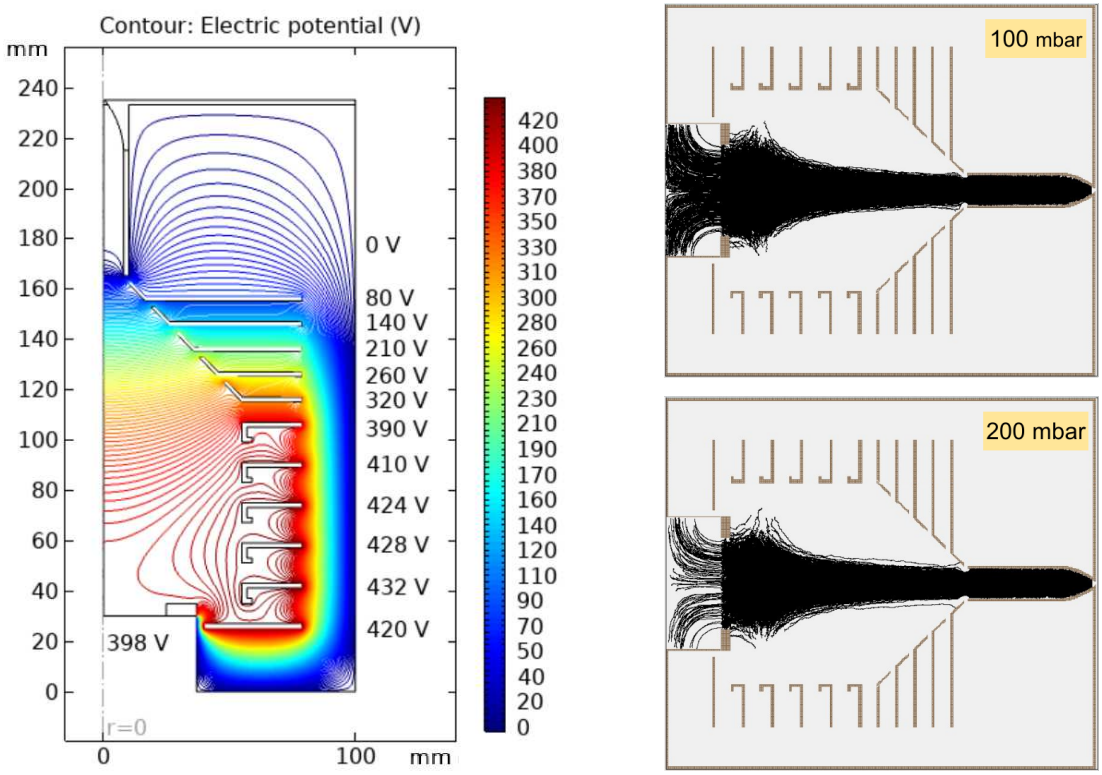

Fig. 5.17. Left: optimized voltage settings for the final version of the practical prototype, showing the electric field as potential contours simulated by COMSOL. Right: SIMION simulation of the ion trajectories in this prototype at 100 and 200 mbar with beam sizes corresponding to S^3 convergent-mode ($\sigma_z = 5$ mm, $\sigma_r = 10$ mm)

The voltage setting has been optimized for the S^3 beam size in converging mode. The left panel represents the electric field calculated by COMSOL and the right panel shows the trajectories of 10^4 $^{133}Cs^+$ ions with the $\sigma_z = 5$ mm, $\sigma_r = 10$ mm beam size at 100 mbar and 200 mbar. The performance of this prototype is listed in Table 5.5.

The performance of the current gas cell installed at S^3-LEB was simulated for a $^{254}No^+$ beam with a spatial spread of 7 mm ($\sigma \approx 2$ mm) [K$^+$16]. At a gas pressure of 500 mbar, with the beam stopped in the center of the cell, the simulations indicate an extraction efficiency of approximately 80 % and an extraction time of about 630 ms. At 100 mbar, the simulations indicate an extraction efficiency of the current gas cell of $\sim$ 20% and much longer extraction time.

Table 5.5 – Performance of the final practical prototype at expected working pressures with the S^3 convergent-mode beam size.

Beam size		100 mbar	150 mbar	200 mbar
$\sigma_z = 5$ mm $\sigma_r = 10$ mm	Efficiency (%)	14	22	29
	Ave. tof (ms)	93	115	132
	T_N (ms)	53	57	58

Before being installed at S^3-LEB, this final practical prototype will be tested on the test bench in advance with the filament evaporated beam. Fig. 5.18 shows the prototype incorporating a flange at the end of the neutralization tube and the trajectories of 10^4 $^{133}Cs^+$ ions with the $\sigma_z = 3$ mm, $\sigma_r = 2.5$ mm beam size at 100 mbar and 200 mbar.

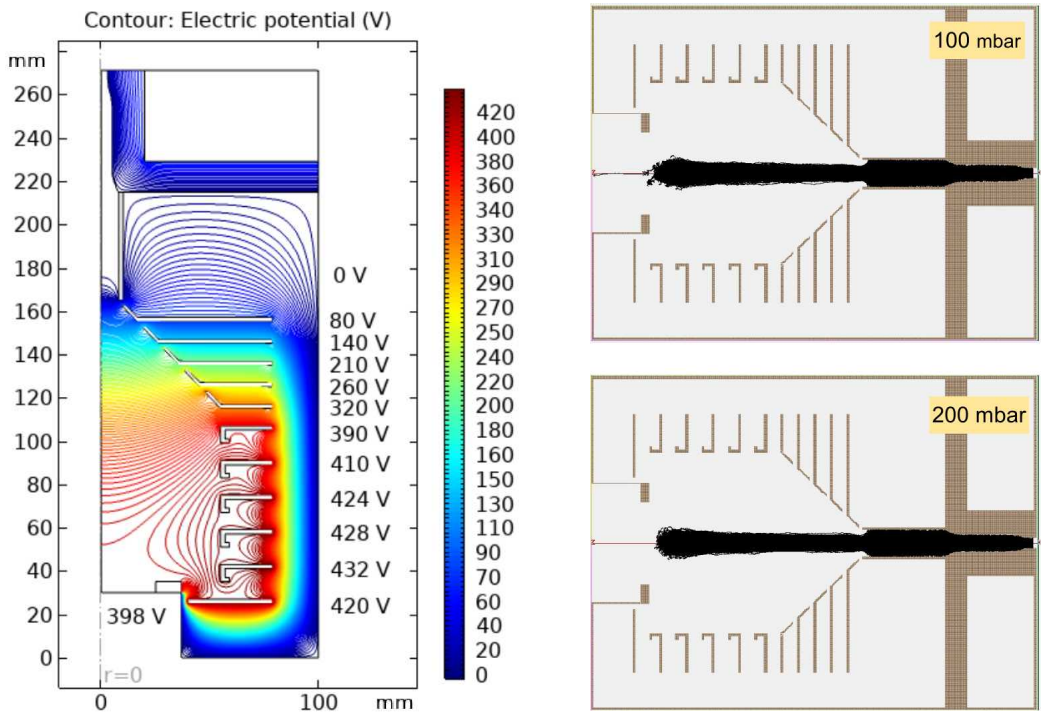

Fig. 5.18. Left: optimized voltage settings for the final version of the practical prototype, showing the electric field as potential contours simulated by COMSOL. Right: SIMION simulation of the ion trajectories in this prototype at 100 and 200 mbar with beam sizes corresponding to evaporation from a filament ($\sigma_z = 3$ mm, $\sigma_r = 2.5$ mm).

The simulated performance of the final practical prototype during offline tests is listed in Table 5.6.

Table 5.6 – Performance of the final practical prototype at expected working pressures with the filament evaporated beam size.

Beam size		100 mbar	150 mbar	200 mbar
$\sigma_z = 3$ mm $\sigma_r = 2.5$ mm	Efficiency (%)	17	30	42
	Ave. tof (ms)	92	110	125
	T_N (ms)	58	61	63

The simulation results will be validated through experimental testing. The CAD rendering of the final prototype, illustrated on the left in Fig. 5.19, is scheduled to be installed on the FRIENDS^3 test bench, which has been fully constructed, to enable experimental performance characterization through extraction and neutralization tests. The test bench, depicted on the right in Fig. 5.19, is equipped with a differential pumping system, which includes both a bent RFQ, provided by KU Leuven, and a custom-designed straight RFQ working in mass filter mode. These RFQs are used to facilitate the efficient transport of ions through the differentially pumped regions of the test bench to a detector.

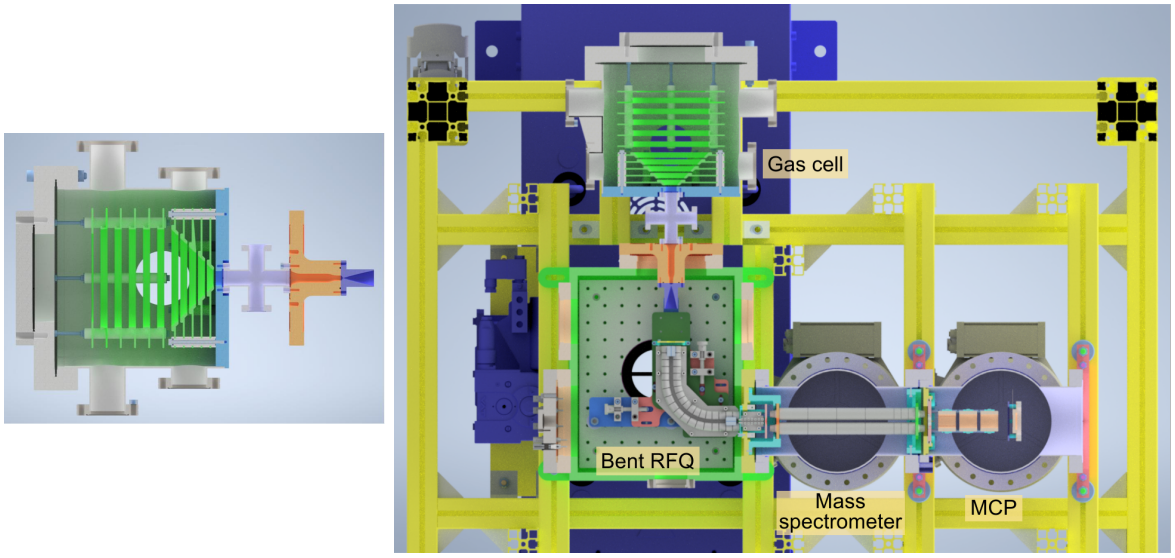

Fig. 5.19. Left: CAD rendering of the final version prototype to be experimentally tested. Right: the test bench designed by the FRIENDS^3 team. Figure courtesy of T. Hourat.

5.3.5 Neutralization by recombination with free electrons

The gas-cell design is intended to facilitate neutralization within a high-density electron cloud formed in the long no-field tube prior to the ions leaving the gas cell. Achieving efficient neutralization necessitates proper electron dynamics within the tube. However, the electrical field present in the gas cell may cause the immediate loss of electrons generated in the tube or trigger unwanted avalanche effects, which could compromise the neutralization process. Therefore, a starting point is to study the electron motion by the Charged Particle Tracing interface in COMSOL. The drag force exerted by the Ar gas on the electrons is added as a Stokes-type user-defined force. The reduced mobility of electrons in argon is $\mu_0 = 5.22{\cdot}10^3$ cm^{2}V^{-1}s^{-1} [HFK+02]. In all the simulations of the electron motion, the pressure of the gas cell was kept at 100 mbar.

Three hundred electrons were released without initial velocity in a Gaussian distribution at different positions in the neutralization tube. Figure 5.20 shows the trend of electron movement, highlighting the fact that electrons released below a certain coordinate (indicated by the red line) are rapidly drawn downwards by the electric field, while electrons released above the red line remain within the tube, moving with the gas flow and unaffected by the electric field. This observation indicates that the optimal placement of the electron source for experimental purposes is approximately 23 mm from the start of the tube. This positioning is likely to enhance the neutralization process by ensuring that the electrons are effectively retained within the neutralization tube.

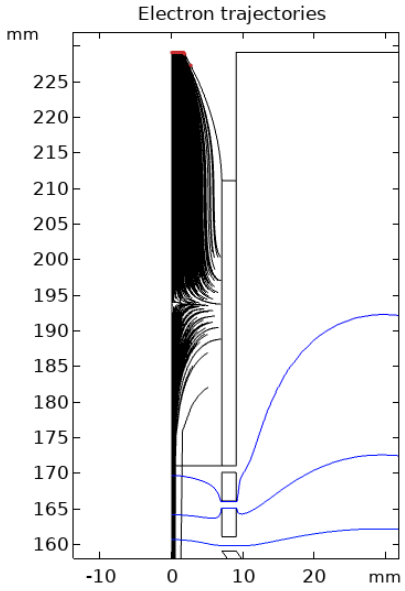

Fig. 5.20. The trajectories of electrons after being released at an arbitrary position in the no-field tube. The blue lines represent electric field equipotential contours.

A ^{90}Sr beta source with an activity of around 40 MBq was purchased and used for electron

production tests. Using the COMSOL Plasma Module, the dynamics of secondary electrons and the equilibrium charge density in argon irradiated by β particles have been investigated. The simulation starts with the formation of secondary electrons. To model the plasma within the argon-filled neutralization tube, it is essential to implement a complete and physically correct reaction network involving all the reactions and species. In the COMSOL Plasma Module, these input data are organized into the following sections: electron impact reactions, gas phase reactions, surface reactions, and species.

In our model, there are four species: argon atoms, electrons, metastable Ar*, and Ar^+ ions. The involved bulk reactions are listed in Table 5.7. For the reaction rate determination, the cross-section data for each of the electron impact reactions R1-5 are supplied through the file Ar_xsecs.txt which is available in the Plasma Module Applications Libraries folder.

For gas phase reactions R6, R7 and R8, the forward rate constants are provided as numeric data from the literature. In an argon discharge plasma, the presence of the metastable argon atoms enhances the plasma density, with the relative contributions of the various ionization processes depending on the electron density, temperature and the gas pressure. At a pressure of hundreds of mbar, electron impact ionization (R3, R5), Penning ionization (R6) and metastable pooling ionization (R7) are the primary ionization mechanisms for metastable argon atoms [BG95, GKW$^+$22]. For the reversible reaction R9, one assumes for simplicity a Gaussian Ar^+-e pair production rate. The forward rate constant k^f [1/s] is calculated for a 3D Gaussian distribution of the secondary electron cloud:

$$k^f = p_e \cdot e^{\frac{-(z-z_0)^2}{2\sigma_z^2}} \cdot e^{\frac{-r^2}{2\sigma_r^2}}, \tag{5.37}$$

where p_e is the production rate of electrons, z_0 the position of the beta source, σ_z the electron depth dispersion, σ_r the electron radius dispersion. The reverse rate constant k^r [m^3/(s·mol)] is determined as:

$$k^r = \alpha_{\text{rec}} N_A. \tag{5.38}$$

where α_{rec} is the Ar recombination coefficient, N_A the Avogadro constant.

Table 5.8 lists the surface reactions, the sticking coefficient being a dimensionless measure of the probability that a particle colliding with a wall or surface in a plasma environment will react on the surface. It ranges from 0 to 1, where 0 indicates no reaction and 1 means all particles react upon collision.

The density of each species in the plasma is therefore calculated by solving a balance equation considering all relevant production and loss processes in the model. As an initial step, the species and electron impact reactions in the plasma simulation are

Table 5.7 – Bulk reactions included in the Plasma model.

	Electron impact reactions	Type of collision	Energy threshold (eV)	Reference
R1	$e + Ar \Rightarrow e + Ar$	Elastic collision	0	[PP85]
R2	$e + Ar \Rightarrow e + Ar^*$	Electronic excitation	11.55	[MN87, BG95]
R3	$e + Ar^* \Rightarrow e + Ar$	Superelastic collision	-11.55	[MN87]
R4	$e + Ar \Rightarrow 2e + Ar^+$	Ionization	15.76	[PP85]
R5	$e + Ar^* \Rightarrow 2e + Ar^+$	Stepwise ionization	4.21	[Hym79]
	Gas phase reactions	Type of collision	Forward rate constant k^f (m^3/(s·mol))	Reverse rate constant k^r (m^3/(s·mol))
R6	$Ar^* + Ar \Rightarrow e + Ar + Ar^+$	Penning ionization	1.57e8 [a]	-
R7	$Ar^* + Ar^* \Rightarrow e + Ar + Ar^+$	Metastable pooling	3.85e8 [b,c]	-
R8	$Ar^* + Ar \Rightarrow Ar + Ar$	Metastable quenching	1.39e3 [d]	-
R9	$Ar \Leftrightarrow e + Ar^+$	Ionization/recombination	Eq. (5.37)	Eq. (5.38)

[a]Ref.[BG95], [b,c]Ref.[FR83, FLR85], [d]Ref. [Tac86]

Table 5.8 – Surface reactions included in the Plasma model.

	Surface reactions	Sticking coefficient
R1	$Ar^* \Rightarrow Ar$	1
R2	$Ar^+ \Rightarrow Ar$	1

simplified, only ionization and recombination processes in the gas: $Ar \Leftrightarrow Ar^+ + e$ and elastic scattering $e + Ar \Rightarrow e + Ar$ are considered and no surface reactions. The equilibrium electron density was calculated numerically (using a program written in Python) and using the COMSOL Plasma Module for comparison.

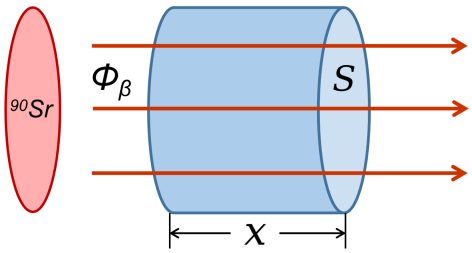

Fig. 5.21. A simplified scheme for an argon gas volume irradiated by a beta source.

In this simplified case, as shown in Fig. 5.21, the primary electron flux generated by the beta source, ϕ_β, can be deduced from the source activity A_β divided by the irradiation

area $S = \pi r_\beta^2$. The energy deposited per unit volume is:

$$\Delta E = s(E) \cdot \phi_\beta \tag{5.39}$$

where $s(E)$ is the stopping power of the beta particles, which can be obtained from literature [BCZ+17]. Thus the electron production rate by ionization p_e:

$$p_e = \frac{\Delta E}{\varepsilon} = \frac{s(E) \cdot \phi_\beta}{\varepsilon} \tag{5.40}$$

where ε is the ionization energy of the argon atom. The produced electrons constantly recombine with argon ions and the recombination processes can be expressed as:

$$\frac{dn_a}{dt} = -\frac{dn_e}{dt} = \alpha \cdot n_i \cdot n_e \tag{5.41}$$

where n_a, n_i, n_e are the density of argon atoms, argon ions and electrons in the investigated volume. The recombination coefficient α can be found in tables. In our case in room temperature at 100 mbar, the value of α is 1.0134e^{-6} [cm^3/s] [CvSB93]. At equilibrium, charge density $n_i = n_e = n_{ie}$ reaches:

$$\frac{dn_{ie}}{dt} = p_e - \alpha_r \cdot n_{ie}^2 = 0 \tag{5.42}$$

$$n_{ie} = \sqrt{\frac{p_e}{\alpha}} = \sqrt{\frac{\phi_\beta \cdot s(E)}{\varepsilon \cdot \alpha}} \tag{5.43}$$

Therefore, p_e and n_{ie} can be estimated numerically, and the results as functions of source activity are presented in Fig. 5.22. The entire activity is considered to be directed forward towards the gas, without any divergence. The value of p_e corresponding to our source activity 40 MBq at different will be used as an input in the COMSOL plasma simulation, allowing n_{ie} to be also determined by the simulation and can then be compared with the numerical result of Eq. (5.43) under the same simplified conditions.

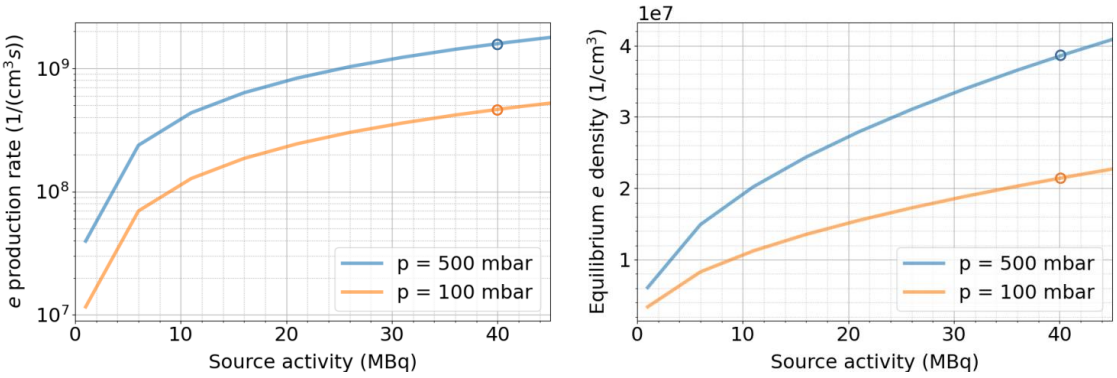

Fig. 5.22. (Left) Electron production rate p_e and (Right) equilibrium electron density ρ_e as a function of beta source activity. These values were numerically calculated using a Python code under simplified conditions, using the experimental spectrum of the ^{90}Sr source and the energy loss rates from NIST. Refer to the main text for detailed methodology and parameter descriptions.

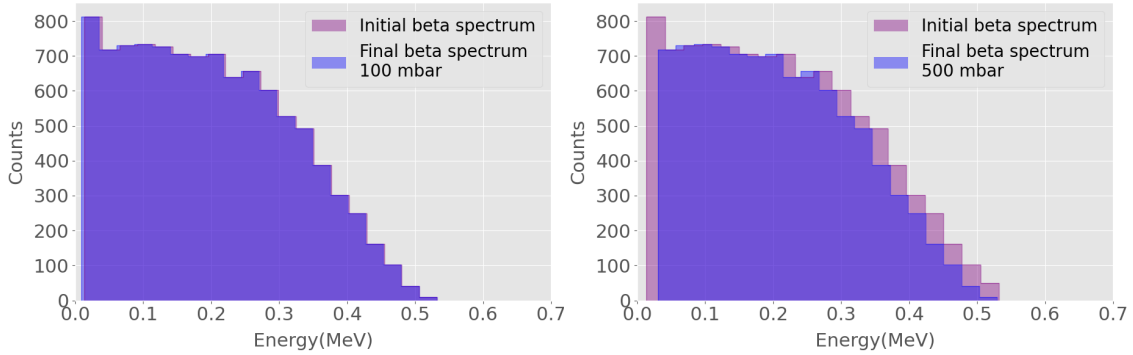

Fig. 5.23. Comparison of initial and final beta spectra before and after 20 mm attenuation in the argon gas environment. Left: at 100 mbar gas pressure. Right: at 500 mbar gas pressure.

Fig. 5.23 presents the estimated transmission rate of a 40 MBq ^{90}Sr source with an 8 mm radius irradiating a pure homogeneous argon gas. At 500 mbar, 91.8% of the beta particles reach a depth of 20 mm, while at 100 mbar, the transmission rate is 100% not considering any window for the gas cell. Based on this estimation, it can be expected that the gas volume within a neutralization tube with a diameter of 16-18 mm can be fully irradiated by the purchased beta source.

The equilibrium space charge density of the 40 MBq source irradiating the argon-filled tube was simulated using COMSOL at pressures of 100 and 500 mbar, with electron production rates taken as p_e of 4.6×10^8 cm^{-3}s^{-1} at 100 mbar and 1.63×10^9 cm^{-3}s^{-1} at 500 mbar, as indicated by Fig. 5.22. Fig. 5.24 presents the simulation results for

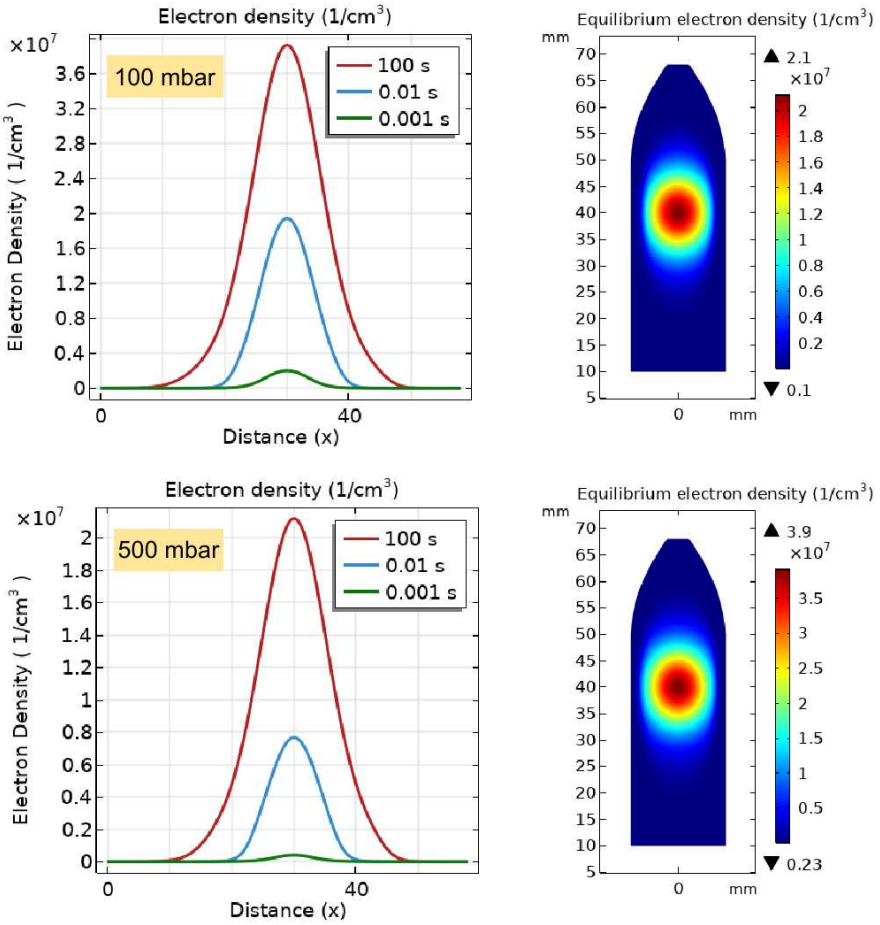

Fig. 5.24. Equilibrium charge density at the axis of the tube calculated with the COMSOL Plasma Module using the electron production rate calculated with the Python code as an input for the simplified condition, at 100 mbar (top) and 500 mbar (bottom) gas pressure. See text for details.

100 and 500 mbar. The red curves represent the electron density distribution along the tube axis as a function of the distance from the tube entrance. The green and blue curves correspond to electron densities at $t = 0.001$ s and $t = 0.01$ s, respectively, providing insight into the temporal evolution of the electron density as the plasma approaches equilibrium. The comparison between the results obtained from Python and COMSOL, as listed in Table 5.9, shows a high level of agreement and confirms the numerical stability of the COMSOL simulation. Subsequently, a comprehensive plasma simulation was conducted, incorporating complete species and reaction mechanisms as detailed in Table 5.7 and Table 5.8. Factors such as gas flow, migration, diffusion, and density variation of the gas were taken into consideration under realistic conditions.

Fig. 5.25 shows the equilibrium electron density as a function of the input electron production rate at 100 mbar under simplified conditions, results from COMSOL simulations (blue) and theoretical calculations $n_{ie} = \sqrt{p_e/\alpha}$ (red) are obtained in

Table 5.9 – Comparison of the equilibrium electron density calculated by theoretical calculation and COMSOL plasma simulation at 100 and 500 mbar, under simplified conditions.

	Equilibrium charge density ($1/cm^3$)	
	Python code	COMSOL simulation
100 mbar	2.1×10^7	2.1×10^7
500 mbar	3.9×10^7	3.9×10^7

good consistency. The figure also illustrates the contributions of the different transport mechanisms by diffusion, migration and convection due to the effect of gas flow. Different from the fact that convection is the dominant transport mechanism of the plasma heavy species in laminar flow, the electrons are characterized by a much higher diffusion coefficient and mobility (several orders of magnitude) due to their significantly lower mass. In our gas discharge setup, with no external electric field applied, diffusion is

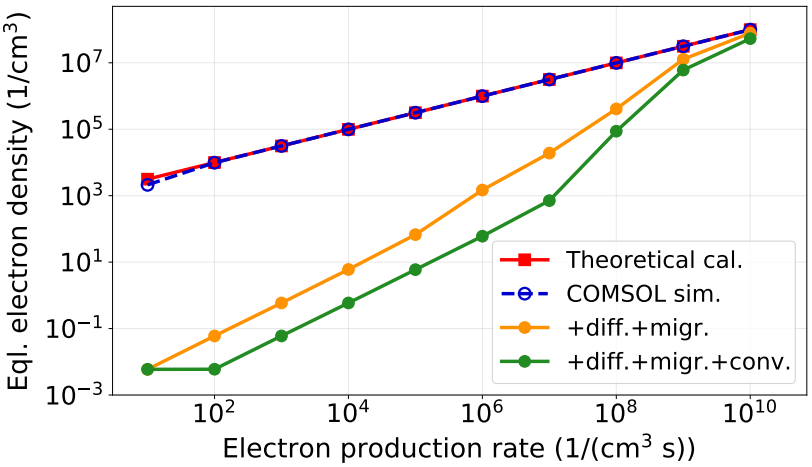

Fig. 5.25. The simulated equilibrium electron density as a function of the input electron production rate at 100 mbar under simplified conditions. The simulation results using the COMSOL Plasma Module (blue dashed curve) are in high consistency with the Python code theoretical calculation (red solid curve), the orange curve shows the COMSOL simulation considering the diffusion and migration effects, the green curve represents the COMSOL simulation considering the diffusion, migration and convection effects.

the primary transport mechanism for electrons, surpassing migration and convection at the gas flow rates studied (approximately 10 m/s). The gas flow spreads out the equilibrium electron density by several orders of magnitude for this simplified case.

Time available for neutralization

The residence time of the ions in the 60 mm long neutralization tube was determined without accounting for the neutralization process. Initially, a stationary study utilizing the Laminar Flow interface was conducted to simulate the gas flow within the tube. Subsequently, a time-dependent study with the Heavy Species Transport interface was performed. In this second study, a specified number of $^{133}Cs^+$ ions, distributed in a 3D Gaussian profile with $\sigma_r = \sigma_z = 2$ mm, were released at a position of 10 mm deeper along the axis from the entrance of the tube at $t = 0$ s. The ion motions were simulated considering only convection and migration effects within the gas environment, without any reactions.

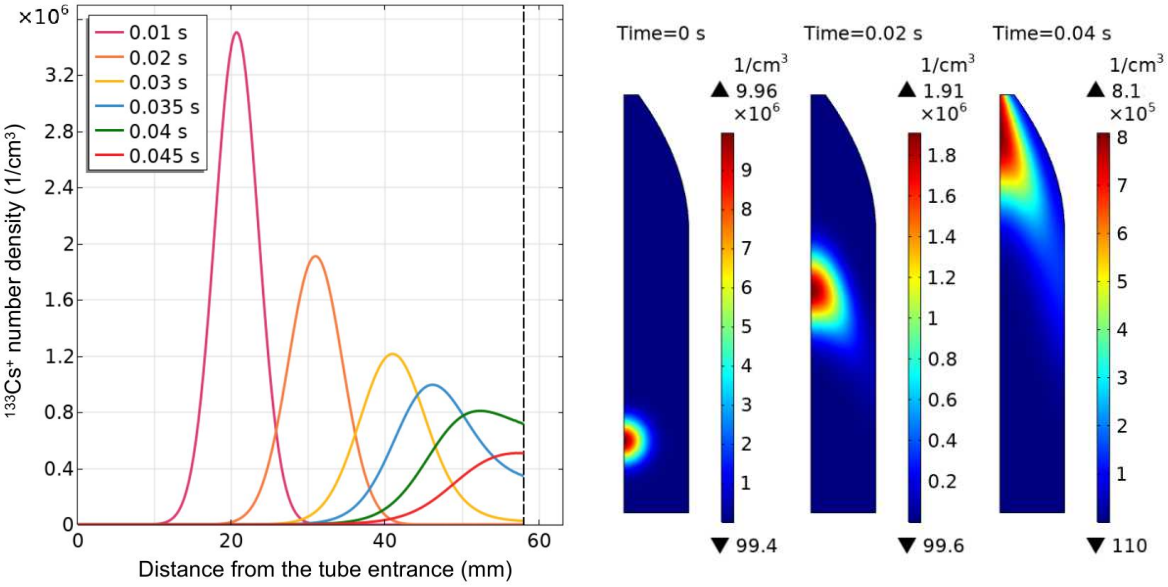

Fig. 5.26. The simulated Cs^+ number density as a function of distance from the tube entrance, taken at the tube axis over time, conducted with COMSOL Plasma Module at 100 mbar. Left: The simulated ion number density is presented as colored Gaussian curves at the tube axis at different times. The grey vertical dashed line indicates the outlet with a 58 mm distance from the entrance of the tube. Right: the ion cloud position in the tube at t=0, 0.02, 0.04 s, with t=0 s marking the release time.

The time-dependent $^{133}Cs^+$ number density was recorded along the tube axis, as shown in Fig. 5.26. The left panel illustrates the Cs^+ number density along the tube axis over time, depicted in colored Gaussian curves. The grey dashed vertical line at a distance of 58 mm to the tube entrance marks the outlet of the simulation volume (2 mm before the tube exit). The red Gaussian curve, corresponding to $t = 0.045$ s, has its centroid located at the outlet, indicating that the average time of flight of the ion cloud in the tube is approximately 45 ms.

Realistic condition simulation

A comprehensive plasma simulation incorporating complete species and reaction mechanisms, as detailed in Table 5.7 and Table 5.8, is essential. This simulation must account for various realistic factors including convection with gas flow, migration influenced by the electric potential, and diffusion. The simulation was conducted through three distinct studies: a stationary study for gas flow, a time-dependent study to determine equilibrium electron density, and a subsequent time-dependent study to evaluate ion extraction time and their neutralization within the plasma. The equilibrium electron density is expected to be higher than the simplified conditions due to additional ionization mechanisms involving metastable atoms, such as stepwise ionization, Penning ionization and metastable pooling ionization, which enhance electron production. The realistic plasma properties are to be simulated and quantified in future work. By releasing a cloud of ions X^+ near the entrance of the tube and transporting them through the plasma via the gas flow, and incorporating the recombination mechanisms that have been described in Section 5.2.4.2, the neutralization of the ions of interest can be characterized.

Conclusions and outlook

In this work, a series of developments were pursued for performing laser spectroscopy studies in a gas cell and in a supersonic gas jet using the S^3 Low Energy Branch.

In the first part of this thesis work, systematic off-line laser ionization and spectroscopy measurements of stable erbium isotopes were performed using the full S^3-LEB setup and its Ti:sa laser system. Three atomic transitions of Er I at 393.7 nm, 400.8 nm and 408.8 nm were selected from the literature and systematically investigated by the IGLIS technique. Gas-cell measurements were performed using the dual-etalon Ti:sa laser for the excitation step. In addition, the 408.8 nm transition was measured in the supersonic gas jet with the narrowband, injection-locked Ti:sa laser. Isotope shifts were determined for the excitation and ionization steps of the three ionization schemes. Field and mass-shift factors and the associated experimental uncertainties for all the excitation steps were extracted from the isotope-shift data using King-plot analysis. Uncertainty correlations of the two factors were discussed. This work presents the first systematic gas-cell laser-spectroscopy measurements with S^3-LEB. The results extracted from the in-gas-cell and in-gas-jet data for the 408.8 nm transition are in good agreement, representing a proof of principle of the apparatus. In gas-cell measurements of 400.8 nm in a power-broadened regime are in general good agreement with the literature, but exhibit systematic effects especially for low statistics due to the multimode nature of the laser. Finally, small but systematic discrepancies were found with literature values in the case of the 393.7 nm transition, which needs to be further investigated using narrowband laser spectroscopy. The stability of the laser system between different measurements was verified. The collisional effects in the gas cell ionization were quantified for the 400.8 nm and 408.8 nm transitions.

A spectral resolution of $\sim$ 200 MHz was obtained for narrowband laser spectroscopy of erbium in the supersonic jet, in good agreement with the expected Mach number $M \sim 8$ of the jet. This allowed the hyperfine structure parameters for the 408.8 nm transition to be determined, to our best knowledge for the first time. These results demonstrate the setup's potential for high-resolution laser spectroscopy of heavy elements in future on-line experiments. The 408.8 nm and 393.7 nm transitions have been identified as promising candidates for the first S^3-LEB online experiments due to their greater sensitivity to the changes in mean-square nuclear charge radii. The global set of

observations and results bring S^3-LEB one step closer to the first on-line experiments at S^3.

The uncertainties in the isotope shift factors extracted from the King plot analysis are substantial, primarily due to the limited availability of muonic charge radii data for erbium in the Fricke&Heilig evaluations. Using a reference transition (583 nm) relies on factors obtained with assumptions on the underlying electronic structure (justifying a negligible specific mass shift). This assumption is shown to be coherent with the data on the 400.8 nm transition, but not 415.1 nm. An alternative approach to obtain the field shift and mass shift factors involves atomic theory calculations. However, given that the electronic configurations of the studied transitions are situated in a region of high level density, these calculations are inherently complex and time-consuming. Ongoing collaborations with atomic theorists aim to address these challenges, and the calculated values will be incorporated into future analyses to improve the precision of the results.

A continuous-wave single-mode tunable Ti:sa laser with a broad tuning range will be used as the seed laser for the injection-locked Ti:sa cavity in the future high-resolution laser spectroscopy. More transitions that are not achievable with the current ECDL will be studied.

A second part of this thesis work was concerned with the FRIENDS^3 project, namely the development of a future version of the S^3-LEB gas cell aimed to extend the IGLIS technique at S^3-LEB to isotopes with half-lives on the order of 100 ms while maintaining acceptable efficiency. In this work, a fast gas cell with an extraction time of around 100 ms has been designed and simulated. The simulated phenomena include laminar gas flow, electrostatic field, and species convection, migration and diffusion in the buffer gas. The interplay between pressure, electric force, drag force, and diffusion in determining the overall performance of the ion extraction process was characterized. With a beam size comparable to the one produced by S^3 in converging mode, simulations show that 14% of particles can be extracted in 93 ms at a pressure of 100 mbar, and 29% can be extracted in 132 ms at 200 mbar.

A method of simulating the dynamics of free electrons created by weak gas ionization was investigated using the plasma module of the COMSOL software. Such electrons can offer a promising path to ion recombination. The chemical reactions involved in the plasma formation for neutralization and the neutralization of the ions by the equilibrium electrons have been discussed in this work. The species convection, migration and diffusion in plasma environment were studied. Simulations of the comprehensive reactions in the plasma and ion recombination mechanism still need to be performed. A test setup has been constructed by the FRIENDS^3 team for the experimental test of the designed gas cell with respect to ion extraction and neutralization. The mechanical drawings of the fast gas cell are finalized based on the simulations performed in this

work. This thesis work thus completed two key steps which will allow the experimental study and simulation of ion extraction or neutralization for the S^3-LEB experiment.

The S^3-LEB setup is currently being installed at the focal plane of S^3, with plans to begin online commissioning using isotopes of erbium. The results from this thesis, alongside future online commissioning measurements, will serve as benchmarking references for the day-1 experiments in erbium. To extend this work to other elements such as tin or heavier elements like uranium, systematic scheme development and testing will be required. The broad tunability offered by the continuous-wave, single-mode, tunable Ti:sa laser cavity will significantly enhance the versatility of the high-resolution RIS technique at S^3-LEB across a wider range of transitions.

Additionally, the $FRIENDS^3$ gas cell and its test setup are expected to be installed at S^3-LEB, with proof-of-principle measurements planned within the next two years. These efforts will further refine and expand the capabilities of the setup, enabling future studies of short-lived isotopes and exotic nuclei. This will significantly advance the scope and precision of nuclear structure research using the IGLIS technique at S^3.

Résumé étendu

Introduction

Cette thèse présente une série de développements visant à réaliser des mesures de spectroscopie laser à ionisation par résonance sur des isotopes radioactifs en utilisant la branche de basse énergie du Spectromètre Super Séparateur (S^3-LEB) à SPIRAL2, GANIL. Le travail s'articule autour de deux axes principaux : des mesures systématiques de spectroscopie laser hors ligne pour les isotopes stables de l'erbium (Er) afin de préparer les premières expériences en ligne à S^3 et le développement d'une future cellule à gaz pour étendre l'applicabilité de S^3-LEB aux isotopes à courte durée de vie.

La première partie de la thèse est consacrée aux études de spectroscopie laser à ionisation hors ligne des isotopes stables de l'erbium. Cette partie du travail sert de preuve de principe de la configuration complète S^3-LEB et de son système laser Ti:saphir (Ti:sa) et vise à identifier un schéma d'ionisation laser optimal pour Er sensible à ses propriétés d'état fondamental nucléaire, qui sont essentielles pour préparer les premières expériences en ligne à S^3. L'erbium a été sélectionné comme premier cas d'étude en raison de ses schémas d'ionisation laser bien établis compatibles avec le système laser S^3-LEB existant et de ses taux de production favorables à S^3. Ce travail a consisté à extraire des facteurs de déplacement isotopique pour les premiers étages d'excitation de trois schémas (408,8 nm, 400,8 nm et 393,7 nm) en utilisant la spectroscopie en cellule à gaz et en jet de gaz, à déterminer les constantes de structure hyperfine par spectroscopie en jet de gaz à haute résolution (pour l'état excité de la transition de 408.8 nm) et à caractériser les effets d'élargissement de pression observés dans la spectroscopie en cellule à gaz.

La deuxième partie du travail se concentre sur le développement d'une cellule à gaz rapide adaptée à la future étude par spectroscopie laser des isotopes à courte durée de vie à S^3-LEB, ce qui est le cas de la plupart des noyaux exotiques près de la "drip line" proton. Cette partie du travail a visé à concevoir une cellule à gaz avec un temps d'extraction des ions rapide tout en maintenant une efficacité d'extraction élevée, et à entamer des études de neutralisation pour ouvrir la voie à l'établissement d'un mécanisme de neutralisation universel et efficace, mettant les bases des avancées futures dans les performances de neutralisation des cellules à gaz.

Structure de la thèse

La structure de la thèse est présentée par la suite.

Le **chapitre 1** présente les propriétés de l'état fondamental nucléaire accessibles par spectroscopie laser et les méthodologies utilisées pour interpréter les observables atomiques correspondantes. Il se concentre sur les déplacements isotopiques et les structures hyperfines, qui donnent un aperçu des propriétés de l'état fondamental nucléaire telles que les changements dans les rayons de charge quadratiques moyens et les moments nucléaires.

Le **chapitre 2** détaille les techniques expérimentales utilisées dans cette recherche, en mettant l'accent sur la technique d'Ionisation et de Spectroscopie Laser par Ionisation Résonnante dans le Gaz (IGLIS) et les lasers Ti :saphir (Ti :sa) accordables. La technique IGLIS est détaillée pour les environnements de cellule à gaz et de jet de gaz supersonique. Les propriétés du jet de gaz et les mécanismes d'élargissement spectral pour la spectroscopie laser en gaz sont analysés. Le jet de gaz froid et collimaté minimise l'effet Doppler et l'élargissement collisionnel en créant un environnement à basse température et basse pression, obtenant ainsi une résolution spectrale élevée. Les lasers Ti:sa accordables sont décrits en termes de principes de fonctionnement, de configurations de cavité et de méthodes de sélection précise des longueurs d'onde. Les techniques de doublage de fréquence pour générer la lumière bleue à ultraviolette requise sont également présentées.

Le **chapitre 3** décrit la configuration S^3-LEB, en se concentrant sur ses composants clés et le système laser pour la mise en œuvre de la technique IGLIS. La cellule à gaz actuelle utilisée dans les études de spectroscopie laser des isotopes stables de l'erbium est décrite. Le comportement des ions dans la cellule à gaz S^3-LEB et le jet de gaz est décrit. Les limitations de la cellule à gaz actuelle sont discutées, fournissant la motivation pour la deuxième partie du travail de thèse, qui consiste à développer une nouvelle version de la cellule à gaz. Le système laser utilisé dans ce travail de thèse est également présenté. Trois types de cavités Ti:sa disponibles à S^3-LEB ont été utilisés : d'un côté, la cavité à double étalon à moyenne résolution (1,5 - 2 GHz largeur à mi-hauteur) et la cavité monomode verrouillée par injection à haute résolution ($\sim$ 35 MHz largeur à mi-hauteur) pour l'étape d'excitation, de l'autre côté la cavité à simple étalon à bande large ($\sim$ 5 GHz largeur à mi-hauteur) pour l'étape d'ionisation.

Le **chapitre 4** présente les résultats des expériences de spectroscopie d'ionisation par résonance (RIS) menées sur des isotopes stables d'erbium. Le chapitre couvre les schémas d'ionisation choisis, l'optimisation des conditions expérimentales, l'extraction des déplacements isotopiques et des coefficients hyperfins, et une discussion des incertitudes associées aux mesures et aux méthodes utilisées pour les quantifier. La caractérisation de l'élargissement et du déplacement de pression de deux transitions étudiées est également

incluse.

Le **chapitre 5** se concentre sur les études de simulation réalisées dans le cadre du projet FRIENDS^3, qui signifie Fast Radioactive Ion Extraction and Neutralization Device for S^3. Ce chapitre fournit la motivation et les objectifs du projet, une discussion approfondie des différents phénomènes impliqués dans les simulations des cellules à gaz, notamment le flux de gaz laminaire, les champs électriques, la création d'électrons pour la neutralisation et le mouvement des ions dans des différentes conditions. La conception et l'optimisation de la géométrie de la cellule à gaz et la version modifiée pour la mise en œuvre sont abordées. Le chapitre présente également des simulations de la génération d'électrons libres et une discussion sur le transport des ions dans le plasma.

Résultats obtenus

Spectroscopie laser des isotopes stables de l'erbium

Les trois transitions atomiques d'Er à 393,7 nm, 400,8 nm et 408,8 nm ont été étudiées systématiquement par la technique IGLIS. Les mesures de la cellule à gaz ont été effectuées à l'aide du laser Ti:sa à double étalon pour l'étape d'excitation. La transition à 408,8 nm a été mesurée dans le jet de gaz supersonique avec le laser Ti:sa à bande étroite verrouillé par injection. Les déplacements isotopiques ont été déterminés pour les étapes d'excitation et d'ionisation des trois schémas d'ionisation. Les valeurs moyennes pondérées des déplacements isotopiques (DI) avec leurs incertitudes correspondantes pour les transitions de première étape des trois schémas étudiés dans ce travail sont présentées dans le tableau R.1.

Les facteurs de déplacement de champ et de masse et les incertitudes expérimentales associées pour les trois transitions ont été extraits des données de déplacement isotopique à l'aide d'une analyse King-plot. Le King plot des données de la transition à 408,8 nm obtenues dans le jet de gaz est présenté dans la Fig.R.1. Les corrélations d'incertitude des deux facteurs ont été discutées dans la thèse.

Ce travail présente les premières mesures systématiques de spectroscopie laser à cellule à gaz avec S^3-LEB. Les résultats extraits des données en cellule à gaz et en jet de gaz pour la transition à 408,8 nm sont en bon accord, ce qui représente une preuve de principe de l'appareil. Dans la cellule à gaz, les mesures à 400,8 nm dans un régime élargi en puissance sont en général en bon accord avec la littérature, mais présentent des effets systématiques, en particulier pour des statistiques faibles en raison de la nature multimode du laser. Enfin, des écarts faibles mais systématiques ont été constatés par rapport aux valeurs de la littérature dans le cas de la transition à 393,7 nm, qui doivent être étudiés plus en détail à l'aide de la spectroscopie laser à faible largeur spectrale.

TABLE R.1 – Valeurs des DI moyennes pondérées extraites $\Delta\nu_{\mathrm{WA}}^{A',170}$ des isotopes stables $^{164-168}$Er par rapport à ^{170}Er pour les transitions de première étage des trois schémas étudiés, comparées lorsque possible à la littérature. Les $\sigma(\Delta\nu_{\mathrm{WA}}^{A',170})$ indiqués entre parenthèses représentent les incertitudes statistiques et systématiques combinées.

A'	Déplacements isotopiques $\Delta\nu_{\mathrm{WA}}^{A',170}$ (MHz)						
	408.8 nm		400.8 nm			393.7 nm	
	cellule	jet [1]	cellule	jet[2]	[F$^+$13]	cellule	[JNKM09]
164	-3147(83)	-3212(6)	2386(118)	2517(39)	2530(22)	-2902(45)	-2681.8(21)
166	-2142(28)	-2159(6)	1748(44)	1720(43)	1681(14)	-2018(34)[3]	-1804(16)
167	-1867(34)	-1870(6)	1415(38)	1395(29)	1384(15)	-1764(20)	
168	-1128(31)	-1099(6)	875(46)	855(13)	841(20)	-1034(18)	-918.4(12)

[1] Mesures dans le jet de gaz avec la cavité Ti:sa verrouillée par injection pour l'étape d'excitation.

[2] Mesures dans le jet de gaz avec la cavité Ti:sa à double étalon pour l'étape d'excitation.

[3] Dans [AD15] cette valeur est rapportée comme -67,6(3,0) $\times$ 10^{-3} cm^{-1}, équivalent à -2027(90) MHz.

La stabilité du système laser entre différentes mesures a été vérifiée. Les effets collisionnels dans l'ionisation de la cellule à gaz ont été quantifiés pour les transitions à 400,8 nm et 408,8 nm. Une résolution spectrale d'environ 200 MHz a été obtenue pour la spectroscopie laser à bande étroite de l'erbium dans le jet supersonique, en bon accord avec le nombre de Mach $M = 8$ attendu du jet. Cela a permis de déterminer les paramètres de structure hyperfine $A = -123.96(6.0)$ MHz, $B = 209.02(7.8)$ MHz pour la transition à 408,8 nm, à notre connaissance pour la première fois. Ces résultats démontrent le potentiel de l'installation pour la spectroscopie laser à haute résolution d'éléments lourds dans de futures expériences en ligne. Les transitions à 408,8 nm et 393,7 nm ont été identifiées comme des candidats prometteurs pour les premières expériences en ligne S^3-LEB en raison de leur plus grande sensibilité aux changements des rayons de charge nucléaire moyens.

Les incertitudes dans les facteurs de déplacement isotopique extraits de l'analyse du tracé de King sont substantielles, principalement en raison de la disponibilité limitée des données sur les rayons de charge absolues pour l'erbium. L'utilisation d'une transition de référence (583 nm) repose sur des facteurs obtenus avec des hypothèses sur la structure électronique sous-jacente (justifiant un déplacement de masse spécifique négligeable). Cette hypothèse s'avère cohérente avec les données sur la transition à 400,8 nm, mais pas avec la transition à 415,1 nm, qui était le premier test hors ligne au S^3-LEB étudié avant ce travail de thèse. Une approche alternative pour obtenir les facteurs de déplacement de champ et de masse implique des calculs de théorie atomique. Cependant, étant donné que les configurations électroniques des transitions étudiées sont situées dans une région

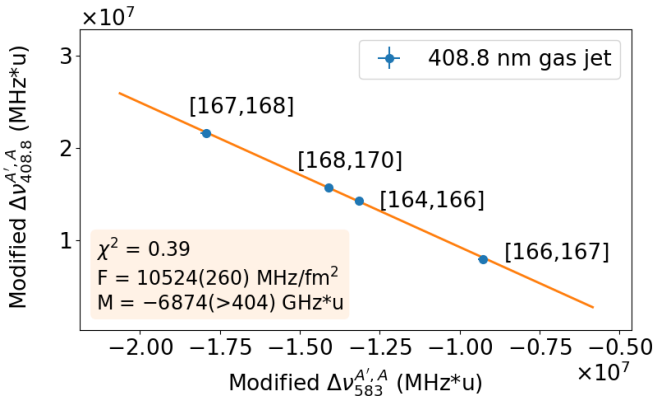

Fig. R.1. King plot du $\Delta\nu^{A',A}_{408.8}$ modifié tracé par rapport au $\Delta\nu^{A',A}_{582.7}$ modifié pour l'ensemble de données de la transition à 408,8 nm mesuré dans le jet de gaz.

de haute densité de niveaux, ces calculs sont intrinsèquement complexes et prennent du temps. Des collaborations en cours avec des théoriciens atomiques visent à relever ces défis, et les valeurs calculées seront incorporées dans les analyses futures pour améliorer la précision des résultats.

Developpement d'une cellule gazeuse rapide de neutralization pour S^3-LEB

Une cellule à gaz rapide capable d'atteindre des temps d'extraction d'ions d'environ 100 ms a été conçue. Les phénomènes simulés comprennent l'écoulement de gaz laminaire, le champ électrostatique et la convection, la migration et la diffusion des espèces dans le gaz tampon ou la décharge de gaz. L'interaction entre la pression, la force électrique, la force de traction et la diffusion pour déterminer les performances globales du processus d'extraction des ions a été caractérisée.

Figure R.2 illustre les performances du prototype optimisé, y compris l'efficacité d'extraction, le temps d'extraction et le temps disponible pour la neutralisation. Ces simulations ont été réalisées en supposant une taille de faisceau comparable à celle produite par S^3 en mode convergent. Les courbes bleues et rouges montrent les performances avec différents diamètres entre la même conception du trou de sortie, 1 mm et 0,8 mm. Pour la cellule à gaz avec 1 mm de diamètre du trou de sortie, les simulations indiquent que 14 % des particules peuvent être extraites en 93 ms à 100 mbar, tandis que 29 % peuvent être extraites en 132 ms à 200 mbar.

La réalisation expérimentale de la version optimisée a nécessité des modifications en raison de contraintes mécaniques et expérimentales, telles que le coût et la complexité de la fabrication, la nécessité d'un montage et d'un espacement appropriés des électrodes et la nécessité d'empêcher le faisceau S^3 arrêté ou le plasma généré de s'approcher des électrodes de la cage et de l'entonnoir. Une révision finale du prototype, comportant

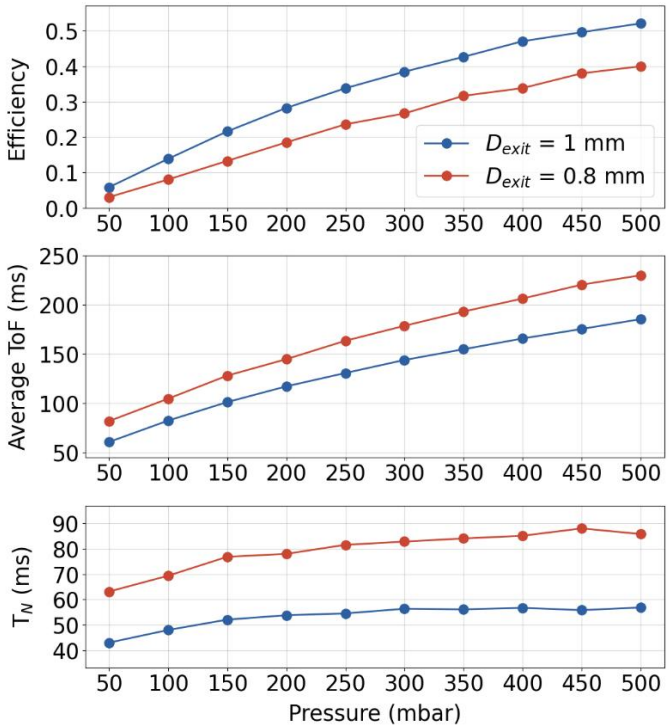

Fig. R.2. Simulation SIMION des performances obtenues avec les réglages haute tension en fonction de la pression pour différents diamètres de trou de sortie : efficacité d'extraction (haut), temps moyen d'extraction (milieu) et temps disponible pour la neutralisation T_N (bas).

des électrodes légèrement simplifiées et un volume d'arrêt plus grand, a été réalisée. Les performances des versions finales, évaluées à l'aide de simulations SIMION, sont détaillées dans le tableau R.2.

TABLE R.2 – Performances du prototype final aux pressions de travail attendues avec la taille de faisceau en mode convergent S^3.

Taille faisceau		100 mbar	150 mbar	200 mbar
$\sigma_z = 5$ mm $\sigma_r = 10$ mm	Efficacité (%)	14	22	29
	Temps extr. moyen (ms)	93	115	132
	T_N (ms)	53	57	58

Une méthode de simulation de la dynamique des électrons libres créés par ionisation faible du gaz a été étudiée à l'aide du module plasma du logiciel COMSOL. Figure R.3 montre la densité électronique à l'équilibre en fonction du taux de production d'électrons à 100 mbar dans des conditions simplifiées (sans prendre en compte les phénomènes de diffusion, de convection dans le gaz et de migration dans le champ électrique). Les résultats des simulations COMSOL (en bleu) sont comparés aux valeurs obtenues via la formule exacte dans les conditions données, $n_{ie} = \sqrt{p_e/\alpha}$ (en rouge).

Les deux séries de résultats montrent un bon accord, ce qui renforce la confiance dans les simulations COMSOL. La figure illustre également les contributions des différents mécanismes de transport par diffusion, migration et convection dues à l'effet du flux de gaz. Contrairement au fait que la convection est le mécanisme de transport dominant des espèces lourdes du plasma dans un flux laminaire, les électrons sont caractérisés par un coefficient de diffusion et une mobilité beaucoup plus élevés (plusieurs ordres de grandeur) en raison de leur masse nettement inférieure. On observe par conséquent une baisse en densité d'équilibre pour des faibles taux de production quand la diffusion des électrons est prise en compte (courbes orange et verte). De tels électrons peuvent offrir une voie prometteuse vers la recombinaison des ions.

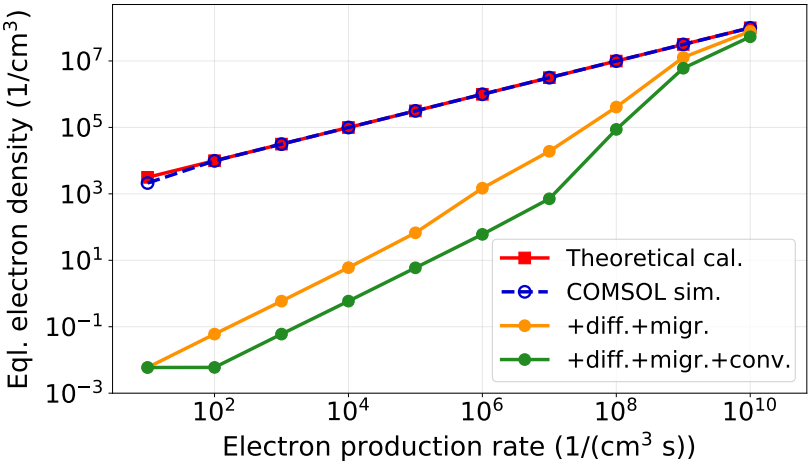

Fig. R.3. La densité électronique à l'équilibre simulée en fonction du taux de production d'électrons d'entrée à 100 mbar dans des conditions simplifiées. Les résultats de simulation utilisant le module plasma COMSOL (courbe pointillée bleue) sont en bon accord avec le calcul théorique (courbe continue rouge). La courbe orange montre la simulation COMSOL prenant en compte les effets de diffusion et de migration, la courbe verte représente la simulation COMSOL prenant en compte les effets de diffusion, de migration et de convection.

Les réactions chimiques impliquées dans la formation du plasma pour la neutralisation des ions par les électrons d'équilibre ont été discutées dans ce travail. Des simulations des réactions complètes dans le plasma et du mécanisme de recombinaison des ions doivent encore être réalisées. Les dessins mécaniques de la cellule à gaz rapide sont finalisés sur la base des simulations effectuées dans ce travail.

Conclusions

Cette thèse présente des contributions à l'avancement de la spectroscopie d'ionisation laser à S^3-LEB. À court terme, des mesures de spectroscopie d'ionisation laser hors

ligne dans le gaz (IGLIS) ont été réalisées dans le cadre des expériences de mise en service à S^3-LEB, établissant la faisabilité et l'optimisation de la technique. À long terme, une future version de la cellule à gaz a été conçue pour faciliter les mesures IGLIS sur les isotopes à courte durée de vie, répondant ainsi aux défis posés par leurs demi-vies limitées et garantissant des performances améliorées dans les études à venir.

Dans ce travail de thèse, les premières mesures IGLIS avec S^3-LEB ont été réalisées sur des transitions avec de grands déplacements isotopiques. Les facteurs de déplacement isotopique ont été déterminés pour ces trois transitions à 408,8 nm, 400,8 nm et 393,7 nm. Les effets d'élargissement de pression dans l'environnement gaz-cellule ont été caractérisés pour les transitions à 400,8 nm et 408,8 nm.

Les résultats obtenus dans la cellule à gaz et le jet de gaz ont montré une bonne concordance entre eux et avec les valeurs de la littérature existante, servant de preuve de principe pour l'appareil S^3-LEB. La stabilité du système laser a été vérifiée par une série de mesures effectuées sur plusieurs semaines. De plus, les transitions à 408,8 nm et 393,7 nm ont été identifiées comme des candidates prometteuses pour déterminer les rayons de charge nucléaires des isotopes radioactifs d'erbium dans les premières expériences en ligne à S^3.

En parallèle, ce travail a entammé le développement d'une cellule à gaz de nouvelle génération optimisée pour les études de spectroscopie laser d'isotopes à courte durée de vie. La méthodologie de simulation du transport des ions au sein de la cellule à gaz et d'optimisation de ses performances d'extraction a été établie.

Sur la base de ces simulations, une conception de cellule à gaz a été proposée, capable d'atteindre un temps d'extraction des ions d'environ 100 ms tout en maintenant une efficacité d'extraction élevée. Cette conception représente une amélioration significative pour les expériences impliquant des isotopes avec des demi-vies de l'ordre de quelques millisecondes.

De plus, la dynamique des électrons dans le gaz a été simulée à l'aide du module COMSOL Plasma, intégrant les effets apportés par l'environnement.

Perspectives

Les résultats de ces travaux ouvrent la voie à de nouvelles avancées sur les deux lignes de développement.

Une cavité Matisse Ti:sa accordable à onde continue et monomode, qui offre une large accordabilité, sera mise en œuvre comme laser d'amorçage de la cavité Ti:sa à bande étroite verrouillée par injection. Cette mise à niveau permettra l'exploration de transitions d'erbium supplémentaires et de transitions d'autres éléments qui ne sont pas accessibles avec le laser à diode à cavité externe actuel (ECDL). Notamment, la

transition à 393,7 nm étudiée dans ce travail sera remesurée.

La haute résolution spectrale (< 200 MHz) obtenue en spectroscopie laser à jet de gaz est prometteuse pour les futures études de structure hyperfine (HFS) d'éléments tels que l'étain et d'éléments plus lourds comme l'uranium. Ces études devraient permettre de déterminer les propriétés électromagnétiques nucléaires de ces éléments.

La cellule à gaz FRIENDS^3 conçue dans ce travail de thèse est en cours de fabrication. Elle sera bientôt montée sur le banc d'essai, qui a été construit par l'équipe FRIENDS^3, pour des tests expérimentaux concernant ses performances d'extraction et de neutralisation des ions.

De plus, la cellule à gaz et son dispositif de test devraient être installés au GANIL, avec des mesures de spectroscopie laser de preuve de faisabilité prévues dans les deux prochaines années. Ces efforts permettront d'affiner et d'étendre les capacités de l'expérience S^3-LEB, permettant ainsi de futures recherches sur la structure nucléaire des noyaux exotiques à courte durée de vie.

Bibliography

[A+23] A. Ajayakumar et al. In-gas-jet laser spectroscopy with S^3-LEB. *Nucl. Instr. Meth. B*, 539:102–107, 2023.

[ABP85] H. Brüggemeyer A. Bernard and V. Pfeufer. Changes in mean-square nuclear charge radii in Er from optical isotope shifts by laser-atomic-beam spectroscopy. *Z. Phys. A: At. Nucl.*, 1985.

[AD05] A.D. Appelhans and D.A. Dahl. SIMION ion optics simulations at atmospheric pressure. *Int. Jour. Mass Spectrom.*, 244:1–14, 2005.

[AD15] B.K. Ankush and M.N. Deo. Isotope shift measurements in the 660 spectral lines of Er I covering the 340–605nm wavelength region with a Fourier Transform Spectrometer. *J. Quant. Spectrosc. Radiat. Transfer*, 155:96–119, 2015.

[AHS87] P. Aufmuth, K. Heilig, and A. Steudel. Changes in mean-square nuclear charge radii from optical isotope shifts. *At. Data Nucl. Data Tables*, 37(3):455–490, 1987.

[Aja23] A. Ajayakumar. *In gas jet laser spectroscopy optimization for high resolution measurement of actinides*. Phd thesis, Normandie Université, 2023.

[Bal88] R. Balescu. *Transport processes in plasmas. Classical transport theory. vol. 1.* North-Holland, 1988.

[BanP01] J. Bieroń and P. Pyykkö. Nuclear Quadrupole Moments of Bismuth. *Phys. Rev. Lett.*, 87:133003, 2001.

[BCZ+17] M.J. Berger, J.S. Coursey, M.A. Zucker, J. Chang, S.M. Seltzer, and P.M. Bergstrom. ESTAR, PSTAR, and ASTAR: Computer Programs for Calculating Stopping-Power and Range Tables for Electrons, Protons, and Helium Ions. [Online] Available: `http://physics.nist.gov/Star`. National Institute of Standards and Technology, Gaithersburg, MD., 2017.

[BG95] A. Bogaerts and R. Gijbels. Modeling of metastable argon atoms in a direct-current glow discharge. *Phys. Rev. A*, 52:3743–3751, 1995.

[BL18] C. K. Birdsall and A. B. Langdon. *Plasma physics via computer simulation*. CRC press, 2018.

[Bla10] B. Blank. The DESIR facility at SPIRAL2. *Pramana*, 75:343–353, 2010.

[BLR21] M. Block, M. Laatiaoui, and S. Raeder. Recent progress in laser spectroscopy of the actinides. *Prog. Part. Nucl. Phys.*, 116:103834, 2021.

[BR90] P. T. Boggs and J. E. Rogers. Orthogonal distance regression. *Contemp. Math.*, 112:183–194, 1990.

[Bra65] S. I. Braginskii. Transport Processes in a Plasma. *Rev. Plasma Phys.*, 1:205, 1965.

[BW50] A. Bohr and V. F. Weisskopf. The influence of nuclear structure on the hyperfine structure of heavy elements. *Phys. Rev.*, 77:94–98, 1950.

[C+16] P. Chauveau et al. PILGRIM, a Multi-Reflection Time-of-Flight Mass Spectrometer for Spiral2-S^3 at GANIL. *Nucl. Instr. Meth. B*, 376:211–215, 2016. Proceedings of the XVIIth International Conference on Electromagnetic Isotope Separators and Related Topics (EMIS2015), Grand Rapids, MI, U.S.A., 11-15 May 2015.

[CCTG98] J. Dupont-Roc C. Cohen-Tannoudji and G. Grynberg. *Atom-photon interactions: basic processes and applications*. John Wiley & Sons, 1998.

[CF10] B. Cheal and K. T. Flanagan. Progress in laser spectroscopy at radioactive ion beam facilities. *J. Phys. G: Nucl. Part. Phys.*, 37(11):113101, 2010.

[CGP83] W. J. Childs, L. S. Goodman, and V. Pfeufer. Hyperfine structure of the $4f^{12}6s^{23}h$ and ^3f terms of ^{167}Er I by atomic-beam, laser-rf double resonance. *Phys. Rev. A*, 28:3402–3408, 1983.

[Cha16] P. Chauveau. *Design, simulations and test of a Time-of-Flight spectrometer for mass measurement of exotic beams from SPIRAL1/SPIRAL2 and gamma-ray spectroscopy of nuclei close to ^{100}Sn*. Phd thesis, Normandie Université, 2016.

[Che12] F. F. Chen. *Introduction to plasma physics*. Springer Science & Business Media, 2012.

[CMP16] P. Campbell, I.D. Moore, and M.R. Pearson. Laser spectroscopy for nuclear structure physics. *Prog. Part. Nucl. Phys.*, 86:127–180, 2016.

[COM] COMSOL Multiphysics v. 5.6. www.comsol.com.

[CvSB93] R. Cooper, R. J. van Sonsbeek, and R. N. Bhave. Pulse radiolysis studies of ion-electron recombination in gaseous argon. *J. Chem. Phys.*, 98(1):383–389, 1993.

[D+14] C. Droese et al. The cryogenic gas stopping cell of SHIPTRAP. *Nucl. Instr. Meth. B*, 338:126–138, 2014.

[D+15] F Déchery et al. Toward the drip lines and the superheavy island of stability with the Super Separator Spectrometer S^3. *Eur. Phys. J. A.*, 51:1–16, 2015.

[D+16] F. Déchery et al. The Super Separator Spectrometer S^3 and the associated detection systems: SIRIUS & LEB-REGLIS3. *Nucl. Instr. Meth. B*, 376:125–130, 2016.

[d+22] R.P. de Groote et al. Precision measurement of the magnetic octupole moment in ^{45}Sc as a test for state-of-the-art atomic- and nuclear-structure theory. *Phys. Lett. B*, 827:136930, 2022.

[Dah00] D. A. Dahl. SIMION for the personal computer in reflection. *Int. Jour. Mass Spectrom.*, 200:3–25, 2000.

[Dem10] W. Demtröder. *Atoms, molecules and photons*. Springer, 2010.

[Dem14] W. Demtröder. *Laser spectroscopy 1: basic principles*. Springer, 2014.

[dG+17] R. P. de Groote et al. Dipole and quadrupole moments of $^{73–78}$Cu as a test of the robustness of the $Z = 28$ shell closure near ^{78}Ni. *Phys. Rev. C*, 96:041302, 2017.

[dGKK+21] R. P. de Groote, S. Kujanpää, Á. Koszorús, J. G. Li, and I. D. Moore. Magnetic octupole moment of ^{173}Yb using collinear laser spectroscopy. *Phys. Rev. A*, 103:032826, 2021.

[DNSc20] A. Drouart, J.A. Nolen, H. Savajols, and S^3 collaboration. The Super Separator Spectrometer (S^3) for the SPIRAL2 facility. *J. Phys. Conf. Ser.*, 1643(1):012032, 2020.

[Dra23] G.W.F. Drake. *Springer handbook of atomic, molecular, and optical physics*. Springer Nature, 2023.

[F+03] V.N. Fedosseev et al. Atomic spectroscopy studies of short-lived isotopes and nuclear isomer separation with the ISOLDE RILIS. *Nucl. Instr. Meth. B*, 204:353–358, 2003.

[F+04] M. Facina et al. A gas cell for thermalizing, storing and transporting radioactive ions and atoms. Part II: On-line studies with a laser ion source. *Nucl. Instr. Meth. B*, 226(3):401–418, 2004.

[F+12] R. Ferrer et al. Performance of a high repetition pulse rate laser system for in-gas-jet laser ionization studies with the Leuven laser ion source @ LISOL. *Nucl. Instr. Meth. B*, 291:29–37, 2012.

[F+13] A. Frisch et al. Hyperfine structure of laser-cooling transitions in fermionic erbium-167. *Phys. Rev. A*, 88:032508, 2013.

[F+17] R. Ferrer et al. Towards high-resolution laser ionization spectroscopy of the heaviest elements in supersonic gas jet expansion. *Nat. Commun.*, 8(1):14520, 2017.

[F+21] R. Ferrer et al. Hypersonic nozzle for laser-spectroscopy studies at 17 k characterized by resonance-ionization-spectroscopy-based flow mapping. *Phys. Rev. Res.*, 3:043041, 2021.

[Fai14] D. C. Faircloth. *Technological Aspects: High Voltage*. CERN, 2014.

[FH04] G. Fricke and K. Heilig. Nuclear Charge Radii · 68-Er Erbium: Datasheet from Landolt-Börnstein - Group I Elementary Particles, Nuclei and Atoms · Volume 20: "Nuclear Charge Radii", 2004.

[FLR85] C. M. Ferreira, J. Loureiro, and A. Ricard. Populations in the metastable and the resonance levels of argon and stepwise ionization effects in a low-pressure argon positive column. *J. Appl. Phys.*, 57(1):82–90, 1985.

[Foo05] C. J. Foot. *Atomic Physics*. OUP Oxford, 2005.

[FR83] C. M. Ferreira and A. Ricard. Modelling of the low-pressure argon positive column. *J. Appl. Phys.*, 54(5):2261–2271, 1983.

[Fri08] A. Fridman. *Plasma Chemistry*. Cambridge University Press, 2008.

[G+06] R. Gobin et al. Development of a permanent magnet light ion source at CEA/Saclay. *Rev. Sci. Instrum.*, 77:03B502, 2006.

[Gal10] S. Gales. SPIRAL2 at GANIL: next generation of ISOL facility for intense secondary radioactive ion beams. *Nucl. Phys. A*, 834(1-4):717c–723c, 2010.

[GKW+22] J.T. Gudmundsson, J. Krek, D.Q. Wen, E. Kawamura, and M.A. Lieberman. Surface effects in a capacitive argon discharge in the intermediate pressure regime. *Plasma Sources Sci. Technol.*, 30(12):125011, 2022.

[GW+18] Bissell M L Gins W, de Groote R P et al. Analysis of counting data: Development of the SATLAS Python package. *Comput. Phys. Commun.*, 222:286–294, 2018.

[H+17a] R. Heinke et al. High-resolution in-source laser spectroscopy in perpendicular geometry: Development and application of the PI-LIST. *Hyperfine Interact.*, 238(1):6, 2017.

[H+17b] Y. Hirayama et al. Doughnut-shaped gas cell for KEK Isotope Separation System. *Nucl. Instr. Meth. B*, 412:11–18, 2017.

[HFK+02] M. Huyse, M. Facina, Yu. Kudryavtsev, P. Van Duppen, and ISOLDE collaboration. Intensity limitations of a gas cell for stopping, storing and guiding of radioactive ions. *Nucl. Instr. Methods B*, 187:535–547, 2002.

[HH11] M. Huber and A. Harvey. *Viscosity of Gases*. CRC-Press, Boca Raton, FL, 92nd edition, 2011.

[Hym79] H. A. Hyman. Electron-impact ionization cross sections for excited states of the rare gases (Ne, Ar, Kr, Xe), cadmium, and mercury. *Phys. Rev. A*, 20:855–859, 1979.

[JNKM09] W.G. Jin, H. Nakai, M. Kawamura, and T. Minowa. High-resolution ultraviolet laser spectroscopy in atomic erbium. *J. Phys. Soc. Jpn.*, 78(1):015001, 2009.

[K+01] Yu. Kudryavtsev et al. A gas cell for thermalizing, storing and transporting radioactive ions and atoms. Part I: Off-line studies with a laser ion source. *Nucl. Instr. Meth. B*, 179(3):412–435, 2001.

[K+16] Yu. Kudryavtsev et al. A new in-gas-laser ionization and spectroscopy laboratory for off-line studies at KU Leuven. *Nucl. Instrum. Meth. B*, 376:345–352, 2016.

[KFH+13] Yu. Kudryavtsev, R. Ferrer, M. Huyse, P. Van den Bergh, and P. Van Duppen. The in-gas-jet laser ion source: Resonance ionization spectroscopy of radioactive atoms in supersonic gas jets. *Nucl. Instr. Meth. B*, 297:7–22, 2013.

[KGBT22] S. Kunze, R. Groll, B. Besser, and J. Thöming. Molecular diameters of rarefied gases. *Sci. Rep.*, 12:2057, 2022.

[Kin13] W. H. King. *Isotope Shifts in Atomic Spectra.* Springer, 2013.

[KS92] S. Kobtsev and N. Sventsitskaya. Application of birefringent filters in continuous-wave tunable lasers: a review. *Opt. Spektrosk*, 73:196–212, 1992.

[KYRN23] A. Kramida, Yu. Ralchenko, J. Reader, and NIST ASD Team. NIST Atomic Spectra Database (ver. 5.11). [Online] Available: `https://physics.nist.gov/asd`. National Institute of Standards and Technology, Gaithersburg, MD., 2023.

[L+16] M. Laatiaoui et al. Atom-at-a-time laser resonance ionization spectroscopy of nobelium. *Nature*, 538:495–498, 2016.

[L+17] X. Ledoux et al. The neutrons for science facility at SPIRAL2. *EPJ Web of Conferences*, 146:03003, 2017.

[L+24a] A. J. Lang et al. A review of hyperloop aerodynamics. *Computers Fluids*, 273:106202, 2024.

[L+24b] J. Lantis et al. In-gas-jet laser spectroscopy of ^{254}No with JetRIS. *Phys. Rev. Res.*, 6(2), 2024.

[M+13] E. Mogilevskiy et al. Area-Mach Number Relationship. Technical report, KU Leuven, 2013.

[MD11] D. J. Manura and D. A. Dahl. *SIMION 8.0/8.1 User Manual: Covering SIMION Version 8.1.0.31.* Scientific Instrument Services, Incorporated, 2011.

[MM73] E. W. McDaniel and E. A. Mason. *Mobility and diffusion of ions in gases.* John Wiley and Sons, Inc., 1973.

[MN87] N. J. Mason and W. R. Newell. Total cross sections for metastable excitation in the rare gases. *J. Phys. B: At. Mol. Phys.*, 20(6):1357, 1987.

[Mog13a] E. Mogelevskiy. Diffusion inside the gas cell for laminar flow. Technical report, KU Leuven, 2013.

[Mog13b] E. Mogelevskiy. Losses in the horn cell. Technical report, KU Leuven, 2013.

[Mou82] P. F. Moulton. Ti-doped sapphire: tunable solid-state laser. *Optics News*, 8:9–9, 1982.

[Mou86] P. F. Moulton. Spectroscopic and laser characteristics of Ti:Al_2O_3. *J. Opt. Soc. Am. B*, 3(1):125–133, 1986.

[MS69] P. C. Magnante and H. H. Stroke. Isotope Shift between ^{209}Bi and 6.3-day ^{206}Bi*. *J. Opt. Soc. Am.*, 59(7):836–841, 1969.

[N$^+$17] R. Neugart et al. Collinear laser spectroscopy at ISOLDE: new methods and highlights. *J.Phys.G*, 44(6):064002, 2017.

[OC97] P. H. Oosthuizen and W. E. Carscallen. *Compressible fluid flow*, volume 179. McGraw-Hill New York, 1997.

[OL77] J. J. Olivero and R. L. Longbothum. Empirical fits to the voigt line width: A brief review. *J. Quant. Spectrosc. Radiat. Transfer*, 17(2):233–236, 1977.

[OM87] H. Okamura and S. Matsuki. Isotope shift in erbium I by laser-atomic-beam spectroscopy. *Phys. Rev. C*, 35(4):1574, 1987.

[PMP$^+$16] P. Papadakis, I. D. Moore, I. Pohjalainen, J. Sarén, and J. Uusitalo. Development of a low-energy radioactive ion beam facility for the mara separator. *Hyperfine Interact.*, 237:1–10, 2016.

[PP85] A. V. Phelps and L. C. Pitchford. Anisotropic scattering of electrons by n_2 and its effect on electron transport. *Phys. Rev. A*, 31:2932–2949, 1985.

[R$^+$20] S. Raeder et al. A gas-jet apparatus for high-resolution laser spectroscopy on the heaviest elements at ship. *Nucl. Instrum. Meth. B*, 463:272–276, 2020.

[R$^+$22] J. Romans et al. First Offline Results from the S^3 Low-Energy Branch. *Atoms*, 10(1), 2022.

[R$^+$23] S. Raeder et al. Opportunities and limitations of in-gas-cell laser spectroscopy of the heaviest elements with radris. *Nucl. Instr. Meth. B*, 541:370–374, 2023.

[RB32] J. E. Rosenthal and G. Breit. The isotope shift in hyperfine structure. *Phys. Rev.*, 41:459–470, 1932.

[Ren12] Karl F Renk. *Basics of laser physics*. Springer, 2012.

[Rot12] S. Rothe. *An all-solid state laser system for the laser ion source RILIS and in-source laser spectroscopy of astatine at ISOLDE, CERN*. PhD thesis, Mainz U., 2012.

[S$^+$91] C. Schulz et al. Resonance ionization spectroscopy on a fast atomic ytterbium beam. *J. Phys. B: At. Mol. Opt. Phys.*, 24(22):4831, 1991.

[S$^+$13] T. Sonoda et al. Development of a resonant laser ionization gas cell for high-energy, short-lived nuclei. *Nucl. Instr. Meth. B*, 295:1–10, 2013.

[SAW85] W. Klempt R. Neugart S.A. Ahmad, C. Ekstrom and K. Wendt. Nuclear spins and moments of radioactive odd-A isotopes of erbium studied by collinear fast-beam laser spectroscopy. In *Proceedings of the "Symposium on Quantum Electronics"*, 1985.

[Sel69] E. C. Seltzer. k x-ray isotope shifts. *Phys. Rev.*, 188:1916–1919, 1969.

[Sor04] E. Sorokin. *Solid-State Materials for Few-Cycle Pulse Generation and Amplification*, volume 95. Springer, 2004.

[ST19] B. E. A. Saleh and M. C. Teich. *Fundamentals of photonics*. John Wiley & Sons, 2019.

[Stu20] D. Studer. *Probing atomic and nuclear structure properties of promethium by laser spectroscopy*. PhD thesis, Mainz, 2020.

[T+12a] T. Thuillier et al. Recent results of PHOENIX V2 and new prospects with PHOENIX V3. In *ECRIS2012, Sydney, Australia*, 2012.

[T+12b] C. Torres et al. Paschen law for argon glow discharge. *J. Phys.: Conf. Ser.*, 370(1):012067, 2012.

[Tab] Atomic weights and isotopic compositions for all elements. `https://physics.nist.gov/cgi-bin/Compositions/stand_alone.pl`.

[Tac86] K. Tachibana. Excitation of the $1s_5$,$1s_4$, $1s_3$, and $1s_2$ levels of argon by low-energy electrons. *Phys. Rev. A*, 34:1007–1015, 1986.

[TFR85] G. Torbohm, B. Fricke, and A. Rosén. State-dependent volume isotope shifts of low-lying states of group-IIa and -IIb elements. *Phys. Rev. A*, 31:2038–2053, 1985.

[TMST07] D. Tskhakaya, K. Matyash, R. Schneider, and F. Taccogna. The Particle-In-Cell Method. *Contrib. Plasma Phys.*, 47(8-9):563–594, 2007.

[V+20] M. Verlinde et al. On the performance of wavelength meters - Part 1: consequences for medium-to-high-resolution laser spectroscopy. *Appl. Phys. B*, 126:1–14, 2020.

[Van20] M. Vandebrouck. Spectroscopy Electron Alpha in Silicon bOx couNter – SEASON. Project ANR-20-CE31-0005, 2020.

[VD+92] P. Van Duppen et al. A laser ion source for on-line mass separation. *Hyperfine Interact.*, 74:193–204, 1992.

[Wad13] M. Wada. Genealogy of gas cells for low-energy RI-beam production. *Nucl. Instrum. Meth. B*, 317:450–456, 2013.

[YWWR23] X.F. Yang, S.J. Wang, S.G. Wilkins, and R.F. Garcia Ruiz. Laser spectroscopy for the study of exotic nuclei. *Prog. Part. Nucl. Phys.*, 129:104005, 2023.

[Z+14] V.I. Zagrebaev et al. Gas-cell-based setup for the production and study of neutron-rich heavy nuclei. *Hyperfine Interact.*, 227:181–189, 2014.

[Z+23] A. Zadvornaya et al. Offline commissioning of a new gas cell for the MARA Low-Energy Branch. *Nucl. Instr. Meth. B*, 539:33–42, 2023.

[Zad18] A. Zadvornaya. *Characterization of the spectral resolution of the in-gas-jet laser ionization spectroscopy method*. PhD thesis, KU Leuven, 2018.

[Zim06] W.B.J. Zimmerman. *Multiphysics Modeling With Finite Element Methods*. World Scientific Publishing Company, 2006.